



The University of  
**Nottingham**

UNITED KINGDOM • CHINA • MALAYSIA

# **BUILDING 3D ARCHITECTURES FOR CARDIOMYOCYTES**

**Aylin Turgut, M.S**

**Thesis submitted to the University of Nottingham  
for the degree of Doctor of Philosophy**

**Faculty of Engineering**

**SEPTEMBER 2020**

**Supervisors: Ricky Wildman, Derek Irvine, Morgan Alexander,  
Andrew Hook and Qin Hu**

## **Acknowledgements**

It has taken commitment and perseverance to get to this point of my doctoral project. I could not have reached this point so easily without the support of so many people I would like to thank here.

Firstly, I am deeply grateful to Professor Ricky Wildman, Professor Derek Irvine and Professor Morgan Alexander for giving me such an interesting research topic. I am also grateful to Dr. Andrew Hook for providing me with advice and assistance in collecting my materials from the department of pharmacy. I would also like to thank the Additive Manufacturing and 3D Printing Research Group, AMHT group and Maria Barbadillo-Munoz from CBS (Centre for Biological Sciences) for their great support and helping me learn to make use of the facilities in the laboratory.

Finally, I would like to thank my family, my mother Margaret Turgut, my father Asim Turgut and my brother Burhan Turgut for their wonderful support and encouragement.

A special thank you goes to my two sisters Carina Ivascu and Sok Kong Taing for their amazing support, encouragement and help during this PhD project.

## ABBREVIATIONS

2PL: 2-photon lithography

2PP: 2-photon polymerisation

AEMA.c: Amino ethyl acrylamide chloride

AEMAM.c: Amino ethyl methacrylamide hydrochloride

APMAM.c: Amino propyl methacrylamide hydrochloride

BDDA: Butanediol diacrylate

CM: Cardiomyocyte

DAPI: Di-amino phenyl-indole

EBL: electron beam lithography

ECM: Extracellular matrix

EC: Endothelial cell

ESC: Embryonic Stem cells

FBS: Foetal Bovine Serum

GPOTA: Glycerol propoxylate triacrylate

HEODA: Hexanediol ethoxylate diacrylate

IM: Immunostaining

iPSCs: Induced pluripotent stem cells

PETrA: Pentaerythritol triacrylate

PI: photoinitiator

pPGDA: Poly propylene glycol diacrylate

TCDMDA: Tricyclodecane dimethanol diacrylate

## Contents

|  |    |
|--|----|
| Chapter 1: Introduction and General Literature Review .....  | 2  |
| 1.1: Introduction .....  | 2  |
| 1.1.1 Background: .....  | 2  |
| 1.1.2 Research Problem and Hypothesis .....  | 4  |
| 1.1.3: Justifications for the Research: Emphasis on the importance of the need to answer the research question and how this will benefit the scientific community and society..... | 5  |
| 1.1.4: Aims and Objectives of the Research .....   | 5  |
| 1.1.5: Limitations: Any limitations the research work may have and how this may affect the outcome. ....   | 6  |
| 1.1.6 Outline of the thesis .....  | 2  |
| 1.1.7: Conclusion .....  | 6  |
| 1.2: Literature Review.....  | 7  |
| 1.2.1: Introduction .....  | 7  |
| 1.2.2: Literature Review.....  | 8  |
| 1.2.3: Mapping the Process: .....  | 34 |
| 1.2.4: Summary.....  | 35 |
| Chapter 2: Methodologies.....  | 36 |
| 2.1 2-photon lithography.....  | 36 |
| 2.1.1 Background .....   | 36 |
| 2.1.2 Formulation Preparation .....  | 37 |
| 2.1.3 2-Photon Lithography .....   | 38 |
| 2.1.4: Designing a systematic screening method using a combination of photoinitiator concentration, laser power and scanspeed parameters .....                                     | 39 |
| 2.1.5 Selection of designs for 2PL.....  | 46 |
| 2.1.6 Post-development .....   | 51 |
| 2.2 Platinum Sputter Coating of glass cover slips.....   | 51 |
| 2.3 Scanning electron microscopy.....  | 52 |
| 2.4 Oxygen Plasma Etching.....   | 52 |
| 2.5 Silanisation.....  | 53 |
| 2.6 Cardiomyocyte Culture .....  | 55 |
| 2.6.1. Cell Culture Procedure .....  | 56 |
| 2.6.2 CM attachment to construct testing .....   | 67 |
| 2.6.3 CM attachment experimental design .....  | 69 |
| 2.7 UV polymerisation .....  | 71 |



|   |     |
|---|-----|
| 2.7.1 Determination of the correct solvent at a suitable concentration for silanisation for polymer attachment to 96-well polystyrene plates .....  | 72  |
| 2.7.2 Determination of the necessity of silanised wells for UV polymerisation..   | 74  |
| 2.7.3 UV polymerisation .....   | 76  |
| 2.7.4 Thin film Design for Cardiomyocyte Seeding.....   | 81  |
| 2.7.5 Fabrication of Complex Architectures .....  | 83  |
| 2.7.6 Open channels of different curvatures.....  | 85  |
| 2.7.7 Plasma activation and silanisation of glass cover slips for 2-photon fabricated structures to be used in CM attachment experiments .....      | 97  |
| 2.8 Immunostaining and DAPI Staining .....  | 99  |
| 2.8.1 Day 1 .....   | 100 |
| 2.8.2 Day 2 .....   | 101 |
| 2.8.3 Preparation for imaging.....  | 102 |
| 2.9 Wide-field confocal microscopy .....  | 102 |
| 2.10 Raman Spectroscopy .....   | 103 |
| 2.11 Reasoning for Methods Selected in the Research.....  | 107 |
| Chapter 3: Determination of materials amenable to 2-photon lithography using a systematic processing approach.....                                  | 109 |
| 3.1 Introduction .....  | 109 |
| 3.2 RESULTS .....   | 110 |
| 3.2.1 Monomer compatibility to 2-photon lithography .....   | 110 |
| 3.2.2 Monomer selection and testing amenability to 2-photon lithography....   | 112 |
| 3.2.2 Operating window determination for 2-photon amenable homopolymers .....   | 128 |
| 3.2.3 Complex architecture design for 2-photon lithography .....  | 147 |
| 3.2.4 2-photon fabricated topologies for CM attachment .....  | 151 |
| 3.3 Discussion and Conclusions .....  | 170 |
| 3.4 Future Work.....  | 174 |
| CHAPTER 4: Cardiomyocyte attachment experiments on UV-polymerized constructs leading to complex structure fabrication by 2-photon lithography ..... | 176 |
| 4.1 Introduction .....  | 176 |
| 4.2 Results.....  | 177 |
| 4.2.1 Determination of the correct solvent at a suitable concentration for silanisation for polymer attachment to polystyrene plates .....          | 177 |
| 4.2.2 Determination of the necessity of silanising wells for UV polymerisation  | 178 |
| 4.2.3 Induced pluripotent stem cell (iPSC) culture .....  | 181 |
| 4.2.4 iPSC differentiation to cardiomyocytes .....  | 184 |

|  |     |
|--|-----|
| 4.2.5. Cardiomyocyte attachment to UV-polymerised constructs .....   | 189 |
| 4.3 Discussion and Conclusions .....   | 198 |
| 4.4 Future Work.....   | 199 |
| Chapter 5: Investigation of the effect of 3D architecture on CM attachment and maturity. Additional effect of post-fabrication method in an attempt to improve degree of cure.....           | 200 |
| 5.1 Introduction .....   | 200 |
| 5.2 Results.....   | 201 |
| 5.2.1 Raman Spectroscopy Measurements .....  | 201 |
| 5.2.2 Comparison of CM attachment and maturity on 2-photon fabricated constructs without post-fabrication treatment versus constructs treated with vacuum and post-fabrication UV cure ..... | 205 |
| 5.3 Discussion and Conclusions .....   | 229 |
| 5.4 Future Work.....   | 233 |
| Chapter 6: Overall Conclusions for the PhD Hypothesis and Future Perspectives....  | 234 |
| 6.1 Overall Conclusions.....   | 234 |
| 6.2 Future Perspectives .....  | 235 |
| Appendix.....  | 238 |
| 1.1 Raman Spectroscopy .....   | 238 |
| 1.1.1 Polymers with no UV or vac treatment .....   | 240 |
| 1.1.2 Polymers with vacuum treatment .....   | 242 |
| 1.1.3 Polymers treated with post-fabrication UV light.....   | 244 |
| 1.2 Statistical tests on CMs.....  | 247 |
| 1.2.1 Statistical Tests on Sarcomere Length .....  | 247 |
| 1.3 Qualitative Results for CM attachment on UV-polymerised acrylates.....   | 254 |

## LIST OF FIGURES

|   |    |
|---|----|
| <b>Figure 1.2: Three main types of substrate Nano topography that are used to study cell-substrate interactions; Nano gratings, Nano posts and Nano pits (Bettinger et al., 2009).</b> .....  | 9  |
| <b>Figure 1.1a: Initiation stage of photo polymerisation (</b> .....  | 18 |
| <b>Figure 1.1b: The generation of free radicals and the 3 stages of polymerization; initiation, propagation and termination. There are three stages of polymerisation: initiation, propagation and termination. Initiation involves absorption of the photons of a specific wavelength by the photo initiator and formation of a radicalised monomer. Propagation is the subsequent attack of the free monomers by the radicalised monomer. Termination occurs when two radicalised monomers react with each other, rendering them neutral (Carragher, 2007).</b> ..... | 18 |
| <b>Figure 2.1: Two-photon lithography system (Ciuciu and Cywiński, 2014).</b> .....   | 36 |
| <b>Figure 2.2: Gear design with dimensions of 100 µm (x), 100 µm (y) and 5 µm (z).</b> .....  | 46 |
| <b>Figure 2.3: top: Close-up view of hatching pattern on gear design. Bottom: Close-up view of slicing showing all 10 slices of gear design.</b> .....  | 47 |
| <b>Figure 2.4: Woodpile design as created in AutoCAD software. Left: View from top. Right: Lateral view showing both layers.</b> .....  | 48 |
| <b>Figure 2.5: Woodpile structure which measured 30 (x) by 30 (y) µm.</b> .....   | 49 |
| <b>Figure 2.6: Woodpile design organised as a 4 by 20 array. Each woodpile structure was processed 4 times at each assigned laser power. The laser power was assigned at increments of 5 from 1-100% starting from the bottom to the top.</b> .....   | 50 |
| <b>Figure 2.7: Oxygen plasma cleaning and activation procedure (Wang et al., 2014).</b> .....   | 53 |
| <b>Figure 2.8: Structure of trimethoxysilane molecules (bottom) attached to the glass cover slip (blue stripes). The terminal acrylate ends of the silane molecules polymerise with the acrylate monomers (top) used in the experiment.</b> .....   | 54 |
| <b>Figure 2.9: Flow diagram of the IPSC T75 flask splitting process. If a differentiation is planned, then one flask is split 1 in 10 and kept as a maintenance flask of iPSCs and the other 4 flasks are split 1 in 5 to prepare for differentiation to cardiomyocytes.</b> .....  | 60 |

|   |           |
|---|-----------|
| <b>Figure 2.10: Schematic of monolayer differentiation of iPSCs to cardiomyocytes highlighting each time point and the small molecules added at each these stages.....</b>  | <b>61</b> |
| <b>Figure 2.11: 96-well plate setup for UV polymerization. A-E refers to the polymers tested. Matrigel (G) serves as a positive control for CM attachment. Tissue culture plastic (TCP, H) is a negative control.....</b>             | <b>68</b> |
| <b>Figure 2.12: 6-well cell culture polystyrene plate schematic illustrating a typical experiment for testing CM attachment on 2-photon fabricated constructs, including positive control Matrigel and negative control TCP. ....</b> | <b>70</b> |
| <b>Figure 2.13: Experimental design showing the range of silane concentrations in acetone and isopropanol in a 96-well plate. ....</b>  | <b>73</b> |
| <b>Figure 2.14: 0.5 µl/ml silane:isopropanol v/v was used for each sample (the optimum concentration, detailed in section 4.2.1.1) and added to 25 µl of a monomer/PI mixture. ....</b>   | <b>75</b> |
| <b>Figure 2.15a: BRAUN© LABstar Argon glovebox for UV polymerisation. ....</b>  | <b>77</b> |
| <b>Figure 2.15b: Argon gas supply controls opposite the Argon glovebox (top left). Sample insertion chamber with associated valves (top right) and oxygen sensor connected to the glovebox (bottom).....</b>                          | <b>78</b> |
| <b>Figure 2.16: 96-well plate setup for UV polymerization. A-E refers to the polymers tested. Matrigel (G) serves as a positive control for CM attachment. Tissue culture plastic (TCP, H) is a negative control.....</b>             | <b>80</b> |
| <b>Figure 2.17: Thin film construct for cardiomyocyte viability testing and enlarged image of one corner showing each fabrication line (bottom). Images were captured from Describe software.....</b>                                 | <b>82</b> |
| <b>Figure 2.18: Images for the DNA double helix and the anatomical heart (bottom) designs captured the Describe software.....</b>   | <b>84</b> |
| <b>Figure 2.19: Flow diagram of the generation of open-channel structures showing the initial cylinder shape until the final open-channel structures on a platform. Images were captured from AutoCAD 2018 software. ....</b>         | <b>86</b> |
| <b>Figure 2.20: Design of 60° (top) and 100°-degree curvature architectures captured from Describe software. ....</b>   | <b>88</b> |
| <b>Figure 2.21: Design of 160° degree curvature architecture captured from Describe software.....</b>   | <b>89</b> |

|  |            |
|--|------------|
| <b>Figure 2.22: Image captured on Describe software of box with grooves design of different curvatures at a smaller scale.....</b>   | <b>89</b>  |
| <b>Figure 2.23: Multiplex construct consisting of flat section on the left followed by the grooves region on the right. The image was captured on Describe software.....</b>   | <b>91</b>  |
| <b>Figure 2.24: Top: grooves with hatching lines in the 90° horizontal direction and bottom: flat region of multiplex construct with hatching direction 60° indicated by the black arrows on both designs. ....</b>  | <b>92</b>  |
| <b>Figure 2.25: New design images captured from Describe software with varying hatching angles in the flat region followed by a 200 µm gap and one stl. file of the grooves regions on the right. The slight variation in colour of the grooves region indicates the different depths with the white one on the left-hand side being the shallowest and the solid blue being the deepest region.....</b> | <b>93</b>  |
| <b>Figure 2.26: The flat region of the new multiplex showing the 0° hatching direction on the left and the 90° hatching direction on the right. (bottom) shows the hatching direction of 120° on the left and 60° on the right. ....</b>   | <b>94</b>  |
| <b>Figure 2.27: Illustration of the grooves region of the new multiplex design. Top: The shallow part of the grooves region with hatching direction 0°. Bottom: The medium-depth of the grooves region illustrating the deeper grooves compared to the one shallow groove on the left hand side. ....</b>  | <b>95</b>  |
| <b>Figure 2.28: The deep grooves region with hatching direction of 0° (bottom): Enlarged image of the corner deep groove. The z scale is illustrated on the right in µm units. The groove depth is 12 µm.....</b>  | <b>96</b>  |
| <b>Figure 2.29: Experimental setup for the silanisation of glass cover slips in an Argon atmosphere. ....</b>  | <b>98</b>  |
| <b>Figure 2.30: 50X light microscopy image of cube structure fabricated for Raman spectroscopy.....</b>  | <b>105</b> |
| <b>Figure 3.1: Molecular structures of the 3 methacrylate homopolymers selected for amenability to 2PL. ....</b>   | <b>112</b> |
| <b>Figure 3.2: SEM images of methacrylate formulations a) tertbutylaminoethylmethacrylate b) furfuryl methacrylate c) isobornyl methacrylate, APMAM.c, AEMA.c and AEMAM.c polymers.....</b>  | <b>114</b> |
| <b>Figure 3.3: Molecular structure of Bisphenol A glycerolate diacrylate (BPAPGDA). ....</b>   | <b>116</b> |
| <b>Figure 3.4a: Molecular structures of multi-functional acrylate monomers that were selected for 2PL processing.....</b>  | <b>117</b> |

|  |            |
|--|------------|
| <b>Figure 3.4b: Molecular structures of multi-functional acrylate monomers that were selected for 2PL processing.....</b>  | <b>118</b> |
| <b>Figure 3.5: Molecular structures and corresponding SEM images taken using highest laser power and low scanspeed at 5% photoinitiator concentration of from left to right: HEODA, HMDA and GPOTA, TCDMDA, PETrA and ZrCEA (centre), BDDA and TMPTA (bottom).119</b>  | <b>119</b> |
| <b>Figure 3.6: SEM images of the 3 methacrylamide salts APMAM.c, AEMA.c, and AEMAM.c that were tested for their amenability to 2PL. No fabrication was observed for any of the monomers.....</b>   | <b>121</b> |
| <b>Figure 3.7: SEM image of gear design taken using highest laser power and low scanspeed at 5% photoinitiator concentration using the HEODA:PPGDA co-polymer formulation. ....</b>  | <b>123</b> |
| <b>Figure 3.8: SEM images of gear designs using 5% PI concentration and the co-polymer compositions in the order outlined in Table 3.4 with the first image being 70:30 ratio and the final image being 99:1 ratio. ....</b>   | <b>124</b> |
| <b>Figure 3.9: SEM image taken using highest laser power and low scanspeed at 5% photoinitiator concentration for HEODA:PPGDA, PPGDA:GPOTA, HEODA:PPGA and BDDA:GPOTA co-polymer formulations. ....</b>  | <b>126</b> |
| <b>Figure 3.10: SEM images of fabricated gear structures at 3% I369 concentration. The energy values utilised were as per protocol in the Methods section, Table 5.....</b>  | <b>129</b> |
| <b>Figure 3.11: 1st round of processing for GPT with zones A, B and C and 1 or 0 scores assigned according the quality scale. ....</b>   | <b>129</b> |
| <b>Figure 3.12: 2nd round of processing for GPT with zones A, B and C and 1 or 0 scores assigned according the quality scale. ....</b>   | <b>130</b> |
| <b>Figure 3.13: 3rd round of processing for GPT with zones A, B and C and 1 or 0 scores assigned according the quality scale. ....</b>   | <b>131</b> |
| <b>Figure 3.14: Trend of how Emax and Emin vary according to photo initiator concentration in GPOTA. ....</b>  | <b>133</b> |
| <b>Figure 3.15: Structures processed using control formulations which consisted of glycerol propoxylate triacrylate only, without photo initiator using the woodpile design. (Energy absorption from left to right and down (pJ), 60, 50, 42.9, 37.5, 33.3,30, 24, 20, 17.1). Bottom right corner: Woodpile structure design on AutoCAD.....</b> | <b>135</b> |

|  |            |
|--|------------|
| <b>Figure 3.16: SEM image of HMDA structures from left to right: Highest focal spot energy absorption at 60 pJ to lowest at 3.6 pJ with a constant scanspeed of 1000 <math>\mu\text{m/s}</math>.....</b>   | <b>136</b> |
| <b>Figure 3.17: SEM images at higher magnification of the same structures from Figure 3.19. Left to right: 60, 30, 15, 10, 7.5, 6, 4.8, and 3.6 pJ.....</b>  | <b>137</b> |
| <b>Figure 3.18: Trend of how <math>E_{\text{max}}</math> and <math>E_{\text{min}}</math> vary according to photo initiator concentration in HMDA.....</b>  | <b>138</b> |
| <b>Figure 3.19: SEM images of HEODA structures at 5% PI concentration. Left to right: 60, 30, 15, 10, 7.5 and 6 pJ. ....</b>   | <b>138</b> |
| <b>Figure 3.20: Trend of how <math>E_{\text{max}}</math> and <math>E_{\text{min}}</math> vary according to photo initiator concentration for HEODA.....</b>  | <b>139</b> |
| <b>Figure 3.21: SEM images of HEODA:EEMA co-polymer structures at 5% PI concentration. Left to right: 30, 20, 18.8, 18.18, 17.14, 15, 10, 7.5, 6 and 5 pJ.....</b>   | <b>140</b> |
| <b>Figure 3.22: Power sweep of woodpile structures, from highest to lowest energy absorption. SEM images of woodpile structures at energy values (from left to right) A: 60, 50, 42.9, 37.5, B: 33.3, 30, 24, 20, C: 17.1, 15, 10 and 7.5 pJ. D: 6, 4.8, 3.6, 2.4, E: 1.8, 1.2, 1.0, 0.9, and F: 0.8, 0.6 and 0.3 pJ. ....</b>                             | <b>142</b> |
| <b>Lower right: Woodpile structure design on AutoCAD which was the ultimate structure desired to be processed.....</b>   | <b>142</b> |
| <b>Figure 3.23: SEM image of woodpile design generated by Describe software. Damage is evident throughout the whole structure which indicates consistency within the whole design. Woodpile array of GPOTA at 3% PI concentration. The lines indicate <math>E_{\text{max}}</math> and <math>E_{\text{min}}</math> at 54 pJ and 18 pJ respectively.....</b> | <b>143</b> |
| <b>Figure 3.24: SEM images of woodpile arrays for HEODA. Whole woodpile array (left) from lowest laser power to highest laser power (left to right). SEM image zoom of left side of the array illustrating the point at which structures begin to fade and the operating window is shown by the blue lines (25-30 pJ).....</b>                             | <b>144</b> |
| <b>Figure 3.25: SEM image of TCDMDA at 3% PI concentration of the woodpile array from lowest to highest laser power values (left to right). ....</b>   | <b>146</b> |
| <b>Figure 3.26: SEM images of woodpile arrays of BDDA:GPOTA, HEODA:PPGDA and PPGDA:GPOTA copolymers at 1% PI concentration.....</b>  | <b>146</b> |

**Figure 3.27: SEM images of anatomical heart structures fabricated by 2PL. Top left: Aerial view of the heart veins and aorta. Top right: Zoomed in image of the vessels on the heart surface, detailing slicing lines. Bottom: Aerial view of the whole heart structure. .... 148**

**Figure 3.28: Aerial views of the DNA double helix structures fabricated by 2PL. .... 149**

**Figure 3.29: Schematic illustrating the concept of how the operating windows of various structure designs relate to each other. .... 150**

**Figure 3.30: SEM images of 50° open-channel structures fabricated by 2PL. Top left: 42 pJ, top right: 39 pJ and bottom: 36 pJ. .... 152**

**Figure 3.31: SEM images of 100° open-channel structures fabricated by 2PL. Top left: 39 pJ, Top right: 30 pJ, Middle left: 27 pJ, Middle right: Enlarged image of structure fabricated with 27 pJ showing damaged side. Bottom: Image of structure fabricated with 27 pJ showing complete side. .... 153**

**Figure 3.32: SEM images of open-channel structures on the platform design. The open-channels at the front have 160° curvatures, the ones in the middle 100° curvature and the ones at the back have 50° curvatures. .... 154**

**Figure 3.33: SEM images of each open-channel structure that were fabricated simultaneously on the platform. Top: 160° curvatures, bottom left: 100° curvature and bottom right: 50° curvatures. .... 155**

**Figure 3.34: Top: Enlarged SEM image of 160° curvature structure. Measurements of hatching distance were made at the locations of labelled numbers on ImageJ software. Bottom: Table of hatching distance measurements. .... 156**

**Figure 3.35: Top: Enlarged SEM image of 100° curvature structure. Measurements of hatching distance were made at the locations labelled as numbers on ImageJ software. Bottom: Table of hatching distance measurements. .... 157**

**Figure 3.36: Top: Enlarged SEM image of 50° curvature structure with measurements of hatching distance done on ImageJ software labelled by number. Bottom: Table of hatching distance measurements. .... 158**

**Figure 3.37: SEM images of open-channel multiplex structure fabricated with TCMDA at 27 pJ. Top: Aerial view and Bottom: Enlarged image of left-hand corner of the structure showing criss-cross 90° hatching direction. .... 160**



|   |            |
|---|------------|
| <b>Figure 3.38: SEM images of multiplex structure fabricated with TCDMDA at 27 pJ. Top: Aerial view of multiplex structure. Bottom: Enlarged image of the flat region and shallow grooves region interface.....</b> | <b>161</b> |
| <b>Figure 3.39: SEM images of medium-depth 5 µm grooves (top) and deepest 10 µm grooves region of TCDMDA multiplex structure.....</b>   | <b>162</b> |
| <b>Figure 3.40: SEM image of 5 µm medium-depth grooves labelled with measurements made on groove width and depth on ImageJ software. Table of all measurements (bottom). .....</b>                                  | <b>163</b> |
| <b>Figure 3.41: SEM image of 10 µm deep grooves labelled with measurements made on groove width and depth on ImageJ software. Table of all measurements (bottom). .....</b>   | <b>164</b> |
| <b>Figure 3.42: SEM image of multiplex structure with flat region and grooves region. The two were separated by a small gap. The polymer used for fabrication was TCDMDA.....</b>                                   | <b>166</b> |
| <b>Figure 3.43: SEM images showing the flat region of the fabricated TCDMDA multiplex construct with 0 and 90 (top, left and right side), 60 (middle) and 120 bottom degrees hatching directions. ....</b>          | <b>167</b> |
| <b>Figure 3.44: PETrA multiplex construct showing 0° hatching distance .</b>  | <b>168</b> |
| <b>Figure 3.45: PETrA multiplex construct showing the flat region and hatching directions from top left: 90°, top right: 0°, bottom left: 60° and bottom right: 120°.....</b>                                       | <b>169</b> |
| <b>Figure 4.1: IPSC colonies ready for splitting after 72 hours.....</b>  | <b>182</b> |
| <b>Figure 4.2: IPSCs 24 hours after splitting.....</b>  | <b>182</b> |
| <b>Figure 4.3: IPSC colonies 48 hours after splitting.....</b>  | <b>183</b> |
| <b>Figure 4.4: Characteristic ‘cheese’ morphology on day 0 of cardiac differentiation.....</b>  | <b>184</b> |
| <b>Figure 4.5: Cells on day 2 of differentiation b: before feeding and bottom: after feeding.....</b>   | <b>185</b> |
| <b>Figure 4.6: Cells on day 4 of cardiac differentiation. The monolayer can be clearly observed at this stage. ....</b>   | <b>186</b> |
| <b>Figure 4.7: Day 6 of cardiac differentiation. Cell death occurs again at this step. ....</b>   | <b>186</b> |
| <b>Figure 4.8: Day 8 of cardiac differentiation. Beating can be observed from this day onwards however they are not ready for dissociation yet. ....</b>  | <b>187</b> |

|  |            |
|--|------------|
| <b>Figure 4.9: Days 10-14 of differentiation. Cardiomyocytes are ready for dissociation at this stage. ....</b>  | <b>188</b> |
| <b>Figure 4.10: Quantitative Analysis of CM attachment on all polymers with 3 different photoinitiator formulations in RILT medium.....</b>  | <b>189</b> |
| <b>Figure 4.11: Quantitative Analysis of CM attachment on all polymers with 3 different photoinitiator formulations in RPMI B27 medium.....</b>  | <b>192</b> |
| <b>Figure 5.1: Comparison of all C=C to C=O ratio values of the 3 polymers under each post-fabrication treatment condition. ....</b>   | <b>203</b> |
| <b>Figure 5.2: Light microscopy image at 10X magnification of TCDMDA construct without post-fabrication treatment. The grooved region shows some cell attachment however visualisation is a challenge for this region therefore immunostaining is performed.....</b>   | <b>206</b> |
| <b>Figure 5.3: Immunostained image of cardiomyocytes attached to glass cover slip surface surrounding the TCDMDA construct (left) and TCDMDA flat region (right) without post-fabrication treatment. ....</b>  | <b>207</b> |
| <b>Figure 5.4: Tcdmda without post-fabrication treatment overall at 20X magnification on the Exciter Wide-field microscope. ....</b>   | <b>208</b> |
| <b>Figure 5.5: 40X (left) and 63X (right) wide-field images of cells on the TCDMDA construct without post-fabrication UV cure. The 63X image highlights the clarity at which sarcomere bands can be visualised, complete with troponin (red) and <math>\alpha</math>-actinin (green) band staining. Top: Light microscopy image from Figure 5.1 indicating where the fluorescent images correspond to.....</b> | <b>209</b> |
| <b>Figure 5.6: Comparison of average sarcomere length against groove depth in TCDMDA construct without post-fabrication treatment.....</b>   | <b>210</b> |
| <b>Figure 5.7: Bar chart showing the levels of roundness in each topological region of TCDMDA without post-fabrication treatment.....</b>  | <b>211</b> |
| <b>Figure 5.8: Image of colour-coded cells after ImageJ Orientation plugin was applied on the flat glass control (top), TCDMDA flat region (top right) and grooves region (bottom) without post-fabrication treatment. Colour chart of orientation degrees (bottom right).....</b>   | <b>212</b> |
| <b>Figure 5.9: Orientation distribution of flat glass control (top), flat region of construct (middle) and grooves region (bottom) on TCDMDA without post-fabrication treatment. ....</b>  | <b>213</b> |
| <b>Figure 5.10: Light microscopy image of TCDMDA construct with post-fabrication UV light treatment at 10X magnification. ....</b>   | <b>214</b> |

|   |     |
|---|-----|
| <b>Figure 5.11: Flat glass control showing cells immunostained for cardiac Troponin-T (red), <math>\alpha</math>-actinin (green) and DAPI (blue). The red and green channels appear orange when all channels are merged.</b> .....  | 215 |
| <b>Figure 5.12: Cells attached to the flat region of the TCDMDA construct with post-fabrication UV cure. Red staining is for cardiac-troponin T, green for <math>\alpha</math>-actinin and blue staining for DAPI in the cell nuclei (top) and cells on a TCDMDA construct with post-fabrication UV cure. Red staining is for cardiac-troponin T, green for <math>\alpha</math>-actinin and blue staining for DAPI in the cell nuclei (bottom).</b> ..... | 216 |
| <b>Figure 5.13: Comparison of average sarcomere length of CMs on topologically different regions of TCDMDA with post-fabrication UV light treatment.</b> .....  | 217 |
| <b>Figure 5.14: Bar chart showing nuclear roundness levels on the various topological features of TCDMDA with post-fabrication UV light treatment.</b> .....  | 220 |
| <b>Figure 5.15: Cell Orientation Colour Survey image and informational colour chart (bottom right) on flat glass control (top left), flat region (top right) and grooves region (bottom) of TCDMDA flat glass control with post-fabrication UV light treatment.</b> .....   | 221 |
| <b>Figure 5.16: Orientation distribution histograms of flat glass control (top), flat region (middle) and grooves region (bottom) of TCDMDA with post-fabrication UV light treatment.</b> .....   | 222 |
| <b>Figure 5.17: Immunostaining image of cells attached to flat glass control (left), TCDMDA flat region (right) and grooved region (bottom) used in the experiments with TCDMDA post-fabrication vacuum treatment.</b> ....   | 223 |
| <b>Figure 5.18: Column chart comparing the average sarcomere length on each topological feature of TCDMDA treated with vacuum post-fabrication.</b> .....   | 224 |
| <b>Figure 5.19: Column chart showing comparing the average nuclear roundness on each topological feature of TCDMDA treated with vacuum post-fabrication.</b> .....  | 225 |
| <b>Figure 5.20: Colour survey of flat glass control (top left), flat region (top right) and grooves region (bottom) for TCDMDA with post-fabrication vacuum treatment. The colour chart indicates how each colour corresponds to a specific angle (bottom left).</b> .....  | 226 |
| <b>Figure 5.21: Orientation distribution histogram of flat glass control (top), flat region (middle) and grooves region (bottom) of TCDMDA construct with post-fabrication vacuum treatment.</b> .....  | 227 |

|   |            |
|---|------------|
| <b>Figure A1: Spectra of uncured TCDMDA, GPOTA and PETrA displaying all 4 repeat measurements.....</b>  | <b>239</b> |
| <b>Figure A.2: Spectra of polymers TCDMA, GPOTA and PETrA with no post-fabrication treatment. ....</b>  | <b>241</b> |
| <b>Figure A.3: Spectra of polymers TCDMA, GPOTA and PETrA with post-fabrication vacuum treatment. ....</b>  | <b>243</b> |
| <b>Figure A.4: Spectra of polymers TCDMA, GPOTA and PETrA with post-fabrication UV light treatment. ....</b>  | <b>245</b> |
| <b>Figure A.5: Image of the nuclei analysed on flat glass control of the TCDMDA constructs experiments without post-fabrication treatment using ImageJ software. ....</b> | <b>251</b> |
| <b>Figure A.6: Image of the nuclei analysed on TCDMDA flat region of the constructs without post-fabrication treatment using ImageJ software. ...</b>                     | <b>251</b> |
| <b>Figure A.7: Image of the nuclei analysed on the grooved region of the TCDMDA construct without post-fabrication treatment using ImageJ software. ....</b>              | <b>252</b> |
| <b>Figure A.8: Light microscopy images of BDDA polymer with CMs attached. ....</b>  | <b>254</b> |
| <b>Figure A.9: Light microscopy images of HEODA polymer with CMs attached. ....</b>   | <b>255</b> |
| <b>Figure A.10: Light microscopy images of TCDMDA polymer with CMs attached. ....</b>   | <b>256</b> |
| <b>Figure A.11: Light microscopy images of PETrA polymer with CMs attached. ....</b>  | <b>257</b> |
| <b>Figure A.12: Light microscopy images of pPGDA polymer with CMs attached. ....</b>  | <b>258</b> |
| <b>Figure A.13: Light microscopy images of GPOTA showing no attachment and round, dead cells. ....</b>  | <b>259</b> |
| <b>Figure A.14: Light microscopy images of BDDA polymer showing no attachment and round, dead cells. ....</b>   | <b>260</b> |
| <b>Figure A.15: Light microscopy images of HEODA polymer with CMs attached. ....</b>  | <b>261</b> |

|  |            |
|--|------------|
| <b>Figure A.16: Light microscopy images of TCDMDA polymer showing no attachment and round, dead cells and with CMs attached (right and bottom).....</b>  | <b>262</b> |
| <b>Figure A.17: Light microscopy images of PETrA polymer with the round morphology of dead cells.....</b>  | <b>263</b> |
| <b>Figure A.18: Light microscopy images of pPGDA polymer showing no attachment and round, dead cells. ....</b>   | <b>263</b> |
| <b>Figure A.19: Light microscopy images of GPOTA polymer showing no attachment and round, dead cells. ....</b>   | <b>264</b> |
| <b>Figure A.20: Light microscopy image of BDDA polymer with CMs attached.....</b>  | <b>265</b> |
| <b>Figure A.21: Light microscopy image of HEODA polymer with CMs attached.....</b>   | <b>265</b> |
| <b>Figure A.22: Light microscopy image of TCDMDA polymer with CMs attached.....</b>  | <b>266</b> |
| <b>Figure A.23: Light microscopy images of PETrA polymer with few CMs attached.....</b>  | <b>266</b> |
| <b>Figure A.24: Light microscopy images of pPGDA polymer showing no attachment and round, dead cells. ....</b>   | <b>267</b> |
| <b>Figure A.25: Light microscopy images of GPOTA polymer showing no attachment and round, dead cells. ....</b>   | <b>267</b> |
| <b>Figure A.26: Light microscopy images of BDDA, HEODA, TCDMDA, PETrA, pPGDA and GPOTA polymerised with I369. None show cell attachment and the round morphology of the cells indicate apoptosis except for GPOTA on the bottom right.....</b> | <b>269</b> |
| <b>Figure A.27: Light microscopy images of BDDA, HEODA, TCDMDA, PETrA, pPGDA and GPOTA polymerised with DMPA. None show cell attachment and the round morphology of the cells indicate apoptosis. ..</b>                                       | <b>270</b> |
| <b>Figure A.28: Light microscopy images of BDDA, HEODA, TCDMDA, PETrA, pPGDA and GPOTA polymerised with DMPA in IPA solvent. None show cell attachment and the round morphology of the cells indicate apoptosis. ....</b>                      | <b>271</b> |

## LIST OF TABLES

|  |            |
|--|------------|
| <b>Table 2.1: Formulation preparations showing relative amounts of photo initiator and monomer. ....</b>   | <b>37</b>  |
| <b>Table 2. 2: Laser Power and scanspeed values utilized during 2PL. The total spot energy absorption is determined by using the power and scanspeed values selected by the user and the repetition rate, nominal spot size and pulse length which are constants characteristic of the Nanoscribe laser beam.....</b>  | <b>41</b>  |
| <b>Table 2. 3: Laser power and scanspeed values used during 2PL. The highlighted values in green show the location of the midpoint parameter that was found for the woodpile array (3.33E-11 pJ). The highlighted row in yellow shows how the midpoint parameter (3.33E-11 pJ) in the woodpile operating window alongside highest laser power (5.00E-02), was used to calculate the equivalent scanspeed value to reduce fabrication time (18,000 <math>\mu\text{m/s}</math>).....</b> | <b>42</b>  |
| <b>Table 2. 4: Range of laser power and scan speed values selected for determination of processing window for selected monomers. Energy values were calculated using a series calculations including laser power, scanspeed and constants such as pulse frequency. ....</b>  | <b>44</b>  |
| <b>Table 2. 5: TMSPMA volume and corresponding concentration values utilised in the solvent and TMSPMA determination experiment. ....</b>  | <b>74</b>  |
| <b>Table 2. 6: Dimensions of large open-channel structures and platform....</b>  | <b>87</b>  |
| <b>Table 2. 7: New multiplex design dimensions showing the flat region and the region with grooves. ....</b>   | <b>90</b>  |
| <b>Table 3. 1: List of acrylate monomers tested for their 2-photon compatibility.....</b>  | <b>111</b> |
| <b>Table 3. 2: Co-polymers of which their homopolymer constituents were selected for amenability to the 2-photon system in this PhD project.....</b>   | <b>112</b> |
| <b>Table 3. 3: Top 10 co-polymer combinations that scored highest for cell density and cell area in serum-free conditions in the Patel study. The writing in bold indicates co-polymers selected for processing ability in the 2-photon system. ....</b>   | <b>122</b> |
| <b>Table 3. 4: List of HEODA:EEMA co-polymer formulations tested on the 2-photon system. ....</b>  | <b>123</b> |
| <b>Table 3. 5: Co-polymer formulations prepared containing at least one multi-functional acrylate.....</b>   | <b>125</b> |

|  |     |
|--|-----|
| <b>Table 3. 6: List of monomers amenable to 2PL and that were previously shown to support CM attachment. The most suitable candidate monomers for the purposes of this project.</b> .....  | 127 |
| <b>Table 3. 7: List of photo initiator concentrations tested with corresponding average E<sub>max</sub> and E<sub>min</sub> values.</b> .....  | 132 |
| <b>Table 3. 8: Dimensions of the readjusted dimensions for the multiplex design.</b> .....   | 165 |
| <b>Table 4. 1: The effect of 2 solvents and TMSPPMA on polystyrene 96-well bottom surfaces.</b> .....  | 177 |
| <b>Table 4. 2: The effect of silane at a range of volumes in each of the solvents acetone and isopropanol.</b> .....   | 178 |
| <b>Table 4. 3: Comparison of the effects of silane on 3 different acrylate polymers. Non-silanised solutions were also tested. All conditions were in isopropanol solvent at the concentration previously determined (1.67 ul/ml).</b> ..... | 179 |
| <b>Table 4. 4: Results of monomer volume effects on gap formation during polymerisation of acrylates.</b> .....  | 180 |
| <b>Table 4. 5: Results of ANOVA single-factor analysis of cell viability, highlighting the polymers that demonstrated significant differences among the 3 different PI formulations.</b> .....   | 190 |
| <b>Table 4. 6: Results of student's t-tests showing the %cell viability with significant differences based on the polymer tested from ANOVA results in Table 4.2.</b> .....  | 190 |
| <b>Table 4. 7: Results of ANOVA single-factor analysis of cell viability, highlighting the PI formulations that resulted in significant differences among the 6 polymers tested for CM attachment.</b> .....                                 | 191 |
| <b>Table 4. 8: Results of student's t-tests showing the polymers that differed significantly from each other in each PI formulation found to have significant differences by ANOVA (Table 4.4).</b> .....                                    | 191 |
| <b>Table 4. 9: Degree of cure of PETrA polymer which was made using the 3 different formulations.</b> .....  | 195 |
| <b>Table 5.1: C=C/C=O ratio values for the 3 polymers under each post-fabrication treatment condition.</b> .....   | 205 |

|   |            |
|---|------------|
| <b>Table 5.2: Summary of DOC values from Raman spectroscopy measurements.....</b>   | <b>204</b> |
| <b>Table 5.3: Summary of Ether Peak Intensity Values pre- and post-vacuum treatment. ....</b>   | <b>204</b> |
| <b>Table 5.4: Results of ANOVA statistical analysis of sarcomere length on TCDMDA construct without post-fabrication treatment. ....</b>  | <b>209</b> |
| <b>Table 5.5: Results of ANOVA statistical analysis of nuclear roundness on TCDMDA construct without post-fabrication treatment. ....</b>   | <b>211</b> |
| <b>Table 5.6: Single-factor ANOVA statistical analysis displaying the calculated F-value, the expected (critical) F-value and the P-value.....</b>  | <b>217</b> |
| <b>Table 5.7: Student’s t-test results of pairwise comparison on sarcomere length measurements of all regions on TCDMDA construct with post-fabrication UV cure. ....</b>   | <b>218</b> |
| <b>Table 5.8: Single-factor ANOVA statistical analysis displaying the calculated F-value, the expected (critical) F-value and the P-value for TCDMDA treated with post-fabrication UV light.....</b>  | <b>219</b> |
| <b>Table 5.9: NOVA statistical analysis of the 5 groups representing sarcomere lengths on 5 different topological fine features. ....</b>   | <b>224</b> |
| <b>Table 5.10: ANOVA statistical analysis to determine presence of a significant difference between the 3 groups of nuclear roundness. ....</b>   | <b>225</b> |
| <b>Table 5. 11: Student’s t-test results of nuclear roundness between the flat glass control versus the flat region, the flat glass control versus the grooved region (middle) and the flat region versus the grooved region of TCDMDA with post-fabrication vacuum treatment. ....</b> | <b>226</b> |
| <b>Table 5.12: Standard deviation values of the 3 post-fabrication treatments on grooved region of TCDMDA. ....</b>   | <b>228</b> |
| <b>Table 5.13: Summary of CM response to topology and post-fabrication treatments. ....</b>   | <b>233</b> |
| <b>Table A 1: Area under the peaks of interest of uncured monomers that were tested for CM attachment in their polymerized form. All intensity values are taken as an average of 4 measurements (n=4).....</b>  | <b>240</b> |
| <b>Table A 2: Area under the peaks of interest of polymers cured by 2PL only (no vacuum or post-fabrication UV light treatment). All intensity values are taken as an average of 4 measurements (n=4).....</b>  | <b>242</b> |



|   |     |
|---|-----|
| <b>Table A 3: Area under the peaks of interest of polymers subject to vacuum treatment only. All intensity values are taken as an average of 4 measurements (n=4).</b> .....                        | 244 |
| <b>Table A 4: Area under the peaks of interest of polymers subject to post-fabrication UV cure treatment only. All intensity values are taken as an average of 4 measurements (n=4).</b> .....      | 246 |
| <b>Table A 5: Sarcomere length measurements from 5 representative cells in each grooves region and their resulting average values on constructs without post-fabrication treatment.</b> .....       | 247 |
| <b>Table A 6: Sarcomere length measurements from 5 representative cells in each grooves region and their resulting average values on constructs with post-fabrication UV light treatment.</b> ..... | 247 |
| <b>Table A.7: Sarcomere length measurements from 5 representative cells in each grooves region and their resulting average values on constructs with post-fabrication vacuum treatment.</b> .....   | 248 |
| <b>Table A. 8: Student’s t-test of all groove regions on constructs with post-fabrication UV light treatment.</b> .....   | 248 |
| <b>Table A.9: Nuclear roundness student’s t-tests on tcdmda construct with post-fabrication vacuum treatment.</b> .....   | 250 |
| <b>Table A.10: Absolute intensity values for C=C and C=O peaks of uncured PETrA under the 3 different formulation conditions.</b> .....   | 253 |
| <b>Table A.11: Absolute intensity values for C=C and C=O peaks of cured PETrA under the 3 different formulation conditions.</b> .....   | 253 |

## Abstract

Pharmaceutical companies currently rely on animal models for drug screening. This is a very expensive, time-consuming process and in some cases has been shown to be a poor predictor of human cardiac toxicity. Animal cells and tissue are not identical to their human counterparts. Therefore, it is not until human clinical trials at the later stages of drug screening that unexpected reactions to the drug are identified (Burrige et al., 2014). It would be greatly beneficial if this process could be shortened by identifying the risks of a drug earlier in the screening stages-chip based screening using mature human cardiomyocytes (CMs) is a route to achieve this. Substrates used to support CM growth have been identified including high-throughput chip-based screening strategies (Hook et al., 2013) (Celiz et al., 2014b) but so far stem cell derived CMs on these substrates do not adequately recapitulate the adult human CMs in terms of maturity (Denning et al., 2016). Many factors can affect how a cell matures from the soluble extracellular signals around it to the chemistry, topography, architecture/shape and mechanics of the substrate on which it is supported (Nikkhah et al., 2012). Mature cardiomyocytes have been successfully grown on 3 polymers synthesised by UV polymerisation-it has been confirmed that polymers like these can be successfully processed by 2-photon lithography. Photo initiator concentration has been optimised to create a complete structure. Glycerol propoxylate triacrylate and Tricyclodecane dimethanol diacrylate were shown to provide a wide operating window. Many relevant structures for CM growth were chosen and designed on AutoCAD to demonstrate the potential application of this material in CM culture. The 3D design freedom of the lithography approach will be used to explore the relationship between architecture and cell maturity. This will then enable a platform to be created using various architectures on a chip which will be utilised to assess cardiomyocyte maturity. This enables structure fabrication with more accuracy compared to previous methods due to the sub-micron scale of 2-photon lithography (Maruo et al., 1997). Greater resolution means improved results as cells interact on the sub-micron scale ( $\sim 1\mu\text{m}$ ) (Guck et al., 2010) Various architectures used for cardiomyocyte culture can show which ones are the most suitable to guide cardiomyocytes to a mature adult form.

# Chapter 1: Introduction and General Literature Review

## 1.1: Introduction

### 1.1.1 Outline of the thesis

This doctoral thesis commences with the methodologies used throughout the doctoral project to reach the objectives in order to answer the research questions.

Chapter 1 introduces the topic of materials that have been previously used to culture cardiomyocytes (CMs) and how these CMs are still not mature enough for accurate drug screening and disease modelling studies. The need for mature CMs is emphasised as heart disease occurs mostly in adults. The reasoning behind manufacturing polymer surfaces to culture CMs is given, as a support for growth and maturation. The various technologies used to fabricate structures for CMs are described and compared, culminating with the importance of 2-photon lithography as the technology of choice.

Chapter 2 describes the methodologies used throughout the doctoral project and the reasoning behind their selection.

Chapters 3-5 are results chapters. Each describe the results found based on the experiments performed, followed by a discussion comparing the results with current literature and future work that could potentially be done around the research field.

Chapter 3 explains how a list of 2-photon compatible polymers are discovered from a library of available materials. The relationship between their chemical structures and their compatibility are discussed. The operating windows of some of these polymers are determined by fabricating these polymers at a range of energy absorption parameters and photoinitiator concentrations. This is followed by the construction of more complex architectures by using previously determined operating windows. Polymerisation shrinkage is also investigated by performing measurements on printed structures versus design files.

Chapter 4 describes how the 2-photon compatible polymers are tested for CM attachment. Determining factors such as photoinitiator type and cell media are

also tested to observe whether they have effects on attachment. The amount of cure is also investigated using 2 different photo initiators which is then related to the CM attachment results.

Chapter 5 describes Raman spectroscopy experiments which determined the degree of cure on polymers subject to 3 different types of post-fabrication treatment. The CM attachment and maturity is compared on grooves of different depths and on post-fabrication treatment.

Chapter 6 combines all of the findings from Chapter 3, 4 and 5 to deliver the overall conclusions of this PhD project and future investigations that could be performed to support the hypothesis further.

### 1.1.2 Background

Defined synthetic substrates have emerged as the preferred matrix for cell culture as they possess fully defined chemical components, are xeno-free which reduces contamination and produce consistent results. These substrates have been tested previously for cell attachment for the potential use in various cell culture studies (Patel et al., 2015) (Celiz et al., 2014a)

Cardiomyocyte culture has become more popular due to their derivation from iPSCs by high-throughput protocols (Burrige et al., 2014). These cardiomyocytes (CMs) have characteristics very similar to adult CMs. However, their phenotype is not identical to their adult counterparts. (Salick et al., 2014). It has been shown that cells interact with the morphology, surface and roughness of the substrates they are in contact with (Nikkhah et al., 2012). Substrate morphology is perhaps one of the less studied characteristics (Nikkhah et al., 2012). Cells are known to interact with their environment at the sub-micron scale (Guck et al., 2010) and techniques such as 2-photon lithography enable the manufacture of structures down to sub-50nm resolution (Emons et al., 2012).

Substrates manufactured by UV polymerisation were already shown to attach CMs (Patel et al., 2015). The question then arose; what if these same structures known to attach CMs could also be manufactured by 2-photon lithography? If

so, do various architectures manufactured by 2PL affect the way CMs attach and mature on the substrate?

Other techniques have been used to fabricate architectures of high resolution. One such technique is electron-beam lithography. However, this method is costly and time-consuming, due to the photo-sensitive film required (Bajaj et al., 2014). 2-photon lithography has the capability of achieving high lateral and in-depth resolution without the requirement of photo-sensitive films and clean rooms. The use of 2PL to fabricate structures with fine features would allow observation of cardiomyocyte viability and maturity on various topologies.

Some studies have already shown that structures fabricated by 2-photon lithography can affect cell behaviour, but this has not been performed on cardiomyocytes. These cells are crucial as they form part of the adult heart muscle. In-vitro drug screening processes could reach a revolutionary turning point and cardiac diseases diagnosed during earlier stages.

### 1.1.3 Research Problem and Hypothesis

Cells interact with their environment in many ways. Material surface chemistry, neighbouring cells and material surface roughness all have a role to play in cell behaviour. The least investigated material feature is substrate architecture. Some studies have shown that architectures fabricated by UV polymerisation, electron beam lithography and 2-photon lithography affect cell behaviour. However, cardiomyocyte attachment and maturity have not been investigated on structures fabricated by 2-photon lithography. Cardiomyocyte maturity is an important factor to consider as cardiovascular diseases occur in the adult stages of life. Current stem cell-derived cardiomyocytes are not as mature as cardiomyocytes of the adult heart. Therefore, it is of utmost importance to discover which specific topological features will coax stem cell-derived cardiomyocytes to a more mature state. 2-photon lithography is a technology that can produce structures at a very high resolution which serves the purpose of investigating how fine features affect cardiomyocyte attachment and maturity. This led to the hypothesis of the PhD project which is '3D architectures produced and controlled by 2-photon lithography affects cardiomyocyte attachment and maturity'.

1.1.4: Justifications for the Research: Emphasis on the importance of the need to answer the research question and how this will benefit the scientific community and society.

The pharmaceutical industry involves costs of drugs passing through the long pipeline of research testing to marketing and manufacture. One of the largest costs is animal testing. High-throughput in vitro drug screening could be a more economical and accurate method of drug testing. Animals are not identical in anatomy and genetics to humans. Drug tests prove inaccurate when they progress to human clinical trials. The discovery of iPSC derivation gives hope as human cells could potentially be used for future drug tests. This would reflect the human response to different drugs. The challenge here is to identify whether differing architectures fabricated by 2PL can affect CM maturity. If CM maturity can be improved by a specific architecture the drug screening process would be even more accurate as most cardiac diseases occur in the adult human heart. This would be more ethical as animals would not be required for drug testing as well as more economical. Most importantly, drug testing would be more efficient which would greatly decrease patient morbidity and mortality.

1.1.5: Aims and Objectives of the Research

The aims and objectives of this doctoral project is to firstly identify acrylate polymers that are amenable to 2PL using a compatible photoinitiator. 2PL is a relatively new technology for which working materials are continuously being searched. The discovery of novel polymers for this technique will not only aid in the biological experiments in this doctoral project but also for future manufacturing projects. **The research question being asked here is; which acrylate polymers are amenable to 2PL?**

Once a list of these polymers is made, the second objective will be to determine which of these polymers support CM attachment. Suitable materials to support and enable CMs to mature will be ideal for future drug screening applications as cardiac diseases occur in the adult heart. Current iPSC-derived CMs do not mimic the adult CM genotype and phenotype. Therefore, this is of utmost importance for accurate drug testing in the future. **The research**

**question being asked here is; which of the 2PL-amenable polymers are able to support CM attachment?**

Afterwards, the polymers that are both amenable to 2PL and support CM attachment will be taken ahead for topological response experiments. The final aim, which will answer the research question of this doctoral project, is to elucidate whether iPSC-derived CMs adopt differential maturity on various topological structures fabricated by 2PL. Topology is a physical cue that can be altered to recapitulate the cell microenvironment, leading to more mature CMs.

The research questions being asked here are;

**Does the level of cure in the acrylate polymer affect CM attachment and maturity by causing cytotoxicity?**

**Does substrate architecture (groove depth) affect CM attachment and maturity?**

1.1.6: Limitations: Any limitations the research work may have and how this may affect the outcome.

Fabrication periods of 2PL structures can take up to 20 hours depending on structure size and complexity. Other experimental work such as cell culture and design work on AutoCAD was performed in conjunction with 2-photon fabrication. This limits the variety of structures that can be fabricated during the experimental period of this PhD project.

IPSC differentiation to cardiomyocytes takes 2 weeks in total during which UV-polymerised and 2PL constructs are prepared. Trial and error during the learning period results in a 2 week wait for the next batch of CMs to be ready. This is part of the research learning procedure, writing up the thesis and literature reviews are done during this time as well as any other experimental work possible.

1.1.7: Conclusion

The importance of the need for novel drug screening methods cannot be underestimated. Inaccurate drug screening due to differences between animal models and humans leads to severe health problems in humans or the loss of a potentially effective drug that was disposed of due to their adverse effects on animal models. This causes immense loss of finance and time. Synthetic are the emerging new platform for testing drugs in vitro. Cardiomyocytes generated

from iPSCs could be the future guinea pig. Improvements on cardiomyocyte maturity have been proved previously however powerful techniques like 2-photon lithography could answer the question of whether cardiomyocytes respond to fine features or not. This will give information on the preferred architectures of cardiomyocytes to create platforms for future drug screening.

## 1.2: Literature Review

### 1.2.1: Introduction

Prior to any research study, a thorough investigation of what has been found previously needs to be retrieved. The current state situation of drug screening methodologies is described and how the need for more accurate methods is very crucial in determining adverse side effects to prevent drug morbidity and mortality during human clinical trials as well as reducing manufacturing costs.

Synthetic substrate uses in determining human iPSC-derived CM attachment is highlighted as well as how various material characteristics such as architecture, surface chemistry and roughness affect cell attachment. The focus in this project is the architecture and the most efficient way to analyse fine features by 2PL is explained giving the reasoning for selecting this technology in comparison to others.

CM type selection is also explained giving the reasoning for iPSC-derived CMs compared to embryonic or adult-derived CMs. Literature studies on the maturity of these cells are compared and how the research question in this study could help address the current lack of maturity in iPSC-derived CMs.

The first investigation commenced with the selection of the appropriate method to fabricate architectures with fine features as this covers the scope of the project. This is followed by how this technology can help the understanding of CM interaction with the architectures compared to other methods.

The next section extends on why architecture is analysed as opposed to other characteristics of a material that affect CM attachment and maturity.

Finally, the last section explains why iPSC-derived CMs are selected for this study and how this will help address the research question.



## 1.2.2: Literature Review

### *1.2.2.1 The importance of nanotopography*

The morphology, or more specifically nanotopography, of substrates has been found to have profound effects on cell fate. This is the feature that plays a big role in cell response. Nano topography is the sub-micron morphology of a substrate and variations at this level are known to affect cell behaviour and function (Bettinger et al., 2009) (Charras and Sahai, 2014). This parameter was only recently discovered to affect cell behaviour and function with the increasing amount of research. Other parameters such as surface chemistry and substrate stiffness have been more extensively investigated in the past (Broughton and Russell, 2015). The fact that Nano topography can play a strong role in cell behaviour and fate proves very advantageous since other molecules would not need to be added to modify cell behaviour like in surface chemistry modification. Nano topographic structures that occur in nature, for example in the ECM of body tissue, provide mechanotransductive signals for cells to proliferate, differentiate, migrate, and many more types of responses. The proteins of the ECM also have specific structures at the nano-scale that contribute to cell signalling. The collective natural phenomenon of cell response to nanotopographic structures and proteins is called contact guidance. Basic Nano topographies such as Nano gratings, nano post arrays and nanopit arrays (Figure 1.2) are known to affect cell morphology, differentiation, proliferation, migration, attachment, adhesion and genotype (Bettinger et al., 2009). Nano gratings are of interest since cells align according to the grating axis and this is desirable for CMs as synchronous beating for correct function requires cell alignment (Bettinger et al., 2009).

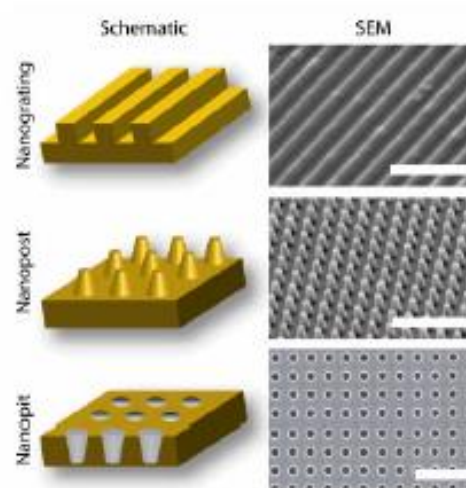


**Figure 1.2: Three main types of substrate Nano topography that are used to study cell-substrate interactions; Nano gratings, Nano posts and Nano pits (Bettinger et al., 2009).**

The shape of a substrate can influence cell growth, adhesion and spreading (Lee et al., 2008). Proper cell adhesion is crucial for cell function and this can be controlled by nanotopographical alteration (Kulangara and Leong, 2009). Figure 1.3 shows the various topographies that were fabricated to test for osteoprogenitor differentiation to osteoblasts (Figure 1.3).

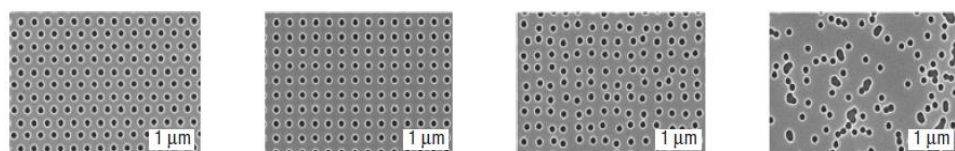


**Figure 1.3: Nano pit topographies used in the studies by Dalby and Biggs; from left to right 1) hexagonal 2) ordered square 3) near-square and 4) disordered Nano topographies (Dalby et al., 2007) (Biggs et al., 2007).**

Many studies have shown that altering surface geometry can alter cell growth, spreading and differentiation. Regarding differentiation, different architectures can support cells depending on which developmental stage they are at. In other words, substrate Nano topography has been discovered to determine stem cell differentiation (Kulangara and Leong, 2009). The effect is apparent with many types of cells. It can determine the stage of differentiation of mouse embryonic stem cells (mESCs) (Lee et al., 2008). The mESCs have a relatively flattened

shape when cultured on grooves, indicating they are about to differentiate whereas on hexagonal substrates they form a rounded shape, retaining their stem cell characteristics. A study performed on multiple Nano topographies showed that osteoprogenitor cells differentiate towards osteoblasts (mature, mineralised bone cells) in near-square topography of Nano pits (Dalby et al., 2007) compared to randomly assigned, hexagonal or highly ordered (perfect square) Nano pits (Dalby et al., 2007). Another study on human embryonic stem cells (hESCs) demonstrated that gratings on substrates induced hESCs to the neuronal lineage whereas pillars and wells induced differentiation to the glial lineage (Ankam et al., 2013). Mesenchymal stem cells, for instance, differentiate towards a neuronal lineage when cultured on 350 nm Nano gratings (Kulangara and Leong, 2009), (Yim et al., 2007) and it was demonstrated that the cells expressed proteins typical of neurons (Yim et al., 2007) compared to no change in protein expression in the planar or micropatterned controls. These studies confirm the possibility of altered CM behaviour and differentiation state (i.e. maturity) on various substrate architectures.

Scaffolds built as supports for CMs have been produced for the purposes of maturation improvement. A recent study of CM development on nanogrid structures of various widths found that CMs cultured on grids of intermediate width (800-1000 nm) exhibited a larger cell area, higher cell perimeter, rectangular morphology, greater degree of alignment with the nanogrids and longer sarcomeres compared to grids of higher or lower widths (Carson et al., 2016). All the stated cell characteristics such as large cell area, large cell perimeter etc. are typical of mature CMs so the study highlights the importance of nanotopographical features in CM development.

There have been numerous technologies to fabricate structures relevant to cardiac tissue. Among these are decellularized, porous, micro-channelled, electrospun fibrous scaffolds and bioprinted scaffolds (Huang et al., 2018). In an earlier study, alginate channel scaffolds with the purpose of recapitulating heart tissue were able to support endothelial cells (ECs) within the channels. This in turn, enabled CM growth between the channels (Zieber et al., 2014). The creation of a bi-layered cardiac tissue comprised of a CM layer and an endothelial cell layer improved the efficiency of the cardiac patch in drug

screening tests and functionality *in vivo* (Schaefer et al., 2018). This study showed one of many methods to improve CM maturity. Another intriguing technique used aligned ESC-derived CMs, named the ‘biowire’ format, and subjected the cells to electrical stimulation which resulted in increased CM maturity (Nunes et al., 2013). Porous fibrin scaffolds to mimic cardiac tissue wherein CMs attach around the pores and vascularisation occurs within the pores have been successfully produced by electrospinning (Thomson et al., 2013). This is a technique useful for the creation of mesh-like scaffolds but not for fine feature alterations. Decellularised scaffolds showed successful interaction of CMs with the scaffold and CM-specific gene expression when transplanted *in vivo* (Akbay and Onur, 2019). Albeit, decellularized scaffolds are obtained directly from animals or humans so there is no capacity to alter topological features. Furthermore, decellularized scaffold studies revealed how CMs exist in the native tissue, namely in layers and vascularised for oxygen diffusion to aid cell survival (Sarig et al., 2012). CMs derived from primary cancer cell lines have also been successfully seeded and incorporated into porous polyurethane scaffolds produced by solvent leaching (Ganji et al., 2016). Sponge-like scaffolds similar to this also showed their ability to support CMs derived from ESCs (Caspi et al., 2007). Solvent leaching can be very toxic and the dimensions created with this technique are limited (Bajaj et al., 2014). Gas foaming and freeze-drying combinatorial approaches have led to successful *in situ* differentiation of iPSCs to CMs (Dattola et al., 2019). In this case, candidate materials suitable for iPSC attachment would need to be found and is a longer procedure in which cells might not be sustained during the differentiation. This is why the CMs are seeded after differentiation on the topological structures as the focus of this doctoral project is solely on the effect of architecture on already-differentiated CMs. Interestingly, a study that used a collagen/Matrigel mesh construct led to the discovery that rat CMs initially dedifferentiated when exposed to a scaffold closely followed by recovery (Wang et al., 2019). CM maturity is determined by how well their sarcomeres (fibres inside the cells) and their nuclei are aligned. In other words, if they are parallel to each other, they will form a good contractile force for efficient function. Substrate morphology is known to influence this too. A study done on polyethylene glycol (PEG) substrates that were patterned to have different widths demonstrated differential

sarcomere alignment and hence CM maturity (Salick et al., 2014). The optimal width found to promote sarcomere alignment and CM maturity was in the range 30-80  $\mu\text{m}$  although substrate morphology did not seem to affect nuclear alignment in this study (Salick et al., 2014). Microgrooves have also been applied to CM differentiation studies. One study in particular focussed on microgrooves' ability to improve the speed of the differentiation process of CMs, in which cell and nuclear elongation values were higher on grooved structures versus flat ones. The progress from cardiac progenitor to CM-like cells was much quicker on grooved versus flat structures (Morez, 2015 #216). An innovative design that was comprised of both channels and cages in which CMs and endothelial cells (ECs) were seeded respectively showed improved CM maturity with longer sarcomeres (Fleischer, 2017 #221). ECs supported CMs and this represented the native heart tissue as it has a constant blood supply.

CM organisation is also important as aligned CMs represent the native ventricular heart. Sarcomere fibres need to be aligned for efficient contraction to pump blood. A study on CM orientation on microgrooves has shown that the cells align along the microgrooves versus their randomly-oriented counterparts on flat structures (Fujita, 2006 #217). Similar results were seen on structures created by microabrasion (Bursac, 2002 #220). The calcium cycling ability of a CM determines its maturity as the cells require a good calcium transfer through the cells for proper sodium-potassium exchange for electrical conductivity. Research done on PDMS microgroove structures showed improved calcium cycling on iPSC-derived CMs (Rao, 2013 #218). Nanopillar structures have also been shown to guide CM adhesion and growth (Deok-Ho, 2005 #219).

Various synthetic materials have been utilised to fabricate structures that mimic the surface topological features of cardiac tissue to test the materials' ability to support cardiomyocyte (CM) attachment. Structures fabricated by UV microcontact printing have been used to study CM behaviour on surfaces containing grooves of different width and depth measurements (Salick et al., 2014). Similar structures have been fabricated by electron beam lithography (EBL) and have been proven to successfully promote CM attachment (Scholten and Meng, 2016). These EBL studies involved the fabrication of polyurethane and polystyrene structures which required the use of significant quantities of

solvents such as toluene and dimethylformamide. EBL is an expensive and time-consuming method due to requirement of clean-rooms post-fabrication as well as the damage caused by the electron beam on the resist (Scholten and Meng, 2016). In one study, various commercially available polymers were tested for CM attachment and their maturity (Patel et al., 2015) using a High Through-Put pin-printing method. It had been recently shown that 2-photon fabricated micro-scaffolds of a rectangular versus hexagonal morphology showed differential maturation of iPSC-CMs (Silbernagel et al., 2020). The utilisation of 2PL for the specific study of CMs is an emerging area of research and this is why it is the highlight of this doctoral project.

#### *1.2.2.2 Two-photon lithography*

2-photon absorption (2PA) was first used for fabrication of 3D structures by Maruo's group. (Maruo et al., 1997). 2PA had been previously used in fluorescence microscopy, 3D memory and lithography but Maruo's group was the first to fabricate structures in both the lateral and depth direction.

Relative to other polymerisation techniques, 2-photon lithography (2PL) is a very recent technology added to the list of techniques that can be utilised in polymer research (Maruo et al., 1997). For this reason, the fundamental understanding of the types of monomeric / macromonomeric materials that are suitable for application to this technique has not been exhaustively studied. Ultimately, one of most important points that will define if a monomer / macromer can be applied in 2PL is the mechanism of the polymerisation reaction as it is this which largely defines the kinetics of the formation of the resultant polymers etc. By definition, 2PL processing must involve a photo initiator molecule that is both activated by 2 photons of input energy and, once "activated" will initiate a polymerisation reaction by interaction with a monomer in such a way as to retain the reactive centre and so extend the process into propagation of the polymer chain.

Previous microfabrication techniques rely on a layer-by-layer fabrication method since the technique depends on single-photon absorption which is a linear process (Bajaj et al., 2014). This means photons can be absorbed at any point along the beam, leading to out-of-focus fabrication and low resolution in

the longitudinal (z) direction. One technique uses mask patterns, but this is very time-consuming and expensive. Maskless photolithography also uses a layer-by-layer technique in which the CAD design is sliced into 25-100  $\mu\text{m}$  layers. This makes these methods time-consuming, expensive and low in-depth resolution. Electron-beam lithography uses an electron beam which shines on an electron-sensitive film in a certain pattern. The resolution is improved immensely, down to 10 nm however this is a very expensive technique, so it is not widely employed.

2PL utilizes the phenomenon of 2PA. This requires 2 photons to be absorbed therefore it can only happen in regions where photon intensity is very high in a laser beam (Maruo et al., 1997). The invention of femtosecond (high-frequency) lasers has enabled the 2PA phenomenon to be used for microfabrication. The simultaneous absorption of 2 photons occurs within a very small focal volume, enabling accurate fabrication with high, 100 nm resolution (Nazir et al., 2014) and even as much as sub-50 nm resolution (Emons et al., 2012). A large number of photons are required to be present in this focal volume at any one time for 2 photons to be absorbed by reaction system and polymerisation to take place (Maruo et al., 1997). The 2-photon system uses a mode-locked laser which consists of pulses that occur on an extremely short time scale (a few femtoseconds). This enables each pulse to have high power so that non-linearity can be created as high intensity infra-red wavelengths within a small focal volume (Sánchez et al., 1997). This small focal volume created due to the laser pulses contains many photons which can then go on to initiate polymerisation (Maruo et al., 1997). Lasers of lower frequencies would not be able to create pulses with a high peak power within a small volume, rendering 2-photon absorption impossible. The absorption outside the focal beam is negligible which prevents out-of-focus fabrication.

The types of polymers that are amenable to 2-photon lithography that have been reported in the literature and thus, the most widely used polymer types for 2PL to date, are acrylates, epoxides and styrenic species (Ifkovits and Burdick, 2007). Epoxides undergo cationic polymerisation which is a different reaction mechanism to what acrylates undergo which is called free radical polymerisation (Decker, 2001). This means different photo initiators would need to be utilised

and reaction conditions would have to be different to achieve optimal performance. In addition, epoxides are formed as a result of cytochrome P450 metabolism in the liver. If they react with a macromolecule (for example, DNA) the results could be detrimental as they can form carcinogenic species (Ouellette and Rawn, 2015). Similarly, styrene can react with oxygen to form styrene oxide which is a mutagen and carcinogen (Phillips and Farmer, 1994). The biological effects of the polymers are crucial when selecting these materials for cell attachment studies. Furthermore, as acrylates have been utilised as synthetic substrates for cell attachment (Patel et al., 2015), and cardiomyocytes in particular, it was this monomer type that was selected for the 2PL-amenability studies that are the core of this report. Urethane acrylates and epoxies were the first materials used for 2PL (Ricci et al., 2017). The range of materials applicable to 2PL has expanded immensely since then. Important factors to consider are the mechanical and chemical properties of the material to be processed so it can be utilized for the desired application whether it is photonics, microfluidics or biomedicine. Biodegradability and biocompatibility of the fabricated scaffold are significant factors in tissue engineering applications (Ricci et al., 2017). 3-dimensional biodegradable methacrylate structures have also been fabricated by 2PL (Claeyssens, 2009 #223). Biodegradability is not essential if the fabricated scaffold is not implanted in vivo or if the scaffold is not required to degrade after implantation. On the other hand, biocompatibility is crucial when fabricating architectures as scaffolds for cell culture. The first demonstration of 2PL to fabricate scaffolds for cell culture used Ormocer® (GmbH) which was able to support the growth of neuroblast-like and epithelial-like cells (Doraiswamy et al., 2006). Lego-like interlocking tissue engineering scaffolds (with pillars of 75  $\mu\text{m}$  diameter and height 20  $\mu\text{m}$ ) and microneedle arrays with unique geometries were constructed which demonstrated how 2PL can be used to construct a diverse arrangement of polymeric structures with a large range of shapes and sizes (Doraiswamy et al., 2006). This kind of diversity and high-resolution is not seen in other microfabrication techniques such as ion etching, injection moulding, UV stereolithography or electrospinning (Doraiswamy et al.).

There is a need for tissue engineering scaffolds and medical devices to be built very accurately, down to sub-micron resolution. Cells interact with surfaces they



are in contact with at distances as small as 3 nm (Azuma et al., 2016) therefore minute differences in architectural dimensions will help recapitulate cells' physiological environment. Scaffolds have been fabricated by 2PL using commercial triacrylate resins to successfully observe cell migration (Tayalia et al., 2008). Medical devices such as microneedles prove advantageous as they reduce pain to the patient, injury at injection site can be reduced and drugs can be delivered in a controlled manner (Doraiswamy et al., 2006). Two-photon lithography will allow exploration of sub-micron dimensions for utilizing these devices in future medicine. Many studies to demonstrate fabrication by 2-photon polymerization utilized commercial resins with proprietary components (Doraiswamy et al., 2006 2005, Juodkazis et al., 2005 2005). Naturally, microfabrication by 2PL with sub-micron resolution was the initial priority regardless of biocompatibility, commencing with simple spiral structures to prove the fabrication ability of 2PL itself (Maruo et al., 1997) however the studies that followed enabled fabrication of scaffolds suitable for cell culture (Doraiswamy et al., 2006). This means 2PL is highly promising for the fabrication of architectures amenable to cardiomyocyte culture. Acrylates have a high rate of polymerization which makes them attractive for 2PL. Acrylic resins have been developed with desirable physical and chemical properties by 2PL (Baldacchini et al., 2004). As there is a wide variety of acrylate monomers available, developing formulations tailored for a future application is a desirable pathway to follow when fabricating structures.

The three crucial components to consider during 2PL are;

- 1) **Resin:** the molecule in which microfabrication will be done
- 2) **Photo initiator:** the light-sensitive molecule which will initiate polymerization and fabrication
- 3) **2PL parameters:** which is laser power and scan speed. These two parameters can be combined into an energy value (given in J). This is the amount of energy that enters the system.

Even though all components are significantly important for the fabrication process, the photo initiator may perhaps be the most crucial. This is because it is the molecule responsible for initiating the whole reaction. Photo initiators are

molecules that absorb photons within a certain wavelength range and typically absorb photons at an optimal wavelength value (Carragher, 2007).

Two-photon polymerisation occurs when a light-sensitive molecule (called a photo initiator) absorbs 2 photons of a certain wavelength and attacks a recipient molecule to create a radicalised monomer. This is a chain reaction which repeatedly occurs to create long polymers until the photo initiator or monomer molecules are used up, whichever comes first (Carragher, 2007).

UV polymerisation is a process in which UV light excites a photoinitiator molecule which releases one or more free radicals. The free radicals then go on to attack a monomer which makes it an activated monomer radical in what is called the initiation stage. An activated monomer transfers the free radical onto another monomer which result in growing polymer chains during the propagation stage, until two activated polymer chains react with each other, leading to termination. (Figure 1.1b). UV polymerisation requires absorption of one photon by the photoinitiator for the reaction to commence, unlike 2-photon polymerisation which requires 2 photons.

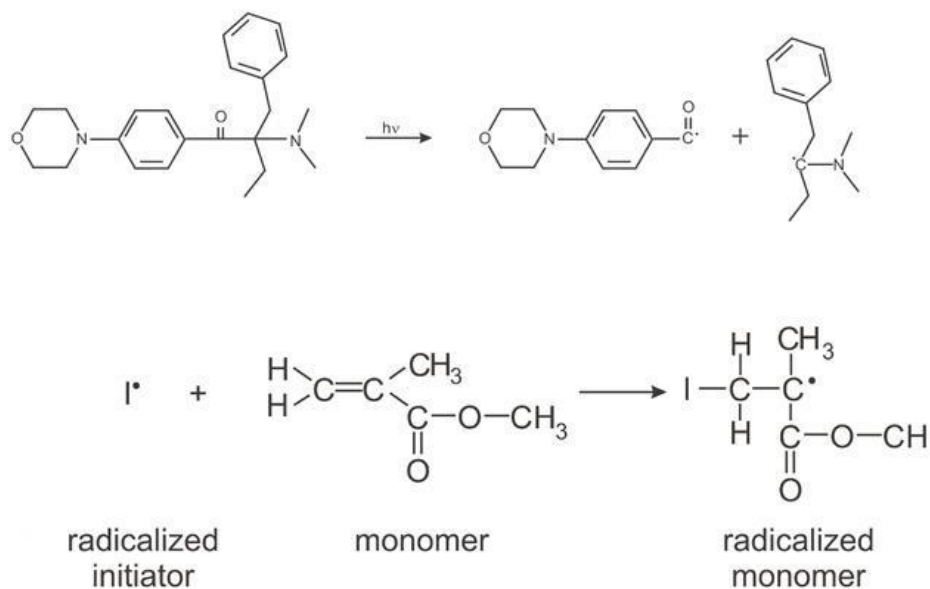


**Figure 1.1a: Initiation stage of photo polymerisation (Ciuciu and Cywiński, 2014)**

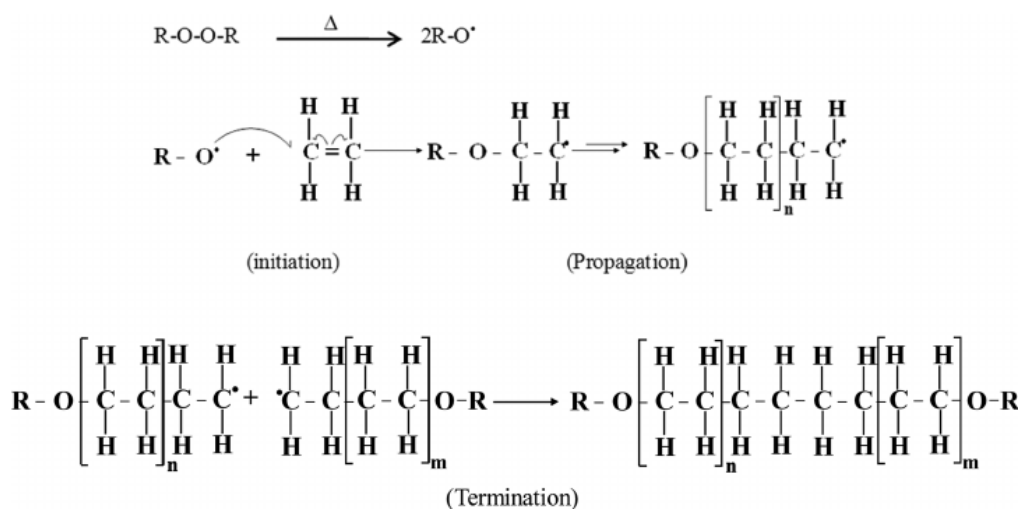


**Figure 1.1b: The generation of free radicals and the 3 stages of polymerization; initiation, propagation and termination. There are three stages of polymerisation: initiation, propagation and termination. Initiation involves absorption of the photons of a specific wavelength by the photo initiator and formation of a radicalised monomer. Propagation is the subsequent attack of the free monomers by the radicalised monomer. Termination occurs when two radicalised monomers react with each other, rendering them neutral (Carragher, 2007).**

Photo initiator characteristics to consider are quantum yield, 2PA cross-section, biocompatibility and solubility of the photoinitiator in the resin material.

Photo initiators operate by various mechanisms and are classified as two types. Type I photo initiators absorb photons to form a free radical species which will then attack a recipient molecule with an electronegative atom to form a radicalised recipient molecule (Carragher, 2007). The advantage of using Type I photo initiators is that no additional reagents are required for the reaction system. Type II photo initiators operate with the aid of a co-initiator and are usually limited by oxygen quenching as they spend more time in the excited state (Carragher, 2007). However, the fact that they spend more time in the excited state means more of the absorbed photons will go towards initiating polymerisation rather than fluorescence or thermal release.

Quantum yield of a photoinitiator is the number of photons emitted divided by the number of photons absorbed. An efficient photoinitiator should have a high number of photons emitted to increase the number of radicalised polymers to commence the polymerisation reaction. Photoinitiators with a poor quantum yield do not have a high number of emitted photons. Instead, the absorbed photons either result in fluorescence or thermal emission. Most commercial PIs, such as the Irgacure series, have a high quantum yield but a poor 2PA cross-section (described below) because they have been designed for 1-photon absorption (Baldacchini, 2011).

The 2-photon absorption cross-section of a photoinitiator is significant to the ultimate success of the process. This characteristic of a photoinitiator is the area of the molecule that is able to retain photons during intersystem transfer plus its ability to retain these photons. Therefore, the larger the 2-photon absorption cross-section, the longer the photons will take for intersystem transfer which increases the chances of the absorption of both photons in a near-simultaneous fashion. This is because 2 photons must be absorbed during the initiation stage. Thus, the longer the 1st photon can sustain the necessary electron transfer (termed intersystem transfer) within the molecule, the more likely the 2nd photon will be absorbed into the system to activate the photoinitiator molecule. An efficient photoinitiator molecule possesses characteristics that include

delocalised electron systems at the centre and an electron donor and acceptor region at the absorption and emission end of the molecule respectively (Ciuciu and Cywiński, 2014). Previous work has shown that addition of benzene rings to the middle of the photoinitiator molecule increases the 2PA cross-section due to the delocalised electron system that is a characteristic of benzene rings (Nazir et al., 2014). A study performed on commercially available photo initiators showed that all except one of them had a low 2PA cross-section (Schafer et al., 2004). This is why efforts to increase 2PA cross-section via addition of benzene groups and amino terminal groups have commenced. Indeed, PIs synthesised this way have been proven to have a significantly larger 2PA cross-section compared to commercially available PIs (Ciuciu and Cywiński, 2014). Among the PIs with lower 2PA cross-sections is Irgacure 369, which is used throughout this doctoral project. This is due to it being one of the few PIs soluble in acrylate monomers. Only certain photo initiators are applicable to 2PL, and these are only viable for use within a specific concentration range and with certain monomers. This is partly related to initiators' physical characteristics, because the photoinitiator has to dissolve with the monomer to ensure the reaction can occur efficiently. If not, a suitable solvent (e.g. isopropanol) can be used to dissolve the photoinitiator prior to addition to the monomer. A solvent is not required for the purposes of this study as I369 is able to dissolve in all but 2 of the acrylate monomers utilised for 2PL fabrication experiments. Most PIs synthesised to have a large 2PA cross-section are water-soluble. Highly efficient water-soluble visible light photo initiators (Na-TPO and Li-TPO) have been synthesised that have significantly higher 2PA cross-sections compared to commercial photo initiators (Benedikt et al., 2016). However, the desirable polymeric materials for the study of CM attachment are not water-soluble. Irgacure 369, as well as the majority of commercially available PIs are miscible in organic solvents. The acrylate monomers studied in this project that had potential to support CM attachment were insoluble in water which is the reasoning for selection of I369. Additionally, for systems that are intended for use in medical applications, the biocompatibility of the photoinitiator must also be considered when cell attachment experiments are performed. I369 is a PI that is biocompatible, as shown by previous fabrication for cell culture studies (Doraiswamy et al.,

2006). Efforts have been made to reduce photoinitiator cytotoxicity by synthesis of the molecule bound to a hyaluronan backbone, the idea being to restrict the location of a novel photoinitiator (named HAPI) to the ECM and not to enter cells (Tromayer et al., 2017). The novel molecule was found to be considerably less cytotoxic than another structurally similar reference molecule E2CK. In this study, biodegradability will not be a consideration as *in vivo* studies are not part of this project. The main goal is to create a potential 2PL based platform technology capable of successfully constructing articles from a broad range of monomers for *in vitro* drug screening studies in the future. The fabrication of various architectures using 2PL will aid the identification of the optimal architecture for the CMs with closest maturity to adult CMs. The utilization of these architectures to create large *in vitro* arrays will enable high-throughput CM culture. Therefore, this doctoral project and similar future studies will aid more high-throughput *in vitro* CM culture to assess drug screening and disease modelling.

#### 1.2.2.3 CM culture

CMs are crucial for drug screening and development. The current cost of bringing a drug from bench to market is very high, about 11 billion USD and takes approximately 12 years (Denning et al., 2016). Many drugs are rejected before they even reach the market due to unexpected side-effects during clinical phase trials. The side-effects can be various, including damage to CMs illustrated by beat irregularity which can lead to seizures and sudden death (Denning et al., 2016).

Current drug safety screening and discovery programs rely on animal models (Burrige et al., 2012). The advantages of using an animal model unfortunately do not outweigh the disadvantages. Even though animal models can be useful for monitoring *in vivo* processes such as drug side effects and tracking molecules within a living organism, they are not genetically identical to humans (Burrige et al., 2012). Therefore, adverse side-effects not observed in rats may be observed in human clinical trials (Denning et al., 2016, Evans-Anderson et al., 2008). Many drugs have been withdrawn from the market due to side effects related to abnormal electrophysiological alterations in the heart (Braam et al., 2010). This greatly increases the cost and time taken for the drug to reach the

market. Conventional drug screening is a long, arduous road involving tests in animal cell lines such as Chinese hamster ovary (Mei et al.) cells or human embryonic kidney (HEK) 293 cells overexpressing IKr protein hERG (human Ether-à-go-go-Related Gene) for detecting cardiotoxicity (Sayed et al., 2016). The drawback with these cells is they do not show the same response as CMs as they cannot recapitulate the complex ion channel pathways of human CMs which are vital for cardiac function (Sayed et al., 2016). As well as some drugs being rejected later in the drug screening process, some cases involve drugs being rejected during the initial screens only later discovered to be safe in humans (Burridge et al.). PSC-CMs have promising potential in the drug screening procedure as they can closely recapitulate CM responses. The more exciting part is that iPSC-CMs (induced pluripotent stem cell-CMs) can pave way to a new field called 'precision medicine'. Every individual has a different epigenetic signature in their cells which affects the way a specific patient responds to drugs (Liang and Zhang, 2013). iPSC-CMs are derived from the skin fibroblasts of a patient therefore CMs can be generated from a patient and drug response assessed specifically for each patient before administration. This will take time to bring into practice but will be a very efficient, safe and beneficial way to administer drugs to patients suffering from cardiovascular disease. Substrates fabricated by 2PL of the precise sub-micron scale architecture will identify and provide the best environment for CM attachment and enhancement of their maturity. In this way, drug screening procedures will be more accurate thus reducing cost and adverse side effects in patients.

The advent of regenerative medicine has prompted the use of autologous stem cells (using skin cells from the patient) and reprogramming these cells to induced pluripotent stem cells (iPSCs) to treat heart disease by differentiating iPSCs to cardiomyocytes and injecting them directly into heart tissue or seeded on a scaffold which is implanted onto the heart afterwards. However, previous clinical trials following these treatments did not give accurate results (Denning et al., 2016) due to the immaturity of the iPSC-derived cardiomyocytes. They did not resemble adult cardiomyocytes in their functional behaviour demonstrated by their electrophysiological profiles and protein expression (Denning et al., 2016). iPSCs have a genetic profile which is not identical to

pluripotent stem cells in the embryo (Takahashi and Yamanaka, 2006). This is possibly the reason CMs generated from iPSCs are not identical to their adult counterparts due to epigenetic differences (Liang and Zhang, 2013). Normally, the first choice would be harvesting CMs from healthy adults. Unfortunately, these are very limited in supply and the harvested myocytes (generic term for muscle cell) tend to dedifferentiate rapidly post-harvest in the cell culture dish (Bird et al., 2003). In addition, myocytes exhibit poor consistency and almost non-existent proliferation in cell culture although intermediate amounts (2%) of serum resulted in CM generation (Bird et al., 2003). This results in primary human adult CMs not being the *in vitro* model of choice, but they can give valuable information on how adult CMs will interact with stem-cell derived CMs in co-culture studies. A second option would be to utilise embryonic stem cells (ESCs). This cell type has been widely used for many differentiation protocols as they can be retrieved directly from the embryo and no reprogramming is required, unlike iPSCs (Klimanskaya, 2019). However more recently, the ethical concerns over the use of ESCs has prompted researchers to seek alternative stem cell sources like iPSCs. Therefore, attempts to enhance CM maturity were performed on iPSC-derived CMs. Prolonged cell culture was observed to improve CM maturity although this would be costly and time-consuming in the long run (Lundy et al., 2013). Late-stage hPSCs, which were cultured for 80-120 days exhibited increased cell area, cell perimeter, sarcomere length and increased nucleation compared to hPSCs cultured for 20-40 days (Lundy et al., 2013). This is a good finding however it would prove very costly to put this into practice on an industrial scale due to the time-consuming, costly process that would be involved. Other reprogramming strategies such temporal modulation of Wnt signalling have been employed to direct hPSC differentiation to CMs which produces more mature CMs, evident by their mRNA expression and electrophysiological profiles (Liang and Zhang, 2013). Direct reprogramming from fibroblasts to CMs is a much quicker method to obtain CMs (BurrIDGE et al., 2012). A protocol demonstrated derivation of spontaneously beating CMs from mouse embryonic fibroblasts in as little as 4 days (Efe et al., 2011). However, this procedure can lead to the formation of ectopic myocardium in scar tissue which may cause arrhythmias and is not efficient enough (BurrIDGE et al., 2012). Partial re-programming involves the re-programming of fibroblasts to a



point before the iPSC stage which is defined as pre-iPSC and then differentiating to the desired cell type. The main advantage of this method over full reprogramming is the speed but the process can leave residual pluripotent cells which are harmful due to the risk of teratoma formation. Due to the lack of maturity observed in hPSC-CMs, methods to alter the biophysical and biochemical environment such as substrate stiffness and chemistry appears to be more desirable.

Differentiation protocols for pluripotent stem cells (PSCs) to CMs are numerous and are comprised of different durations and culture vessels to derive the most mature CM that demonstrates functions most similar to the adult heart. Some earlier differentiation protocols involved the use of a feeder layer which was a layer of mitotically inactivated fibroblasts at the bottom of the cell culture wells to act as a physical support and provide extracellular signals to the iPSCs during differentiation (Yue et al., 2012). Production of the fibroblast feeder layers is time-consuming and tedious work, which is why later protocols used matrix support layers such as Matrigel™ and Geltrex™. The extracellular matrix plays a crucial role in the development of CMs which has led to differentiation protocols involving CM culture between 2 ECM layers. This ‘matrix sandwich’ method yields a high percentage (98%) of CMs (Zhang et al., 2012). Others involved the derivation of embryoid bodies which are small clusters of cells which are morphologically similar to embryos. The formation of embryoid bodies is thought to aid the cell-to-cell contact necessary for differentiation. Specialised cell culture wells coated with agarose help stem cells to cluster and form embryoid bodies, which improves the yield of differentiation (Dahlmann et al., 2013). Some protocols involve the differentiation of iPSCs to CMs alongside other cell types, such as mesenchymal stem cells (MSCs). This is advantageous as CMs require the support of pro-angiogenic cells like MSCs for cardiac repair (Wei et al., 2012). The purpose of this project is to elucidate the effect of topological variation on CMs only therefore influential factors, including other cell types, were not desired in the experiments performed. However, MSCs may be important for future cell culture studies for transplantation and cardiac repair. Another pluripotent cell type commonly used for differentiation are amniocytes. These are stem cells derived from the

amniotic fluid. Studies have shown that amniocytes are resistant to direct differentiation to CMs (Maguire et al., 2018). Another, more recent cell type used in cardiac differentiation, have been adipocytes which has been achieved with the use of fibrin or trichostatin A scaffolds (Bagheri-Hosseini et al., 2017). Ideally, the less xenogenic components the protocol has, the better. This is why PSC culture and differentiation protocols have evolved to exclude the ECM-mimicking materials such as Matrigel™ that were previously mentioned. The move to synthetic substrates for CM culture has provided more consistent and scalable results (Patel et al., 2015). The PSC to CM pathway is not only affected by the surrounding matrix, however, the various growth factors and small molecules added and their timing are important in determining cell fate (Spater et al., 2014). CMs are derived from the mesoderm lineage of the developing embryo. The growth factors involved are Activin A and Bmp4. It was found that optimal levels of Activin A and Bmp4 determine the efficiency of cardiac differentiation and variation among iPSC lines meant that levels of growth factors and small molecules had to be optimized (Kattman et al., 2011). The ‘monolayer differentiation approach’ has been developed as a xeno-free and 2D protocol in which iPSCs were maintained on a flat layer of Matrigel™ which were then subjected to addition of various small molecules (including Activin A and Bmp4) at different stages of the procedure (Burrige et al., 2014). The procedure was an in-house derivative of the Burrige, 2014 protocol and gave rise to CMs with up to 96% purity. The protocol has been optimised to suit the cell lines being used in the stem cell laboratory at the University of Nottingham, which is the reasoning of the selection of this method for this doctoral project. A full description of the protocol is in the Methodologies 2.6.1.4 Differentiation to CMs.

#### *1.2.2.4 Determination of CM attachment using UV polymerisation*

Matrices have been used in cardiomyocyte (CM) culture for decades. They serve as a physiological mimic of the cells’ in vivo environment to help enhance their response to other cells, drugs and extracellular matrix (ECM) proteins. Initially, natural matrices such as collagen and laminin (Gibco™)

were used however these are costly and contain xenogenic materials that alter the physiological cell response. Tumour-derived matrices such as Matrigel™ support most cell types very successfully and is commonly used in cell culture, induced pluripotent stem cells (iPSCs) in particular. Matrigel provides the cells with the necessary ECM proteins for efficient growth and differentiation without the need for serum and growth factors (Kleinman et al., 1987). The drawback of this matrix is that it is derived from mouse tumour meaning xenogenic components are present (Kleinman et al., 1982). The ultimate aim of cell biologists is to completely avoid the use of xenogenic components to recapitulate *in vivo* processes as accurately as possible. Synthetic substrates have become increasingly popular as they do not contain xenogenic components and due to their ease of manufacture. Synthetic matrices have been previously shown to support CM attachment both in serum and non-serum culture (Patel et al., 2015). Serum provides cells the ECM proteins required for faster attachment to the matrix surface. However, since serum is derived from animals (bovine sources), it is not favourable if the research is going to be utilised for *in vivo* purposes. Currently, iPSCs are cultured on Matrigel™ and then differentiated serum-free and feeder-free to cardiomyocytes in the absence of Matrigel™. This procedure is the most efficient method to produce the most mature CMs possible to date (BurrIDGE et al., 2014). Despite the continuous efforts in CM derivation, the end result of all the current methods is that they produce CMs that are still not as mature as native adult heart CMs. Consequently, the morphology of the cells are drastically different, adult CMs having a distinct rectangular rod-like shape whereas iPSC-CMs are more circular (Denning et al., 2016). Their functionality also differs in that they produce different proteins, with adult CMs expressing CM-specific SERCA2-ATPase while iPSC-CMs do not, among many other differential protein and gene expression patterns (Denning et al., 2016). More specifically, CMs of different maturity express different genes and hence different proteins, some being unique to CMs at a particular developmental stage (Denning et al., 2016). Adult CMs also possess a higher resting membrane potential compared to iPSC-CMs which means that the adult CMs have the capability of greater electrical conductivity (Denning et al., 2016).

The fabrication of complex architectures for cardiomyocyte attachment experiments commenced with a literature review on various structures that were built to test for differences in CM attachment and maturity, regardless of polymerisation method. This initial study was to investigate whether general structure architecture affected CM attachment and maturity. Indeed, some studies proved that this was true (Carson et al., 2016, Salick et al., 2014). According to the Salick study, optimal groove width was between 30 and 80  $\mu\text{m}$  for ESC-derived CMs and the Carson study demonstrated that iPSC-CMs preferred groove widths between 800 and 1000 nm. This was proved by immunofluorescence and quantitative analysis of cardiomyocyte morphology. The next step for the purposes of this project was to design architectures with high-resolution features to take full advantage of 2PL technology to determine whether these fine features affect CM attachment and maturity. The pattern dimensions from previous literature studies were utilised as constant dimensions in the designs for this study. Groove width was selected to be about 30  $\mu\text{m}$  as this value would be wide enough to observe multiple cell attachment, as opposed to 800-1000 nm. The groove depth was selected as a variable since the 2PL can fabricate structures at high resolution in the z dimension. Flat structures were also fabricated by 2PL to serve as a 2D control surface for CM attachment. The direction of the hatching lines is known to affect the way cells extend along a surface. This is known as 'contact guidance'. This means the topology provides guidance as to how cells will attach and spread on them. This phenomenon, which was first discovered by Curtis and Wilkinson in the 1970s demonstrates that cells respond to various topographies and align themselves along these structures. Contact guidance of corneal epithelial cells can be observed at the nanoscale, which models the human corneal basement membrane (Teixeira et al., 2003). The term 'contact guidance' was hypothesised in the 1970s however the discovery of cell response to topographical cues had been made in 1912 (Harrison, 1912) with the terminology 'stereotropism' defined in 1945 (Weiss and Wang, 1945). 'Tropism' is essentially the movement of an organism in response to an external stimulus. In this case, the stimulus is a solid body or rigid surface which adds the word 'stereo' to define the term 'stereotropism'. The fact that 2PL produces structures with resolution values as low as 100 nm serves as the perfect technique to test these parameters.

The purpose of this project is to demonstrate how different structural topologies affect CM attachment and maturity. Prior to this, the ability of the materials alone to support CM attachment, regardless of topology had to be studied in an efficient way. UV curing technology has been used to initiate free radical polymerization since the 1960s (Christmas et al., 1986) and has been extensively used (Decker, 1998) to polymerise biomaterials and this process of generating solid structures is much quicker compared to 2PL. Therefore, UV polymerisation was selected as the initial method to use to generate flat constructs of each polymer to be tested for CM attachment. UV polymerisation of epoxides and acrylates have been studied previously (Decker et al., 2001). The technology has been utilised to create constructs for biomedical applications ranging from scaffolds to support cell adhesion to drug delivery devices (Almeida et al., 2011). The reasoning behind using UV polymerization is due to the ability of this technique to confer high polymerization rate of reaction. This is thanks to the high intensity of the UV energy which typically has a wavelength in the 300-400 nm region (Davidson, 1999). 2-photon polymerisation (2PP) occurs using laser pulse wavelengths of ~785 nm. However, because 2 photons of 785 nm wavelength are required, the initiation rate is slower compared to the initiation rate of UV polymerization. UV polymerisation fabricates with much lower resolution however this was not the priority as only CM attachment to the material surface was being tested. The ease at which many monomer samples can be polymerized simultaneously in a 96-well plate in less than an hour allowed testing of all the 2-photon amenable homopolymers (as described in Chapter 4).

Silanisation was also found to be an important element of the procedure of polymer sample preparation. It was required to undertake this process when using coverslips as the target substrate to ensure polymers do not detach from the polystyrene plates. This is especially important for structures printed on glass cover slips by 2PL. Meanwhile, in this study, UV polymerisation was performed in 96-well plates which contains small wells that are 11.3 mm deep (Nunc™ MicroWell™ 96-well microplates, Thermo Scientific™) therefore the risk of polymer detachment was potentially significantly reduced. Silanisation also allows the silane molecules to serve as linkers between two surfaces that

would otherwise possess weak or inert bonding (Tham et al., 2010).

Silanisation has been applied in tissue engineering to connect biocompatible hydrogel materials to inert solids such as glass *via* covalent bonding (Yuk et al., 2016). It has been demonstrated that silanisation creates strong bonds that even hydrogels which contain significant amount of water can bind tightly to glass, opening avenues to applications in robotics and prosthetics (Yuk et al., 2016). Many factors influence the final effectiveness of the surface such as solvent type, silane concentration and silane type (Monticelli et al., 2006). 3-(trimethoxysilyl) propyl methacrylate (TMSPMA) was the silane type used in the experiments in this project, because the methacrylate groups at the end of the silane molecules bind to the polymer acrylate groups, which is the principle matrix resin type being studied. Other silane types such as epoxy, amino and mercapto silanes form bonds with resins too. Each silane type is suited a different resin depending on the kind of bonds formed (Aissaoui et al., 2012, Monticelli et al., 2006, Pasternack et al., 2008). Aminosilanes are suitable for binding DNA as the positively charged amino groups form electrostatic attraction with the negatively-charged DNA phosphate backbone (Nakagawa et al., 2005). The purpose of solvent use during silanisation is to form as anhydrous an environment as possible during the reaction. This is because water molecules can interfere with the formation of chemical bonds between the silane and glass interface (Silberzan et al., 1991). The solvent utilised during the silanisation procedure is crucial for the effectiveness of the silane-resin bond formation as some solvents can irreversibly damage the surface to be coated. Solvents have been tested for silanisation on polystyrene in previous studies (McGovern et al., 1994). A solvent's effectiveness is observed by how well it can remove water that is in contact with the glass or polystyrene surface being silanised without damaging the surface (Asay and Kim, 2005). Toluene is deemed to be a very effective solvent (McGovern et al., 1994), although this highly depends on the silane type and other reaction conditions such as temperature and the surrounding gaseous atmosphere. The solvents for silanisation of the polystyrene plates that were tested for their applicability in this project over a range of silane concentrations were acetone and isopropanol. The silane type is chosen as 3-trimethoxy silyl propyl methacrylate as these molecules contain the vinyl reactive sites and can polymerize with the acrylic

resin (Aissaoui et al., 2012). Indeed, there are a few ways to approach surface modification. The easiest method is physical adsorption because it is a rapid process. However, physical adsorption is not as strong as chemical modification as the bonds formed are hydrogen bonds, Van der Waals forces, electrostatic forces and hydrophobic interactions. Chemical modification enables the formation of covalent bonds which are the strongest bond type. Chemical modification can be performed by plasma treatment or UV light to graft acrylic polymers onto the substrate which utilizes a lot of energy. Indeed, Liu et al's work demonstrated a chemical modification method using plasma treatment to activate glass followed by self-assembled monolayer (SAM) (Mei et al.) in toluene solvent. Thus, toluene is selected as the solvent of choice in this study for the silanisation of glass cover slips because it has previously demonstrated good ability to extract water from reaction systems (McGovern et al., 1994) and will not damage the chosen substrate. This is because the resins are acrylate polymers and SAMs provide a strong adhesion to the glass surface to prevent loss of the 2-photon fabricated structures. In contrast, the solvents that are potentially the most suitable for silanisation of the 96-well polystyrene plates were either acetone or isopropanol since toluene solvent is known to damage polystyrene (Sword, 2017).

2-photon lithography (2PL), like with any 3D-printing technique has a certain degree of manufacturing error associated with it (Emons et al., 2012) (Zhou et al., 2015). 3D-printing involves design of the desired structure on computer design software packages such as AutoCAD which allow the user to design, set dimensions and manufacturing settings. This is all stored as a .stl file which is then sent to the printer for the design to be fabricated. The most common fabrication error is that the end product dimensions will differ from the design dimensions in .stl format (Jiang et al., 2016). However, this is usually a small difference in measurement, but it is important to know how large the error is if the material is to be utilized for future fabrication of complex architectures for specific applications. The various topologies will be tested for their ability to attach CMs which can respond to features at the sub-micron scale (Salick et al., 2014). Therefore, it is crucial to attain the fabrication error data of the multi-functional acrylates to be used in the CM attachment experiments.

The multi-functional acrylates discovered to be amenable to 2PL, as outlined in Chapter 3, were polymerised by UV light in the effort to deduce their CM attachment ability prior to progressing onto fabrication of complex architectures by 2PL. Once CM attachment onto a particular material is confirmed, studies of their attachment and maturity on the various topologies would be investigated.

#### *1.2.2.5 Construction of topologies for CM attachment and post-fabrication treatments to improve degree of cure*

It is well known that cells respond to topological features (Charras and Sahai, 2014, Bettinger et al., 2009). This translates to changes in morphology, motility and gene expression which result in varying maturity Denning et al. (2016).

Several studies have been carried out using CMs to prove that these cells respond to various topological fine features using different fabrication methods 1.2.2.2 Two-photon lithography. What has not been studied yet is how CMs behave on various topological structures fabricated by 2PL, i.e. on features varying by a few microns or less in the z-dimension. The previous studies discussed in 1.2.2.2 Two-photon lithography confirm the possibility of altered CM behaviour and differentiation state (i.e. maturity) on various substrate architectures. The Carson study showed that CMs preferred grooves of 800-1000 nm width when a range of 350-2000 nm groove widths were tested (Carson et al., 2016). CMs on 800-1000 nm were found to have significantly larger sarcomere lengths and significantly lower circularity indices, which are both indicative of enhanced CM development (Carson et al., 2016). A more recent study showed the pre-seeding polydimethylsiloxane (PDMS) substrates with human primary CMs, which are CMs directly derived from adult human heart, and then culturing iPSC-CMs on these pre-seeded substrates induced a more mature CM genotype and phenotype (Abadi et al., 2018). Another study has shown that iPSC-CMs in a biomaterial 3D structure developed into more mature CMs after xenotransplantation into rat heart (Narita et al., 2017). The period of time CMs are culture *in vitro* once they have already been differentiation has also been proven to be an important factor in stimulating maturity (Lewandowski et al., 2018). The question remains on whether CMs respond to different groove depths



fabricated by 2PL. As stated previously, there are many factors involved during the attachment of CMs to a substrate and the effect on their maturity (Denning et al., 2016).

The treatment the substrate is subject to which have an influence of CM attachment. The degree of cure (DOC) of the polymer is known to be important. The DOC of a polymer is defined as how much of monomer material is converted to polymer as a percentage of the total monomer at the start of the reaction (Carragher, 2007). The lower the DOC, the higher the amount of unreacted monomer which means there are a higher number of radicalised monomers in the polymer network. The monomers are radicalised because they have been electrophilically attacked by the photoinitiator molecules but have not reacted with a polymer chain to complete the polymerisation reaction. In addition, free radical photoinitiator may also remain in the polymer mixture that can cause cytotoxicity. The reason free radicals can cause cytotoxicity is that free radicals can enter cells and damage the DNA, proteins and lipids which causes cell death (Silva and Coutinho, 2010). Free radicals at a certain level are considered normal in cell physiology however if this exceeds the specified level, the process of autophagy (induced cell death) commences (Petersen et al., 2018). Free radicals remaining in uncured polymer substrates have been known to cause cytotoxicity (Beriat et al., 2010, Kamalak et al., 2018, Lee et al., 2017). UV light is used in polymerization reactions and in this project, it is used in an effort to increase DOC after constructs are fabricated by 2PL This is to compare the DOC between 2-photon constructs that are not treated by UV light post-fabrication and ones that have not. In addition UV light-treated 2-photon polymerised structures show improved stability compared to structures without UV light treatment (Purtov et al., 2018). Vacuum oven does not directly increase DOC since the process does not involve light. The vacuum environment removes any remaining solvent and unreacted monomer molecules if they are sufficiently volatile (whether radicalised or not). The reduction in the amount of unreacted radicalised monomer molecules is postulated to reduce cytotoxicity. Therefore, post-fabrication treatments by UV light and vacuum oven are performed in order to increase the DOC in an effort to reduce the occurrence of cell cytotoxicity (Taormina et al., 2018). Indeed, optical polymer sensors subject to post-

fabrication vacuum heat treatment demonstrated increased sensitivity (Zhong et al., 2016). The differences in the effects of these post-fabrication treatments on polymer DOC as well as CM attachment and maturity are analysed in this PhD study.

Raman spectroscopy is a long-standing method used to identify the chemical structure of an unknown material or the investigation of changes in chemical structure in known materials (Pulay, 2008). The 2-photon fabricated samples are very small and transparent. The size and height of the polymer materials makes signal detection more difficult as the signal detection depends on the amount of light scattered by the sample. Currently, Raman spectroscopy has advanced features such as use of high-magnification lenses and software to allow for multiple readings over longer periods of time in order to detect enough signal from photon scattering by the chemical bonds to generate data. Other analytical techniques such as mass spectrometry and nuclear magnetic resonance (NMR) spectroscopy give information on the chemical structure itself and not the amount of signal from chemical bonds. A further investigation into post-fabrication processes is the use of solvent during polymer rinsing after 2PL. The current methodology (n=4) involves the use of Polypropylene glycol monomethyl ether acetate (PGMEA) as a solvent. It was postulated this solvent may remain post-fabrication and have a role in cytotoxicity in the case of TCDMDA. This is because TCDMDA contains a cyclic ring structure which is electron rich and can attract the ether group of PGMEA. Therefore, Raman spectroscopy measurements were set so as to ensure detection of the ether group peak which is the distinguishing part of this molecule. The amount of remaining PGMEA will be compared between the three polymers TCDMDA, GPOTA and PETrA.

The fabrication of various architectures using 2PL will aid the identification of the optimal architecture for the CMs with closest maturity to adult CMs. Post-fabrication methods are aimed to increase polymer DOC and improve CM attachment. The utilization of these architectures to create large *in vitro* arrays will enable high-throughput CM culture. Therefore, this doctoral project and similar future studies will aid more high-throughput *in vitro* CM culture to assess drug screening and disease modelling.

1.2.3: Mapping the Process: Experiments needed to be followed in a specific order (Figure 1.4). The project was divided into four main tasks;

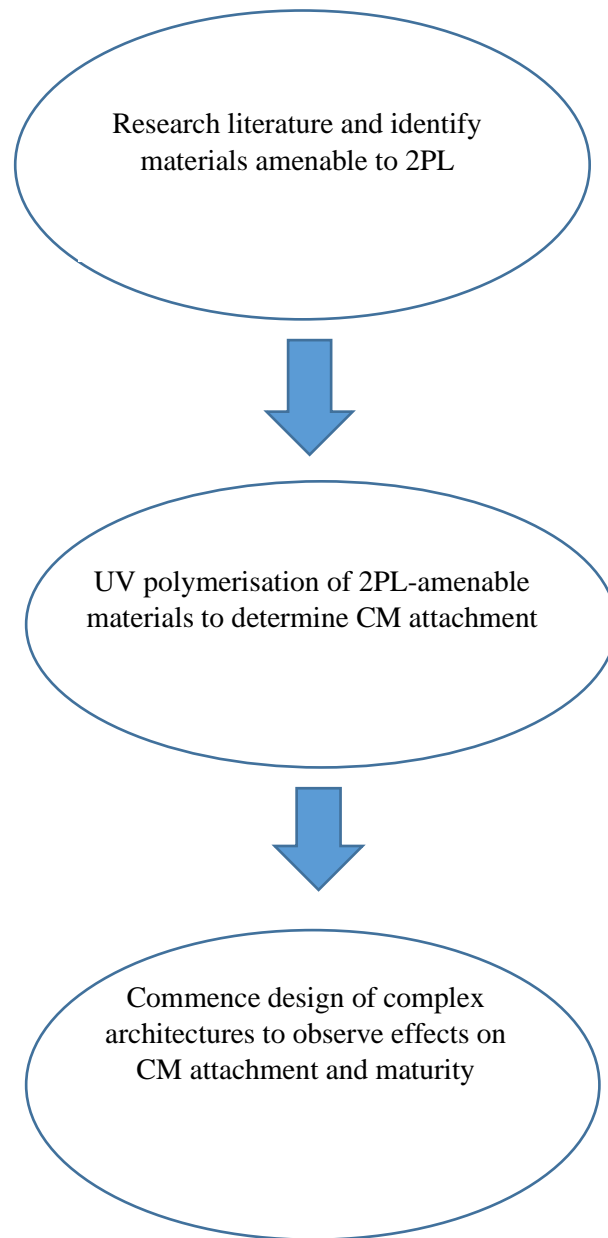


**Figure 1.4: Workflow illustrating the steps taken to test the hypothesis of this doctoral project.**

#### 1.2.4: Summary

The combination of 2PL to construct highly accurate architectures with sub-micron resolution and the selection of materials to enhance the attachment and maturity of CMs offers great scope for in vitro drug screening methodologies. The time and finances spent on bringing a drug to the market could be vastly reduced if a high-throughput in vitro methodology is established as it would enable early detection of possible adverse side effects of drugs. The method could also pave a way to personalised medicine with the use of iPSCs as each cell line carries the epigenetic signature associated with the donor patient they are taken from (Kim et al., 2010). The identification of the optimal architecture to support mature CMs would aid in the creation of a high-throughput in vitro methodology. In this way, drug screening will ultimately result in the most accurate CM response. This study works towards this goal by identifying materials successfully processed by 2PL that can support CM maturity and attachment, then by analysing the effect of various architectures manufactured with these materials on the attachment and maturity of CMs. This will allow selection of the architecture that supports the most mature CMs, thereby ultimately leading to more accurate drug screening methodologies.

## Chapter 2: Methodologies

### 2.1 2-photon lithography

#### 2.1.1 Background

2-photon lithography utilizes the phenomenon of 2-photon absorption to manufacture structures at high resolution. Briefly, a femtosecond pulsed laser is directed through a set of mirrors which passes through a beam splitter. This separates part of the beam to a camera and a part through the objective to the sample. Samples can range from acrylates, urethane monomers and epoxies. They come in liquid form and upon excitement by the laser beam are polymerised to form a solid. The laser beam has a wavelength of about 780nm. The monomer contains a light-sensitive molecule called a photoinitiator, which absorbs light within a certain range of wavelengths. Most commercially available photo initiators absorb within the UV-wavelength region (300-400 nm). Therefore, the laser is pulsed so that many photons are packaged into each pulse in order to achieve 2-photon absorption by the photoinitiator. Lasers of lower frequencies would not be able to create pulses of a high peak power within a small volume, rendering 2-photon absorption impossible. The absorption outside the focal beam is negligible which prevents out-of-focus fabrication. The apparatus for a 2PL system includes a laser source, galvanomirrors, a CCD camera, a piezo-stage and a microscope (Figure 2.1).

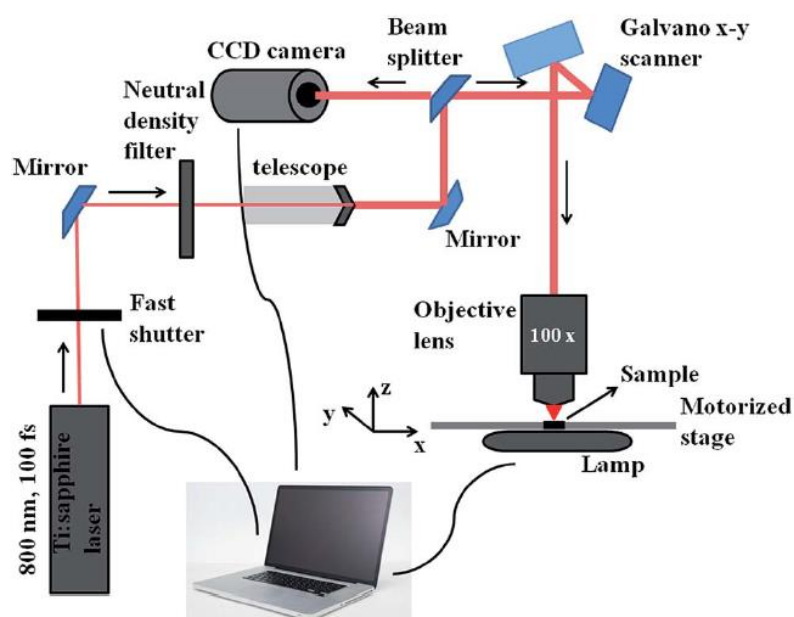


**Figure 2.1: Two-photon lithography system (Ciuciu and Cywiński, 2014).**

The laser beam is typically a Ti: Sapphire femtosecond laser pulse of wavelength 800nm which is excited by an Argon-ion source. The laser beam is directed into the resin by acousto-optic modulators which strengthen the laser beam and galvano-mirrors which adjust the position of the laser beam in the X-Y axes. The piezo-electric stage adjusts the position of the sample in the z-direction. The microscope is positioned below the stage from which the laser is directed through into the resin. A CCD camera detects the photons reflected from the sample and records the process with the aid of the beam splitter (Figure 2.1).

#### 2.1.2 Formulation Preparation

The photoinitiator Irgacure 369 (I369) (Sigma-Aldrich™) is used in the polymerization experiments as it is known to dissolve in organic solvents. Prior to 2-photon polymerization, samples are prepared by weighing out I369 on a balance and completing to a suitable volume with the monomer to obtain the required I369 concentration. Table 2.1 lists all the photoinitiator weights and monomer volumes used for each formulation.

**Table 2.1: Formulation preparations showing relative amounts of photo initiator and monomer.**

| <b>Formulation (%)</b> | <b>Photo initiator weight (mg)</b> | <b>Monomer volume (ml)</b> |
|------------------------|------------------------------------|----------------------------|
| <b>1.0</b>             | 11.2                               | 1                          |
| <b>2.0</b>             | 22.5                               | 1                          |
| <b>3.0</b>             | 33.7                               | 1                          |
| <b>4.0</b>             | 45.0                               | 1                          |
| <b>5.0</b>             | 56.2                               | 1                          |
| <b>6.0</b>             | 67.5                               | 1                          |
| <b>8.0</b>             | 90.0                               | 1                          |
| <b>10.0</b>            | 112                                | 1                          |

The relative molar mass of both Irgacure 369 and the candidate monomers were considered in order to produce an accurate formulation. For instance;

1 mol Irgacure 369 = 380.5 g and 1 mol glycerol propoxylate triacrylate (one of the candidate monomers) = 428 g

Therefore, the molar ratio =  $380.5 \text{ g} / 428 \text{ g} = 0.889$

Applying this ratio to a 1.0% w/v formulation in 1 ml;

1% of 1000  $\mu\text{l}$  is 10 mg =  $10 / 0.889 = 11.2 \text{ g}$  of Irgacure 369 (Table 4, 1<sup>st</sup> row).

This calculation was repeated for all photoinitiator concentrations applied in the experiment (Table 2.1).

Control formulations were prepared for each monomer investigated. The formulation was composed of 1ml of monomer without I369 photo initiator.

All formulations were placed on a hot plate for 10-15 minutes at 65°C prior to sample loading to ensure all of the photoinitiator had dissolved in the monomer solution.

### 2.1.3 2-Photon Lithography

Two-photon polymerization was performed using the Nanoscribe-Gmbh system. After formulation preparation, a drop of immersion oil was placed on the centre of a cover slip (20mmx20mm) which was taped onto the sample tray. Then, 50 $\mu\text{l}$  of the formulation mixture was loaded onto the other side of the glass slide and the sample loaded onto the Nanoscribe system using the 63X oil immersion objective. This is the most suitable objective when structures to be fabricated are not high (more than 140  $\mu\text{m}$ ).

The designs for the printing process are made on Nanoscribe's own coding software (Describe, GmbH) which uses a series of basic lines that can be modified to create layers of lines of different spacing. Complicated structures can be designed on AutoCAD<sup>®</sup> which have to be converted to .stl format for the Nanoscribe system (Nanoscribe, GmbH<sup>®</sup>) to recognise. Once the file is loaded, dimensions, hatching type, hatching distance and slicing distance can

be modified accordingly. When the design is ready, it is loaded onto the NanoWrite<sup>®</sup> software to begin the printing process.

Once processing was complete, the cover slip was removed from the sample tray and kept in developer solution, called Polypropylene glycol monomethyl ether acetate (PGMEA) (Sigma-Aldrich<sup>®</sup>), for at least 10 minutes to ensure all unreacted monomer is washed off the solid, printed polymer. After development, the cover slip was held with tweezers and gently washed with isopropanol followed by drying with a hand pump. The gentle washing ensures that the structure does not detach from the glass cover slip. Glass cover slips can be silanised to strengthen structure attachment (see section 2.6). The slides were taped into, labelled and kept in a petri dish until further analysis. Petri dishes were stored in the dark until further use.

2.1.4: Designing a systematic screening method using a combination of photoinitiator concentration, laser power and scanspeed parameters

*2.1.4.1 Calculation of Total Spot Energy Absorption and Reverse Calculation to Achieve Workable Scanspeed values for 2PL*

Table 3.8 shows a list of various laser power and scanspeed values along with the constant parameters related to the 2-photon system. Repetition rate in column 3 is the number of times the laser is pulsating, in other words the frequency of the laser. Nominal spot size in column 4 is the largest size the laser focal spot can achieve and the pulse length in column 5 signifies how long each laser pulse lasts in duration (seconds). The units in columns 6, 7, 8 and 9 are calculated accordingly;

**Energy per pulse**= Nominal Power\*Pulse Length

**Translation time across spot (s)** = Nominal Spot Size/Scanspeed

**Number of pulses per spot** = Repetition rate\*Translation time across spot

**Total Spot Energy Absorption** = Energy per pulse\*Number of pulses per spot



The last row highlighted in yellow in Table 2.2 contains the energy value 3.33 pJ that is used in the determination of an unknown scanspeed in Table 2.3. Table 2.3 shows a series of different laser powers that result in different total spot energy absorption values which were calculated in the exact same way as above. The only difference is the total spot energy absorption values were already known and either the scanspeed or the nominal power was calculated. In the situation that a user knows the optimal total spot energy absorption of a particular structure as highlighted in green in Table 2.3. The energy value is 3.33 pJ with the equivalent scanspeed being 1000  $\mu\text{m/s}$  and the laser power 2.75E-02. The scanspeed of 1000  $\mu\text{m/s}$  is a very slow scanspeed to work with therefore the question was asked what if the same total spot energy absorption can be applied using a higher scanspeed. By placing the energy value 3.33 pJ shown at the bottom of Table 2.3 highlighted yellow, the calculations were done in reverse to achieve the scanspeed of 18,000  $\mu\text{m/s}$ . This is a much more practical value to work with during 2PL as the fabrication time is reduced without compromising the energy value applied. Note that the laser power also had to be increased to reach the same total spot energy absorption value (Table 2.3).

The total spot energy absorption in pJ is the unit used throughout this chapter to describe how much energy is being transferred during the fabrication of the structures. This way, the laser power and scanspeed values are merged into 1 unit. Therefore, the graphs for the operating windows are plotted easily with total spot energy absorption against photoinitiator concentration.

**Table 2. 2: Laser Power and scanspeed values utilized during 2PL. The total spot energy absorption is determined by using the power and scanspeed values selected by the user and the repetition rate, nominal spot size and pulse length which are constants characteristic of the Nanoscribe laser beam.**

| Scanspeed | Nominal Power (W) | Repetition Rate (Hz) | Nominal Spot size (m) | Pulse length (sec) | Energy per pulse (J) | Translation time across spot (s) | Number of pulses per spot | Total spot energy absorption (J) |
|-----------|-------------------|----------------------|-----------------------|--------------------|----------------------|----------------------------------|---------------------------|----------------------------------|
| 0.001     | 5.00E-03          | 80000000             | 0.00000015            | 1E-13              | 5E-16                | 0.00015                          | 12000                     | 6E-12                            |
| 0.001     | 1.00E-02          | 80000000             | 0.00000015            | 1E-13              | 1E-15                | 0.00015                          | 12000                     | 1.2E-11                          |
| 0.001     | 1.75E-02          | 80000000             | 0.00000015            | 1E-13              | 1.75E-15             | 0.00015                          | 12000                     | 2.1E-11                          |
| 0.001     | 1.50E-02          | 80000000             | 0.00000015            | 1E-13              | 1.5E-15              | 0.00015                          | 12000                     | 1.8E-11                          |
| 0.001     | 2.00E-02          | 80000000             | 0.00000015            | 1E-13              | 2E-15                | 0.00015                          | 12000                     | 2.4E-11                          |
| 0.001     | 2.25E-02          | 80000000             | 0.00000015            | 1E-13              | 2.25E-15             | 0.00015                          | 12000                     | 2.7E-11                          |
| 0.001     | 2.50E-02          | 80000000             | 0.00000015            | 1E-13              | 2.5E-15              | 0.00015                          | 12000                     | 3E-11                            |
| 0.001     | 2.75E-02          | 80000000             | 0.00000015            | 1E-13              | 2.75E-15             | 0.00015                          | 12000                     | 3.3E-11                          |
| 0.001     | 3.00E-02          | 80000000             | 0.00000015            | 1E-13              | 3E-15                | 0.00015                          | 12000                     | 3.6E-11                          |
| 0.001     | 3.10E-02          | 80000000             | 0.00000015            | 1E-13              | 3.1E-15              | 0.00015                          | 12000                     | 3.72E-11                         |
| 0.001     | 3.50E-02          | 80000000             | 0.00000015            | 1E-13              | 3.5E-15              | 0.00015                          | 12000                     | 4.2E-11                          |
| 0.001     | 4.00E-02          | 80000000             | 0.00000015            | 1E-13              | 4.00E-15             | 0.00015                          | 12000                     | 4.80E-11                         |
| 0.001     | 4.50E-02          | 80000000             | 0.00000015            | 1E-13              | 4.50E-15             | 0.00015                          | 12000                     | 5.40E-11                         |
| 0.001     | 5.00E-02          | 80000000             | 0.00000015            | 1E-13              | 5E-15                | 0.00015                          | 12000                     | 6E-11                            |
| 0.018     | 5.00E-02          | 80000000             | 0.00000015            | 1E-13              | 5E-15                | 8.33333E-6                       | 666.667                   | 3.33333E-11                      |

**Table 2. 3: Laser power and scanspeed values used during 2PL. The highlighted values in green show the location of the midpoint parameter that was found for the woodpile array (3.33E-11 pJ). The highlighted row in yellow shows how the midpoint parameter (3.33E-11 pJ) in the woodpile operating window alongside highest laser power (5.00E-02), was used to calculate the equivalent scanspeed value to reduce fabrication time (18,000  $\mu\text{m/s}$ ).**

| Scanspeed | Nominal Power (W) | Repetition Rate (Hz) | Nominal Spot size (m) | Pulse length (sec) | Energy per pulse (J) | Translation time across spot (s) | Number of pulses per spot | Total spot energy absorption (J) |
|-----------|-------------------|----------------------|-----------------------|--------------------|----------------------|----------------------------------|---------------------------|----------------------------------|
| 0.001     | 5.00E-02          | 80000000             | 0.00000015            | 1E-13              | 5E-15                | 0.00015                          | 12000                     | 6E-11                            |
| 0.0012    | 5.00E-02          | 80000000             | 0.00000015            | 1E-13              | 5E-15                | 0.000125                         | 10000                     | 5E-11                            |
| 0.0014    | 5.00E-02          | 80000000             | 0.00000015            | 1E-13              | 5E-15                | 0.000107143                      | 8571.429                  | 4.28571E-11                      |
| 0.0016    | 5.00E-02          | 80000000             | 0.00000015            | 1E-13              | 5E-15                | 0.00009375                       | 7500                      | 3.75E-11                         |
| 0.0018    | 5.00E-02          | 80000000             | 0.00000015            | 1E-13              | 5E-15                | 8.33333E-05                      | 6666.667                  | 3.33333E-11                      |
| 0.002     | 5.00E-02          | 80000000             | 0.00000015            | 1E-13              | 5E-15                | 0.000075                         | 6000                      | 3E-11                            |
| 0.0025    | 5.00E-02          | 80000000             | 0.00000015            | 1E-13              | 5E-15                | 0.00006                          | 4800                      | 2.4E-11                          |
| 0.003     | 5.00E-02          | 80000000             | 0.00000015            | 1E-13              | 5E-15                | 0.00005                          | 4000                      | 2E-11                            |
| 0.0035    | 5.00E-02          | 80000000             | 0.00000015            | 1E-13              | 5E-15                | 4.28571E-05                      | 3428.571                  | 1.71429E-11                      |
| 0.004     | 5.00E-02          | 80000000             | 0.00000015            | 1E-13              | 5E-15                | 0.0000375                        | 3000                      | 1.5E-11                          |
| 0.006     | 5.00E-02          | 80000000             | 0.00000015            | 1E-13              | 5E-15                | 0.000025                         | 2000                      | 1E-11                            |
| 0.008     | 5.00E-02          | 80000000             | 0.00000015            | 1E-13              | 5E-15                | 0.00001875                       | 1500                      | 7.5E-12                          |
| 0.01      | 5.00E-02          | 80000000             | 0.00000015            | 1E-13              | 5.00E-15             | 0.000015                         | 1200                      | 6E-12                            |
| 0.01      | 3.00E-02          | 80000000             | 0.00000015            | 1E-13              | 3.00E-15             | 0.000015                         | 1200                      | 3.6E-12                          |
| 0.01      | 2.00E-02          | 80000000             | 0.00000015            | 1E-13              | 2.00E-15             | 0.000015                         | 1200                      | 2.4E-12                          |
| 0.01      | 1.00E-02          | 80000000             | 0.00000015            | 1E-13              | 1.00E-15             | 0.000015                         | 1200                      | 1.2E-12                          |
| 0.01      | 5.00E-03          | 80000000             | 0.00000015            | 1E-13              | 5.00E-16             | 0.000015                         | 1200                      | 6E-13                            |
| 0.018     | 5.00E-02          | 80000000             | 0.00000015            | 1E-13              | 5E-15                | 8.33333E-6                       | 666.667                   | 3.33333E-11                      |

#### 2.1.4.2 Selection of the range of total spot energy absorption values for 2PL

The total spot energy absorption in pJ is the unit used throughout this chapter to describe how much energy is being transferred during the fabrication of the structures. This way, the laser power and scanspeed values are merged into 1 unit. Therefore, the graphs for the operating windows are plotted easily with total spot energy absorption.

Optimum photo initiator concentration for the monomer in question was determined by observation of operating window size over three experimental repeats ( $n=3$ ). The operating window was determined by observation of processed structures over a range of energy absorption values. The energy absorption values were used to determine the operating window for the purpose of combining laser power and scanspeed parameters into one unit. These could then be directly compared to the other variable being tested, which was PI concentration. Table 2.4 shows the laser power and scanspeed units used in the 2PL fabrication experiments in this chapter. The corresponding energy value in pJ is shown column 3 (Table 2.4).

**Table 2. 4: Range of laser power and scan speed values selected for determination of processing window for selected monomers. Energy values were calculated using a series of calculations including laser power, scanspeed and constants such as pulse frequency.**

| <b>Laser Power<br/>(mW)</b> | <b>Scanspeed<br/>(mm/s)</b> | <b>Energy<br/>(pJ)</b> |
|-----------------------------|-----------------------------|------------------------|
| <b>50</b>                   | 1                           | 60                     |
| <b>50</b>                   | 1.2                         | 50                     |
| <b>50</b>                   | 1.4                         | 42.9                   |
| <b>50</b>                   | 1.6                         | 37.5                   |
| <b>50</b>                   | 1.8                         | 33.3                   |
| <b>50</b>                   | 2.0                         | 30                     |
| <b>50</b>                   | 2.5                         | 24                     |
| <b>50</b>                   | 3.0                         | 20                     |
| <b>50</b>                   | 3.5                         | 17.1                   |
| <b>50</b>                   | 4.0                         | 15                     |
| <b>50</b>                   | 6.0                         | 10                     |
| <b>50</b>                   | 8.0                         | 7.5                    |
| <b>50</b>                   | 10                          | 6                      |
| <b>40</b>                   | 10                          | 4.8                    |
| <b>30</b>                   | 10                          | 3.6                    |
| <b>20</b>                   | 10                          | 2.4                    |
| <b>10</b>                   | 10                          | 1.2                    |

#### *2.1.4.3 Design of the key for fabrication quality*

A series of total spot energy absorption values were used to determine the operating window of the selected polymers. Three experimental repeats were done using a fresh formulation each time at PI concentrations of 1, 2, 3, 4, 5, 6, 8 and 10%.

E<sub>max</sub> and E<sub>min</sub> values were determined by observation of scanning electron microscopy (Aissaoui et al.) images of all fabricated structures and following a carefully designed quality scale of which the key is given below;

0= no structure visible or a lot of damage observed

1=structure processed and visible

A sub-category was generated for structures scoring

A=structure processed with damage

B=complete structure without any damage

C=structure processed but with most parts incomplete

E<sub>max</sub> was defined as the maximum energy value at which a complete structure can be fabricated and E<sub>min</sub> was defined as the minimum energy values at which complete structure can be fabricated. Any structures above E<sub>max</sub> appeared damaged and any structures below E<sub>min</sub> appeared incomplete, faded or no fabrication was visible.

The average E<sub>max</sub> and E<sub>min</sub> was calculated using the energy values from the 1<sup>st</sup>, 2<sup>nd</sup> and 3<sup>rd</sup> rounds of processing at each photo initiator concentration and these were plotted as a trend of how E<sub>max</sub> and E<sub>min</sub> differ according to photo initiator concentration.

The processing window was determined by identifying the region between the maximum energy at which a structure can be fabricated without any visible damage (E<sub>max</sub>) and the minimum energy at which a structure can be fabricated with all parts complete i.e. no incomplete polymerization (E<sub>min</sub>).

### 2.1.5 Selection of designs for 2PL

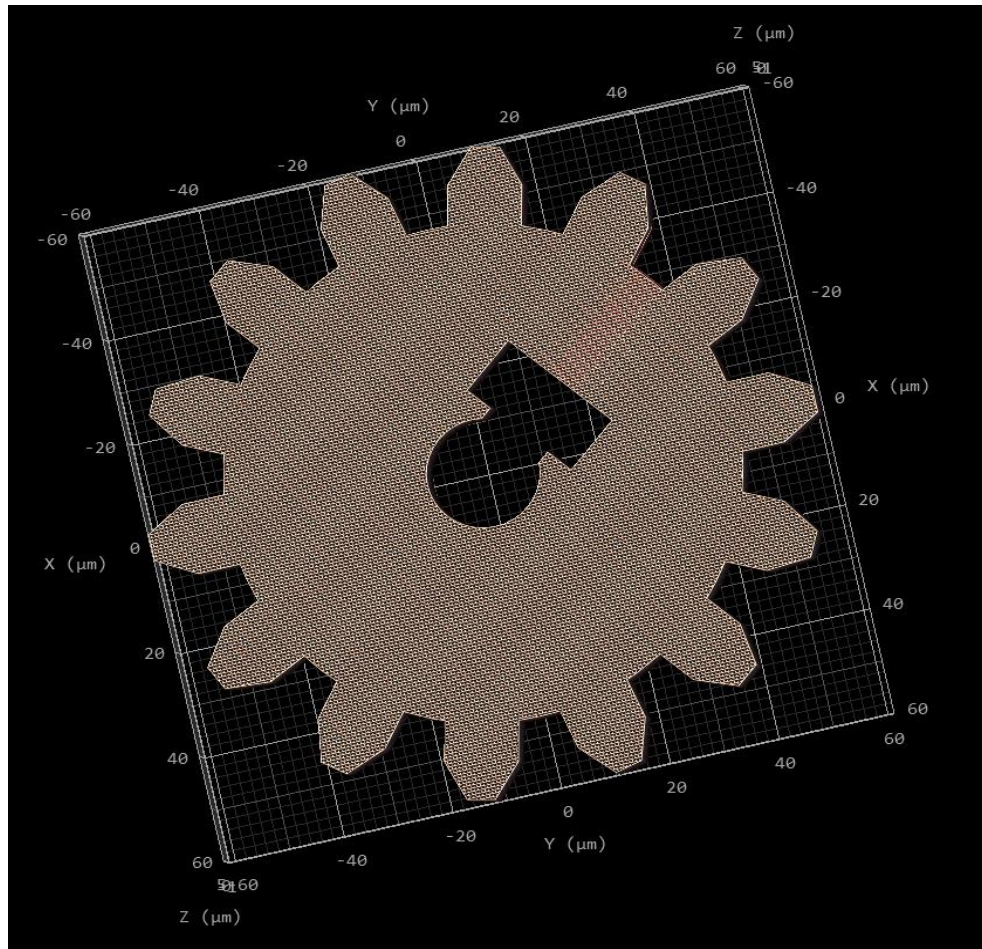


**Figure 2.2: Gear design with dimensions of 100  $\mu\text{m}$  (x), 100  $\mu\text{m}$  (y) and 5  $\mu\text{m}$  (z).**

A gear design was selected to facilitate visibility during processing of formulations (Figure 2.2). In addition, the diameter was large enough to ensure immediate identification of the structure after development. The structure was not too high to ensure that height was not a limiting factor during processing and slicing distance was set to 0.5  $\mu\text{m}$  to stabilise the structure. Hatching distance was set to 0.5  $\mu\text{m}$  with the offset at 90° for further stabilisation (Figure 2.3, top). The bottom picture in Figure 2.3 shows the lateral view of the gear design.

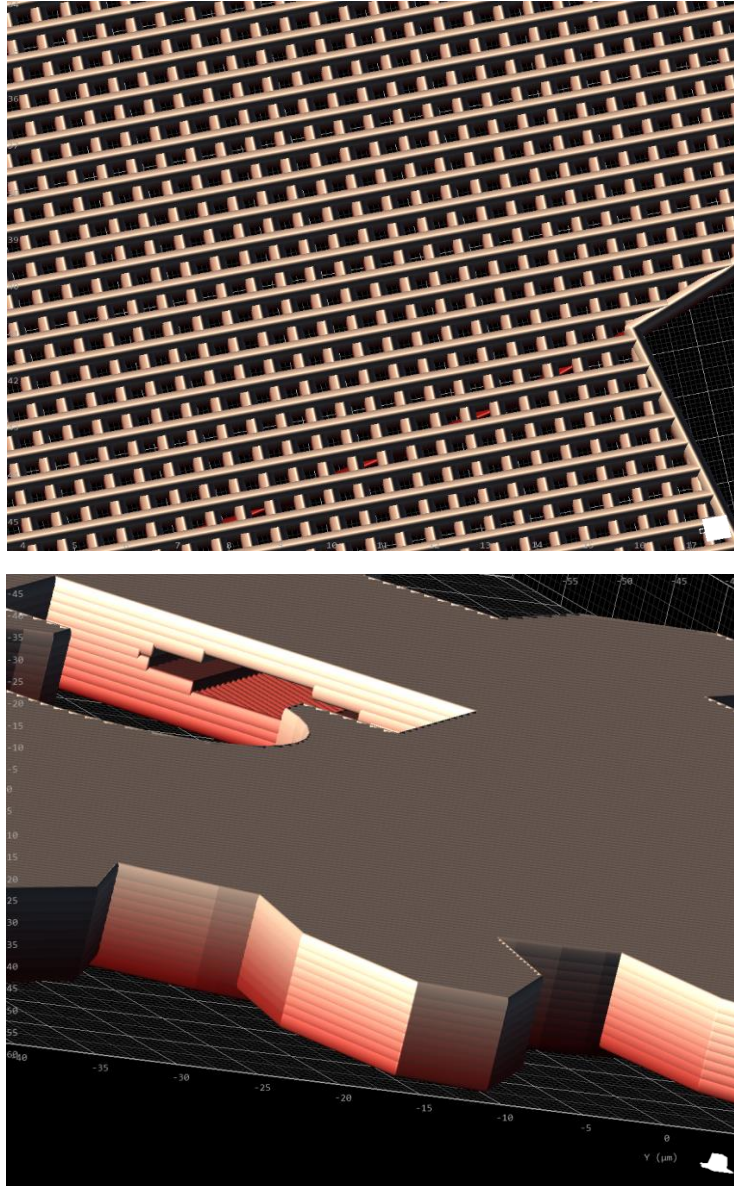


**Figure 2.3: top: Close-up view of hatching pattern on gear design. Bottom: Close-up view of slicing showing all 10 slices of gear design.**



To eliminate the factor of hatching distance and structure complexity, a new woodpile design was created on AutoCAD (Figure 2.4). The woodpile design consisted of a row of cylinders with another row of cylinders on top which were in the orthogonal direction. The dimensions were set to 30  $\mu\text{m}$  (x), 30  $\mu\text{m}$  (y) and 5  $\mu\text{m}$  (z) as a structure of this size is still easily visible and speeds processing for the power sweep.

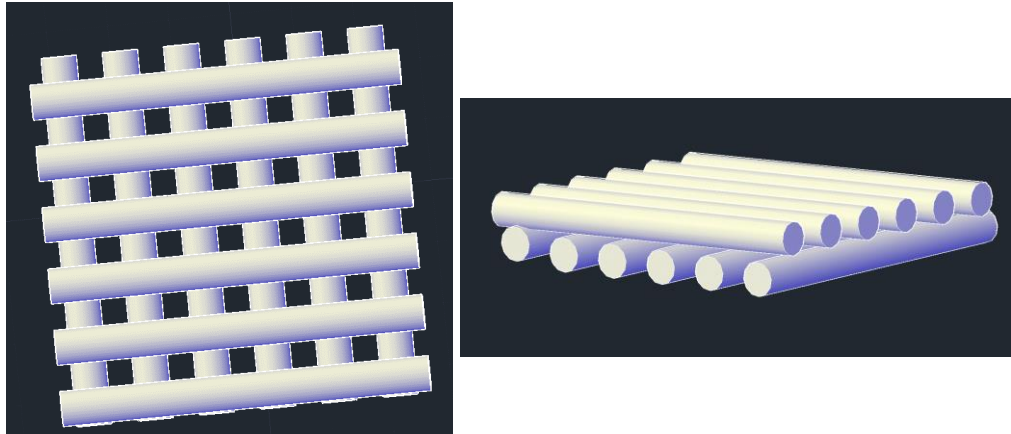


**Figure 2.4: Woodpile design as created in AutoCAD software. Left: View from top. Right: Lateral view showing both layers.**

To simplify the design even further for determination of optimal photo initiator concentration, a woodpile structure was designed using the coding system of Describe software (Nanoscribe GmbH). Figure 2.5 shows how one woodpile design looks from above on the Describe software. The dimensions were large enough to observe easily on the SEM albeit small enough for reduced fabrication time. This process required efficient fabrication as many polymers at a range of PI concentrations were setup for the experiment.

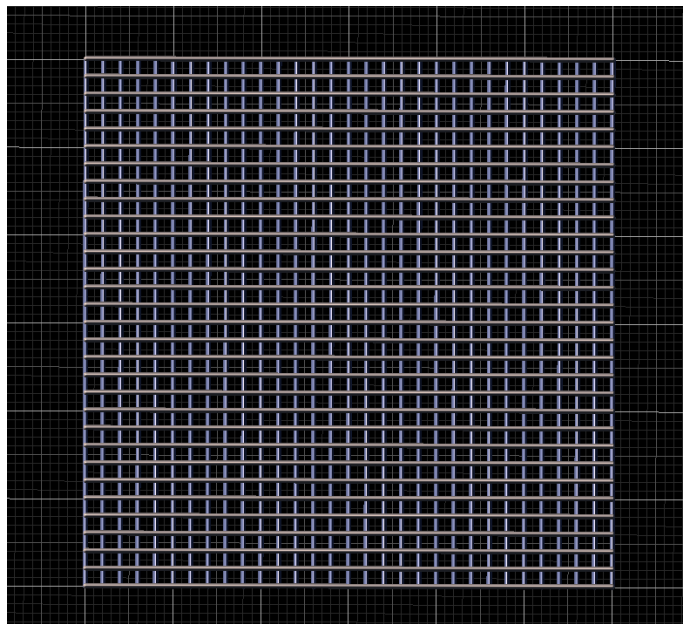


**Figure 2.5: Woodpile structure which measured 30 (x) by 30 (y)  $\mu\text{m}$ .**

The already designed woodpile structures were combined into an array of woodpiles so that a range of laser powers could be applied in one fabrication run. This ensured the process was even more efficient. Figure 2.6 shows the woodpile array design. The measurements were the same as in Figure 2.6 and the programme was written to enable manufacture of a number of repeats so that each repeat was processed at different laser powers. The processing was set to commence from bottom to top starting from the left-hand corner.

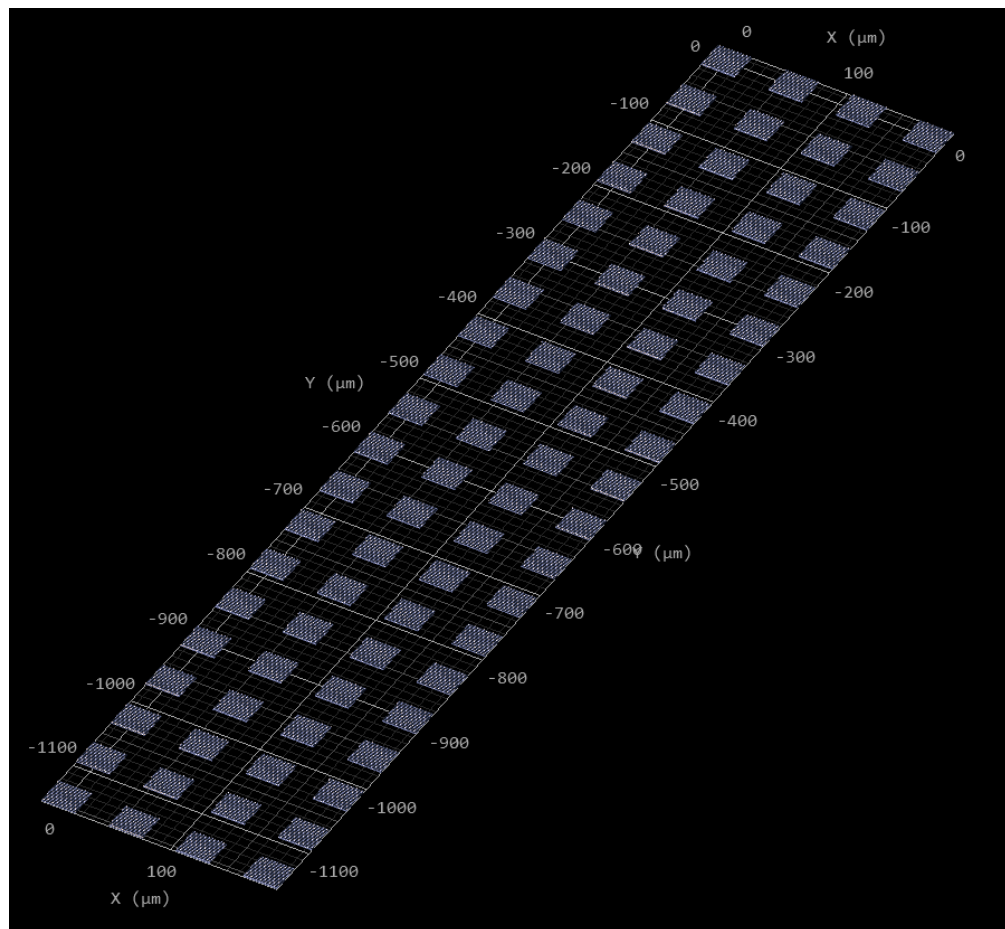


**Figure 2.6: Woodpile design organised as a 4 by 20 array. Each woodpile structure was processed 4 times at each assigned laser power. The laser power was assigned at increments of 5 from 1-100% starting from the bottom to the top.**

#### 2.1.6 Post-development

Constructs to be used in cardiomyocyte culture experiments were carefully rinsed three times with water by holding the glass cover slip with tweezers whilst rinsing. Then they were dried using a hand pump and placed in the vacuum oven for a week to eliminate any remaining uncured monomer.

Constructs to be used for SEM were platinum coated (refer to section 2.2).

#### 2.2 Platinum Sputter Coating of glass cover slips

Prior to scanning electron microscopy (Aissaoui et al.), some samples require coating with a type of metal and these can be Platinum, gold, silver or palladium. The reason for this is that most samples are not conductive and therefore do not let electrons pass through them. A beam of electrons is directed on the sample during SEM and if electrons accumulate in the sample, it will get charged up creating white, blurred regions causing lack of visualisation. Therefore, it is essential to coat the sample with a conductive metal.

Sputter coating is a technique used to coat samples using an ion gas source (usually Argon) in a vacuum chamber directed towards a negatively charged metal cathode. The gas ions knock metal atoms off the cathode that travel down towards the anode, where the sample is located. This results in a layer of metal deposition on top of the sample.

The metal applied depends on the type of sample. Gold is suitable for larger samples or ones where fine features are not the priority as gold deposits as a thicker layer compared to platinum. This is due to the high sputtering rate of gold compared to other metals. If fine feature observation is essential, then platinum is the preferred metal. Carbon is also used for this technique; however, this is only used for X-ray microanalysis and support films on transmission electron microscopy (TEM) grids as this material deposits a very fine layer which is suitable for these high-grade techniques.

Slides were coated with platinum using a Platinum coater (Polaron Range Sputter Coater) in an Argon vacuum for 90 seconds at 2.2kV and 15-20mA.

### 2.3 Scanning electron microscopy

SEM is a powerful microscopy technique used to image samples down to the nanometre range. The magnification ranges from 10X-1,000,000X. It outruns any other microscopy technique when it comes to imaging small samples at high resolution. The most important features of SEM are the ease of changing magnification, large depth of focus and stereographic image display.

Briefly, the method works by an electron beam generated by an electron gun that is deflected down the tube by magnetic fields to reach the sample. Electrons hit the sample which are emitted in different ways. Secondary electrons knock out orbital electrons from the atoms in the sample. This is useful for topographical imaging as it occurs closer to the surface of the specimen. Backscattered electrons occur from electrons in inner orbitals of the atoms therefore they are useful for acquiring compositional information of the sample surface. Some of the electrons are transmitted through the specimen and this gives information on the internal structure. The emitted information is converted into an electric signal, amplified and fed into an observation cathode ray tube (CRT). The CRT shows the electron beam scanning the specimen in real-time and an image is displayed. Topographical SEM using secondary electron deflection is the technique used throughout this project as the interest in the surface topography of the polymers as this is the region the cells will interact with when seeded onto the structures.

Slides were viewed using JEOL 6060LV or JEOL6490LV scanning electron microscopes. Firstly, the stubs were carefully handled with gloves and placed into the sample holder of the SEM. The order of samples on the holder were sketched into the laboratory notebook in order to remember the location of each stub.

### 2.4 Oxygen Plasma Etching

Plasma is defined as the 4<sup>th</sup> state of matter and is a highly ionised gas or vapour. Plasmas are used to modify surfaces which is termed as etching or coat substances onto surface (deposition). The essential conditions to create plasma

are high pressure and an electric field. An electrical motor pump connected to a liquid nitrogen container creates the required base pressure of the system. Oxygen is allowed to flow through the system and the electric field switched on which creates the plasma.

Plasma oxygen cleaves the bonds between carbon atoms of contaminants and the glass surface. This results in water and carbon dioxide being released and pumped out of the system (Figure 2.7).

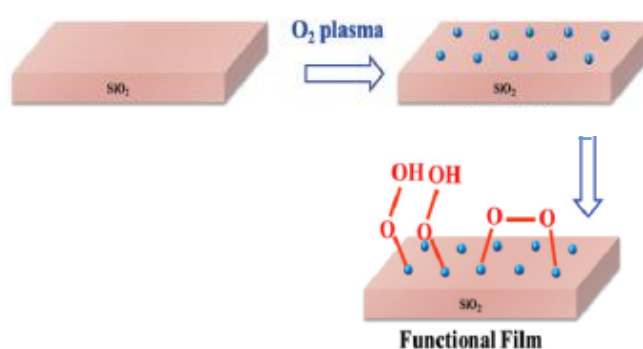


**Figure 2.7: Oxygen plasma cleaning and activation procedure (Wang et al., 2014).**

In this way, plasma oxygen cleans the contaminants off glass surfaces and creates an activated surface because oxygen will bind the silicon atoms on the glass surface. This allows certain desired molecules to attach to the glass which is covered in the next section.

Oxygen plasma etching in a vacuum chamber was used to clean glass cover slips and the well-bottoms of 96-well polystyrene plates for 10 minutes at 10 MHz radiofrequency and less than 100 base pressure.

## 2.5 Silanisation

Silanisation is a process performed on silicon glass in which molecules with specific functional groups are attached the activated silicon atoms on the glass surface. The part of the molecule that reacts with the glass surface is the trimethoxysilane (Figure 2.8). This is hydrolysed upon exposure to the thin film

of water already adsorbed on the glass. The process forms silanols which can form hydrogen bonds with silanol groups on the glass surface. The silicon atom of the trimethoxysilane can directly form a covalent bond with an oxygen atom on the glass surface (Figure 2.8, blue-striped area represents glass).

In the case of silanisation for this project, the R group is a methacrylate group to ensure polymerisation occurs between the acrylate resin utilised for 2-photon fabrication and the methacrylate group on the TMSPPMA (Figure 2.8).

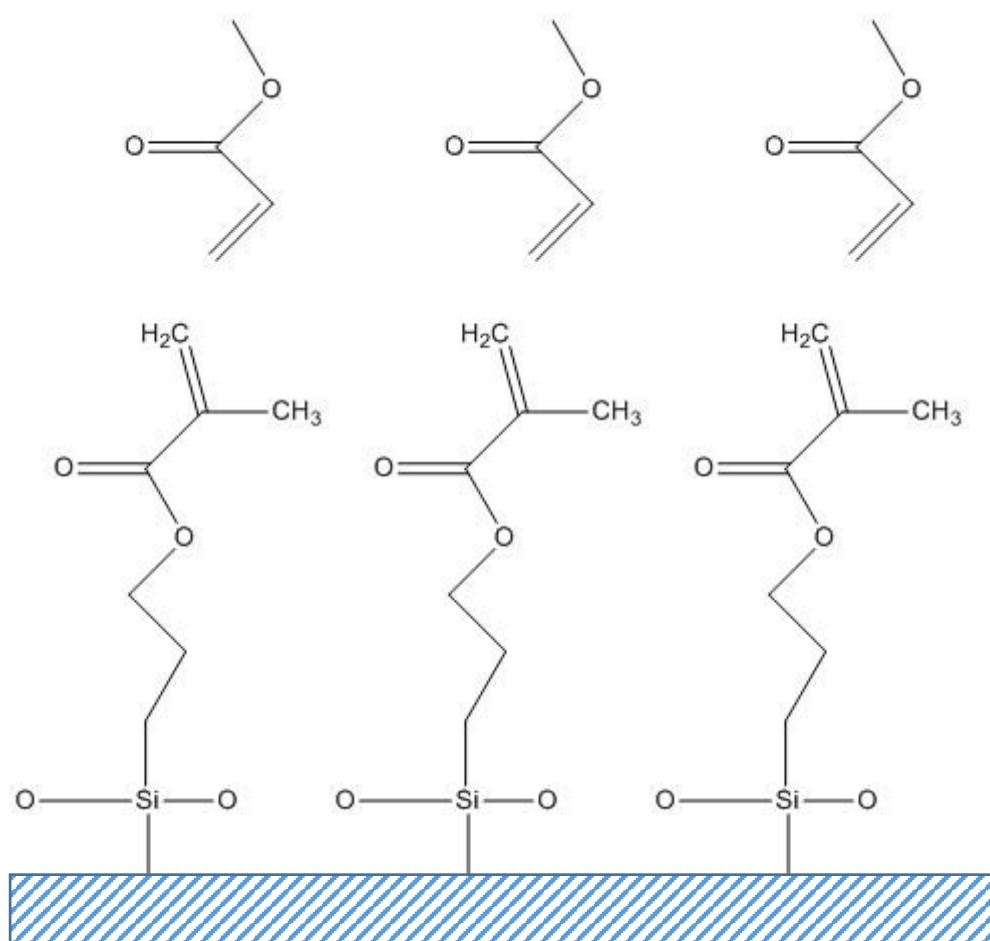


**Figure 2.8: Structure of trimethoxysilane molecules (bottom) attached to the glass cover slip (blue stripes). The terminal acrylate ends of the silane molecules polymerise with the acrylate monomers (top) used in the experiment.**

Silanisation is performed in a dry atmosphere in Argon gas in a sealed apparatus setup. The glass cover slips are immersed in dry toluene to ensure a dry environment. Wet conditions result in multiple layers of water forming on the glass. This causes a nonuniform silane coating to form since trimethoxysilane monomers polymerise with each other before reaching the silicon oxide surface.

A methacrylate was selected as the R-group for the purposes of this project however it can also be an amino, epoxy or thiol group. Amino groups are selected for DNA-containing samples as DNA contains  $-NH_2$  groups that will hydrogen bond with the amino groups of the silane.

The silanisation process varies slightly depending on the substrate involved. Borosilicate glass can withstand a strong solvent such as toluene. Polystyrene, on the other hand, will degrade if placed in toluene or acetone. Therefore, when polystyrene plates are being silanised, a gentler solvent such as isopropanol is used in this study.

## 2.6 Cardiomyocyte Culture

Cardiomyocytes were derived from iPSCs using the Monolayer Differentiation protocol. There are various methods to derive CMs from iPSCs however monolayer differentiation produces the most mature cardiomyocytes to date (Burridge et al., 2012).

iPSCs were obtained from the RPAT cell line (University of Nottingham). iPSCs were fed every day with either home-brewed E8 medium (home-brewed supplement added to home-brewed E8 basal medium) or commercial E8 medium (commercial E8 supplement Gibco™ added to commercial E8 basal medium Gibco™) and split at an appropriate ratio when confluency was reached which was every 72 hours. The differentiation was commenced when iPSCs reached approximately 70% confluency. The protocol has a preconditioning stage which is considered day -1 of the differentiation. Stem Pro preconditioning media (refer to detailed protocols for exact components) was prepared according to the number of flasks utilised for differentiation and enough for 2 days as the media would be used on day 0 as well.



## 2.6.1. Cell Culture Procedure

### 2.6.1.1. Growth and maintenance of iPSCs

All cell culture was performed in T75 flasks (156472, Nunc™ EasYFlask™, ThermoFisher Scientific). iPSCs were obtained from the stem cell bank (Cell and Biological Sciences, University of Nottingham) and maintained until differentiation was commenced. iPSCs were fed every day using standard aseptic technique with home-brewed E8 medium or commercial E8 medium. Home-brewed E8 medium consists of DMEM/F12 (Corning, cat. no. 10-092-CM) with home-brewed E8 supplement consisting of multiple components listed below according to the most efficient monolayer differentiation protocol to date (Burridge et al., 2014).

- 1) 1 L DMEM/F12 (Corning, cat. no. 10-092-CM)
- 2) L-ascorbic acid 2-phosphate tri sodium salt (Wako USA, cat. no. 321-44823)
- 3) Recombinant human insulin (Life Technologies, cat. no. A11382ij)
- 4) Recombinant human transferrin (Sigma-Aldrich, cat. no. T3705-5G)
- 5) Heparin sodium salt (Sigma-Aldrich H3149-250KU), a 10 mg/mL stock solution in WFI water was made and stored at 4 °C.
- 6) Sodium selenite (Sigma-Aldrich, cat no. S5261-10G), A 1.4 mg/mL stock solution (70 mg/50 mL in WFI water) was made immediately prior to use.
- 7) Recombinant human FGF2 (Peprotech, cat. no. 100-18B)
- 8) Recombinant human TGFB1 (Peprotech, cat. no. 100-21)
- 9) DPBS without calcium and magnesium (Corning, cat. no 21-031-CV)
- 10) 0.5 M EDTA, pH 8.0 (Life Technologies, cat. no. 15575-020)

The components were utilised to generate home-brewed E8 supplement aliquots as described below. The recipe will produce 100 x 1.5 mL E8 supplement aliquots. This will generate 100 L of E8 medium.

1. 50 mL of room temperature WFI water was added to a 250 mL cell culture bottle, while slowly adding 6.4 g of L-ascorbic acid 2-phosphate and inverting intermittently. This was mixed until clear.

2. 46 mL of room temperature WFI water was placed in a sterile 100 mL glass beaker with a stir bar on a stir plate, 2 g of insulin added, pH adjusted to 3 with 1M HCl to dissolve (~1.4 mL), pH adjusted to 7.4 with 10M NaOH (~200  $\mu$ L), 500 mg of transferrin, 1 mL of 10 mg/mL heparin sodium salt and 1 mL of 1.4 mg/mL sodium selenite added. This was made up to 50 mL and added to the ascorbic acid solution. Insulin will go back through its isoelectric point and come back out of solution as it progresses from pH 3 through to pH 7.4. As it passes pH 7 it will go back in to solution.

3. 48 mL of WFI water was added to a 50 mL Falcon tube, this was used to resuspend the contents of 10 x 1 mg vials of FGF2.

4. 2 mL of WFI water was added to 2 x 100  $\mu$ g vials of TGFB1.

5. The growth factors were added to the 250 mL cell culture bottle, mixed well, filtered and sterilized. 1.5 mL aliquots were made in 2 mL microfuge tubes, labelled and stored at -20 °C.

6. When media was required for use, one thawed aliquot of supplement was added to a 1L bottle of DMEM/F12.

This is more economical than purchasing commercial E8 medium (Gibco™). The laboratory switched to commercial E8 medium later on and this consists of commercial E8 supplement (Gibco™) which is manufactured as a 10 ml vial. The contents of the vial were transferred to a 500 mL bottle of basal E8 medium (Gibco™) when required.

#### *2.6.1.2 Cell feeding*

The appropriate amount of home-brewed E8 media or commercial E8 media (Gibco™) was aliquoted to a 30 ml universal tube at 5 ml per flask and placed in the water bath at 37°C for 10 minutes. Old medium was aspirated and replaced with E8 medium at 5 ml per flask.

RPMI B27 was made simply by thawing the 10 ml vial of B27 supplement (Gibco™) and adding to RPMI 1640 (Gibco™) 500 ml bottles.

RILT medium was made using RPMI medium 1640 (Gibco™), chemically defined lipids (CDLs, Gibco™), insulin-transferrin-selenium (ITS, Gibco™) and thioglycerol (Sigma-Aldrich™). Thioglycerol is a very concentrated stock solution therefore a working solution was made prior to addition to medium. A 50 ml working solution contained 434.8 µl of thioglycerol in 50 ml of PBS (Gibco™). This was mixed well and 200 µl of this working solution was added to the final medium. 500 µl of ITS and 500 µl CDL were also added to the final medium. Therefore, a 50 ml aliquot of RILT medium would contain 49 ml RPMI, 1 ml ITS, 1 ml CDLs and 200 µl from the working solution of thioglycerol.

#### *2.6.1.3 Cell Splitting*

IPSCs were checked under the light microscope before the splitting was commenced. IPSCs should be very dense with few spaces by this time-point. Only flasks with a confluency of 60% or more were split at the standard 1 in 10 ratios for maintenance flasks. The split is required to be carried out after 72 hours so if the cells were not confluent enough then they were split at a lower ratio such as 1 in 5 or 1 in 6.

Matrigel (354234, Corning®) flasks were prepared beforehand and incubated overnight in the fridge if prepared the day before using pre-prepared 200 µl aliquots of Matrigel®. Alternatively, Matrigel (354234, Corning®) flasks were prepared on the same day and incubated at room temperature for 40 minutes prior to splitting. Matrigel (354234, Corning®) flasks were prepared using 4 ml of DMEM (Gibco™) per flask with 1 in 100 Matrigel (354234, Corning®) thawed from -180°C. Usually 5 flasks were prepared for splitting before a differentiation was commenced, otherwise the required number of flasks were prepared depending on further application. Therefore, 20 ml of DMEM (Gibco™) was prepared with 200µl of Matrigel (354234, Corning®) for every 5 flasks.

E8 medium was prepared with Rock inhibitor (Y-27632 dihydrochloride, Tocris®) at 1 in 1000. This was 25 ml for 5 flasks plus an extra 5 ml for cell collection at the end of the splitting protocol. 30 µl of Rock inhibitor (Y-27632 dihydrochloride, Tocris®) was added to a total of 30ml E8 medium. When

Matrigel flasks were ready, DMEM (Gibco™) medium was aspirated from the flasks, rinsed with DPBS without calcium and magnesium (Gibco™) at 3 ml per flask and replaced with the fresh E8 medium and Rock inhibitor (Y-27632 dihydrochloride, Tocris®) mixture. The flasks were placed in the incubator to warm to 37°C.

The old medium was aspirated, washed with DPBS without calcium and magnesium (Gibco™) and 2 ml of TrypLE™ (Thermo Fisher Scientific, Gibco™) added and the flask placed in the incubator at 37°C for 3 minutes. The cells were checked under the microscope (Fluorescent Microscope Nikon Diaphot 300) which should be rounded up and still attached to the bottom of the flask. The TrypLE™ was aspirated and the flask was tapped firmly on the sides to detach the cells from the bottom of the flask. The cells were checked under the microscope again, ensuring the cells were detached and floating. 4.5 ml of the remaining E8 medium with Rock inhibitor (Y-27632 dihydrochloride, Tocris®) was added to the flask. 1 ml of cell suspension was transferred to the newly prepared flasks for differentiation and 0.5 ml for the maintenance flask. This is because differentiation flasks require a higher confluency for differentiation to commence whereas the maintenance flask need not be as iPSC growth continues until the next split in 3 days' time.

The splitting ratio depends on the future application of the iPSCs. Standard procedure dictates 1 in 5 split ratios for differentiation to cardiomyocytes and a 1 in 10 split for maintaining cells as iPSCs (Figure 2.9). Usually, if a flask was split into 5, one was kept as a maintenance flask in case the differentiation was not successful. The other 4 flasks were used for differentiation. Since the cells are suspended in 5 ml of medium, a 1 in 10 split would mean 500 µl of the cell suspension was transferred to the new flask and a 1 in 5 split would mean 1 ml of the cell suspension was transferred to the new flask. The flasks were placed back in the incubator at 37°C until further use.

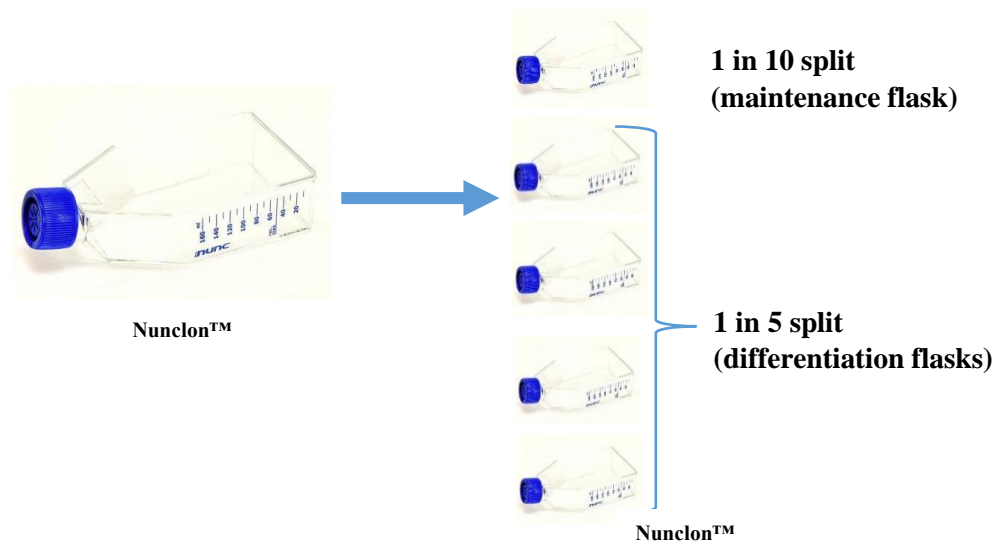


**Figure 2.9: Flow diagram of the iPSC T75 flask splitting process. If a differentiation is planned, then one flask is split 1 in 10 and kept as a maintenance flask of iPSCs and the other 4 flasks are split 1 in 5 to prepare for differentiation to cardiomyocytes.**

#### *2.6.1.4 Differentiation to CMs*

The differentiation process was also carried out in T75 flasks (Nunc™ EasYFlask™, ThermoFisher Scientific). Differentiation to CMs was commenced 2 days following a split, provided the flasks were split at a 1 in 5 ratio. If the flasks were not confluent enough, i.e. less than 60% confluency, then they were fed with 5 ml E8 medium per flask and incubated for a further 24 hours at 37°C. iPSCs were differentiated to CMs using a well-established protocol called the monolayer differentiation approach (Figure 2.10). Monolayer cultures were shown to produce more mature CMs compared to other approaches such as embryoid body culture (Burrige et al., 2014). CMs were detached after 12-14 days and seeded in cell culture plates for observation of attachment to 3D-printed constructs.

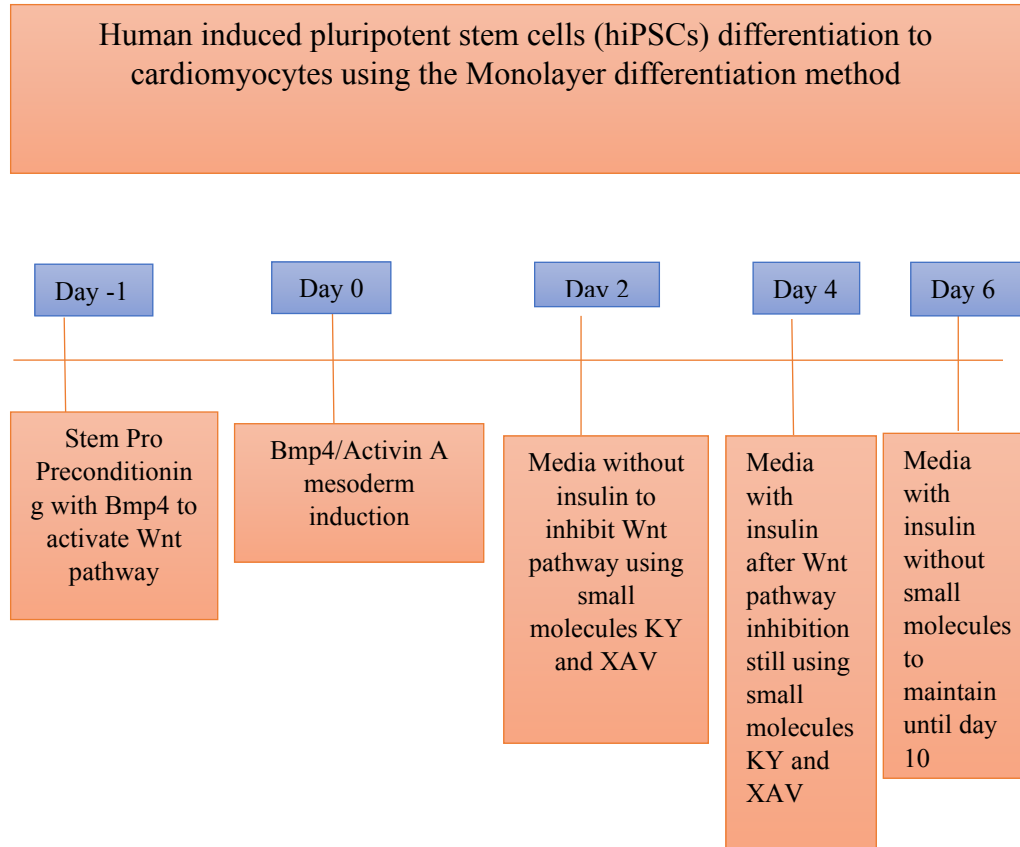


**Figure 2.10: Schematic of monolayer differentiation of iPSCs to cardiomyocytes highlighting each time point and the small molecules added at each these stages.**

On the second day following a split, iPSCs were fed as normal in the morning with fresh E8 medium. At the end of the day, iPSCs were checked for confluency. Ideally, iPSCs should be at least 60% confluent when differentiation is commenced (Burridge et al., 2014). Once this is confirmed, StemPro preconditioning media was prepared for the first 2 days of the differentiation (day -1 and d 0). Usually, 4 flasks were used for a differentiation therefore 40 ml of preconditioning media was prepared. Briefly, 39 ml of StemPro™ 34 medium (Gibco™) was aliquoted to a 50 ml falcon tube and 1 ml of StemPro supplement™ (Gibco™), 385 µl of an L-glutamine aliquot (25030081, Gibco™) were added. The StemPro aliquot was divided in two, one for day -1 and one for day 0 each being 20 ml. A matrigel® aliquot was added 1 in 100 (200 µl) to the day -1 aliquot followed by 1 in 10,000 Bmp4 (Biotechne™) (2 µl). The day 0 aliquot was stored at 4°C until the next day.

**Day -1:** The day -1 aliquot was added immediately after preparation and division of Stempro aliquots. The old E8 media was aspirated from the flasks and day -1 Stem Pro media added to the flasks at 5 ml per flask. No prior warming in the water bath was required as doing so would polymerise Matrigel and solidify the media. This would prevent media addition to the flasks.

**Day 0:** It is crucial that this media change is done in the morning as the whole outcome of the differentiation may change if this step is delayed. The day 0 aliquot was taken out of the fridge and Bmp4 (Biotechne™) added 1 in 1000 (20 µl). Activin A (Gibco™) was also added 1 in 625 (32 µl). Old media was aspirated from the flasks and new day 0 media was warmed for 10 minutes in the water bath at 37°C and added at 5 ml per flask.

**Day 2:** The small molecules KY02111 and XAV939 (Biotechne™) were taken out of the -180°C freezer and thawed in the incubator at 37°C for 15-20 minutes. Then they were vortexed for approximately 30 seconds. This was to ensure all crystals were completely thawed. Then each molecule was added 1 in 1000 (20 µl in 20 ml) of RPMI medium without insulin supplemented with B27 in a universal tube. The aliquot was warmed in the water bath at 37°C for 10 minutes. Old media was aspirated and replaced with the fresh, warmed medium at 5 ml per flask.

**Day 4:** The small molecules KY02111 and XAV939 were taken out of the -180°C freezer and thawed in the incubator at 37°C for 15-20 minutes. Then they were vortexed for approximately 30 seconds. This was to ensure all crystals were completely thawed. Then each molecule was added 1 in 1000 (20 µl in 20 ml) of RPMI medium with insulin supplemented with B27 in a universal tube. The aliquot was warmed in the water bath at 37°C for 10 minutes. Old media was aspirated and replaced with the fresh, warmed medium at 5 ml per flask.

**Day 6:** RPMI medium with insulin supplemented with B27 was aliquoted (20 ml) and warmed in the water bath at 37°C for 10 minutes. Old media was aspirated and replaced with the fresh, warmed medium at 5 ml per flask.

**Day 8:** The procedure was repeated as on day 6. Cell beating can be observed from this day onwards.

**Day 10:** The procedure was repeated as on day 8.

**Day 12:** The flasks were checked for confluency. A lot of cell vigorous beating is observed at this stage. If cells had become 70-80% confluent and formed a monolayer which was flat and covered the bottom of the flask, then the cells were dissociated. If not, the media was changed as on day 6 and the cells kept for another 2 days.

#### *2.6.1.5 CM Dissociation*

Differentiation is usually complete between days 10 and 14, depending on the confluency of the tissue culture flask. A 70-80% confluency of beating cardiomyocytes visible by the light microscope is regarded as ready for dissociation (Burrige et al., 2014,).

UV and 2-photon polymerised constructs are prepared when the dissociation day is estimated. 6-well and 96-well plates (Nunclon™, Thermo Fisher Scientific) were labelled with sample names and prepared for overnight incubation 1 day prior to dissociation. 3D-printed constructs were UV-sterilised for 15 minutes on both sides to prevent contamination by placing in the cell culture hood under a UV lamp (Blak-Ray® XX-15L, 15 Watt, 365 nm). Then the glass cover slips were placed, one per well, into the 6-well plates. The wells were washed with DI water 3 times. Alternative to UV sterilisation, constructs were placed in the 6-well plates which were filled with IPA and left to sterilise for 20 minutes. 96-well plates were filled with IPA in the same manner and sterilised for 20 minutes. Then the wells were washed twice with DI water at 50 µl per 96-wells and 2 ml per 6-wells. An appropriate aliquot of DI water (Gibco™) with Penicillin/Streptomycin (P/S, Gibco™) was made 1 in 100 with P/S (Gibco™) depending on the number of wells to be used for cell culture. The wells were filled with DI water P/S (Gibco™) solution at 50 µl per well for 96-well plates and 2 ml per well for the 6-well plates. The plates were placed in the incubator overnight at 37°C.

The dissociation protocol begins with thawing a 10 ml collagenase aliquot (Sigma Aldrich™). Once thawed, HEPES (Sigma Aldrich™), BTS (Sigma Aldrich™) and Rock inhibitor (Y-27632 dihydrochloride, Tocris®) are all



thawed and added to the collagenase in a 1:1000 ratio to form the collagenase mix.

The CM flasks were taken out of the incubator and the old medium aspirated. The flask is washed twice with Hank's balanced salt solution (HBSS) without calcium chloride and without magnesium chloride (Sigma-Aldrich®). 2.5 ml collagenase mix is added per flask and incubated for 3-3.5 hours at 37°C in the incubator.

3D-printed constructs are prepared during the collagenase incubation step prior to CM seeding.

On the day of CM dissociation, all wells in all plates were washed with DI water at 50 µl per well for 96-wells and 2 ml per 6-wells. Matrigel was prepared for the appropriate number of wells using DMEM medium (Gibco™) with 1 in 100 Matrigel. Then the test wells were prepared; an appropriate number with RPMI B27 media (Gibco™) and an appropriate number for RILT medium (Refer to Section 4.2.2.2). If CM attachment in both media were being tested then two 96-well or 6-well plates were prepared, one for each medium type. The plates were incubated at room temperature for at least 45 minutes for the Matrigel to settle down to the bottom of the wells and form a coating. The DMEM (Gibco™) was aspirated from the Matrigel-coated wells and replaced with the appropriate medium (RPMI B27 or RILT). The wells without Matrigel which contained the UV-polymerised or 2-photon fabricated constructs were also filled with either RPMI B27 or RILT media depending on the variable being tested for the CM attachment experiment. Then all of the plates were placed in the incubator at 37°C until cell seeding.

DNAse mix (Sigma-Aldrich™) is prepared by thawing out DNAase and adding at a ratio of 1 in 500 to RPMI basal media (Gibco™). 2.5 mL of DNAase mix should be prepared per cell culture flask.

The flasks containing collagenase are taken out of the incubator and viewed under the light microscope. The CMs should be floating and detaching off the bottom of the flask. Not all CMs will have completely detached however as long as most are floating and the rest partly detached it is time to collect them. The flask can be lightly tapped on the sides and tilted very gently side to side to

detach the rest of the CM. The collagenase-CM mixture is obtained with a 10 mL stripette and transferred to a 50 mL falcon tube. The remaining CMs in the flasks are washed down with the DNAase mix at 2.5 ml per flask and added to the falcon tube. The CMs are then centrifuged at 100xg for 15 minutes.

The supernatant is aspirated very carefully and the liquid close to the pellet can be taken using a P1000 pipette. The resuspension volume depends on the size of the pellet. A small pellet is suspended in 2.5 mL and a large pellet in 8mL of RPMI B27 medium or RILT medium. CMs are mixed in resuspension very gently a few times. 10 µl is taken from the middle of the suspension immediately after mixing to ensure that the solution is homogenous. A haemocytometer (Neubauer®) was used for a cell count. The cells are counted manually using a mechanical counter. The cell number is used to determine the volume of cell plus RPMI solution to transfer to the 6-well plates. The cell density utilised for 6-well plates is 1,000,000 cells per well and 70,000 cells per well in a 960 well plate. For instance, if 3,000,000 cells were obtained in a cell count and a 6-well plate was to be used;  $3,000,000/1,000,000= 3$  mL of cell plus RPMI from the falcon tube would be transferred to a well in a 6-well plate. A 6-well plate usually requires a 3 mL working volume therefore if the volume calculated from the cell count was less than 3 mL, the rest would be made up with RPMI basal medium. In some experiments the Cedex automated cell counter was used. This is a more accurate way of counting cells as human error is eliminated and trypan blue is used as part of the procedure which gives a measure of cell viability. Briefly, 300 µl of cell-media solution was transferred to a Cedex cup (provided by the supplier, Roche©) and inserted into the tray of the Cedex HiRes Analyzer (Roche©). The program was started which takes approximately 10 minutes. The device obtains 14 measurements of cell count and calculates an average cell count, average live cell count and average cell viability as a percentage. 96% is regarded the standard result for cell counts. Following this, the cell density was calculated from haemocytometer measurements. The 4 numbers read by the mechanical counter from the 4 grid-lined corners are added and the total divided by 4 to obtain an average. This is multiplied by 10,000 to retrieve the number of cells per 1 ml to give the cell density value. The cell density value from the Cedex HiRes Analyzer (Roche©) is obtained directly from the results calculated

by the software which is named the 'live cell count' as the dead cells excluded with the Trypan Blue (Roche©) stain.

The resulting cell density value was divided by the cell density required for the 6-well plates and the 96-well plates to obtain the volume of cell resuspension media per well.

For instance, if the live cell count in a particular experiment was 3 million per ml then 1 million was divided by 3 million to give approximately 300  $\mu$ l per well for a 6-well plate. The required cell density for 96-well plates is 70,000 cells per well which was divided by 3 million to give 23  $\mu$ l per well. The total well volume for 6-well plates to prevent drying out is 2 ml per well and 50  $\mu$ l per well for 96-well plates. Therefore, the remaining volume required in the wells was made up with the appropriate media, either RPMI B27 or RILT. For example, if 23  $\mu$ l of cell suspension was pipetted into a well, the remaining media added was 27  $\mu$ l. Wells with 2-photon fabricated constructs were seeded at 140,000 cells per construct and only a few drops were very carefully added on top of the constructs. The wells were not filled up with media at this point to ensure cells settled onto the constructs.

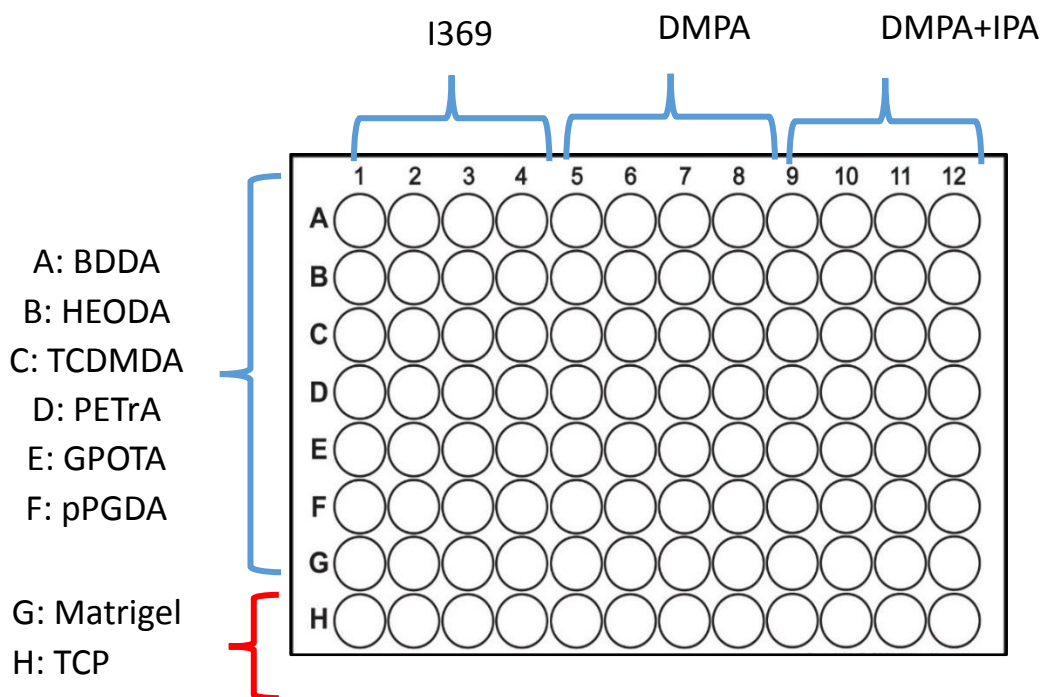
All wells were checked under the light microscope to ensure cells were present and roughly appeared to be a suitable density. If the cell density did not appear to be enough another aliquot of cell suspension was added (about half the volume of what was originally added). If the cell density appeared too to be too large then approximately a third of the well volume was aspirated and replaced with the appropriate medium in order to dilute the mixture.

Cell seeding onto the 2-photon fabricated constructs required careful observation of the cells under the light microscope to ensure they commenced settling onto the constructs. These wells were left and the plates placed in the incubator at 37°C for 1.5-2 hours. Then the wells were filled up to the total volume (2 ml for 6-well plates) with the appropriate media.

### 2.6.2 CM attachment to construct testing

CM attachment was initially tested on UV-polymerized constructs as this is much more efficient due to the benefit of the utilization of 96-well plates to test many materials simultaneously (Figure 2.11). In addition, polymerization duration is one hour rather than the many hours required to fabricate just one structure by 2-photon lithography.

Figure 2.11 shows the experimental layout. Cells were seeded directly onto the polystyrene well-bottom. I369 and DMPA are photo initiators (Sigma-Aldrich™) utilised for the first and second experimental groups respectively. Isopropanol (IPA) solvent was used for the third experimental group (Figure 2.11, top right). I369 is the photoinitiator selected for 2-photon fabrication therefore testing polymerised samples with this PI was essential. DMPA is a photoinitiator previously used in defined synthetic substrate studies (Patel et al., 2015) and DMPA+IPA is DMPA mixed 50/50 with IPA, a method used previously for successful CM attachment studies (Patel et al., 2015). The positive control matrigel was prepared for a set of 3 wells. The matrigel wells were prepared on dissociation day. Tissue culture plastic (TCP) controls were also set up, which was a set of 3 wells with no material coating but just media. TCP served as a negative control meaning the well bottom did not have any coating so cells were not expected to attach as they do not favourably adhere to polystyrene in the absence of serum (Curtis et al., 1983). Therefore, if attachment was observed in the test wells it will be due to the polymer only and not the TCP underneath. CMs suspended in medium were seeded at a density of 1 million cells per well or 70,000 cells per well for a 96-well plate.



- 1) BDDA (Butanediol diacrylate)
- 2) HEODA (Hexanediol ethoxylate diacrylate)
- 3) TCDMDA (Tricyclodecanedimethanol diacrylate)
- 4) PETrA (Pentaerythritol triacrylate)
- 5) GPOTA (glycerol propoxylate triacrylate)
- 6) pPGDA (Polypropylene glycol diacrylate)

**Figure 2.11: 96-well plate setup for UV polymerization. A-E refers to the polymers tested. Matrigel (G) serves as a positive control for CM attachment. Tissue culture plastic (TCP, H) is a negative control.**

The polymers that could successfully support CM attachment were tested for their amenability to 2PL. The polymers found to have a wide operating window below 1% PI concentration were selected for further fabrication of complex architectures. Designs relevant to cardiac muscle cell behaviour and response were created on AutoCAD, converted to .stl files and fabricated. Glass cover slips containing the 3D-printed constructs were sterilised the same as highlighted in the dissociation section 4.4.2.5. The only difference in the protocol with the 6-well plates is that after cell resuspension, the cells were seeded at 140,000 per construct and the appropriate volume (a few drops) of cell suspension placed directly onto the constructs. The wells were carefully filled with media (3 ml)

from the corner of the wells after a minimum of 2 hours to ensure the cells settled onto the construct (refer to section 4.4.2.5).

Experiments that involved media with serum had a medium formulation as follows;

1 in 1000 Rock inhibitor

4% serum (FBS)

1 in 100 P/S

If the experiments tested cell attachment with and without serum 2 universal tubes were used to spin down the cells and resuspended in each medium, with and without serum. The same principle was applied if the two types of medium were used; RILT and RPMI B27. In experiments where both media were tested, 2 96-well plates were used with exactly the same layout with one plate being tested for RPMI B27 and the other for RILT thioglycerol medium.

Cell viability was assessed using image j. Cell counts were made based on the roundness of cells. The roundness limit was set to 0.6. Any score higher than this indicated a dead cell. Statistical t-tests and ANOVA were performed to compare viability among the variables tested.

### 2.6.3 CM attachment experimental design

IPSC to CM differentiation and dissociation procedures were carried out exactly the same as in Chapter 2, Section 2.6.1. The aforementioned protocols in Section 4.4.2 describe how cells dissociated into 6-well plates would be seeded at  $1 \times 10^6$ /ml. The smallest cell culture plates 2-photon fabricated constructs on 22 mm x 22 mm glass cover slips could fit into were 6-well plates therefore these were used to contain them. The seeding density of  $1 \times 10^6$  applies to the wells. The Matrigel positive control wells received this treatment. However, the wells containing the glass cover slips were treated a little differently. The constructs measured 1000  $\mu\text{m}$  in length and 800-2000  $\mu\text{m}$  in width depending on structure design. This meant cells seeded at a density of  $1 \times 10^6$  would prevent any visualisation of cell behaviour on construct fine features. Therefore, the

construct area was taken into account and by referring to previous literature a lower cell density was utilised for seeding. The constructs were viewed under the light microscope. If cell numbers appeared to be too low on the construct another 50  $\mu$ l of cell suspension was pipetted directly onto the construct until sufficient cell numbers could be visualised as settling onto all sections of the construct.

6-well plates were utilized in the most efficient way possible by using every well for a glass cover slip where possible. The remaining wells were labelled as positive control Matrigel wells or tissue culture plastic (TCP) negative control wells (Figure 2.12). TCP is purely no coating or construct in the wells, cells are seeded in media (either RILT or RPMI B27) only. Matrigel was prepared as described in Chapter 4, Section 4.4.2 and 2 ml of Matrigel per well used in the 6-well plates.

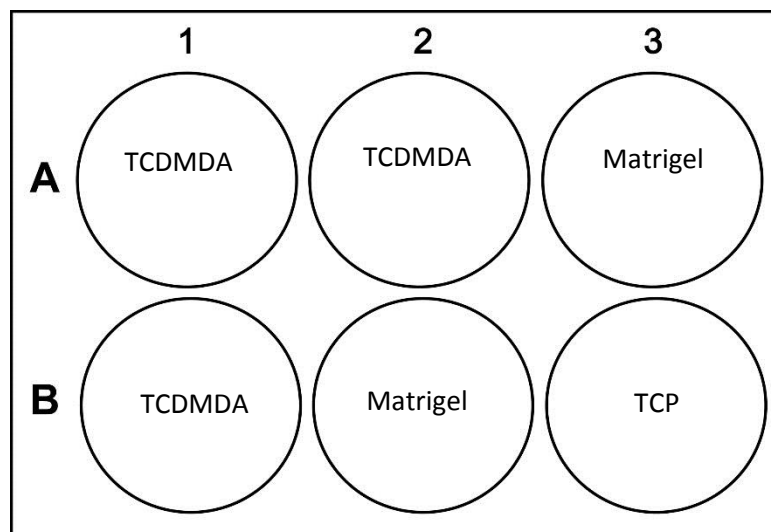


**Figure 2.12: 6-well cell culture polystyrene plate schematic illustrating a typical experiment for testing CM attachment on 2-photon fabricated constructs, including positive control Matrigel and negative control TCP.**

CM attachment experiments were also performed on 3 acrylate polymers TCDMDA, GPOTA and PETrA under 4 different curing conditions; with post-fabrication UV cure treatment, with post-fabrication vacuum treatment, with post-fabrication UV cure and vacuum treatment and no post-fabrication treatment. All samples were analysed by wide-field imaging following

immunostaining to observe differences, if any, in cell attachment, cell maturity and cell orientation.

## 2.7 UV polymerisation

UV polymerisation can be carried out various ways, under a UV lamp (Blak-Ray® XX-15L, 15 Watt, 365 nm) or in an enclosed box. The closed atmosphere of a box provides protection against UV damage. Some enclosed containers can be supplied with Argon gas to remove oxygen from the reaction surroundings. This increases the efficiency of the reaction as oxygen can form radicals which can react with the photoinitiator or monomeric radicals. Following oxygen plasma etching 96-well plates are prepared for UV polymerisation. Firstly, the plates are placed in the fume hood and pre-prepared formulations containing monomer-photoinitiator mixtures are dispensed into the appropriate wells. An experimental plan is made by drawing a 96-well plate layout with formulations and controls assigned for specific groups of wells. 96-well plates are placed in the Argon glove box and Argon gas is purged through the box to remove oxygen until the experimental environment reaches 2000 ppm. Finally, the UV light is switched on and the plates are polymerised for one hour. The plates are removed once the reaction is complete and subject to the post-polymerization wash steps. Then they are placed in the vacuum oven for a minimum of 1 week.

2PL-amenable polymers were polymerised by UV light in an Argon atmosphere in polystyrene plates. This way, all materials could be polymerised simultaneously in less than an hour. This increases the speed of determining CM attachment as many polymers can be tested simultaneously in a 96-well plate. 2PL would pose longer fabrication times and more challenge during cell culture as the constructs are difficult to pinpoint due to their size and transparency. Each monomer would have to be placed on separate glass cover slips as only 1 resin can be used per cover slip which results in a longer and tedious method to determine CM attachment. When CM attachment ability of these materials is confirmed they can then be utilised for the topology studies with various complex designs.



All 96-well plates and glass cover slips that underwent the silanisation procedure were subject to oxygen plasma etching prior to silanisation.

#### 2.7.1 Determination of the correct solvent at a suitable concentration for silanisation for polymer attachment to 96-well polystyrene plates

The solvent used in the silanisation procedure is crucial as 96-well plates are composed of polystyrene which can react with certain chemical compounds. Two commonly used solvents in the silanisation procedure are acetone and isopropanol therefore both solvents were deposited on the lid of a 96-well plate at a range of silane concentrations in an orderly manner (Figure 2.13) to determine the threshold silane concentration that causes cloudiness. Figure 2.13 shows a schematic of the 96-well plate with the silane concentration values indicated at the top using the solvents acetone and isopropanol. The samples were placed in the first row at the silane concentration and solvent combination indicated above each designated well in the first row. An equal volume of 15  $\mu$ l was dispensed into each of the assigned wells to determine the effect of silane concentration on both acetone and isopropanol solvents when put in contact with polystyrene. Control wells were assigned to rows D, E and F with 3 wells per row (Figure 2.13). These were silane only, acetone only and isopropanol only treatments respectively. This was to question whether the cloudiness was arising from the solvent or the silane solution. The plate was left to stand for 30 minutes at room temperature to ensure all solvent had evaporated.

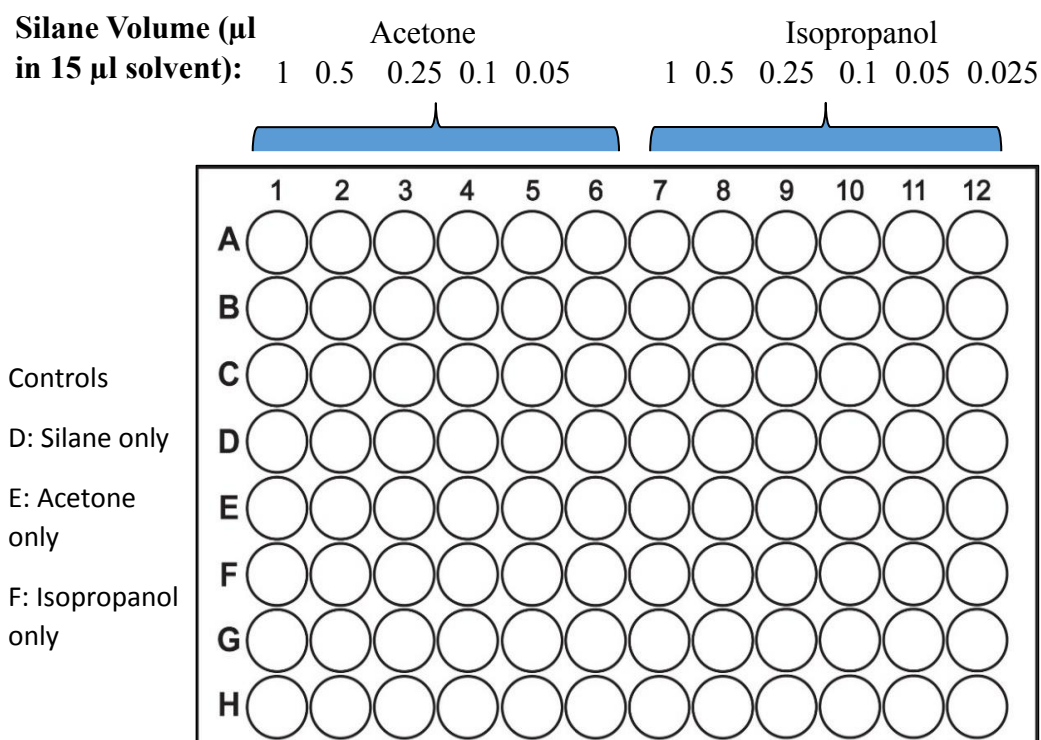


**Figure 2.13: Experimental design showing the range of silane concentrations in acetone and isopropanol in a 96-well plate.**

The maximum concentration of silane possible without causing cloudiness for either solvent would be the one used in future experiments. The maximum concentration is desired as the effect of the silane coating aids the polymers attach to the plate post-polymerisation. A silane concentration with maximum functionality and without causing cloudiness would be the ideal value. Table 2.5 summarizes all volume and concentration values of TMSPMA used in the experiment.

**Table 2. 5: TMSPMA volume and corresponding concentration values utilised in the solvent and TMSPMA determination experiment.**

| <i>TMSPMA</i> | <i>Volume<br/>(<math>\mu</math>l)</i> | <i>Concentration<br/>(<math>\mu</math>l/ml)</i> | <i>Percentage<br/>(%)</i> |
|---------------|---------------------------------------|---|---------------------------|
|               | 1                                     | 66.7  | 7                         |
|               | 0.5                                   | 33.3  | 3                         |
|               | 0.25                                  | 16.7  | 2                         |
|               | 0.1                                   | 6.7   | 0.7                       |
|               | 0.05                                  | 3.33  | 0.3                       |
|               | 0.025                                 | 1.67  | 0.2                       |

#### 2.7.2 Determination of the necessity of silanised wells for UV polymerisation

3 monomers were tested as they were being used for UV polymerisation and future CM attachment experiments; GPOTA, TCDMDA and PETrA each in silanised and non-silanised conditions. Controls were set up without monomers in silanised and non-silanised conditions to demonstrate the effect of silanisation without monomers. Figure 2.14 shows all labels with their designated wells for the samples. The solvent selected from section 4.2.1.1 was isopropanol as it demonstrated no cloudiness at higher silane concentrations compared to acetone. The aim of this experiment was to observe whether the monomers themselves were generating cloudiness in the samples. The volume of total solution was increased to 25  $\mu$ l to extend evaporation time and hence reduce the cloudiness associated with the silane solution.

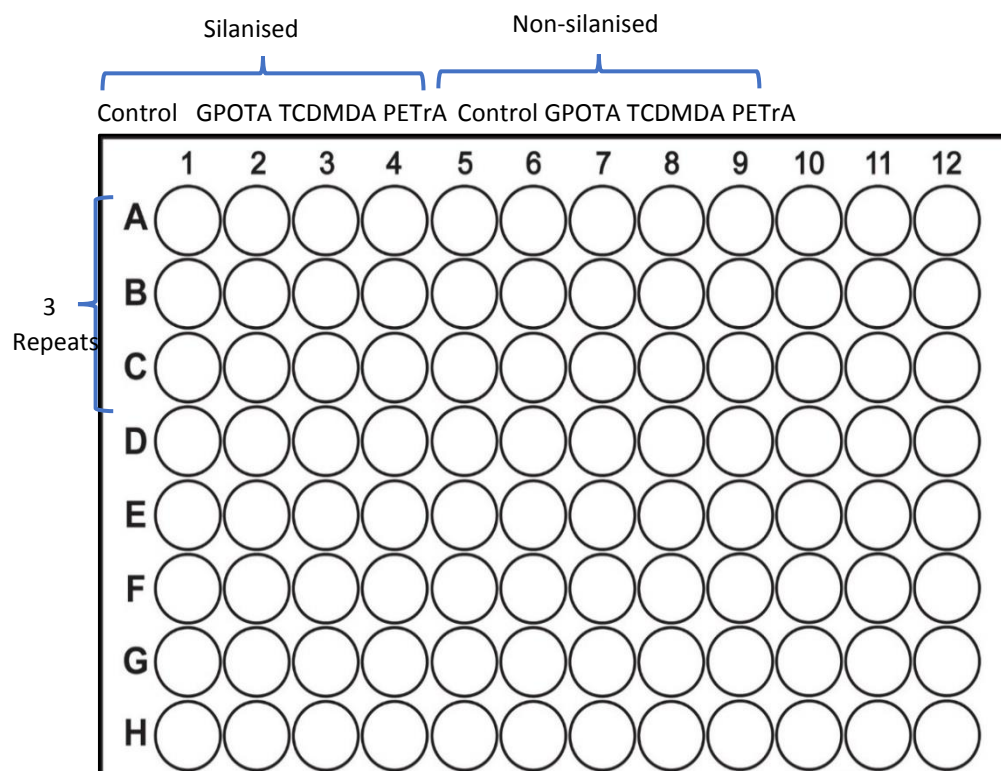


**Figure 2.14: 0.5  $\mu\text{l/ml}$  silane:isopropanol v/v was used for each sample (the optimum concentration, detailed in section 4.2.1.1) and added to 25  $\mu\text{l}$  of a monomer/PI mixture.**

Photos were taken before UV polymerisation and 1, 20 and 45 minutes after UV exposure to compare the effects of duration of UV polymerisation on silanised and non-silanised samples.

### 2.7.3 UV polymerisation

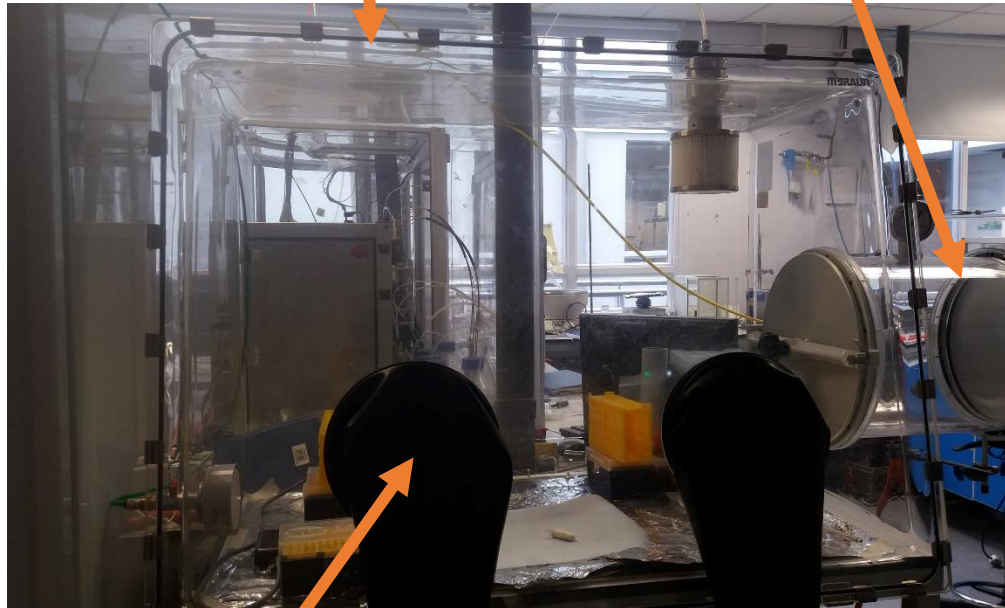
UV polymerisation was carried out on silanised glass cover slips and on both silanised and non-silanised 96-well plates in an oxygen-free atmosphere using a glovebox supplied by Argon (LABstar Glove Box Workstation, Braun®, MB-10-G). 96-well plates were only silanised for the determination of the necessity of silanised wells for UV polymerisation experiments (Section 4.4.1.2).

Monomer and photoinitiator formulations were degassed using a sonicator for 10 minutes. Pipettes were used to transfer 15 or 30  $\mu$ l of monomer (depending on the experiment) into their corresponding wells in the 96-well plate and onto the glass cover slips. In the meantime, the argon glovebox (MBraun® GB 2202-P-VAC) valve for Argon flow was opened to let Argon gas flow into the chamber (Figure 2.15).

The glovebox (MBraun® GB 2202-P-VAC) was sealed and Argon allowed to flow through the system for 10 minutes until the level on the oxygen sensor (Cambridge Sensotec®) dropped to 2000 parts per million (Figure 2.15b. bottom). Afterwards, the samples were placed inside the small cylindrical annexe chamber (Figure 2.15b, top right). The pump was switched on to carry out the flushing process. The annexe chamber was also flushed with argon 3 times using the 2 valves at the back of the small chamber (Figure 2.15b, top right). The motor pump was switched off and the valves closed. Then hands were placed through the black gloves into the large chamber. The small chamber door was now opened from the inside of the large chamber and the 96-well plate placed under the UV lamp (Blak-Ray® XX-15L, 15 Watt, 365 nm). The UV lamp was switched on and the samples left to polymerize for 1 hour. Silanised glass cover slips utilised for post-fabrication UV curing were placed under the UV lamp for 30 minutes.

**Argon glovebox (MBraun©  
GB 2202-P-VAC) chamber**

**Sample insertion chamber  
with door and separate  
regulators at the rear (Figure  
2.10b).**



**Gloves**

**Figure 2.15a: BRAUN© LABstar Argon glovebox for UV polymerisation.**

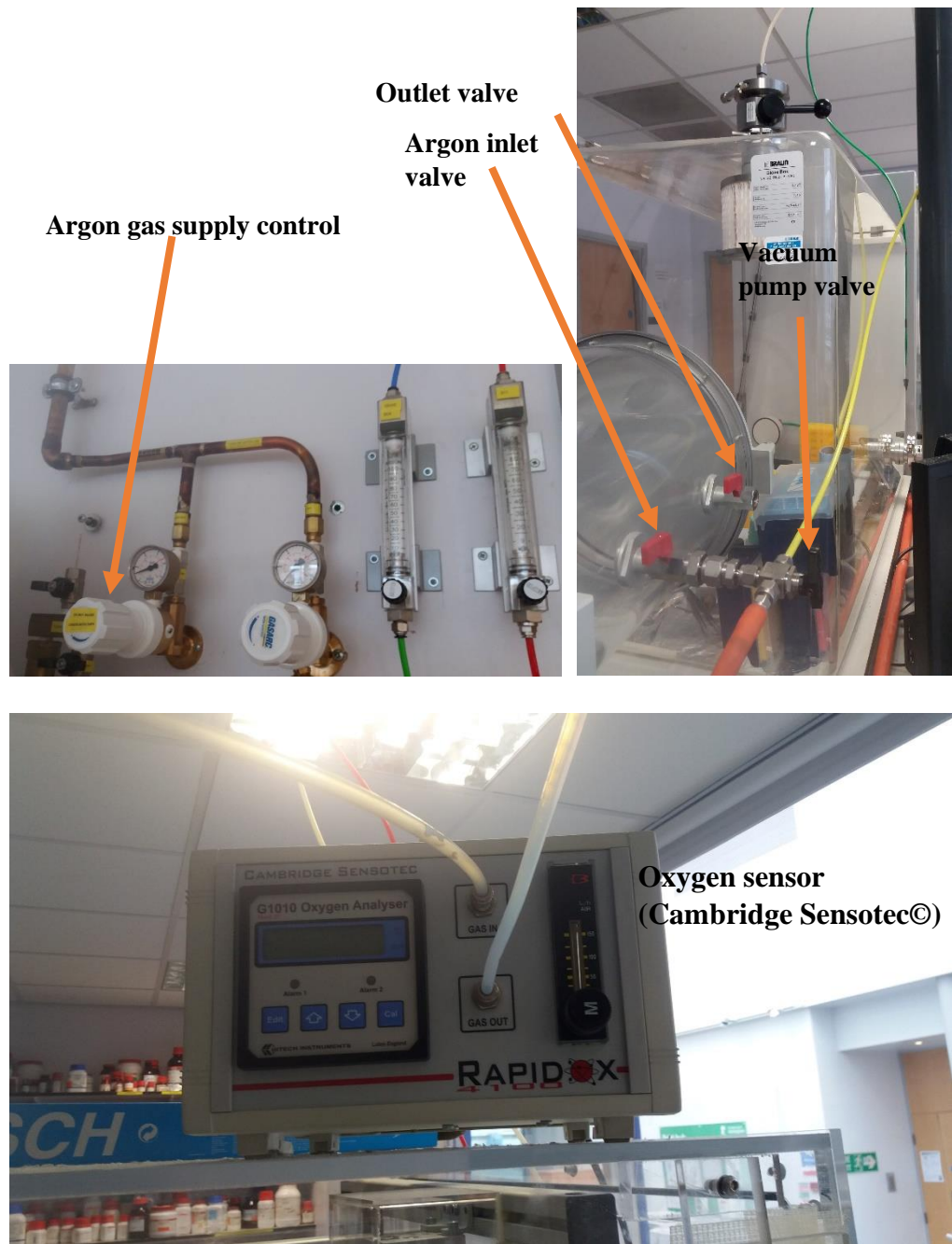


**Figure 2.15b: Argon gas supply controls opposite the Argon glovebox (top left). Sample insertion chamber with associated valves (top right) and oxygen sensor connected to the glovebox (bottom).**

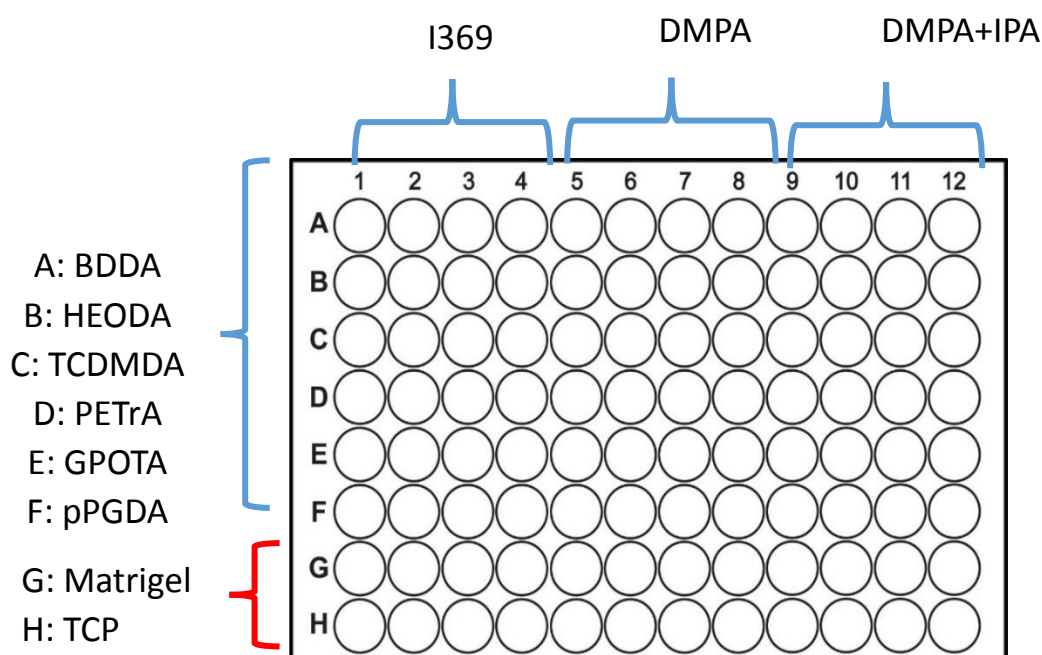


Formulations were prepared the same way as for 2-photon fabrication. UV polymerisation, unlike 2-photon polymerisation, requires 1 photon to be absorbed by the photoinitiator for the polymerisation reaction to occur. The probability of the reaction occurring is much higher. Therefore, the lowest PI concentration utilised for 2-photon polymerisation of 0.5% (5 mg/ml) was applied to UV polymerisation.

I369 was the photoinitiator used in 2-photon lithography studies to produce complete structures using TCDMDA, GPOTA and PETrA (Chapter 3). 2,2-Dimethoxy-2-phenylacetophenone (DMPA) photoinitiator combined with IPA solvent was selected as this was previously used to polymerise acrylates in CM attachment experiments (Patel et al., 2015). IPA renders the formulation less viscous, which could potentially make 2-photon polymerisation less likely therefore DMPA photoinitiator by itself was also added to the protocol (Figure 2.16).

RPMI medium (RPMI 1640, ThermoFisher Scientific™) is currently the most commonly used medium in cell culture. It is suitable for culture for a variety of mammalian cell lines. The reason for the preference for RPMI versus previously used media such as Dulbecco's modified eagle medium (DMEM), is that it contains the antioxidant glutathione and high concentrations of vitamins and no growth factors, which can adversely affect cells. RPMI has to be supplemented and this is done by adding a formulation of 27 essential components which are vitamins and minerals (B27) that enhance cell survival. RILT medium is composed of RPMI medium plus thioglycerol, ascorbic acid and insulin-transferrin-selenium components that act as antioxidants, all of which can help prevent cytotoxic effects of remaining photoinitiator radicals. RILT medium was shown to support CM attachment on many synthetic substrates, one of them being GPOTA (Patel et al., 2015). RPMI B27 medium is the one currently used in the protocols at the University of Nottingham. This is why all acrylate polymers were tested for CM attachment in the presence of both RILT and RPMI B27 media using the 3 different photoinitiator formulations, I369, DMPA and DMPA:IPA mixture (Figure 2.16).





- 1) BDDA (Butanediol diacrylate)
- 2) HEODA (Hexanediol ethoxylate diacrylate)
- 3) TCDMDA (Tricyclodecanedimethanol diacrylate)
- 4) PETrA (Pentaerythritol triacrylate)
- 5) GPOTA (glycerol propoxylate triacrylate)
- 6) pPGDA (Polypropylene glycol diacrylate)

**Figure 2.16: 96-well plate setup for UV polymerization. A-E refers to the polymers tested. Matrigel (G) serves as a positive control for CM attachment. Tissue culture plastic (TCP, H) is a negative control.**

Once UV-polymerisation was complete, 96-well plates were washed twice with isopropanol and three times with DI water after the 1-hour UV polymerisation period. Then they were placed in the vacuum oven for 1 week until CM attachment experiments were commenced. The silanised glass cover slips to be used for CM attachment were divided into three groups. The first group were treated with 1-week vacuum incubation only, the second group with post-fabrication UV curing only and the third group with vacuum and post-fabrication UV curing. Therefore, the second group were treated with UV light for 30 minutes and samples placed back into the petri dish wrapped in aluminium foil at room temperature until sterilisation treatments for CM attachment

experiments. The third group was incubated in the vacuum for 1 week followed by the 30-minute UV light treatment after which they were also stored in petri dishes wrapped in aluminium foil at room temperature. All treatment groups were sterilised the next day to commence pre-CM dissociation and seeding procedures (See Section 2.6.1).

#### 2.7.4 Thin film Design for Cardiomyocyte Seeding

Thin film structures were constructed to test for cardiomyocyte viability using Describe software. It is essentially the same concept as the woodpile design albeit with a much smaller hatching distance. This design was selected due to ease of manufacture and a quick method to assess cardiomyocyte viability (Figure 2.17). Dimensions were 1000  $\mu\text{m}$  (x) x 1000  $\mu\text{m}$  (y) and 1  $\mu\text{m}$  (z).

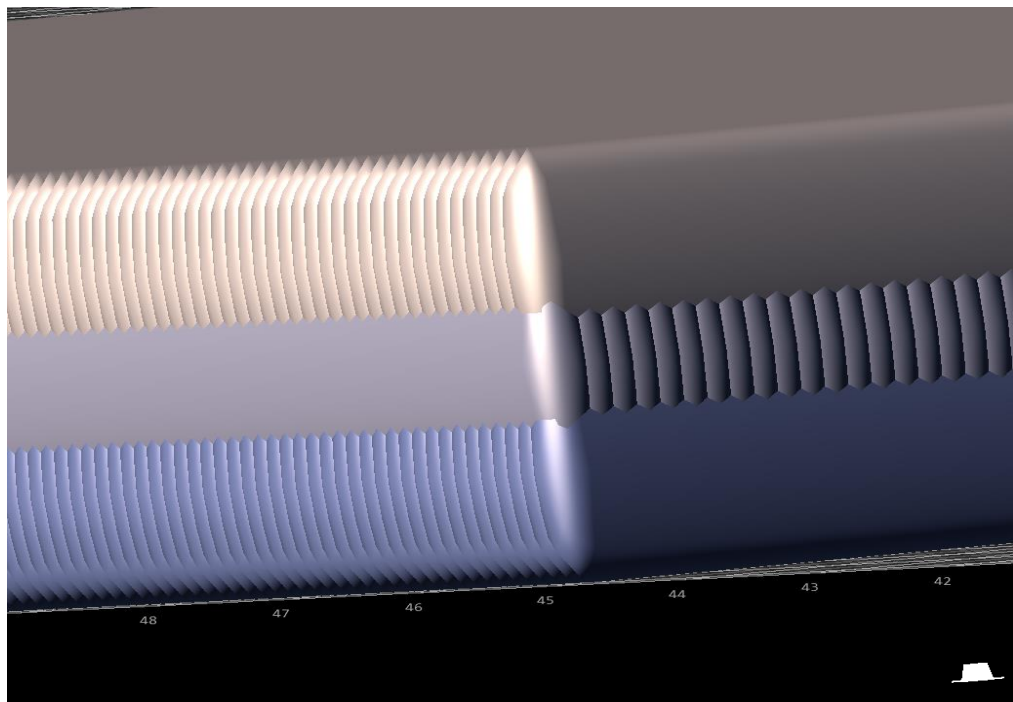
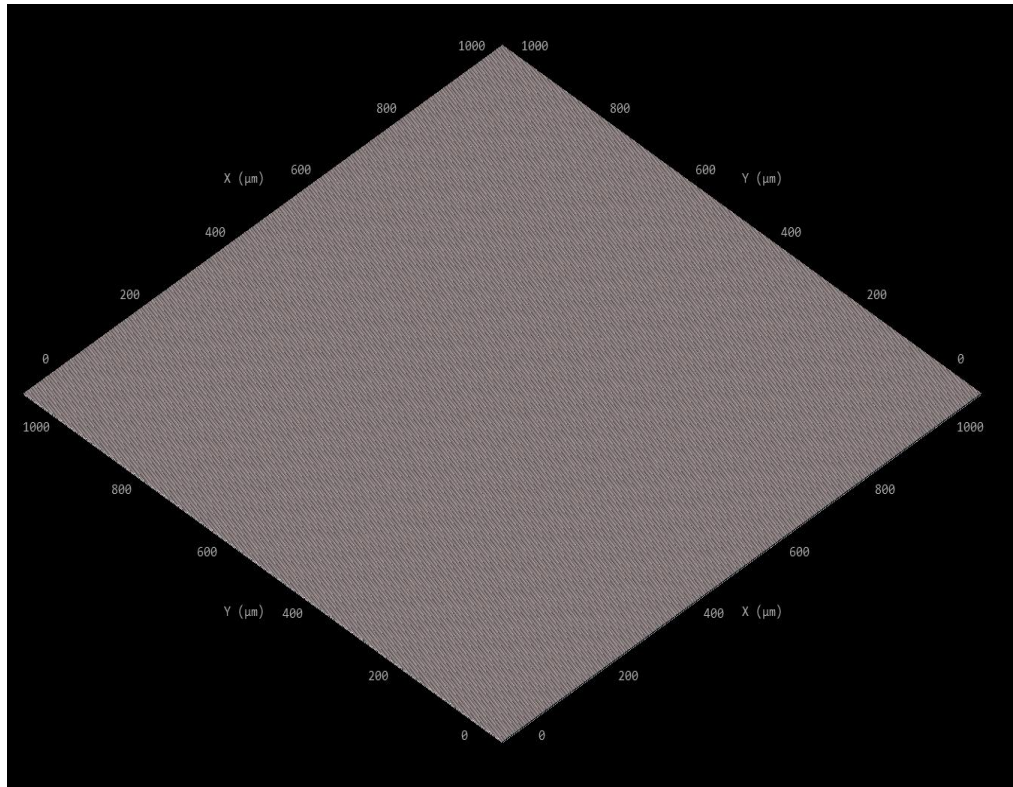


**Figure 2.17: Thin film construct for cardiomyocyte viability testing and enlarged image of one corner showing each fabrication line (bottom). Images were captured from Describe software.**

Describe software was used to write the thin film design composed of different hatching distances for each layer (Figure 2.17). The overlap between layers was set to 0.5  $\mu\text{m}$  to ensure structure stability. The hatching distance of each layer was adjusted to 0.1  $\mu\text{m}$  to ensure the structures had as smooth a surface as possible to ensure the cardiomyocytes would be seeded onto a continuous chemistry to evaluate attachment. (Figure 2.17). The optimal fabrication parameters were selected according to the results obtained in the 2-photon lithography studies in Chapter 3 according to the polymer being manufactured.

The first 2 layers had larger hatching distances to reduce fabrication time. The 3<sup>rd</sup>, which was the topmost layer, had 0.1  $\mu\text{m}$  hatching distance which is the minimum hatching distance on the Nanoscribe system. This was to ensure the design surface was as smooth as possible so that CMs could attach to the polymer being tested.

#### 2.7.5 Fabrication of Complex Architectures

Initially, the operating window values obtained from the thin film array SEM image data were utilized to calculate a more appropriate scan speed for a suitable fabrication period. Firstly, the midpoint energy value from the operating window, alongside the maximum laser power for fabrication was used to determine a suitable scan speed value for optimal fabrication time (Section 3.2.2.4). These parameters were then utilized to fabricate two complex architectures; a depiction of a heart and a DNA double helix model (Figure 2.18). These designs were downloaded from thingiverse.com and fabrication parameters as well as dimensions adjusted on Describe software prior to printing.



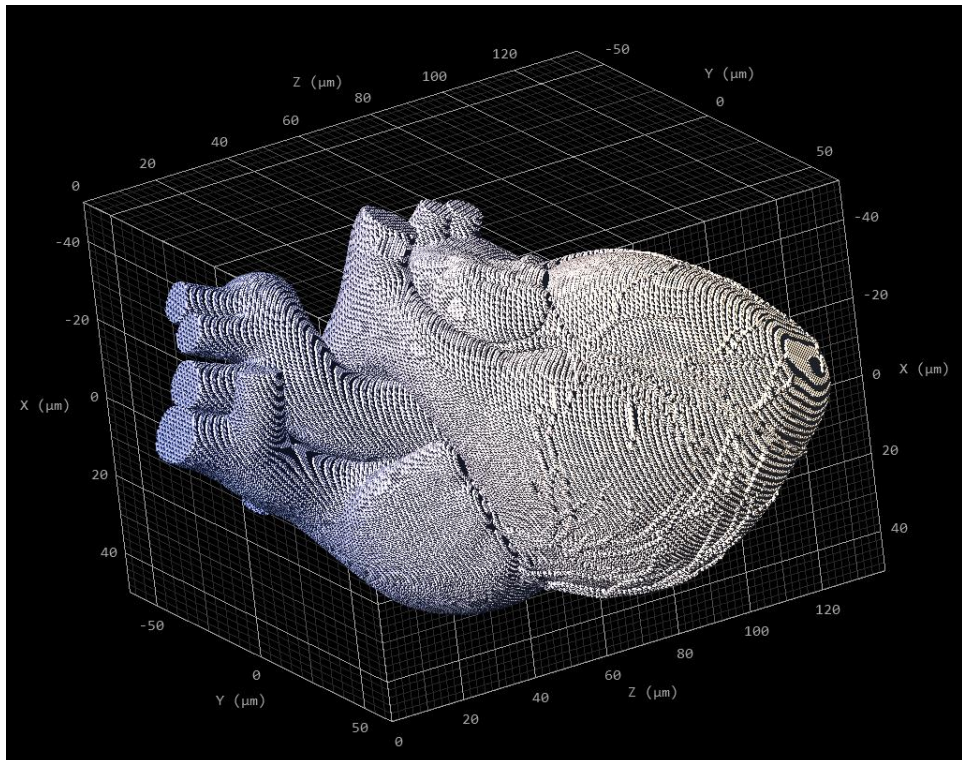
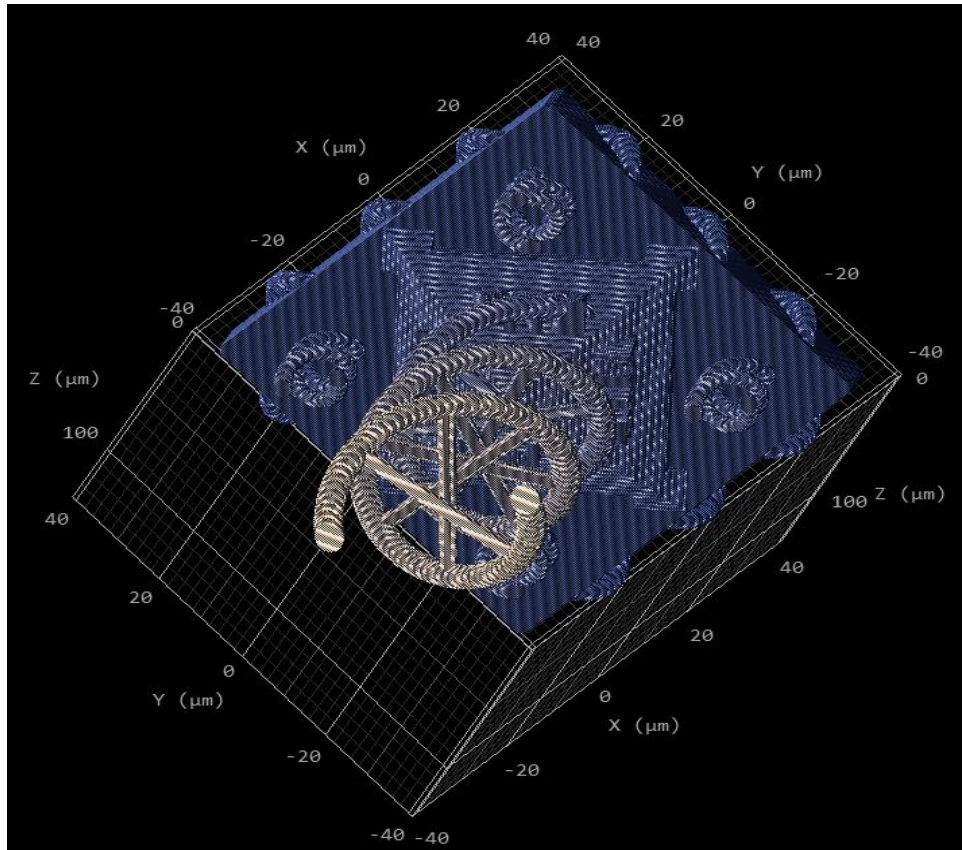


**Figure 2.18: Images for the DNA double helix and the anatomical heart (bottom) designs captured the Describe software.**

### 2.7.6 Open channels of different curvatures

The initial fabrication of complex architectures commenced with a series of open channels (Figure 2.19). Cardiomyocytes have been shown to align along grooves of certain lengths, widths and depths (Carson et al., 2016).

AutoCAD structures were designed utilizing AutoCAD 3D modelling tools starting from a cylinder shape followed by slicing and sculpting to generate open channels (Figure 2.19). AutoCAD 2018 software was opened and the '3D modelling' mode was selected for design. Firstly, a 3D cylinder was generated followed by slicing it in half using the 'slice' function. An arc was drawn on the surface of the half-cylinder followed by the 'presspull' function to generate the open-channel shape (Figure 2.19, stage 3). The closed part was sculpted off so that only the open-channel remained. Additional sculpting of the bottom and the sides of the structure resulted in a design illustrated in Figure 2.19, stage 4. The structure could still be functional from stage 3 however it is crucial to consider whether the bulk of the structure is necessary for fabrication. 2PL is a high-resolution method and therefore long fabrication times are required to produce any structure. The various fabrication times were discovered through a trial-and-error basis hence the extra sculpting steps were added to generate the structure at stage 4. Once a desired open-channel was generated 4 additional copies were made and placed onto a thin rectangular platform. The platform was drawn separately so that the height was as low as possible. This ensured that the open-channels had a flat and stable structure to adhere to during and post-fabrication. In addition, the platform has a larger surface area which means it bonds to the surface of the glass cover slips at many points to prevent structure loss during the washing steps post-fabrication. 5 was selected as a suitable number which is higher than the standard 3 repeats for experiments but also not too high, to minimize fabrication time.

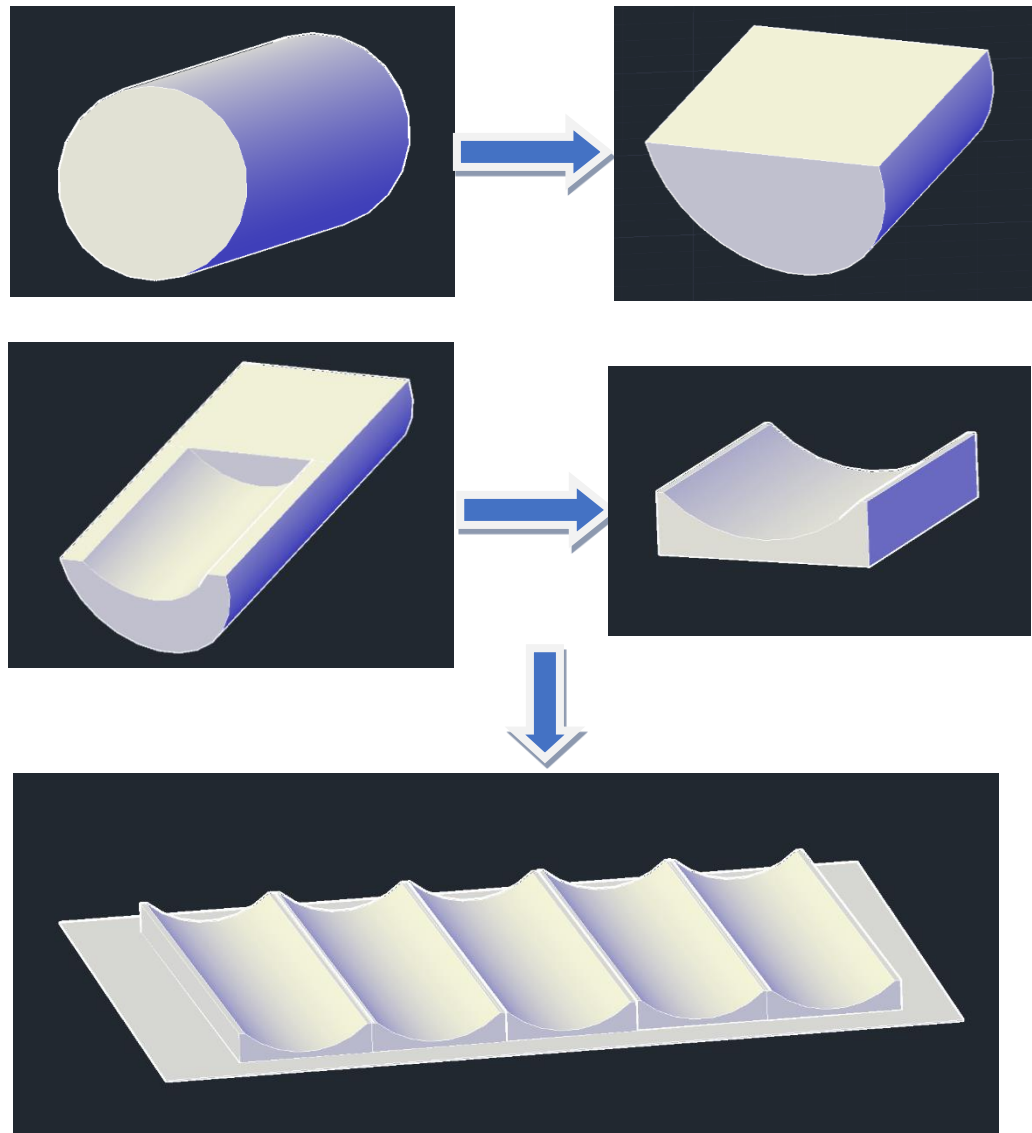


**Figure 2.19: Flow diagram of the generation of open-channel structures showing the initial cylinder shape until the final open-channel structures on a platform. Images were captured from AutoCAD 2018 software.**

AutoCAD works in arbitrary units which translate to micrometres when converted to lithography (.stl) files required for 2PL. Hence, arbitrary measurements during AutoCAD design were made bearing in mind the micrometre scale (Table 2.6). The main dimensions were set during AutoCAD design (Table 2.6). Additional parameters such as hatching distance, slicing distance and stitching dimensions were adjusted during .stl file generation to produce the final designs (Figures 2.20 and 2.21).

**Table 2. 6: Dimensions of large open-channel structures and platform.**

| <b>Parameters</b>             | <b>Cylinder</b>    | <b>Platform</b> | <b>Smaller design with various curvatures</b> |
|-------------------------------|--------------------|-----------------|---|
| Length<br>( $\mu\text{m}$ )   | N/A                | 1300            | 220   |
| Width<br>( $\mu\text{m}$ )    | N/A                | 1200            | 1000  |
| Height<br>( $\mu\text{m}$ )   | 300                | 2 $\mu\text{m}$ | 16  |
| Diameter<br>( $\mu\text{m}$ ) | 15                 | N/A             | 0.8 $\mu\text{m}$ (per groove)                |
| Curvatures<br>( $^\circ$ )    | 60, 100 and<br>160 | N/A             | 100, 150 and 200                              |

All arbitrary units in AutoCAD are equal to the measurements in micrometres on the Describe software. The values in Table 4.4 are the same values in arbitrary units of the AutoCAD designs. Parameters that could potentially affect cardiomyocytes were considered, keeping in mind what has been previously investigated in literature. Channel curvature was selected as a parameter to vary and investigate since this was not studied before. In addition, curvature is an important parameter to consider as the mesoderm, which eventually becomes heart tissue, undergoes morphological changes during development (Moorman et al., 2003). Recapitulating these changes by varying architecture curvature would be very informative in determining whether CMs will vary in their maturity.

Figure 2.20 shows the design of the platform with  $60^\circ$  and  $100^\circ$  open-channel structures (bottom). The x, y and z axes and the units are displayed in increments of 200  $\mu\text{m}$ . All open-channel structures are aligned and in contact with each other without overlapping (Figure 2.20). The platform is thin (2  $\mu\text{m}$ ) albeit thick enough for the open-channels to be slightly submerged into the platform to prevent it from falling apart.



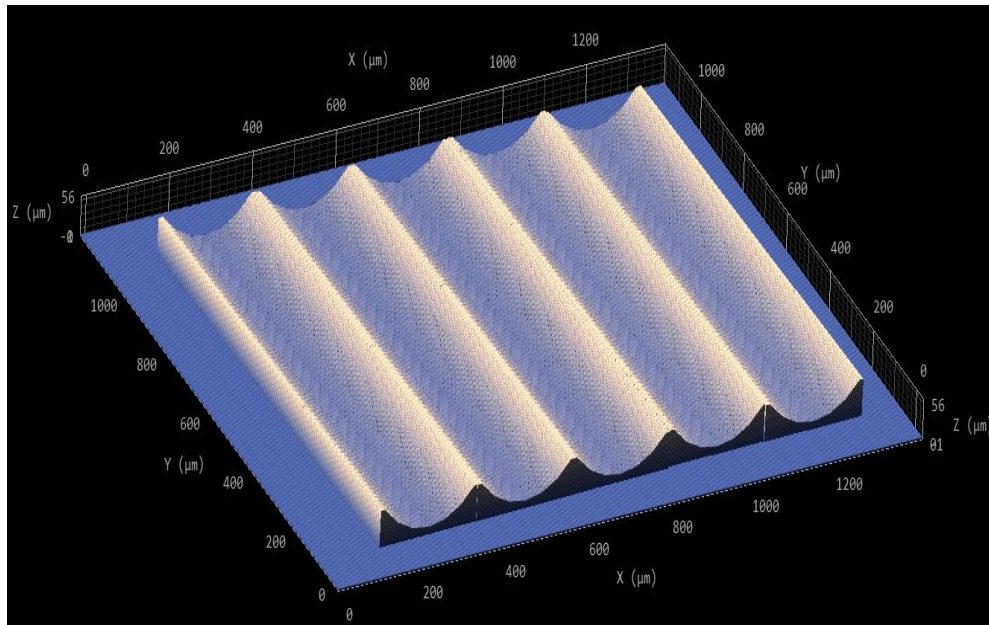
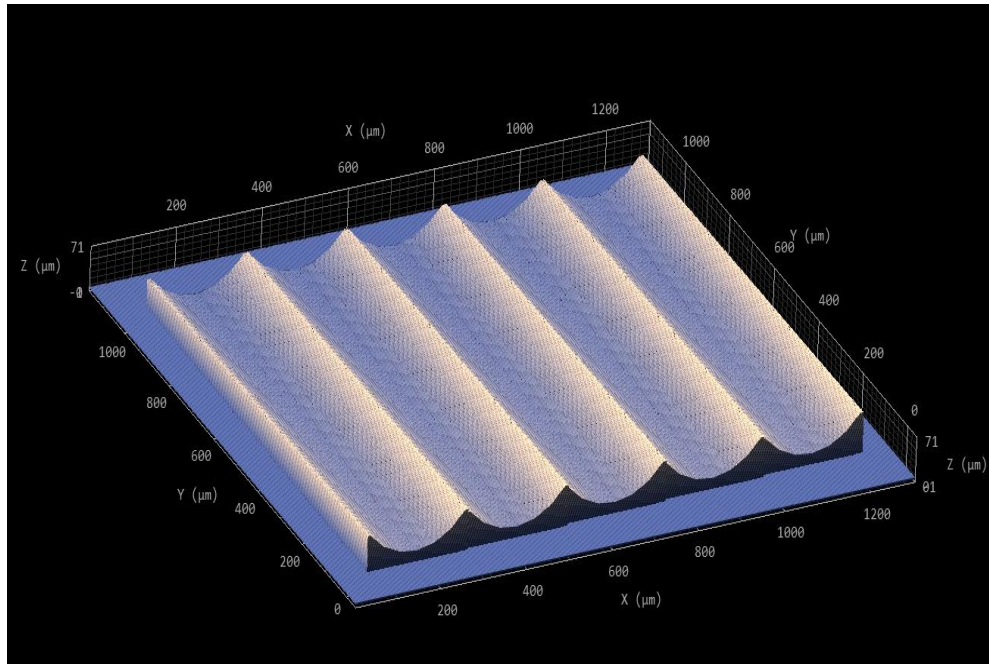


**Figure 2.20: Design of 60° (top) and 100°-degree curvature architectures captured from Describe software.**

Figure 2.21 shows the 160° curvature open-channels on a platform design. The lesser degree of curvature is clearly visible on the .stl design when compared to the 60° and 100°. stl designs (Figure 2.20).

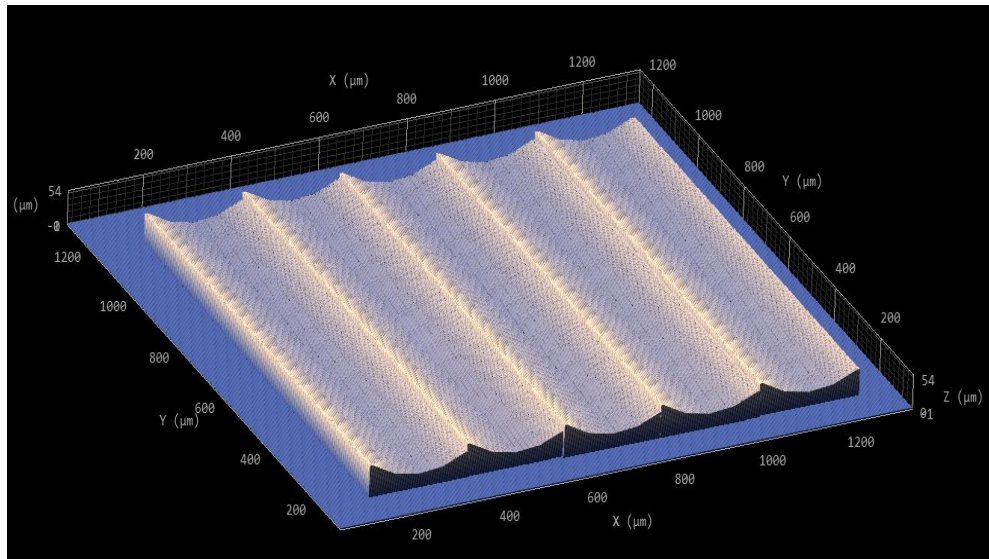


**Figure 2.21: Design of 160° degree curvature architecture captured from Describe software.**

Wider grooves will allow for the observation of multiple CM attachment and any maturity changes that may occur due to the architectural morphology of their surroundings.

A structure was designed for the purpose of combining all the structures with different groove depths into 1 stl. file (Figure 2.22). The groove width and depth dimensions were maintained the same as the previous .stl designs.

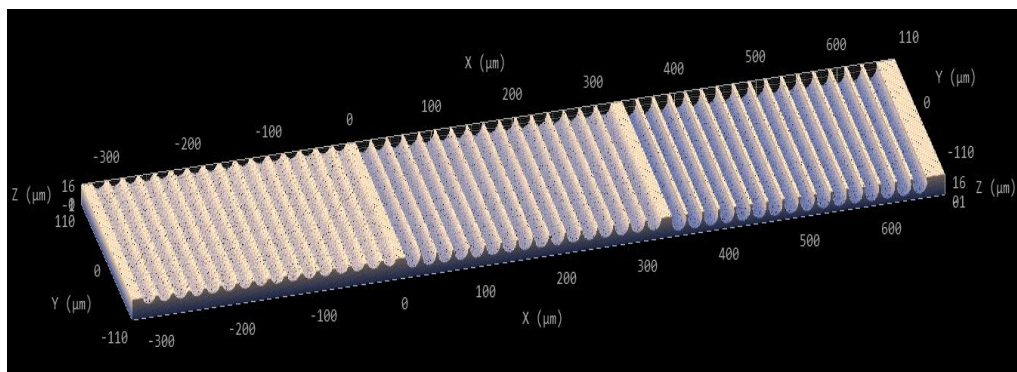


**Figure 2.22: Image captured on Describe software of box with grooves design of different curvatures at a smaller scale.**

Concerns arose with groove dimensions, especially when 2-photon fabricated constructs are placed into a 6-well plate after which cells are seeded onto the tiny structure. As a mature CM is approximately 125  $\mu\text{m}$  in length it would pose a challenge for the cells to settle into the grooves. The probability of 2 cells lining along each groove on the structure (Figure 2.22) would be very low. Therefore, new design dimensions with longer groove lengths were considered. A combined flat region and a region composed of all the groove depths was designed on AutoCAD software. Briefly, a rectangular block was fabricated at 2  $\mu\text{m}$  height and part of the flat region fused with the grooves region (approximately 1  $\mu\text{m}$  overlap). Both designs were combined and exported together as an .stl file. The new design had 1000  $\mu\text{m}$  length (Figure 2.23, Table 2.7) to ensure an adequate number of cells (approximately 10) could adhere inside the grooves. A 2000  $\mu\text{m}$  width for the whole structure was necessary to ensure that each groove width was 27  $\mu\text{m}$  (Figure 2.23, Table 2.7). This is slightly larger in width than a mature cardiomyocyte (25  $\mu\text{m}$ ) so that the most mature CMs and the less mature CMs would be able to fit into the grooves. These dimensions also ensured that the shallowest grooves were set to 6  $\mu\text{m}$ , allowing cells to have space in the z direction to settle into the features.

**Table 2. 7: New multiplex design dimensions showing the flat region and the region with grooves.**

| <b>Parameters</b> | <b>Flat Region</b> | <b>Grooves Region</b>         |
|-------------------|--------------------|-------------------------------|
| Length            | 2000 $\mu\text{m}$ | 2000 $\mu\text{m}$            |
| Width             | 1000 $\mu\text{m}$ | 1000 $\mu\text{m}$            |
| Height            | 2 $\mu\text{m}$    | 15 $\mu\text{m}$              |
| Diameter          | N/A                | 27 $\mu\text{m}$ (per groove) |
| Groove Depths     | N/A                | 6, 9 and 12 $\mu\text{m}$     |

A flat region was added to the construct so that CM attachment can be compared on a flat control fabricated with the same material (Figure 2.23). The grooves region begins from 400  $\mu\text{m}$  towards the right. The grooves region was divided into three sections. The first section from 450-950  $\mu\text{m}$  was comprised of the grooves with 6  $\mu\text{m}$  depth. The second section from 950-1450  $\mu\text{m}$  consisted of grooves with 9  $\mu\text{m}$  depth and the far section on the right from 1450-2000  $\mu\text{m}$  was composed of grooves 12  $\mu\text{m}$  deep. All groove widths were kept constant at 27  $\mu\text{m}$  which was slightly wider than the width of a mature human cardiomyocyte. This was to ensure all CMs could fit into the grooves without difficulty so that cell response could be observed.

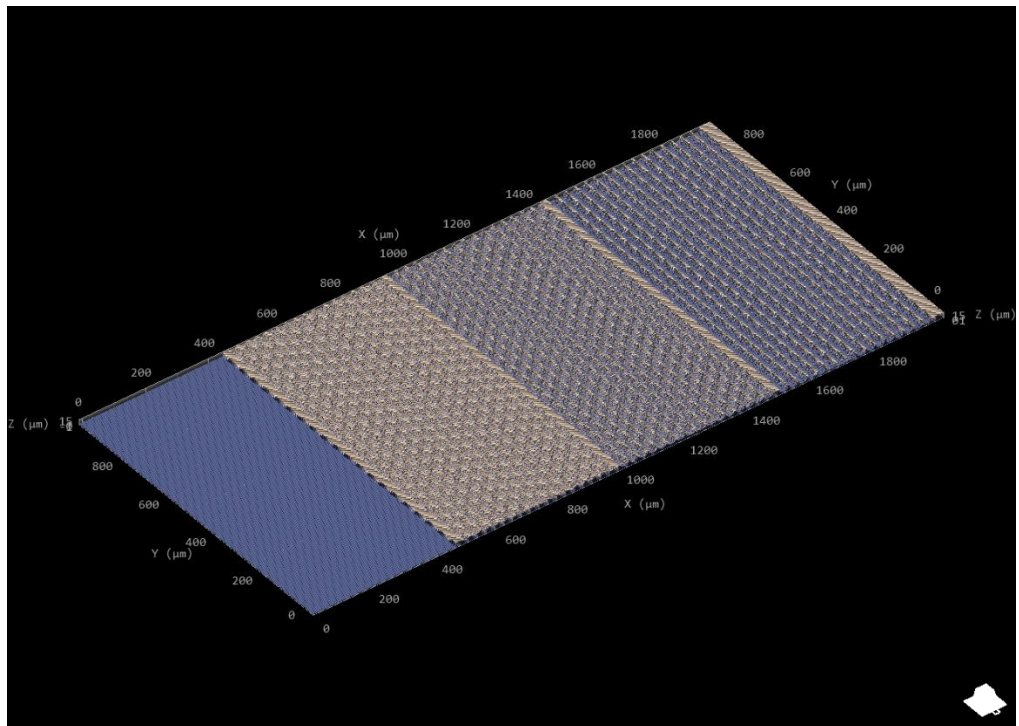


**Figure 2.23: Multiplex construct consisting of flat section on the left followed by the grooves region on the right. The image was captured on Describe software.**



The hatching distance and slicing distance of this design was set to  $0.6\ \mu\text{m}$  to reduce fabrication time without losing structure stability. The hatching direction was altered, considering that cells respond to the direction of the grooves, termed, ‘contact guidance’, which is a phenomenon first discovered in 1912 (Harrison, 1912). One .stl file was used per construct therefore 4 separate constructs were made so that each hatching direction of  $0^\circ$ ,  $90^\circ$ ,  $60^\circ$  and  $120^\circ$  could be tested. Figure 2.24 shows enlarged images of hatching directions of  $0^\circ$  and  $60^\circ$  on two .stl designs.

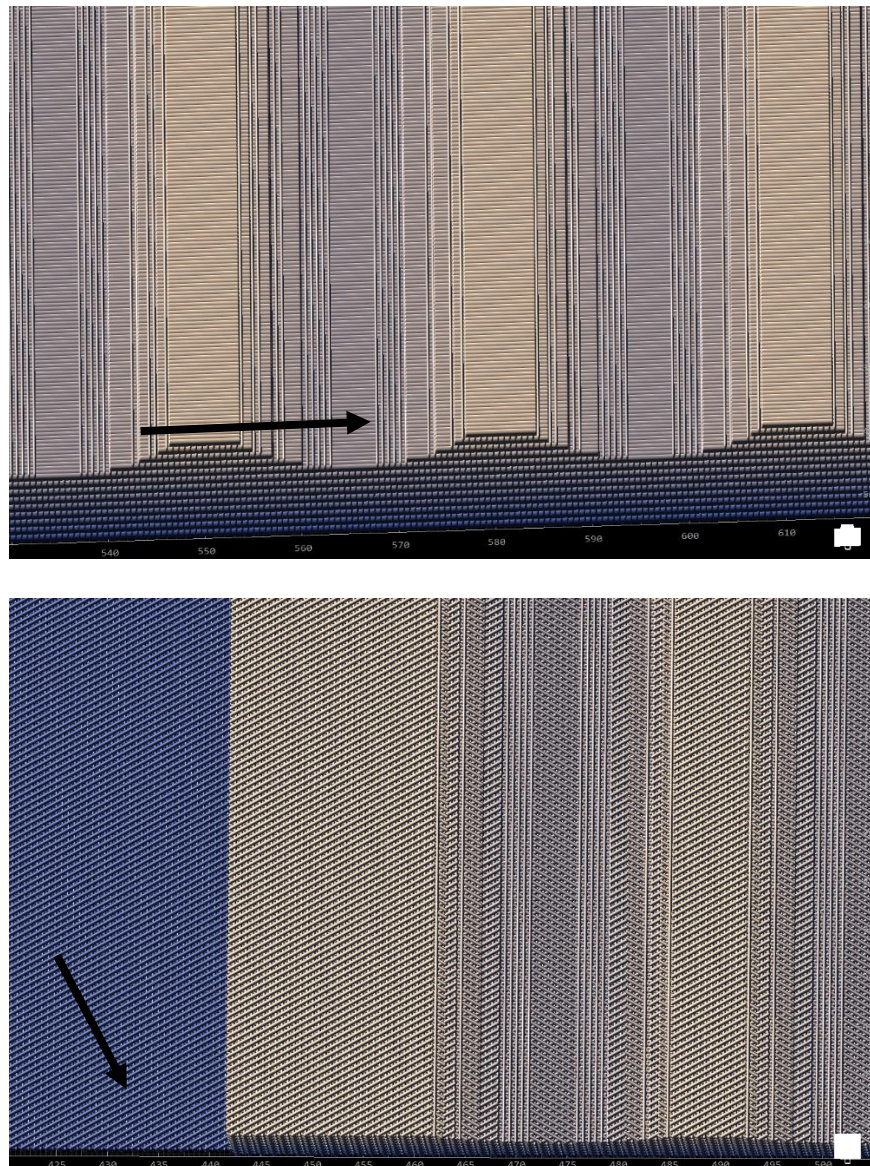


**Figure 2.24: Top: grooves with hatching lines in the  $90^\circ$  horizontal direction and bottom: flat region of multiplex construct with hatching direction  $60^\circ$  indicated by the black arrows on both designs.**

The only complication with this design was that if hatching direction was altered, then the hatching direction in the grooves was automatically altered too. The purpose of modifying hatching direction was to test this variable only therefore it is only desirable for the flat region to have varying hatching directions. Cells showing varying behaviour in the grooves will not necessarily be due to the groove depth but perhaps the hatching direction within the groove. An upgrade of this design was created using separate .stl files for the flat region and the grooves regions. The flat region was created as four separate .stl files, each having the hatching direction being tested. The whole grooves region with each depth measurement being tested was created as one .stl file with a constant hatching direction as  $0^\circ$  (Figure 2.25).

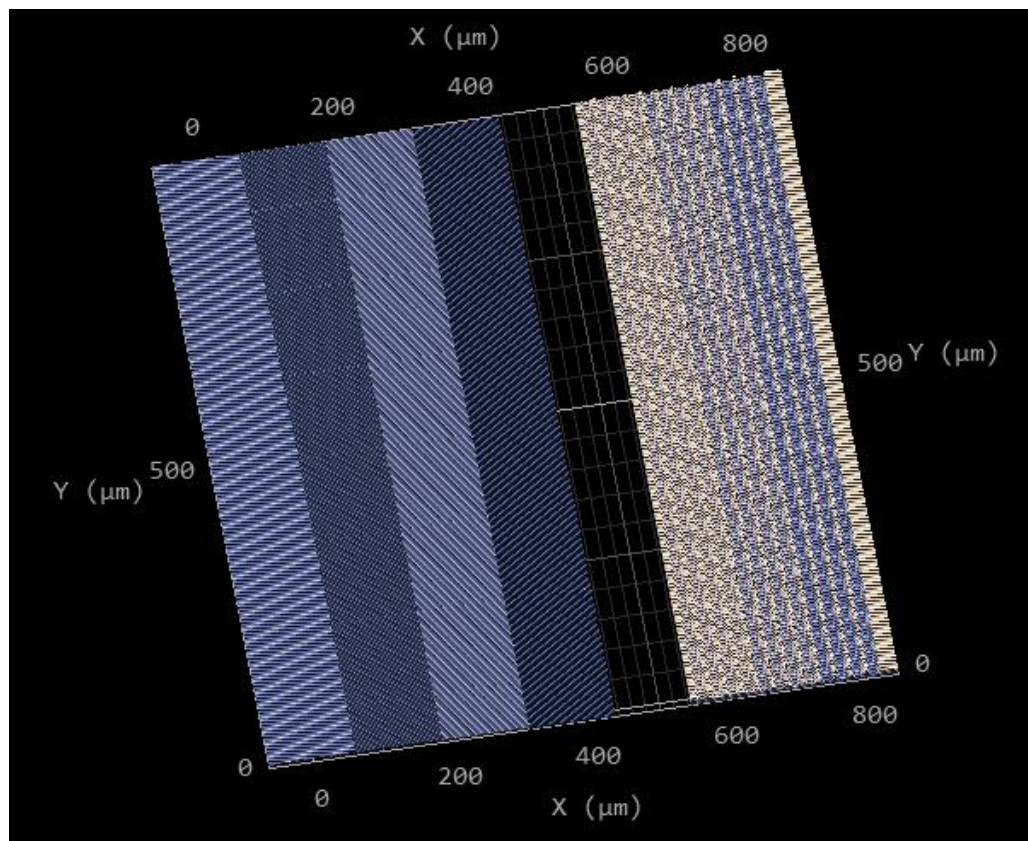


**Figure 2.25: New design images captured from Describe software with varying hatching angles in the flat region followed by a 200  $\mu\text{m}$  gap and one stl. file of the grooves regions on the right. The slight variation in colour of the grooves region indicates the different depths with the white one on the left-hand side being the shallowest and the solid blue being the deepest region.**



The flat region was created as four separate .stl files and created in the order of 0°, 90°, 120° and 60° hatching directions (Figure 2.26).

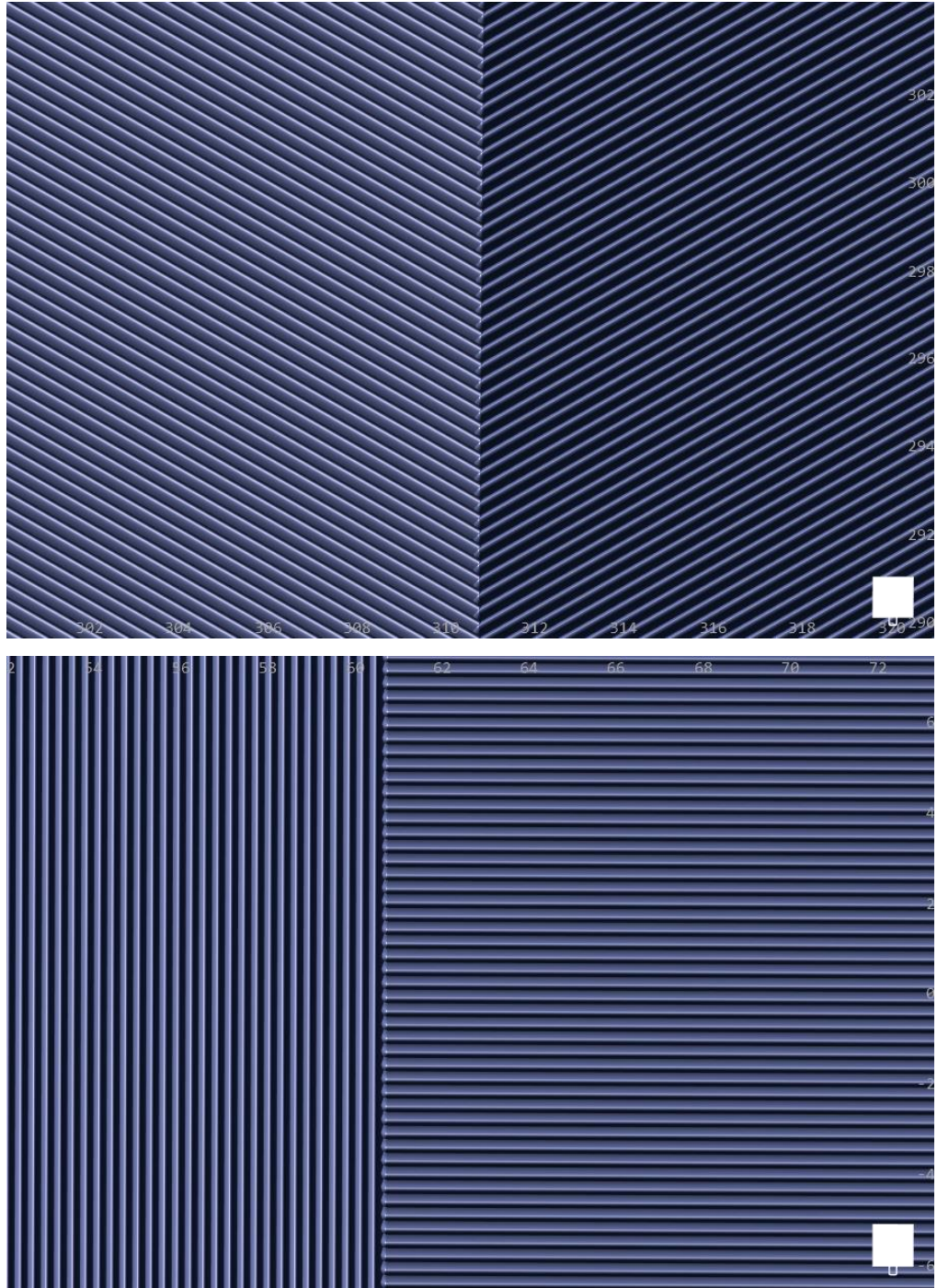


**Figure 2.26: The flat region of the new multiplex showing the 0° hatching direction on the left and the 90° hatching direction on the right. (bottom) shows the hatching direction of 120° on the left and 60° on the right.**

All grooves had the same hatching direction of  $0^\circ$  to ensure that any differences in CM attachment and maturity would be due to the groove depth and not any other variable. The shallowest grooves had a depth measuring  $6\ \mu\text{m}$  (Figure 2.27). The grooves in the next region had a depth of  $9\ \mu\text{m}$  (Figure 2.27, bottom).

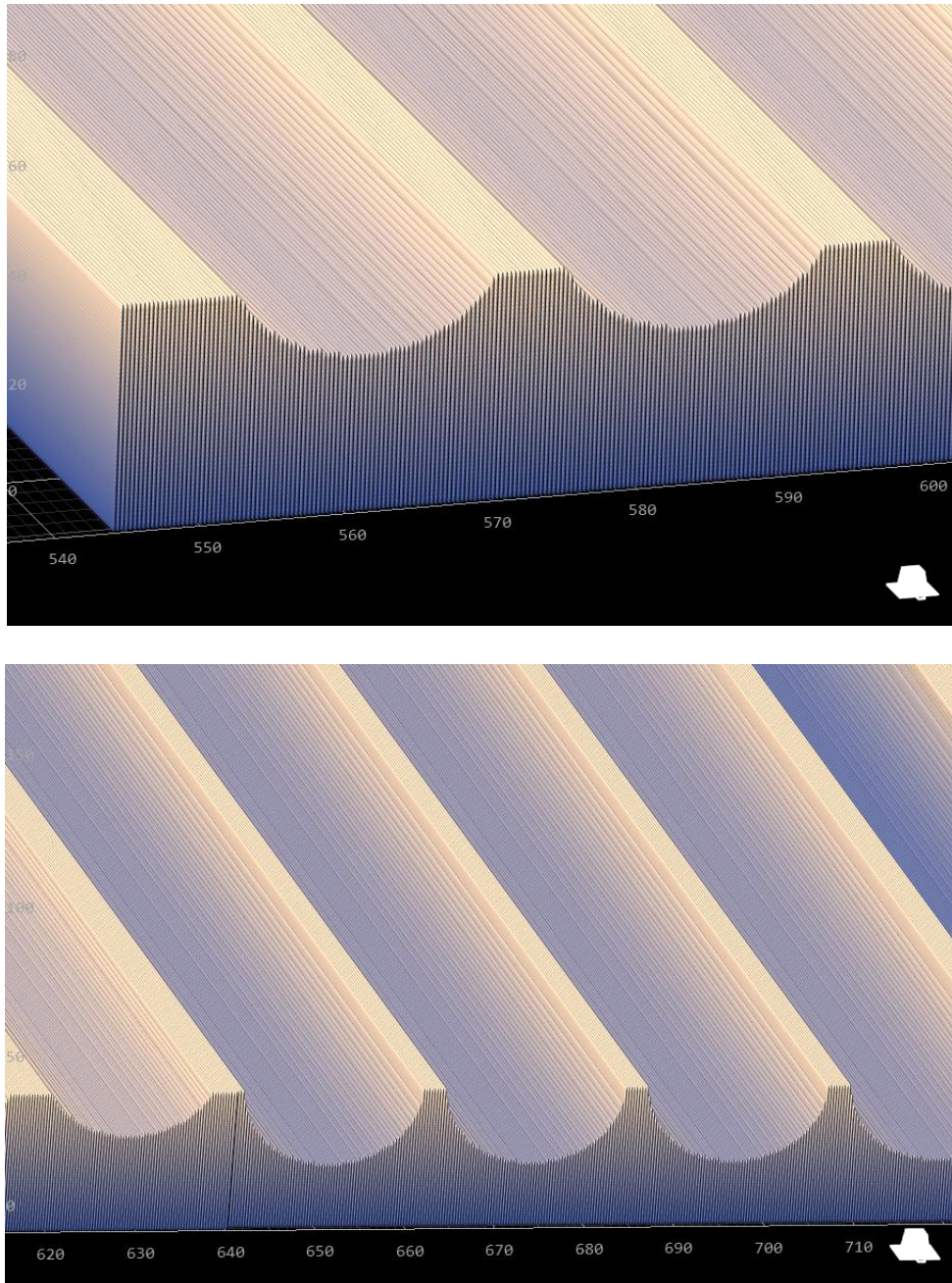


**Figure 2.27: Illustration of the grooves region of the new multiplex design. Top: The shallow part of the grooves region with hatching direction  $0^\circ$ . Bottom: The medium-depth of the grooves region illustrating the deeper grooves compared to the one shallow groove on the left hand side.**



The deepest grooves region (Figure 2.28) contained 4 grooves like the other regions, with each groove measuring 12  $\mu\text{m}$  in depth (Figure 2.28). The hatching direction was also  $0^\circ$  in this region to keep all other variables constant.

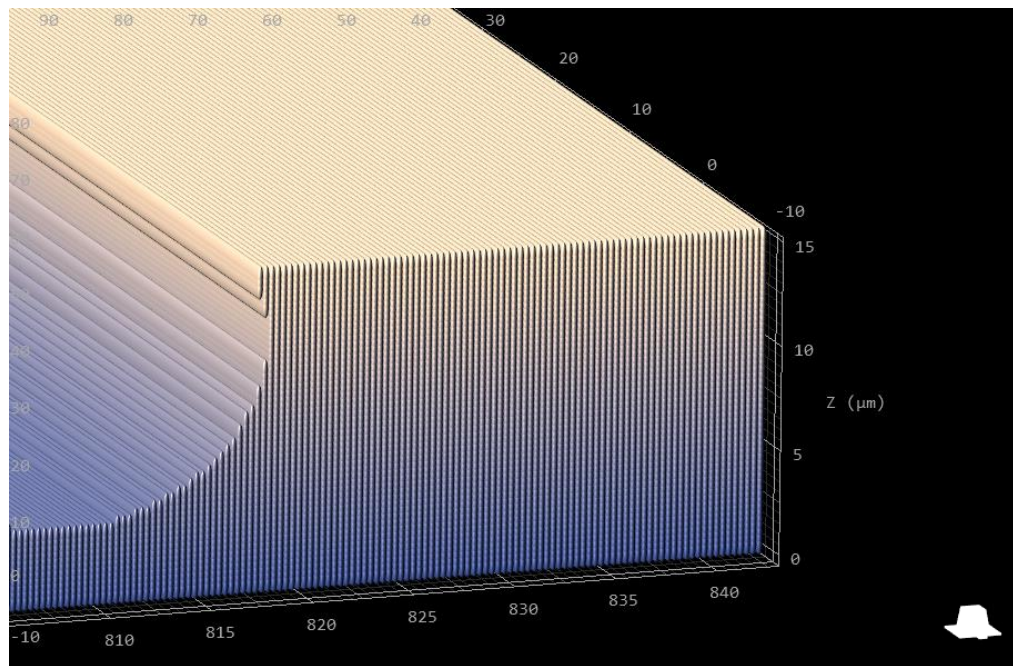
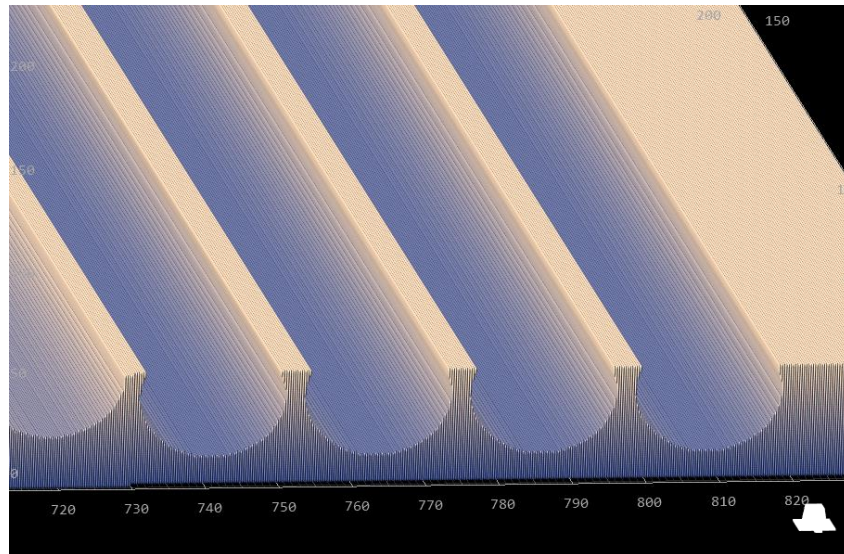


**Figure 2.28: The deep grooves region with hatching direction of  $0^\circ$  (bottom): Enlarged image of the corner deep groove. The z scale is illustrated on the right in  $\mu\text{m}$  units. The groove depth is 12  $\mu\text{m}$ .**

### 2.7.7 Plasma activation and silanisation of glass cover slips for 2-photon fabricated structures to be used in CM attachment experiments

All glass slides were activated by oxygen plasma using in-plasma air treatment. The chamber was degassed to get rid of contaminating gases until base pressure was reached (18mTorr). All valves were closed and the chamber brought back to atmospheric pressure by opening the release valve. The slide rack with 8-10 glass cover slips (20mmx20mm) was placed inside the glass chamber and evacuated until base pressure was reached (18mTorr). When at base pressure, the valve to oxygen was opened until the pressure was higher than 300mTorr and the valve closed again to ensure a clean plasma. When the reactor reached back to base pressure, the chamber valve was closed and opened one turn. The oxygen valve was opened again and the oxygen needle valve stabilised to 300mTorr. The radiofrequency was turned on which caused radio waves to excite the oxygen to the plasma state as evidenced by a glow discharge of blue/white light. Adjusting the output power to 50Watts and minimum reflected power <1 Watt, the glass cover slips were cleaned for 3 minutes.

Following oxygen plasma etching, glass cover slips were placed into a metal sample holder with slots that fit the glass cover slips and separate them from each other. This sample holder was placed into a 1 ml large glass beaker. The beaker was filled with 500 ml of anhydrous toluene solvent. TMSPMA bottle cap was opened and a syringe inserted through the rubber seal of the bottle. Then another needle was attached to a pipe from the Argon supply in the hood and this needle was also placed into the rubber seal of the TMSPMA bottle. The syringe was then used to suck air out of the bottle and released into the atmosphere 3-4 times to ensure the bottle was purged with Argon. 10 ml of TMSPMA was taken out using the syringe and added to the beaker containing toluene and the sample holder. The beaker was placed onto a hot plate at 50 °C. A glass funnel was inverted and placed on top of the beaker making sure it completely covered the rims, as illustrated in Figure 2.29. Then a pipe from the Argon supply was inserted into the bottom end of the funnel. The funnel was secured to the rest of the apparatus with the aid of a clamp stand. The Argon flow rate was ensured to be at a slight positive pressure. The setup was left for 16 hours overnight.

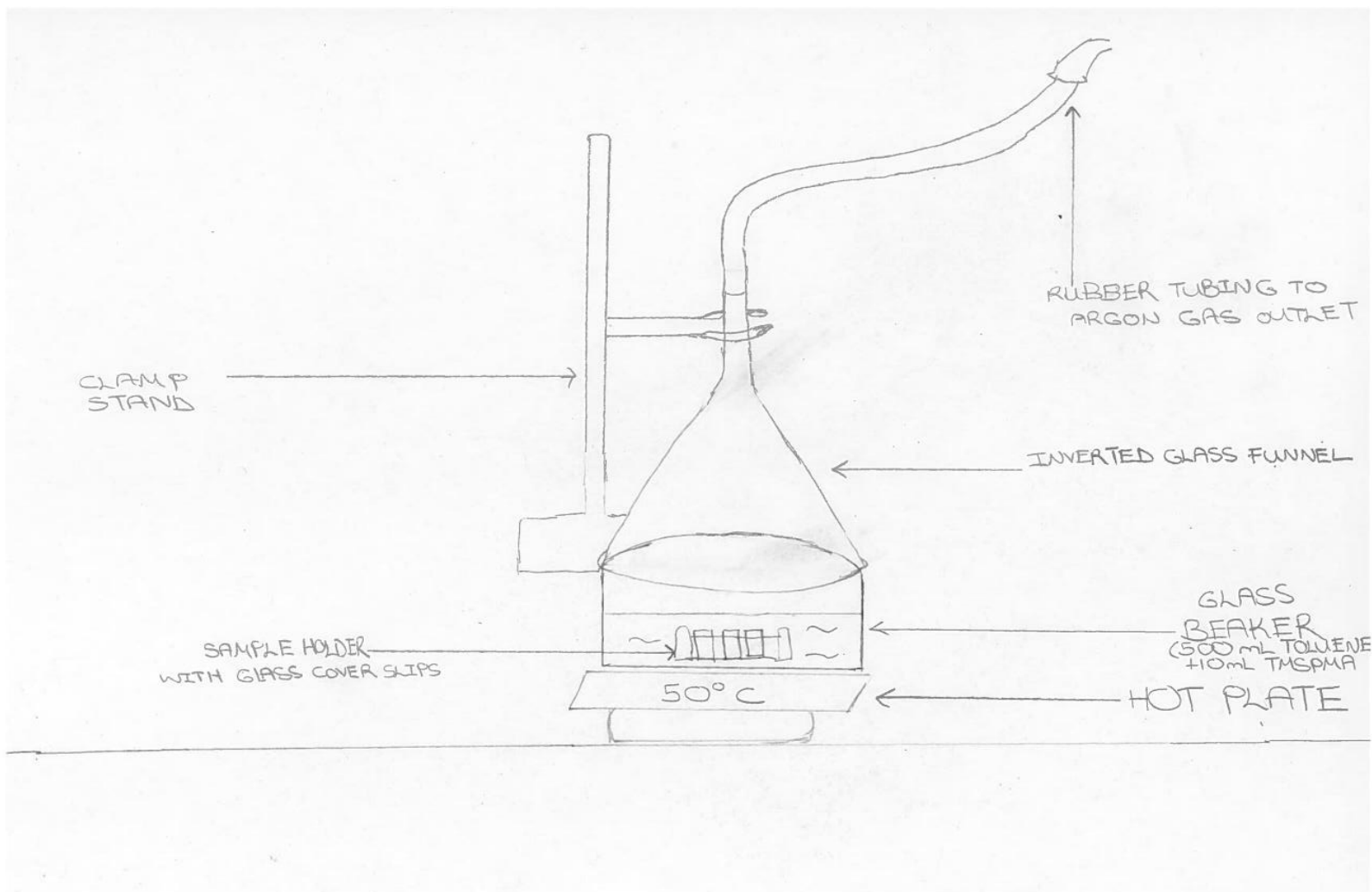


**Figure 2.29: Experimental setup for the silanisation of glass cover slips in an Argon atmosphere.**

The next day the sample holder was taken out of the beaker and left to cool for 30 minutes at room temperature in the hood. Then the sample holder containing all the glass cover slips were rinsed twice with 100 ml of anhydrous toluene solvent. They were left to dry and placed in the vacuum oven for 24 hours until further use. The plate holder and Argon supply was switched off. Toluene waste was discarded into the non-halogenic solvent waste.

## 2.8 Immunostaining and DAPI Staining

Immunostaining is a widely used technique which enables the identification of the expression of a specific protein within a group of cells or a tissue section. When the sample is a tissue section it is usually referred to as immunohistochemistry whereas when the sample is from cell culture the technique is called immunocytochemistry.

Immunostaining relies on the ability of an antibody labelled with a fluorescent protein or enzyme (referred to as a conjugated antibody) to target and bind specifically to the protein being studied. In some cases, only one antibody is used to bind a specific target protein such as the identification of disease biomarkers. In most other cases, a secondary antibody is used to bind the primary antibody which targets the specific protein. The primary and secondary antibodies come from different animal species, so they can bind each other. Serum from the same source as the secondary antibody is used so that non-specific binding by the secondary antibody can be identified in a separate secondary antibody-only control sample. Serum blocks non-specific binding of the primary antibody as well. Serum contains albumin and other proteins that can bind all non-specific binding sites in the sample.

Antibodies are composed of a constant (Fc) domain and a variable (Fv) domain. Since the Fc domain is constant within one animal class, one type of secondary antibody is capable of binding different types of primary antibodies. This means one type of secondary antibody can be used to label primary antibodies that attach to various proteins of interest. In addition, more than one secondary antibody can bind a primary antibody which enhances sensitivity and signal amplification.

The sample is then analysed by wide-field confocal microscopy. The fluorescent signals are detected by the microscope. The secondary antibody is conjugated to a fluorophore which is detected by the microscope and the exact location of the protein of interest can be visualised.

DAPI chemical tag binds DNA *via* electrostatic attraction and hydrogen bonding, making it a great stain for cell nuclei. It is added to the samples after both antibodies have been added. The DAPI chemical tag fluoresces blue when exposed to UV light which can also be visualised by confocal microscopy.

### 2.8.1 Day 1

Firstly, goat serum was thawed out for preparation. Cell Culture plates were washed twice with PBS (Gibco™) and then fixed with 4 % paraformaldehyde and incubated for 15 minutes to fix the proteins in the cells. Afterwards, all wells were washed twice again with PBS (Gibco™) at 1 ml per well for 6-well plates. A vacuum pump was used to remove the PBS (Gibco™). The wells were incubated in 0.1% Triton for 15 minutes to permeabilise the cell membranes. The final triton solution was made from a stock solution of 2% Triton by transferring 6 ml PBS(Gibco™) into 12 ml Falcon tube and adding 300 µl of Triton (1 in 20 dilution). The tube was mixed well and 1 ml of the final solution was added to each well of a 6-well plate. The Triton was aspirated, washed 3X with PBS(Gibco™) and incubated in goat serum for 1 hour at or 1 ml per well for 6-well plates in order to block all non-specific protein binding sites. The total volume of goat serum required was calculated based on the number of wells to be analysed and the goat serum prepared at 4% concentration in PBS (Gibco™). After an hour the goat serum was aspirated and washed 3X with PBS (Gibco™) at the appropriate volume. The amount of antibody required was also calculated based on the number of samples to be analysed. The concentration of each antibody is also optimised for maximum functionality. The protein to be analysed is  $\alpha$ -actinin (Sigma-Aldrich™) which requires a working concentration of 1 in 800 of which the rest of the solution was made up with 4% goat serum and PBS (Gibco™). The first primary antibody was added at 700 µl per well and incubated at room temperature for 3 hours wrapped in aluminium foil as antibodies are light-sensitive. The first secondary antibody was goat anti-mouse

Alexa488 (Sigma Aldrich™) and was made 1 in 1000 in PBS(Gibco™) with 4% goat serum to a working concentration. Therefore, the final solution contained in a 3000 µl solution of PBS(Gibco™); 3 µl secondary antibody and 120 µl goat serum. This was added at 1 ml per well and incubated for 1-2 hours at room temperature wrapped in aluminium foil. The second primary antibody targeted was cardiac troponin T which has maximum functionality at a dilution of 1 in 100. This is a much higher concentration than  $\alpha$ -actinin and cardiac troponin T was of limited supply. Therefore, a volume just enough to cover the surface of the construct and the immediate area was prepared. The volume chosen was 300 µl per well so that 3 µl of cardiac troponin T (Sigma Aldrich™) was enough for each 2-photon fabricated sample. This solution was enough to cover the area to be analysed within the well but was also not too low so as to prevent drying out of the wells during the overnight incubation. The samples were incubated overnight at 4°C wrapped in aluminium foil.

### 2.8.2 Day 2

All samples were washed with PBS (Gibco™) Tween to remove excess and weakly bound mouse primary antibody. PBS (Gibco™) Tween was made from a 2% stock solution in the same way as the Triton solution on day 1. 6 ml of PBS (Gibco™) was transferred to a 12 ml falcon tube and 300 µl Tween added. This would be enough for 2 wells for 3X rinsing with Tween at 1 ml per well. The second secondary antibody was goat anti-mouse Alexa555 (Sigma Aldrich™) and was made 1 in 1000 in PBS(Gibco™) with 4% goat serum to a working concentration. Therefore, the final solution contained in a 3000 µl solution of PBS(Gibco™); 3 µl secondary antibody and 120 µl goat serum. This was added at 1 ml per well and incubated for 1-2 hours at room temperature wrapped in aluminium foil. The samples were then washed 3X with PBS and DAPI (1 in 500 in PBS) added at 1 ml per well. Finally, the samples were washed 2X with PBS and kept at 4°C until imaging analysis.



### 2.8.3 Preparation for imaging

The best results are obtained as soon as immunostaining is complete. The protocol for immunostaining day 2 is short so it is ideal to prepare samples for imaging on this day as another overnight incubation is required.

Firstly, the cover slips are taken out of the wells and dried on tissue, construct side facing up. Then an appropriate number of glass slides of thickness maximum 1.7 mm are lined up and labelled with the sample names. A 25  $\mu$ l drop of Vectashield® (without DAPI, Maraval LifeSciences) solution is transferred to each point on the glass slides where the cover slips would be placed. Once the cover slips were dry, they were inverted and placed on top of the Vectashield® (Maraval LifeSciences) drop making sure the solution covered the construct. The glass slides were placed into petri dishes, wrapped with foil and placed in the fridge overnight for the Vectashield® (Maraval LifeSciences) to set.

### 2.9 Wide-field confocal microscopy

Conventional confocal microscopy consists of an inverted microscope and a confocal hole which confines the light upon exit from the source. This ensures that only relevant transmitted light is shone on the sample which greatly reduces background fluorescence. A novel addition to the confocal microscope is the ability to view the whole sample without the confocal hole. This allows for a wider field of view but compensates on image quality. The background fluorescence is eliminated by deconvolution on computer software instead. This is especially important for samples that require detailed imaging at high magnification which is why this method is highly suitable for the analysis of the sarcomeres in the cardiomyocyte-polymer samples in this project.

Fluorescence imaging was performed using the Exciter Wide-field fluorescence microscope (Zeiss). This device has both confocal and wide-field modes for imaging. Wide-field was selected for imaging of cardiomyocytes on 2-photon fabricated constructs as the constructs are very small. Wide-field also allows for higher-resolution images due to wider field of view hence detailed images of the

sarcomeres could be obtained. Micromanager software on the PC was used to take multiple photos of the samples using z-stacking. The gaps between stacks were chosen as 0.1  $\mu\text{m}$  and the three fluorescence channels DAPI (blue), FITC (green) and TRITC (Mei et al.) to detect fluorescence emitted by the secondary antibodies. Images taken from samples for cell viability tests with PrestoBlue required the DAPI (blue), TRITC (Mei et al.) and brightfield channel.

Photographs were taken as z-stacks of all regions of each 2-photon fabricated construct; flat region, shallow 6  $\mu\text{m}$  grooves region, medium-depth 9  $\mu\text{m}$  grooves region and deepest 12  $\mu\text{m}$  grooves region. Photographs were also taken of cells of each sample on surrounding glass cover slip to serve as a flat control with no acrylate polymer present. Images were processed using Fiji (is just imageJ) software to eliminate background fluorescence, deconvolution was performed using advanced Huygens software and Fiji was used take measurements from cardiomyocytes.

## 2.10 Raman Spectroscopy

The inelastic scattering of light rays was first observed by Raman and Krishnan in 1928 and hence called Raman spectroscopy (Lewandowski et al., 2018, Dent, 2005). The interaction of light with matter can have 3 effects; absorption, transmission or scattering. If the energy of the incident photon matches the energy difference between the ground state and excited state of the molecules, then absorption occurs. Infrared spectroscopy works on this principle. However, the photon can also interact with the molecules so that it is scattered. There is no need for the photon energy to match the energy difference between the ground state and the excited state in this situation. Detection is achieved when the scattered photons are collected at an angle to the incident light beam. The amount of scattering that occurs depends on the vibrational frequencies of the chemical bonds within a molecule. The scattering is translated to a spectrum of intensity values which is the Raman spectrum (Dent, 2005). Therefore, each bond type will produce a characteristic peak on the Raman spectrum. The intensity is plotted against frequency or wavenumber scales as they are linearly related with



energy. Although the principle of the technique uses radiation which would be assumed to have wavelength ( $\lambda$ ) as a scale, the interaction of the radiation with states of the molecule are being investigated and this is referred to as an energy scale. Hence the frequency or wavenumber units applied. The energy changes detected during Raman spectroscopy are ones that result from nuclear motion (distortion of the electron cloud of the molecules) which bring the molecule to a short-lived virtual state. Sometimes a photon's energy is only enough to cause a distortion in the electron cloud which cause very small frequency changes. This is called elastic scattering (or Rayleigh scattering in the case of molecules) and mostly this occurs. However, if nuclear motion is caused by the incoming photons energy will be transferred from the molecule to the scattered photon or from the incident photon to the molecule. The energy difference here is one vibrational unit and is named Raman scattering. There are 2 types of inelastic scattering; Stokes and anti-Stokes. Stokes scattering is the most common, which brings a molecule from the ground state to an excited vibrational state. Anti-stokes scattering is the exact opposite, causing molecules in the excited state to descend to the ground state. The populations of the various states of the molecules varies however more often than not, will be in the ground, hence Stokes scattering will occur. Raman spectra are most commonly derived from Stokes scattering.

Polymerisation occurs by the conversion of C=C bonds to C-C bonds. Therefore, the more complete a polymerisation reaction is the more conversion has occurred. This can be exploited to determine the degree of cure in polymer samples. The characteristic peaks C=C and C=O are  $1640\text{ cm}^{-1}$  and  $1720\text{ cm}^{-1}$  respectively. Cytotoxicity can be caused by remaining unreacted monomer and unreacted photoinitiator radicals on the surface of a polymer material. Raman spectroscopy can give valuable information on how much of the toxic monomer is still present in the sample by analysis of how much C=C bond still present in the molecule, giving an indication of how much unreacted monomer remains in the sample.

The amount of cure in the polymers tested for cardiomyocyte attachment (TCMDMA, PETrA and GPOTA) was determined by Raman spectroscopy. The aim was to measure the amount of cure between polymers that were subjected to

vacuum for a week post-fabrication, polymers subjected to vacuum and UV-cure post-fabrication and polymers subjected to neither of these treatments. Therefore, the necessity of UV or vacuum treatment or both will be established.

30 (x) by 30 (y) by 10 (z)  $\mu\text{m}$  cubes were fabricated with all three materials TCDMDA, PETrA and GPOTA with 3 cubes per glass cover slip (Figure 2.30).



**Figure 2.30: 50X light microscopy image of cube structure fabricated for Raman spectroscopy.**

The whole process was performed 3 times to have a set of glass cover slips for each of the 3 conditions (vacuum incubation, post-fabrication UV-cure and neither treatment). The uncured samples for each material were prepared immediately prior to Raman spectroscopy. Briefly, a drop of the formulation was placed onto a glass cover slip using a Pasteur pipette and the cover slip taped onto the glass slide that was to be placed under the Raman microscope. All other samples were treated the same way.

Firstly, the 785 nm laser power box was switched on. Then, it was made sure the laser control switch was off on the controller box prior to opening the microscope stage doors. The calibration sample of silicon was placed under the 50X lens and the system calibrated with the LabSpec 6 software. The silicon was replaced with a sample and the data collected using the settings mentioned below.

Horiba Raman microscope (Horiba LabRAM HR microscope, Horiba Scientific) was utilized with a 785nm laser and a 600 nm laser grating so as to not damage the acrylate polymer samples. Higher frequency lasers impose the risk of damage on small, transparent samples like the acrylate polymers used for this investigation. The acquisition time was found by implementing values between

3 seconds and increasing the value at 30s increments and 120 seconds was the value found to acquire sharp peaks at the expected intensity values for C=C and C=O bonds. The confocal was set to 50 to allow the least amount of out-of-focus laser as possible. The filter was set to 100% in order to allow full laser intensity to reach the sample for maximum signal detection. The real-time display time (RTD time) was set to 15 seconds which indicates how the spectra will appear in 15 seconds prior to full signal detection. This is useful in order to change the settings as appropriate as opposed to waiting for all the signal to be detected in all the acquisition time of 120 seconds. The accumulation was set to 4 which means the signal is collected from the samples 4 times to collect into a spectrum. The spectrum resolution improves with more accumulation as more total signal is collected. The 100X NIR lens was used to collect the most signal possible from the sample. The transparency and size of 2-photon fabricated acrylate polymers make Raman signal detection a challenge. This is the reason for fabricating the cubes at 10  $\mu\text{m}$  height. This is approximately the minimum height at which signal can be detected using such a transparent material. LabSpec software was used to determine a baseline under each relevant peak and the software generated values for the areas under the peaks. These values were then substituted into the formula;

$$\% \text{ Degree of conversion (DC)} = 1 - \left[ \frac{C=C}{C=O} \text{ cured} \right] / \left[ \frac{C=C}{C=O} \text{ uncured} \right]$$

Where cured and uncured refer to the state of the polymer.

## 2.11 Reasoning for Methods Selected in the Research

2-photon lithography has been selected as the method to be utilised for the duration of the project. This is a very new technology that can fabricate structures at a resolution as low as 50 nm. (Emons et al., 2012). Architectures can be fabricated at very high resolution with fine features to fulfil the main aim of this project which is to investigate whether these fine features affect cardiomyocyte viability and maturity. Electron beam lithography is another method which can fabricate structures with a resolution as low as 250nm (Scholten and Meng, 2016). This can vary from one material to another but regardless, this method is expensive and requires clean room facilities. Therefore, 2-photon lithography was selected to fabricate high-resolution structures. The high resolution attained by 2PL is ideal for the purposes of this project compared to other methods such as UV stereo-lithography or electrospinning, the aim being the investigation of cardiomyocyte behaviour and maturity as cells interact at the sub-micron level.

UV polymerisation in an Argon glovebox (MBraun© GB 2202-P-VAC) was performed prior to 2-photon lithography as it was necessary to prove whether certain polymers that previously supported CM attachment could do so again. Once CM attachment was established, then selected polymers were investigated as to whether they were amenable to 2PL or not. The reason for performing UV polymerisation is due to the ability polymerize many monomers in one 96-well plate in a short period of time (one hour) as opposed to fabricating each material by 2PL separately. This was an efficient way to determine which polymers could support CM attachment consistently.

Silanisation was performed on the glass cover slips utilised for 2PL as the post-fabrication washing steps led to loss of structures. Silanisation ensures that silane groups attach to the oxygen atoms on the glass surface. The silane groups themselves have terminal end groups which vary depending on the material to be applied to the surface. In this project, all materials utilised were of an acrylate nature, therefore methacrylate silanes were used during the silanisation process. This way the acrylate structure fabricated could polymerise with the methacrylate silane group on the glass surface, ensuring firm attachment and prevention of structure loss.

Structures fabricated by 2PL were analysed by scanning electron microscopy (Aissaoui et al.). This technique allows analysis of very small structures down to a few nanometres with high resolution compared to bright-field and confocal microscopy. Prior to SEM glass cover slips were coated with a Platinum sputter coater to reduce background noise. Platinum was selected due to its low granularity. This way, samples can be viewed in greater detail. Gold sputter coating is usually applied to larger biological specimens.

IPSCs were obtained from the stem cell bank (University of Nottingham) and maintained in home-brewed Essential 8 (E8) medium. The media was changed every day and split at an appropriate ratio when they reached confluency which was every 72 hours. CMs were differentiated from iPSCs using the Monolayer Differentiation Method. This protocol ensures the production of the most mature CMs to date (Burrige et al., 2014).

Briefly, iPSCs were differentiated over a period of 10 days in total, applying various small molecules every 2 days during this period. After 10-12 days, CMs were dissociated and reseeded onto UV- or 2PL-fabricated constructs. Samples were viewed under a light microscope after 72 hours to determine possible CM attachment.

If CM attachment was observed, the relevant samples were taken for immunostaining. CMs were fixed with paraformaldehyde and incubated with the appropriate primary antibodies overnight. Then they were incubated with DAPI (nuclear chemical tag) and secondary antibody for an hour each the next day. Markers specific to mature cardiomyocytes were selected;  $\alpha$ -actinin, troponin-T and myosin light chain II as primary antibodies. Secondary antibodies conjugated to a fluorescent tag were then added to the samples. This allowed for observation of the markers by confocal fluorescence microscopy. Immunostaining allows for the observation of specific proteins in a cell culture or tissue sample. The fluorescence can be measured to give quantitative data on the amount of each specific protein which would reflect cardiomyocyte maturity.

## Chapter 3: Determination of materials amenable to 2-photon lithography using a systematic processing approach

### 3.1 Introduction

A set of acrylate monomers selected from the library of available materials at the University of Nottingham were processed by 2PL. Their amenability to 2PL was tested by initial investigation of a visible product using the highest laser power, lowest scanspeed and highest photoinitiator concentration combination. The acrylate materials themselves were chosen based on a combination of previous work that used acrylates for biological application, 2PL or both (explained in the 1.2: Literature Review).

The first selection was based on how well the acrylate monomers could support CM attachment. Following this, different acrylate monomers were tested based on their likelihood to be successfully processed by 2PL. The successfully processed monomers were then tested for their range of working photoinitiator concentrations and upper to lower energy absorption limits. Operating windows for some acrylates were determined and these were used as a reference point for the construction of complex architectures. Structures relevant to CM attachment were fabricated and the limitations of the 2PL technique discussed.

This chapter addresses the initial stages of the doctoral project in which 2PL technology is explored for the utilisation of novel acrylate monomers with possible CM attachment capabilities. The functional working range of the materials and the building of complicated structures is described.

## 3.2 RESULTS

### 3.2.1 Monomer compatibility to 2-photon lithography

The procedure for the selection of monomers compatible to 2-photon lithography was progressive and followed a step-wise fashion. Specifically, methacrylate monomers were initially selected due to their ability to support CMs in previous studies. Their lack of fabrication to 2PL led to selection of monomers with multiple acrylate functional groups. This was followed by selection of co-polymers to test whether small amounts of methacrylate could be included in the monomer mixture. The whole procedure of findings and progression from one set of experiments to the next are explained in detail in this chapter.

The list of monomers tested in the 2-photon system as well as which ones were compatible are outlined in Table 3.1.

**Table 3. 1: List of acrylate monomers tested for their 2-photon compatibility.**

| <b>Monomer Name</b>   | <b>Compatibility to 2PL</b> |
|---|-----------------------------|
| <b>Tetrahydrofurfuryl methacrylate</b>                                  | No                          |
| <b>Isobornyl methacrylate</b>   | No                          |
| <b>Ethoxyethyl methacrylate</b>   | No                          |
| <b>Tricyclodecanedimethanol diacrylate</b>                              | Yes                         |
| <b>Glycerol propoxylate triacrylate</b>                                 | Yes                         |
| <b>Pentaerythritol triacrylate</b>                                      | Yes                         |
| <b>Butanediol diacrylate</b>  | Yes                         |
| <b>Polypropylene glycol diacrylate</b>                                  | Yes                         |
| <b>Hexanediol ethoxylate diacrylate</b>                                 | Yes                         |
| <b>Hexamethylene diacrylate</b>   | Yes                         |
| <b>Trimethylol propane triacrylate</b>                                  | Yes                         |
| <b>Bisphenol A glycerolate diacrylate</b>                               | No                          |
| <b>Zirconium carboxyethyl acrylate</b>                                  | No                          |
| <b>Hexanediol diacrylate:Polypropylene glycol diacrylate</b>            | Yes                         |
| <b>Butanediol diacrylate: Glycerol propoxylate triacrylate</b>          | Yes                         |
| <b>Hexanediol diacrylate: Poly propylene glycol acrylate</b>            | Yes                         |
| <b>Polypropylene glycol diacrylate:Glycerol propoxylate triacrylate</b> | Yes                         |
| <b>Hexanediol diacrylate: Ethoxy ethyl methacrylate</b>                 | No                          |
| <b>Aminopropyl methacrylamide hydrochloride</b>                         | No                          |
| <b>Amino ethyl acrylamide chloride</b>                                  | No                          |
| <b>Amino ethyl methacrylamide hydrochloride</b>                         | No                          |

Table 3.1 is a list of monomers that were tested and which ones were found to be compatible to 2PL. This is a result of sequential series of experiments. This is because the results of initial experiments let to more selective decisions on monomers for the next experiments. The whole working procedure is described in detail in the next sections.



### 3.2.2 Monomer selection and testing amenability to 2-photon lithography

Monomers 14, 15 and 17 were selected for their amenability on the 2-photon system for this PhD thesis project (Table 3.2). None of these polymers have been fabricated by 2PL previously and this technology has great promise for CM response studies as it can fabricate with high resolution. Fine features will enable analysis of CM response to minute topological features that is not possible with other fabrication techniques as easily or as economically. They showed the highest score for cell attachment and cell size as co-polymers however their homopolymer constituents were tested individually as a first investigation to test their amenability on 2-photon system prior to preparing co-polymer formulations (Figure 3.1).

**Table 3. 2: Co-polymers of which their homopolymer constituents were selected for amenability to the 2-photon system in this PhD project.**

| Co-polymer number | Name   |
|-------------------|--|
| 14/17             | Tetrahydrofurfuryl methacrylate/Tert-butylamino-ethyl methacrylate |
| 15/17             | Isobornyl methacrylate/Tert-butylamino-ethyl methacrylate          |
| 3/18              | Hexanediol ethoxylate diacrylate/ Ethoxyethyl methacrylate         |

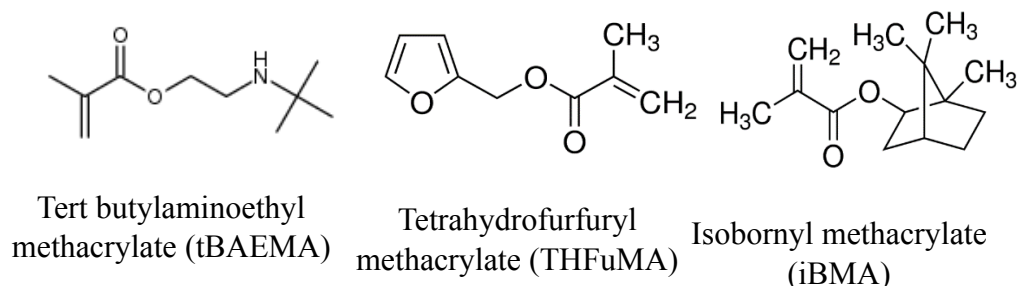


**Figure 3.1: Molecular structures of the 3 methacrylate homopolymers selected for amenability to 2PL.**

The most efficient way to commence testing the individual monomers for amenability was by utilizing the highest laser power and lowest scan speed on the Nanoscribe™ system. This ensured the maximum energy possible was applied to the monomer so that any small amount of fabrication could be observed, no matter how low the reactivity of the monomer. The galvo mode which is the setting used for faster, less precise fabrication allows up to 20,000 µm/s scan speed values and 100% laser power which corresponds to 50 mW. These values were set in Describe command file alongside 5% photoinitiator (Irgacure 369®) concentration (1000 mg/ml) which is a value that was found to cross the dissolving threshold of Irgacure 369®. If no fabrication was visible under these conditions, the monomer was classified as not amenable to 2-photon lithography. If a structure could be fabricated, whether with or without defects, the PI concentration was lowered in 1% increments down to 1% photoinitiator concentration (1mg/ml). If fabrication was still possible at 1% Irgacure 369®, then the laser power was gradually lowered in 20% increments to observe any effects on fabrication.

No fabrication was observed (either before or after development with PGMEA), with tert-butylamino ethyl methacrylate (tBAEMA), isobornyl methacrylate (iBMA) or furfuryl methacrylate (THFuMA) at 10% photo initiator concentration and the highest energy value applied (Figure 3.2). APMAM.c, AEMA.c and AEMAM.c showed no visible fabrication by 2PL either (Figure 3.2).

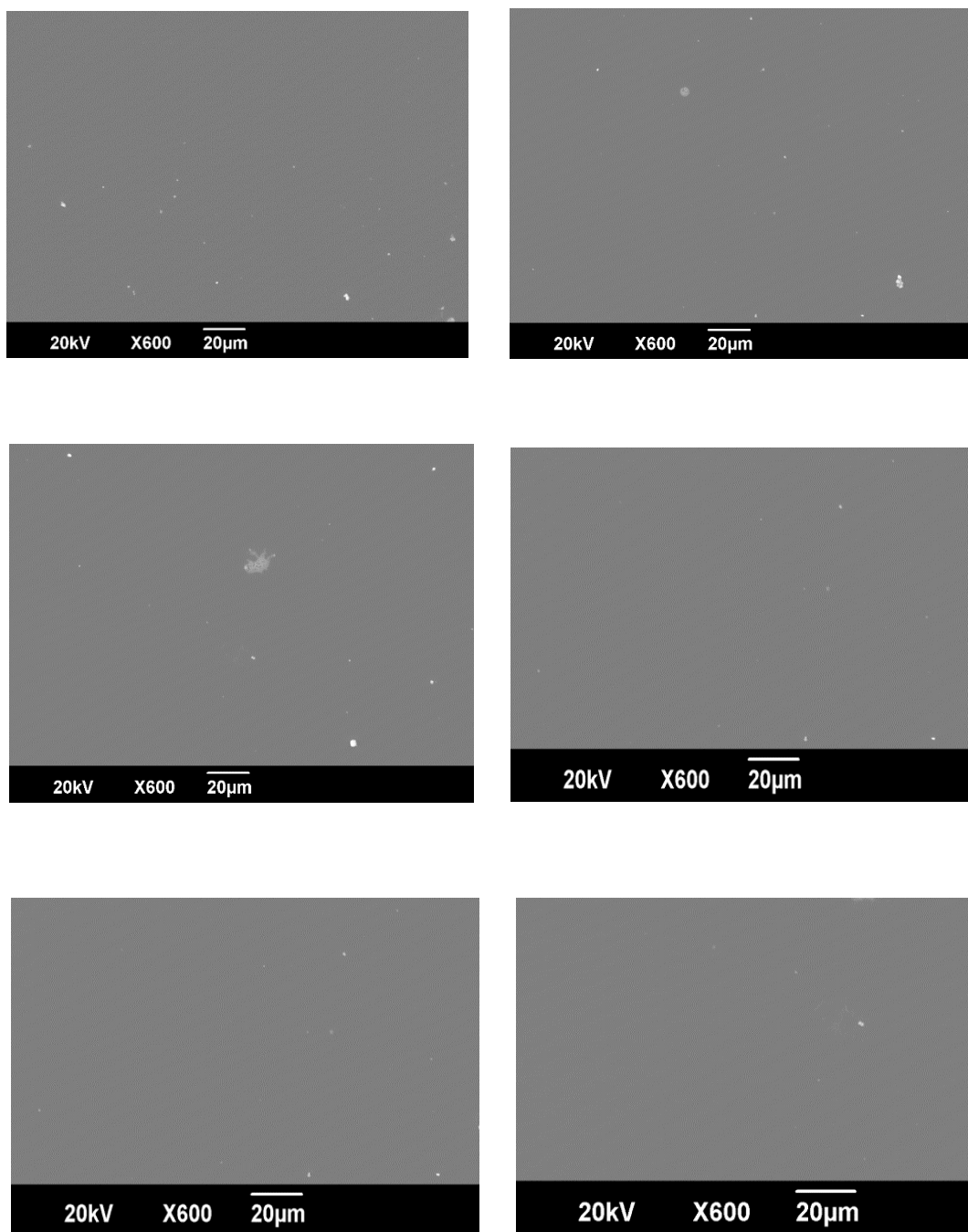


**Figure 3.2: SEM images of methacrylate formulations a) tertbutylamino-ethylmethacrylate b) furfuryl methacrylate c) isobornyl methacrylate, APMAM.c., AEMA.c and AEMAM.c polymers.**

The lack of processing was attributed to the low polymerisation rate of methacrylates (Jansen et al., 2003). Even though these materials were easily processed by UV polymerisation (Patel et al., 2015), the efficiency of any given photo initiator during two-photon polymerisation will be less compared to UV polymerisation. This is because two photons need to be absorbed almost

simultaneously (in a matter of femtoseconds) for two-photon polymerisation to occur. The reaction requires the photo initiators to have a large two-photon absorption cross-section or to spend a longer period in the excited triplet state, in other words a low fluorescence quantum yield (Denning et al.) (Baldacchini et al., 2004). The lack of fabrication of these 6 polymers was attributed to the presence of the methyl group in the reactive region of the molecule, i.e. adjacent to the vinyl group. The proposed electronic effects that the amide group could provide were not enough to counteract the steric hindrance effect of the methyl group in the methacrylamide monomers. Monomers amenable to 2PL were required for progression to the next steps in this doctoral project. This is why the methacrylamide monomers were not used after this point. This study faced with a new challenge; the need for a material that can be processed by two-photon lithography but that can also support CM attachment and enhance CM maturity. Keeping these in mind, monomers were then selected based on their multi-functionality (di-acrylate or tri-acrylates) due to their higher rate of polymerization (Jansen et al., 2003) while still maintaining the highest cell density and area possible during this selection. After confirmation by literature review on the reactivity of acrylates versus methacrylates (Jansen et al., 2003), various available di- and triacrylates that previous showed CM attachment (Patel, 2015 #44) were selected for processing by 2PL in this doctoral project.

Another study showed a range of synthetic polymers tested for induced pluripotent stem cell (iPSC)-derived CMs using the UV-polymerization microarray pin-printing method (courtesy of Laurence Burroughs and Jordan Thorpe). Only specific polymers showed significant CM attachment in their study which consisted of a methacrylamide salts and multi-functional acrylates. However, only multi-functional acrylates Tricyclodecanedimethanol diacrylate (TCDMDA), Pentaerythritol triacrylate (PETrA), Zirconium carboxy ethyl acrylate (ZrCEA) were selected from the list of polymers studied as it was concluded that polymers containing methyl groups in their reactive centre are not amenable to 2PL.

Figures 3.4a and 3.4b show the multi-functional acrylates selected for 2PL. TCDMDA, Butanediol diacrylate (BDDA), HEODA, Polypropylene glycol

diacrylate (pPGDA) and HMDA are all diacrylates. GPOTA, Trimethylolpropane triacrylate (TMPTA) PETrA are triacrylates. ZrCEA is a tetra acrylate salt and was selected due to its ability to form electrostatic attractions with multiple acrylate molecules. The central positively charged Zinc ion is devoid of 4 electrons that bonds with 4 negatively charged acrylate anion molecules (Figure 3.4a).

One other diacrylate illustrated in Figure 3.3 named Bisphenol A polyglycerolate diacrylate (BPAPGDA) was chosen however was not taken forward for 2PL studies as this diacrylate was found to be very viscous. The viscosity of BPAPGDA prevented the dissolution of PI I369.

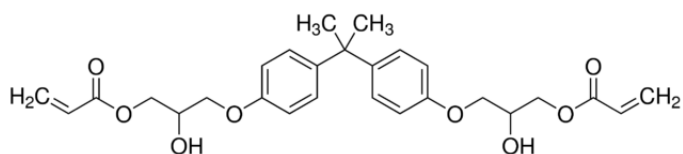


**Figure 3.3: Molecular structure of Bisphenol A glycerolate diacrylate (BPAPGDA).**

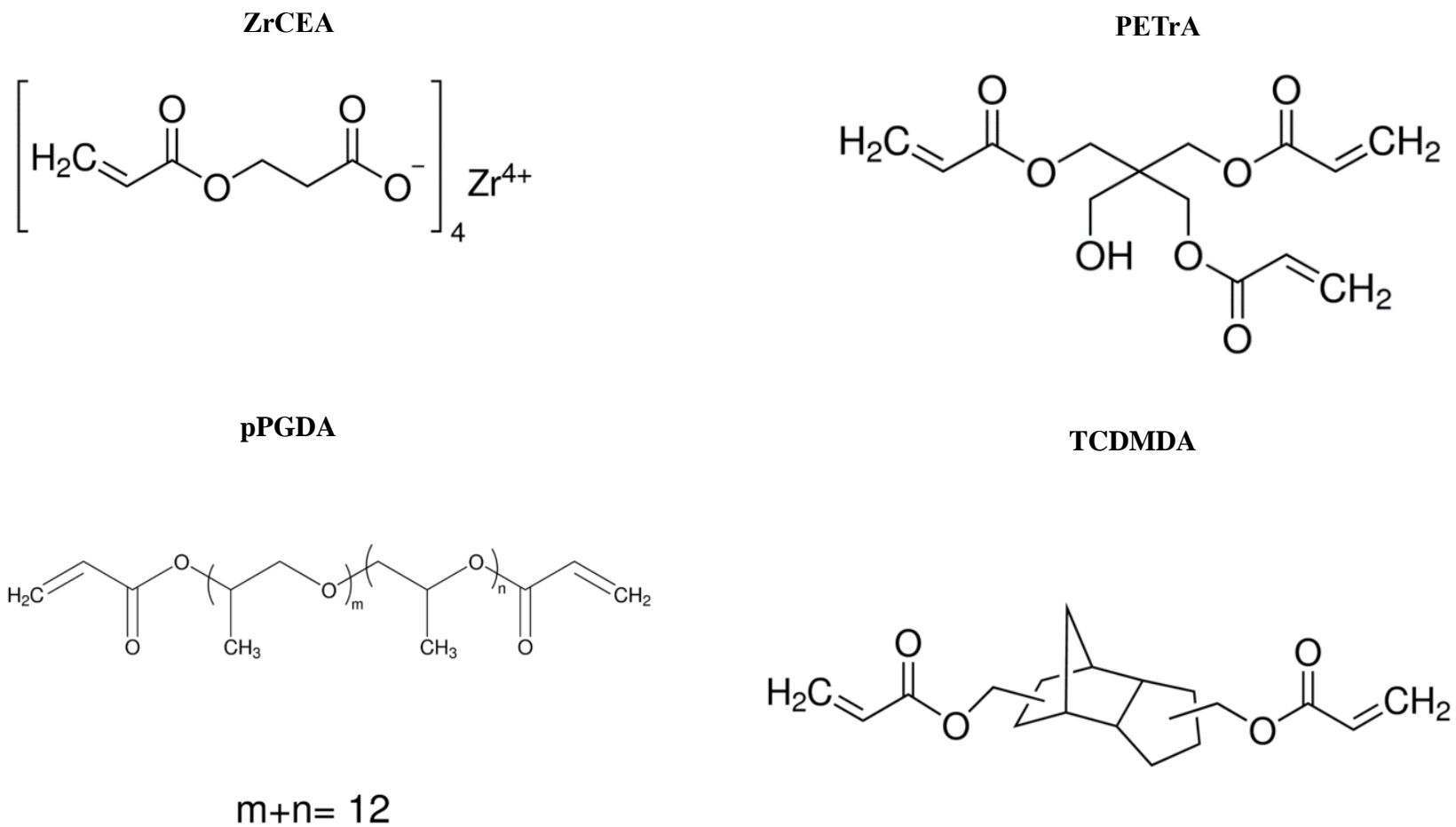
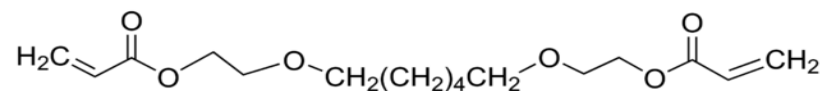
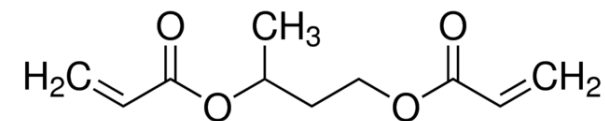


**Figure 3.4a: Molecular structures of multi-functional acrylate monomers that were selected for 2PL processing.**

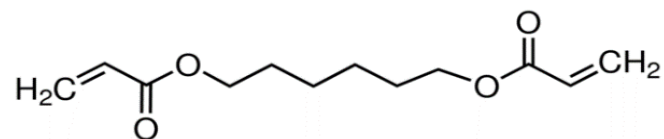
**HEODA**



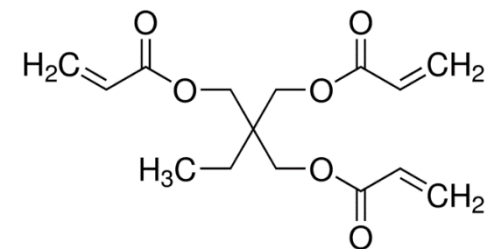
**BDDA**



**HMDA**



**TMPTA**



**GPOTA**

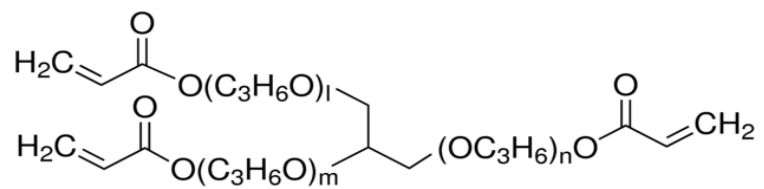


**Figure 3.4b: Molecular structures of multi-functional acrylate monomers that were selected for 2PL processing.**

8 out of 9 of the multi-functional monomers selected for processing were successfully polymerised in the two-photon system (Figure 3.5). 5 were diacrylates (HEODA, BDDA, pPGDA, HMDA and TCDMDA) and 3 were triacrylates (GPOTA, TMPTA and PETrA).

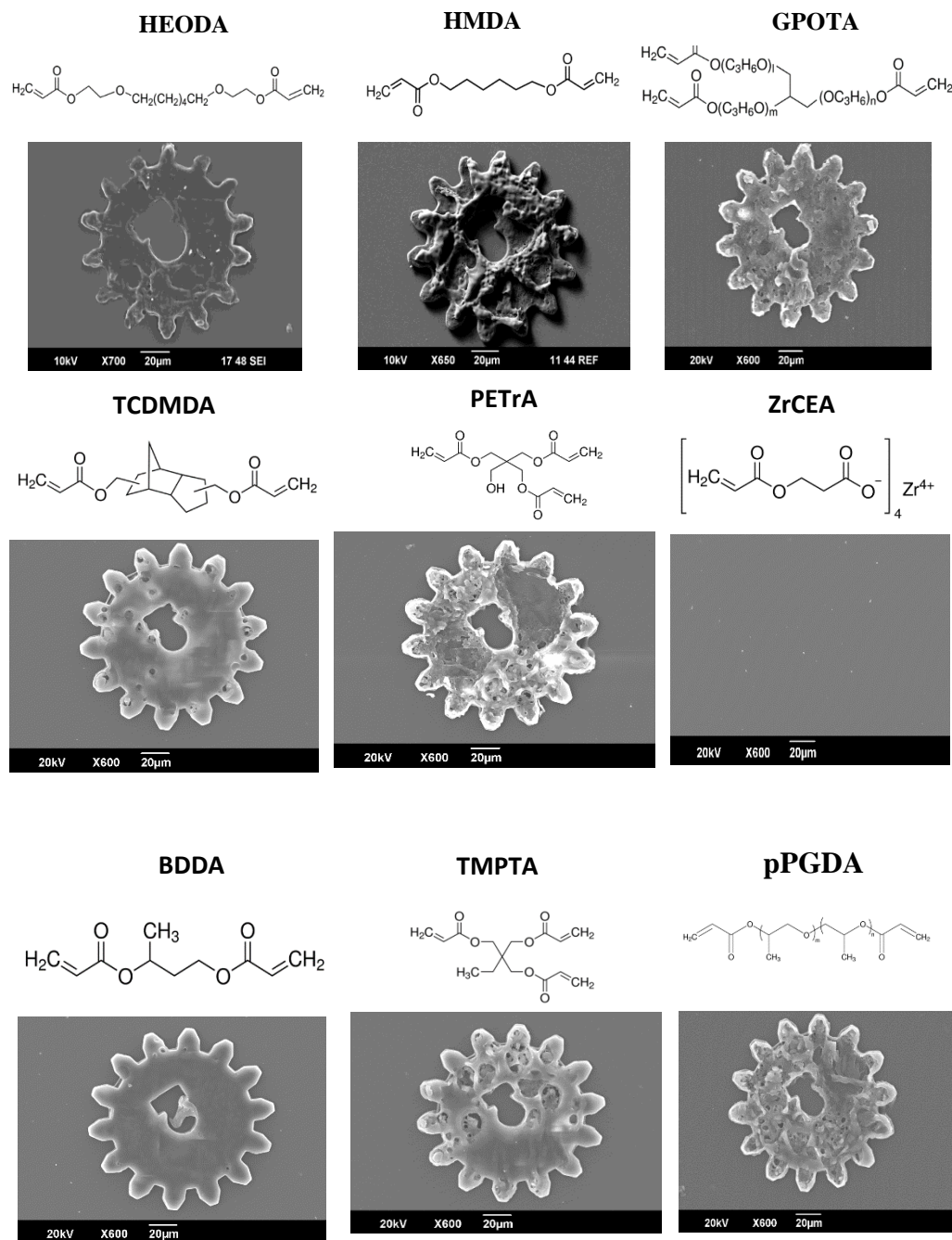


**Figure 3.5: Molecular structures and corresponding SEM images taken using highest laser power and low scanspeed at 5% photoinitiator concentration of from left to right: HEODA, HMDA and GPOTA, TCDMDA, PETrA and ZrCEA (centre), BDDA and TMPTA (bottom).**



The structures fabricated at high energy (50mW laser power and 10,000  $\mu\text{m/s}$ ) and 10% PI concentration showed many defects illustrated by surface damage (Figure 3.5). This means all 8 polymers are amenable to 2-photon lithography.

The reason for methacrylates not being processed by 2PL and multi-functional acrylates showing positive results was attributed to their chemical structure. Methacrylates have a methyl group in their reactive acrylate functional group which causes steric hindrance during the polymerisation reaction. The photoinitiator molecule trying to attack the reactive carbon atom in the reactive centre is hindered by the methyl group. Multi-functional acrylates do not have methyl groups to cause steric hindrance and they contain at least 2 acrylate functional groups. This means they have a higher rate of polymerization compared to methacrylate monomers.

It was concluded that HEODA, HMDA, BDDA, pPGDA, TMPTA, GPOTA, TCDMDA and PETrA were amenable to 2PL. It was also concluded that methacrylate polymers are very unlikely to be amenable to 2PL as verified by the 3 methacrylates already processed (Figure 3.2).

Methacrylamide salts APMAM.c, AEMA.c and the lack of fabrication of these 3 polymers was attributed to the presence of the methyl group in the reactive region of the molecule, i.e. adjacent to the vinyl group. The proposed electronic effects that the amide group could provide were not enough to counteract the steric hindrance effect of the methyl group AEMAM.c were tested for their amenability to 2PL as APMAM.c had previously shown CM attachment (courtesy of Laurence Burroughs, University of Nottingham). It was also thought the amide group may help in the initiation of the polymerisation reaction to make the monomer more amenable to 2PL.

The lack of fabrication of these 3 polymers was attributed to the presence of the methyl group in the reactive region of the molecule, i.e. adjacent to the vinyl group (Figure 3.6). The proposed electronic effects that the amide group could provide were not enough to counteract the steric hindrance effect of the methyl group.

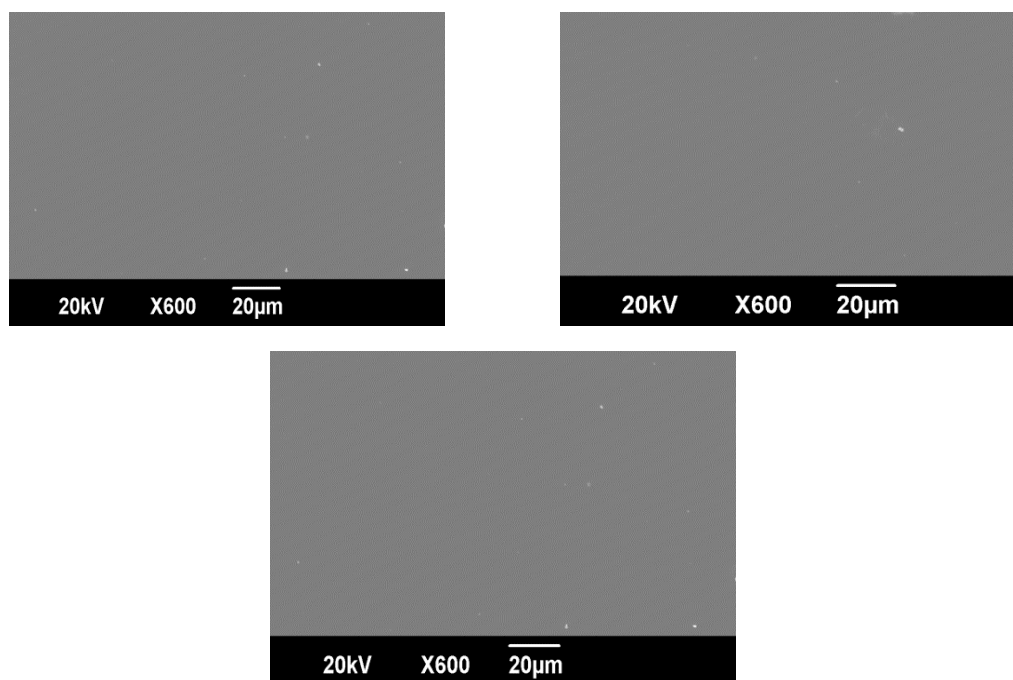


**Figure 3.6: SEM images of the 3 methacrylamide salts APMAM.c, AEMA.c, and AEMAM.c that were tested for their amenability to 2PL. No fabrication was observed for any of the monomers.**

Co-polymers were selected based on their ability to support both CM attachment and maturity enhancement (Patel et al., 2015). As stated previously, the homopolymers processed successfully by two-photon lithography were considered a priority when selecting co-polymer formulations (Table 3.3). GPOTA and HEODA were two of the monomers successfully processed by the 2-photon system therefore co-polymer formulations containing GPOTA or HEODA were selected. Co-polymers containing homopolymer components of either HEODA, HMDA or GPOTA were prepared at a 70/30 ratio to observe whether they could be amenable to 2PL.

**Table 3. 3: Top 10 co-polymer combinations that scored highest for cell density and cell area in serum-free conditions in the Patel study. The writing in bold indicates co-polymers selected for processing ability in the 2-photon system.**

|           | Co-Polymer         | Cell Density    | Co-Polymer          | Cell Area ( $\mu\text{m}^2$ ) |
|-----------|--------------------|-----------------|---------------------|-------------------------------|
| <b>1</b>  | <b>EGDMA:GPOTA</b> | 0.53 $\pm$ 0.14 | MAEA: HTFDA         | 1089 $\pm$ 150                |
| <b>2</b>  | <b>OFPMA:GPOTA</b> | 0.51 $\pm$ 0.20 | <b>BnMA:GPOTA</b>   | 1043 $\pm$ 257                |
| <b>3</b>  | OFPMA:EEMA         | 0.50 $\pm$ 0.09 | <b>HEODA: pPGDA</b> | 1039 $\pm$ 510                |
| <b>4</b>  | <b>BnMA:HEODA</b>  | 0.49 $\pm$ 0.13 | F7BA: THFuA         | 1035 $\pm$ 469                |
| <b>5</b>  | BDDA:OFPMA         | 0.48 $\pm$ 0.05 | F7BA: pPGDA         | 1022 $\pm$ 275                |
| <b>6</b>  | THFuA: EGDMA       | 0.47 $\pm$ 0.10 | pPGDA:BnMA          | 999 $\pm$ 334                 |
| <b>7</b>  | THFuA:BDDA         | 0.46 $\pm$ 0.18 | BnMA: THFuA         | 975 $\pm$ 72                  |
| <b>8</b>  | THFuA: pPGDA       | 0.45 $\pm$ 0.08 | BnMA: tBAEMA        | 914 $\pm$ 67                  |
| <b>9</b>  | <b>HEODA:EEMA</b>  | 0.44 $\pm$ 0.22 | <b>HEODA:EEMA</b>   | 899 $\pm$ 100                 |
| <b>10</b> | LMA:BDDA           | 0.44 $\pm$ 0.18 | pPGDA: THFuA        | 883 $\pm$ 318                 |

The number of materials available for processing by 2PL were largely narrowed down following the discovery that monoacrylates or multi-functional acrylates are likely to be processed on the system.

Co-polymers comprising one of the 2-photon amenable multi-functional acrylates were tested for amenability to the 2-photon system. Only 1 out of the 7 co-polymers tested could be fabricated by 2PL using 10% I369 and a 70:30 major to minor monomer composition. This co-polymer, named hexanediol ethoxylate diacrylate:polypropylene glycol diacrylate (HEODA:PPGDA) has HEODA as its major monomer and pPGDA as the minor monomer. The major monomer HEODA is a diacrylate and the minor monomer is also a diacrylate. The other 6-copolymers did not have this polymer composition.

HEODA:pPGDA co-polymer formulation was processed successfully by 2PL as shown in Figure 3.7. The structure appears slightly damaged at the highest laser power of 50 mW and 10,000  $\mu\text{m/s}$ .

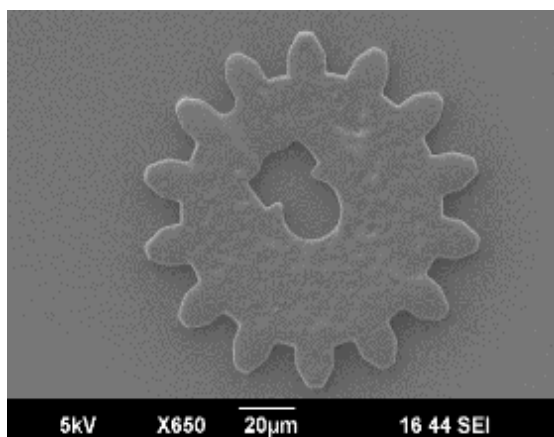


**Figure 3.7: SEM image of gear design taken using highest laser power and low scanspeed at 5% photoinitiator concentration using the HEODA:pPGDA co-polymer formulation.**

The only other co-polymer containing HEODA as its major monomer was HEODA:EEMA but in this case the minor monomer EEMA was a methacrylate. The co-polymer composition of HEODA:EEMA shown in Table 3.4 was varied by increasing the percentage of HEODA to observe whether the new formulation would be amenable to 2PL.

**Table 3. 4: List of HEODA:EEMA co-polymer formulations tested on the 2-photon system.**

| Co-polymer composition ratio<br>(HEODA:EEMA) | Amenability to 2PL |
|--|--------------------|
| <b>70:30</b>                                 | No                 |
| <b>80:20</b>                                 | No                 |
| <b>90:10</b>                                 | No                 |
| <b>95:5</b>                                  | No                 |
| <b>98:2</b>                                  | No                 |
| <b>99:1</b>                                  | <b>Yes</b>         |

Figure 3.8 shows that no fabrication was observed using the co-polymer compositions of 70:30, 80:20, 90:10, 95:5 and 98:2. The final co-polymer composition of 99:1 showed fabrication of the gear design with some damage. A 99:1 composition is invalid in terms of consideration of this formulation as a co-polymer since only 1% is EEMA. The effect of the methacrylate EEMA is negligible in this case. HEODA:EEMA co-polymer was studied to observe the minimum amount of the multi-functional acrylate required to observe fabrication on the 2-photon system so that other co-polymer combinations could be prepared for 2PL testing. Since this co-polymer is not amenable to 2PL, other co-polymers containing only multi-functional acrylates were prepared and tested for 2PL.

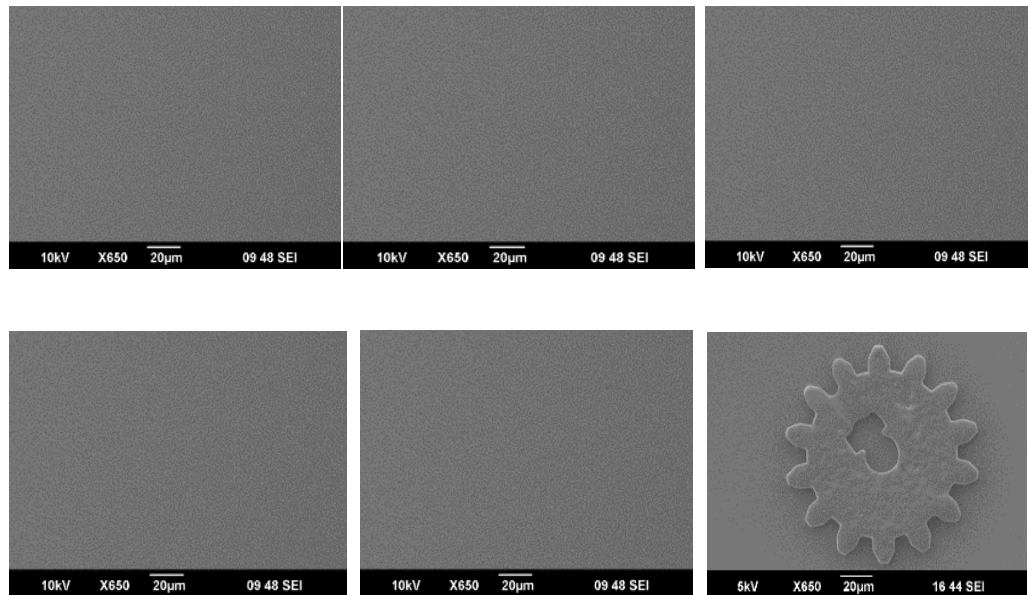


**Figure 3.8: SEM images of gear designs using 5% PI concentration and the co-polymer compositions in the order outlined in Table 3.4 with the first image being 70:30 ratio and the final image being 99:1 ratio.**

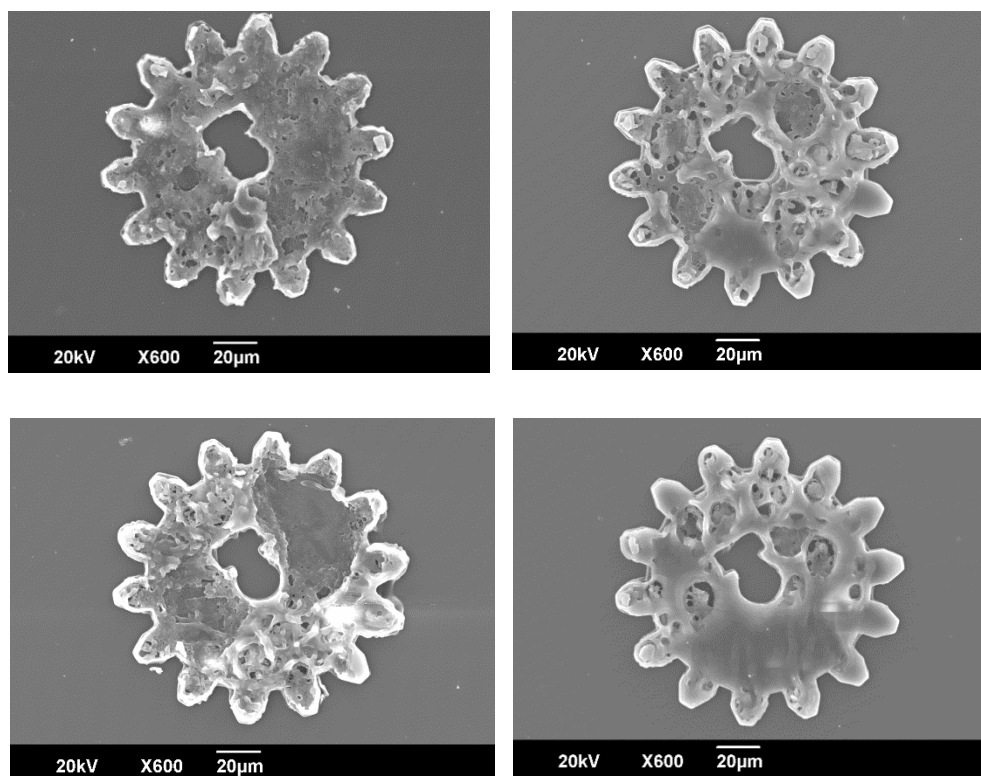
Following this finding, other co-polymers containing a diacrylate or triacrylate as the major and minor monomers were selected for processing by 2PL (Table 3.5).

**Table 3. 5: Co-polymer formulations prepared containing at least one multi-functional acrylate.**

| <b>Co-polymer<sup>a</sup></b> | <b>Amenability to 2PL</b> |
|-------------------------------|---------------------------|
| <b>HEODA:PPGDA</b>            | Yes                       |
| <b>BDDA:GPOTA</b>             | Yes                       |
| <b>HEODA:PPGA</b>             | Yes                       |
| <b>PPGDA:GPOTA</b>            | Yes                       |
| <b>HEODA:EEMA</b>             | No                        |

**a: SEM images of the results of the 4 successfully processed co-polymers are shown in Figure 3.10.**

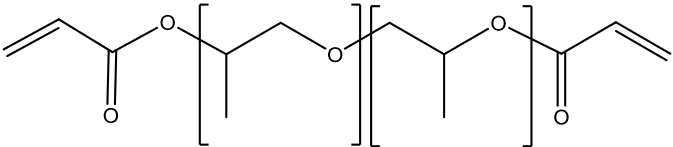
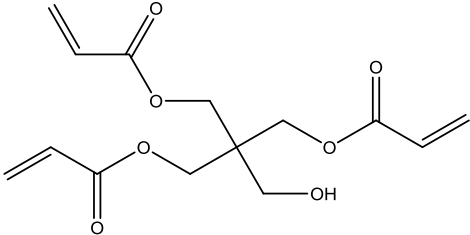
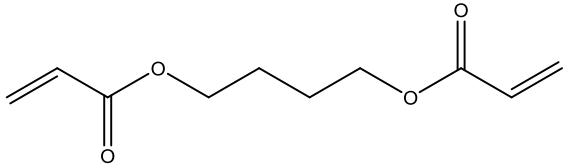
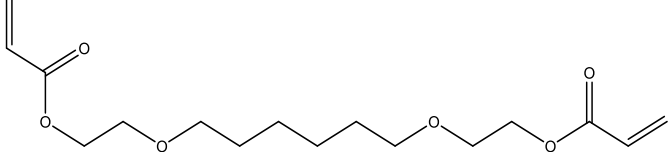
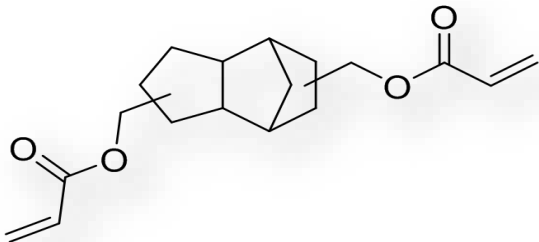
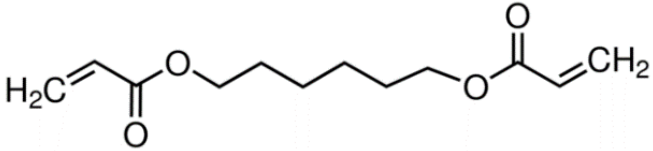
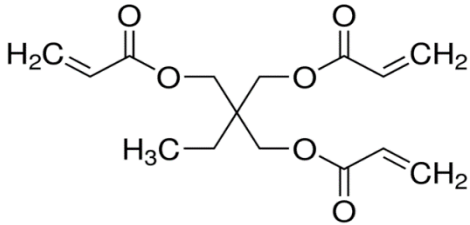
The 4 co-polymers processed by 2PL were HEODA:PPGDA, PPGDA:GPOTA, HEODA:PPGA and BDDA:GPOTA. All were processed and appeared damaged at a 70:30 ratio of major to minor monomer respectively with a 5% PI concentration as illustrated in Figure 3.9.



**Figure 3.9: SEM image taken using highest laser power and low scanspeed at 5% photoinitiator concentration for HEODA:PPGDA, PPGDA:GPOTA, HEODA:PPGA and BDDA:GPOTA co-polymer formulations.**

All of the multi-functional acrylates successfully processed by 2PL are shown in Table 3.6. These multi-functional acrylates were processed at a high PI concentration of 5% and the highest laser power and scanspeed parameter combination. Some photo initiators are cytotoxic, including I369. This should be addressed by lowering the PI concentration to 0.5-1% to percent cytotoxicity. Therefore a few of the polymers in Table 3.6 were selected to identify the optimal PI concentration at which they could be fabricated in combination with the laser power and scanspeed values they worked best at.

**Table 3. 6: List of monomers amenable to 2PL and that were previously shown to support CM attachment. The most suitable candidate monomers for the purposes of this project.**

| Acronym | Chemical Structure   |
|---------|--|
| pPGDA   |    |
| PETrA   |    |
| BDDA    |    |
| HEODA   |  |
| TCDMDA  |  |
| HMDA    |  |
| TMPTA   |  |



### 3.2.2 Operating window determination for 2-photon amenable homopolymers

#### *3.2.2.1 Operating window determination using the cogwheel design*

The multi-functional acrylates processed by 2PL were required to be assessed for their optimal fabrication parameters. GPOTA was selected as the first homopolymer for 2PL fabrication experiments.

Structures exhibited significantly high damage from 60pJ to 37.5pJ showing holes and defects where microexplosions occurred (Figure 3.10). Microexplosions happen when the laser power is high and the scan speed is low, resulting in high energy at each focal point during manufacturing. If the energy of a photon is equal to the difference between the resting state and excited state of the photo initiator, then it is absorbed by the photo initiator to form free radicals, some will go into actually activating monomers to polymerise and build the structure and the remainder will dissipate as thermal energy. If the energy, hence the photon density at each focal point is very high, it will activate many photo initiator molecules which will activate many monomers to initiate polymerisation however some photo initiator molecules will release thermal energy instead of forming a free radical. High energy will mean more photo initiator molecules will end up releasing thermal energy, leading to the microexplosions and damage.

Glycerol propoxylate triacrylate homopolymer can be processed from a maximum energy value of 24pJ to a minimum energy value of 3.6pJ (Figure 3.11). Below 3.6pJ, the structures start to appear incomplete. Specifically, the layers are not processed successfully and the teeth shrink at 2.4pJ. At 1.2pJ no structure is present, illustrating the lack of energy for polymerisation to occur in order to build a structure.

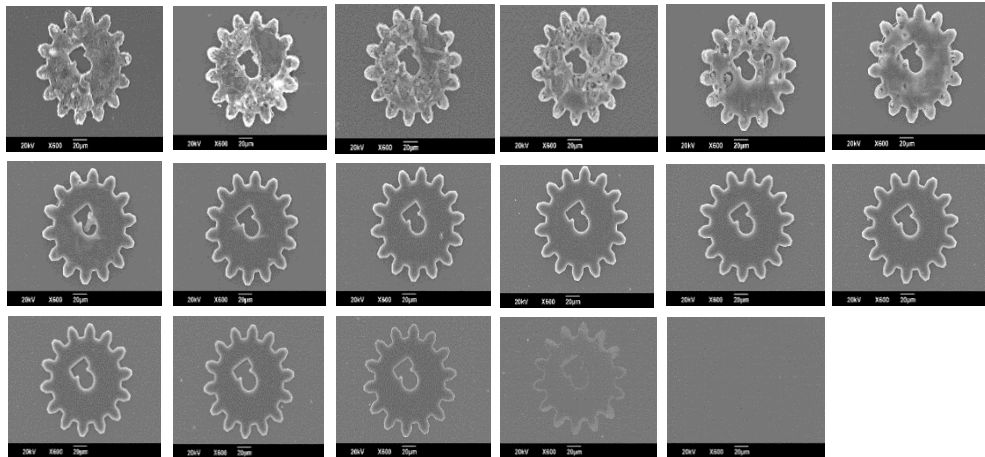


**Figure 3.10: SEM images of fabricated gear structures at 3% I369 concentration. The energy values utilised were as per protocol in the Methods section, Table 5.**

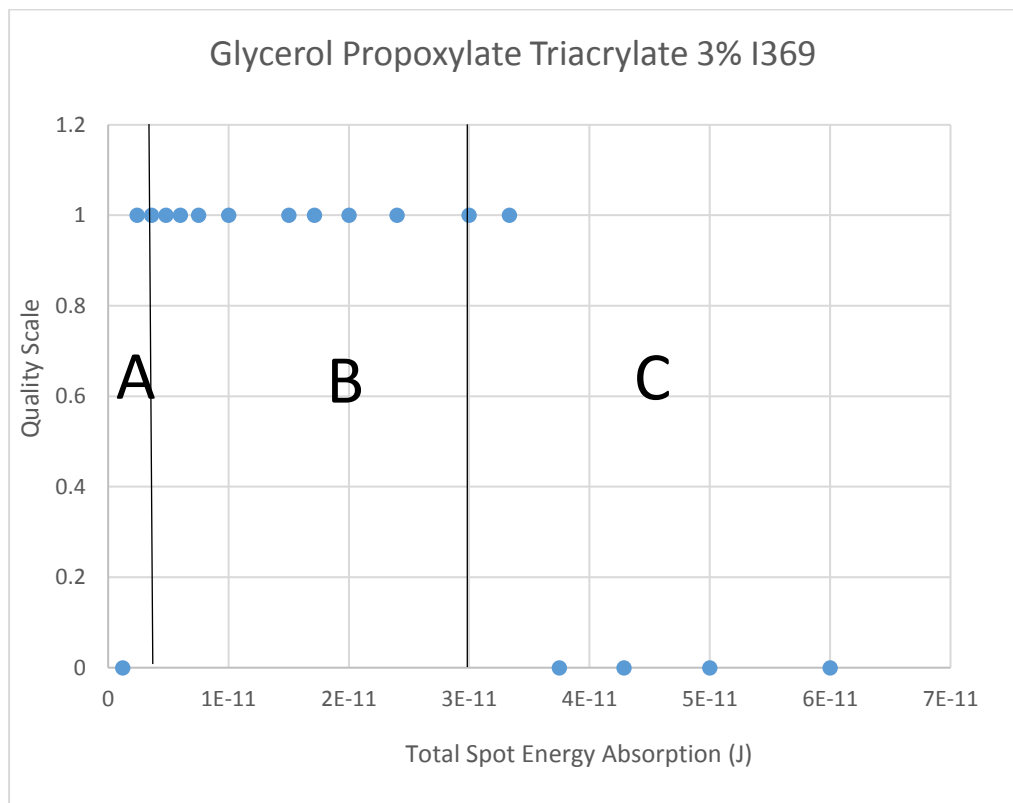


**Figure 3.11: 1st round of processing for GPT with zones A, B and C and 1 or 0 scores assigned according the quality scale.**

The lines bordering zone B are Emax (line between zone B and zone C) and Emin (line between zone A and zone B) (Figure 3.11). Emax is the maximum energy that can be applied to produce a structure without any visible damage and Emin is the minimum energy required to produce a complete structure without any missing parts. The operating window (the range between Emax and Emin) is slightly larger in the 1<sup>st</sup> round of processing (Figure 3.11), compared to the 2<sup>nd</sup> and 3<sup>rd</sup> rounds of processing (Figures 3.12 and 3.13). This can be attributed to experimental error and the average was calculated as n=3 repeats and the values plotted (Figure 3.14).

Nine complete structures can be fabricated using 3% glycerol propoxylate triacrylate (Figure 3.10). This demonstrates the wide operating window of GPT with 3% I369. A wide operating window is desired so that there is the largest room possible for fabrication error. This ensures that fabricated structures do not fall within zone A, where they could be fabricated with incomplete parts or in zone C where they could be highly damaged due to microexplosions.

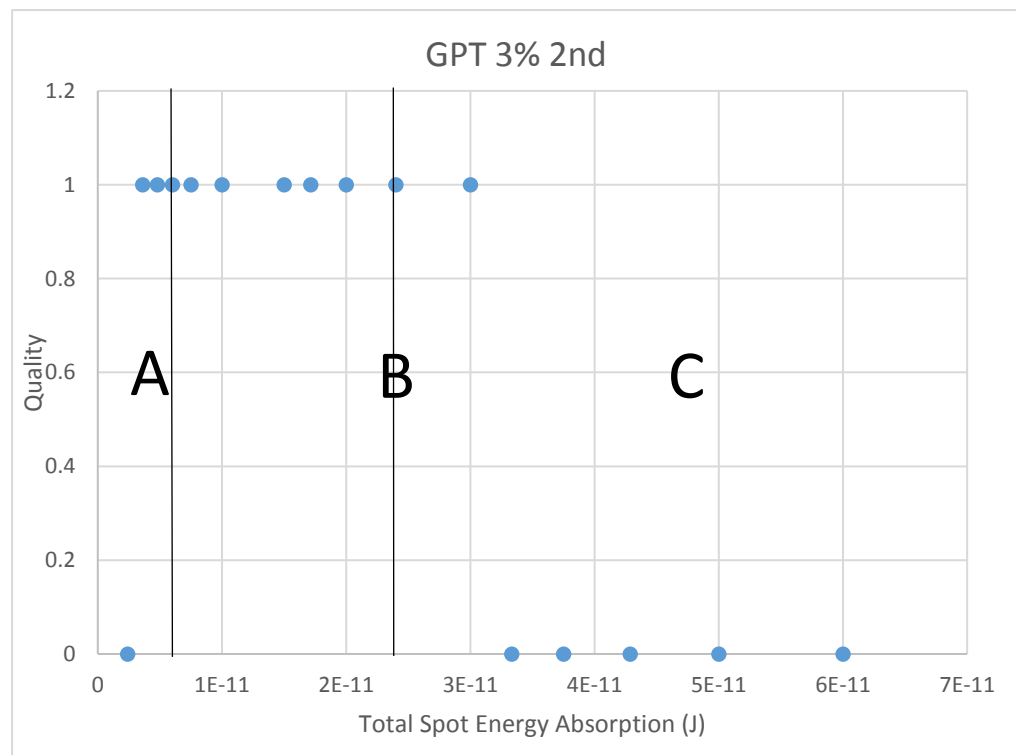


**Figure 3.12: 2nd round of processing for GPT with zones A, B and C and 1 or 0 scores assigned according the quality scale.**

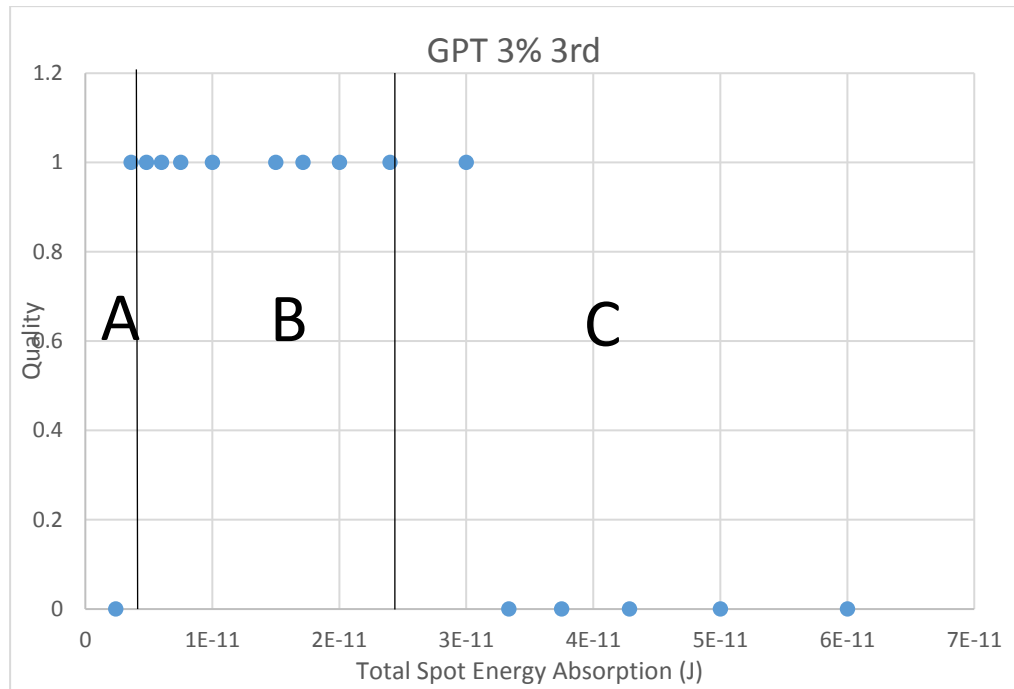


**Figure 3.13: 3rd round of processing for GPT with zones A, B and C and 1 or 0 scores assigned according the quality scale.**

The 2<sup>nd</sup> and 3<sup>rd</sup> fabrication sessions for GPOTA showed the same, if not similar results in regards to the operating window. This demonstrates the reproducibility of the information for the GPOTA operating window.

The average Emax and Emin was calculated using the energy values from the 1<sup>st</sup>, 2<sup>nd</sup> and 3<sup>rd</sup> rounds of processing at each photo initiator concentration and these were plotted as a trend of how Emax and Emin differ according to photo initiator concentration (Table 3.7, Figures 3.11-3.13).

**Table 3. 7: List of photo initiator concentrations tested with corresponding average Emax and Emin values.**

| <i>Photoinitiator<br/>Concentration<br/>(%)</i> | <b>Average Emax<br/>(J)</b> | <b>Average Emin<br/>(J)</b> |
|---|-----------------------------|-----------------------------|
| 1   | 1.16667E-11                 | 9.04762E-12                 |
| 2   | 2.33E-11                    | 6E-12                       |
| 3   | 3E-11                       | 4.8E-12                     |
| 4   | 2.6E-11                     | 4E-12                       |
| 5   | 2.4E-11                     | 2.8E-12                     |
| 6   | 2.16667E-11                 | 2E-12                       |
| 8   | 1.64286E-11                 | 3.2E-12                     |
| 10  | 1.5E-11                     | 3.3E-12                     |

\

To better observe the trend between photo initiator concentration and the operating window the data (Table 3.7) was plotted to identify the largest operating window for glycerol propoxylate triacrylate (Figure 3.14).

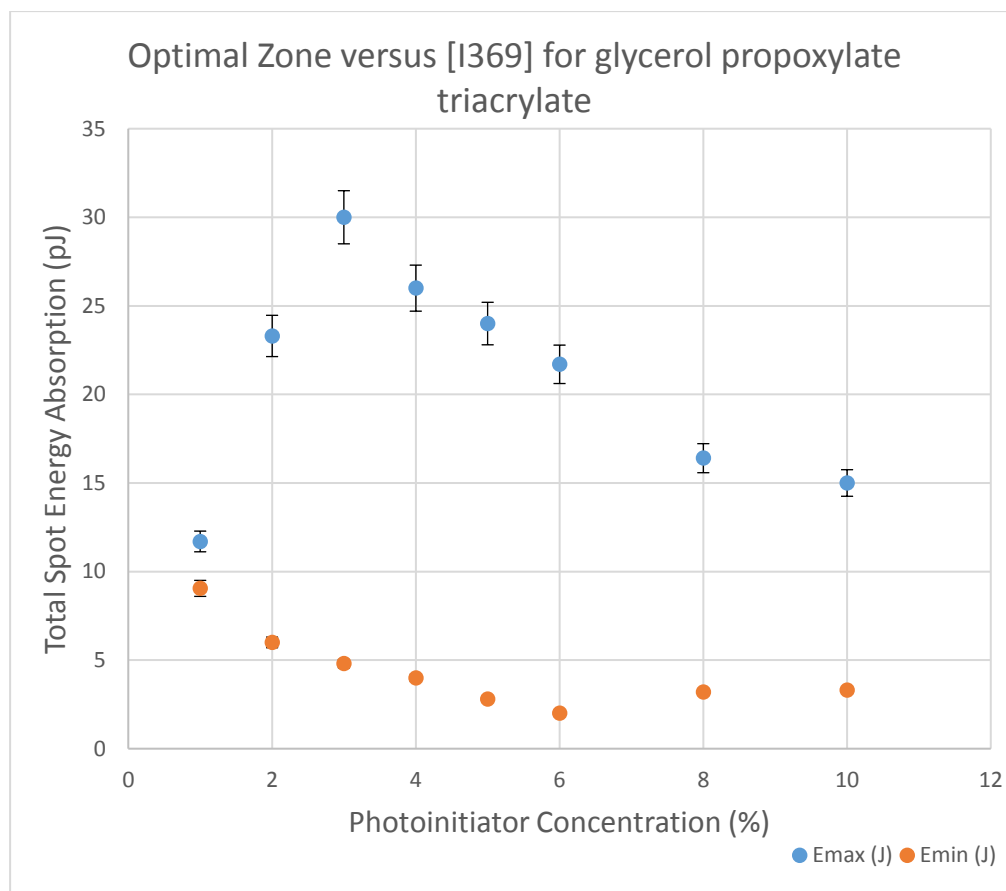


**Figure 3.14: Trend of how Emax and Emin vary according to photo initiator concentration in GPOTA.**

As the photo initiator concentration increases, Emax also increases until 3% photo initiator concentration, which is the peak. At low photo initiator concentrations, the amount of photo initiator molecules is low which means there is less competition between polymerisation and side-reactions such as oxygen quenching and monomer quenching. Less energy is required to complete polymerization and cause damage. As the photo initiator concentration increases, the higher number of photo initiator molecules in the reaction mixture begin to compete with each other for polymerisation. This is why a higher energy input is required to observe damage to the structure. Emin decreases due to increasing photo initiator concentration which means complete structures are

formed at lower energy values. This is why the operating window is small at low photo initiator concentrations and increases until the optimal photo initiator concentration, which is 3% in this case.

After 3% photo initiator concentration  $E_{max}$  starts to decrease as less energy is required to cause microexplosions and damage as structures are being processed. This is due to the fact that more photo initiator molecules are available at the higher photo initiator concentrations which mean less energy is required to initiate polymerisation and cause damage. This outweighs the competition between polymerisation and side reactions as observed for the low (1-3%) photo initiator concentrations.  $E_{min}$  also increases slightly after 6% photo initiator concentration. This may be due to their need of higher energy to form a complete structure as there are a higher number of photo initiator molecules to initiate the polymerisation. However, this can be counter-productive if the amounts are too high, as the large amount of activated monomers can combine to terminate the reaction (Carragher, 2007).

Control formulations for glycerol propoxylate triacrylate gave rise to structures albeit with a much narrower processing window (Figure 3.15). No complete structures were fabricated. All structures were either damaged or incomplete (Figure 3.15). This was expected as acrylates can undergo photo initiator-free UV curing (Bauer et al., 2014). This occurs due to some monomers in the formulation undergoing self-initiation from high-energy photons (Bauer et al., 2014), as may be the case here. Another possibility could be thermal polymerisation which also induces self-initiation of monomers (Grady et al., 2002, Srinivasan et al., 2010) (Grady et al.). The build-up of energy from the laser is also dissipated as heat which could lead to spontaneous thermal polymerisation of the acrylate monomers (Baldacchini et al., 2004).

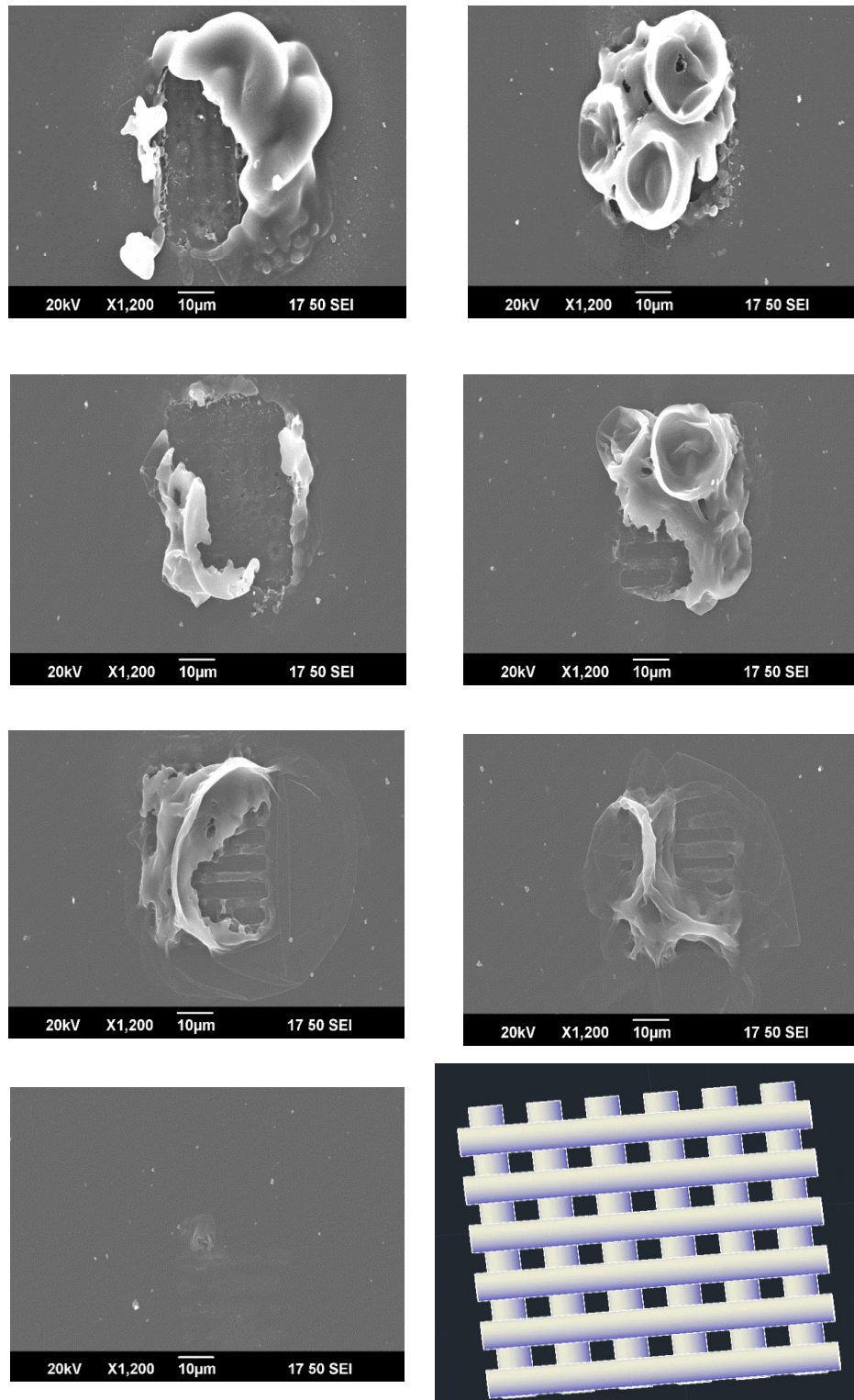


**Figure 3.15: Structures processed using control formulations which consisted of glycerol propoxylate triacrylate only, without photo initiator using the woodpile design. (Energy absorption from left to right and down (pJ), 60, 50, 42.9, 37.5, 33.3, 30, 24, 20, 17.1). Bottom right corner: Woodpile structure design on AutoCAD.**



The operating window for HMDA was determined in the same way as for GPOTA. Figure 3.16 shows the SEM image of all gear structures fabricated at a series of laser power values from the highest on the left side to the lowest on the right-hand side. Structures appear damaged on the left with gradually decreasing defects towards the middle culminating with an incomplete structure on the right-hand side. The final energy value of 3.6 pJ did not show any fabrication which was attempted next to the incomplete structure on the right-hand side. This trend is expected for the same reasons as outlined for the GPOTA fabrication findings which is also outlined on the next page.

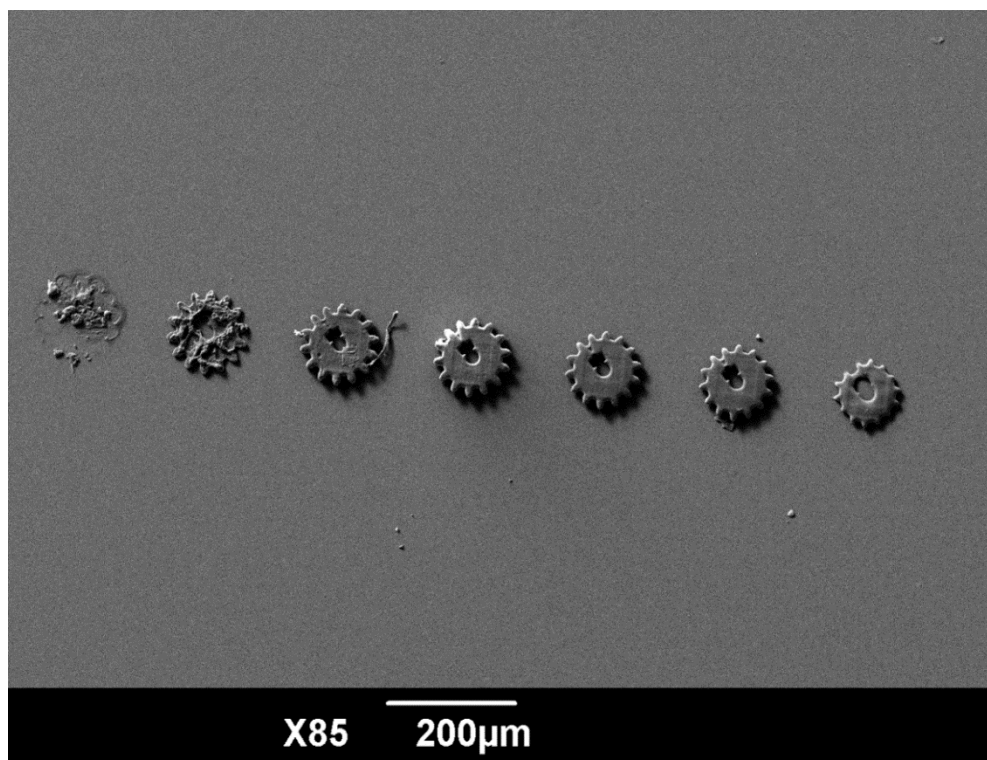


**Figure 3.16: SEM image of HMDA structures from left to right: Highest focal spot energy absorption at 60 pJ to lowest at 3.6 pJ with a constant scanspeed of 1000  $\mu\text{m/s}$ .**

The first two structures fabricated with the energy absorption equivalent of 60 and 30 pJ display a lot of damage due to the microexplosions during fabrication (Figure 3.17). The structures fabricated at 15 and 10 pJ display a little damage as seen by the small dents and holes. The structures fabricated with 7.5 pJ and 6 pJ energy values show the best quality as evidenced by a structure most similar to the AutoCAD design and the last at 4.8 pJ was an incomplete structure as evidenced by a bigger keyhole in the middle and incomplete teeth. Even though fabrication was performed for the lower focal spot energy absorption values (3.6 pJ), nothing was visible after the gear on the far right which was fabricated at 4.8 pJ. Therefore, the minimum energy value at which a gear structure can be fabricated using HMDA at 5% PI concentration is approximately at 4.8 pJ.

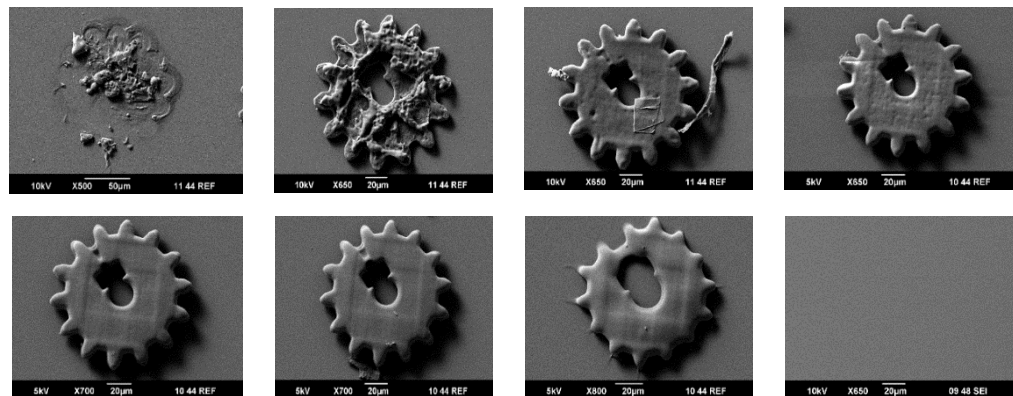


**Figure 3.17: SEM images at higher magnification of the same structures from Figure 3.19. Left to right: 60, 30, 15, 10, 7.5, 6, 4.8, and 3.6 pJ.**

The operating window of HMDA at the PI concentrations varied significantly to the operating window of GPOTA at these same PI concentrations (Figure 3.21). No fabrication was observed until 5% PI concentration at which the operating window is very narrow. This widens until 12% PI concentration after which it begins narrow again as there exists a PI concentration threshold. The addition of more photoinitiator does not increase the polymerisation reaction efficiency after this concentration value. HMDA is a diacrylate 2-photon amenable homopolymer however the results for the 2PL operation parameters differed greatly compared to GPOTA (Figure 3.18).

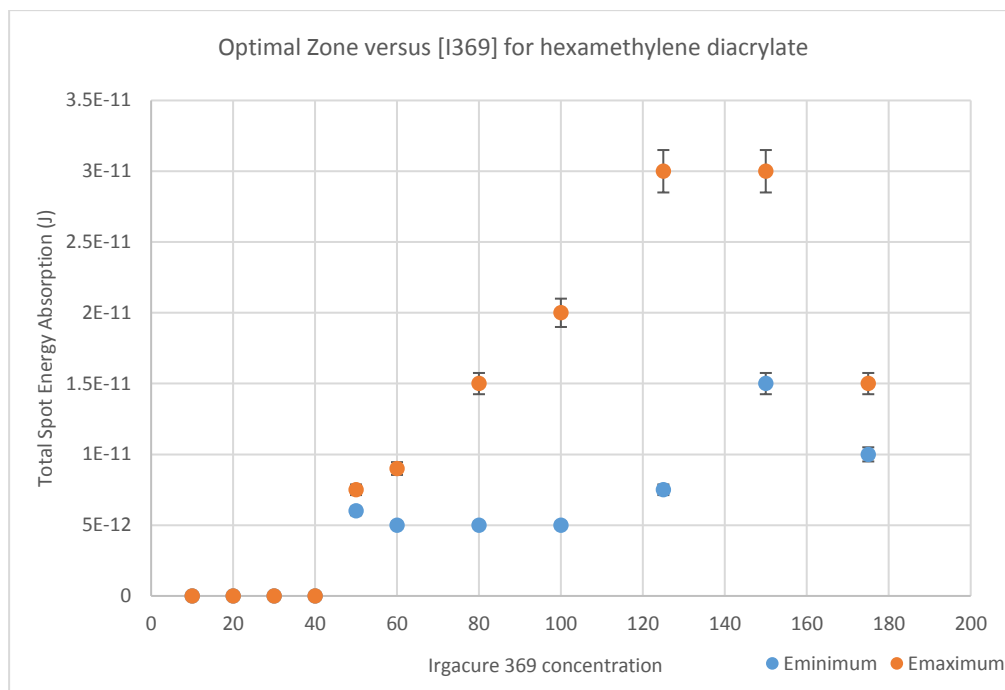


**Figure 3.18: Trend of how Emax and Emin vary according to photo initiator concentration in HMDA.**

HEODA has a much narrower operating window at 5% PI compared to GPOTA at the same concentration or GPOTA at 3% optimal PI concentration. The structures appear complete at 15 pJ and 10 pJ (Figure 3.19). The structure appears incomplete at the next energy value of 7.5 pJ and no fabrication is observed at 6 pJ. This means the operating window of HEODA is limited to approximately between 10-15 pJ.

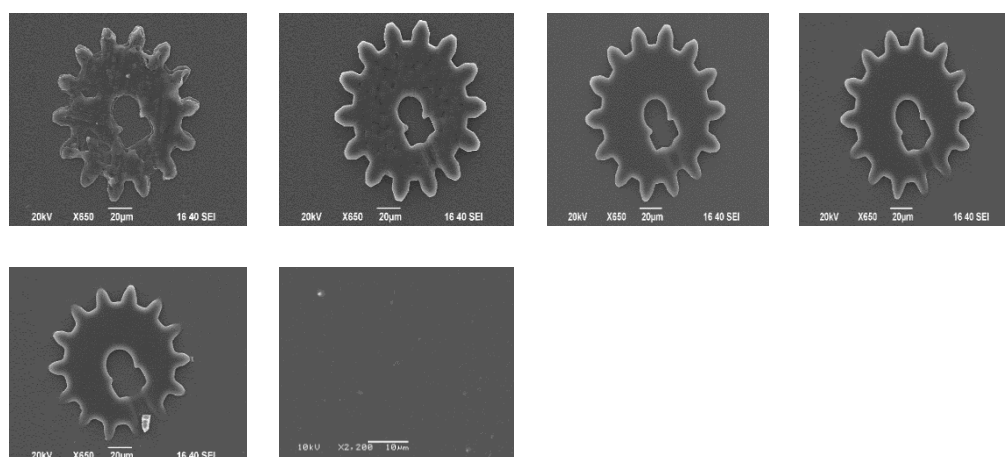


**Figure 3.19: SEM images of HEODA structures at 5% PI concentration. Left to right: 60, 30, 15, 10, 7.5 and 6 pJ.**

There is no fabrication at 1, 2 and 3% PI concentration values. Fabrication commences at 4% PI concentration with a small operating window (Figure 3.20). This is the same for 5% PI concentration. The operating window begins to widen at 6% PI concentration until 100 mg/ml after which it begins to narrow again until the last tested PI concentration of 175 mg/ml. The trend is similar to GPOTA operating windows albeit HEODA fabrication commences at a higher concentration (30 mg/ml).

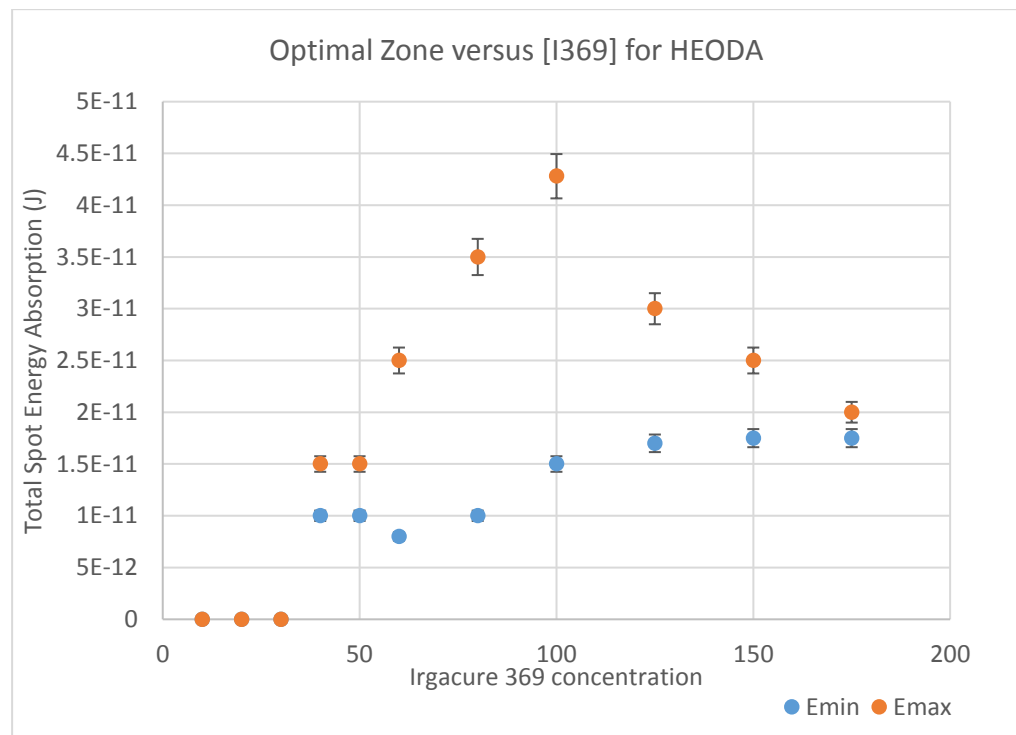


**Figure 3.20: Trend of how Emax and Emin vary according to photo initiator concentration for HEODA.**

The processing window of HEODA homopolymer with 5%PI (Figure 3.20) was used as a guide to select the energy parameters for testing HEODA:EEMA co-polymer (Figure 3.21). The SEM images below (Figure 3.21) show that HEODA:EEMA has a very narrow processing window at 5% PI. In addition, the copolymer composition used was 99% HEODA and 1% EEMA. This means the material could not be defined as a co-polymer as the contribution of the methacrylate component to the polymerization reaction was negligible. Therefore, this co-polymer was not tested further for CM attachment experiments.

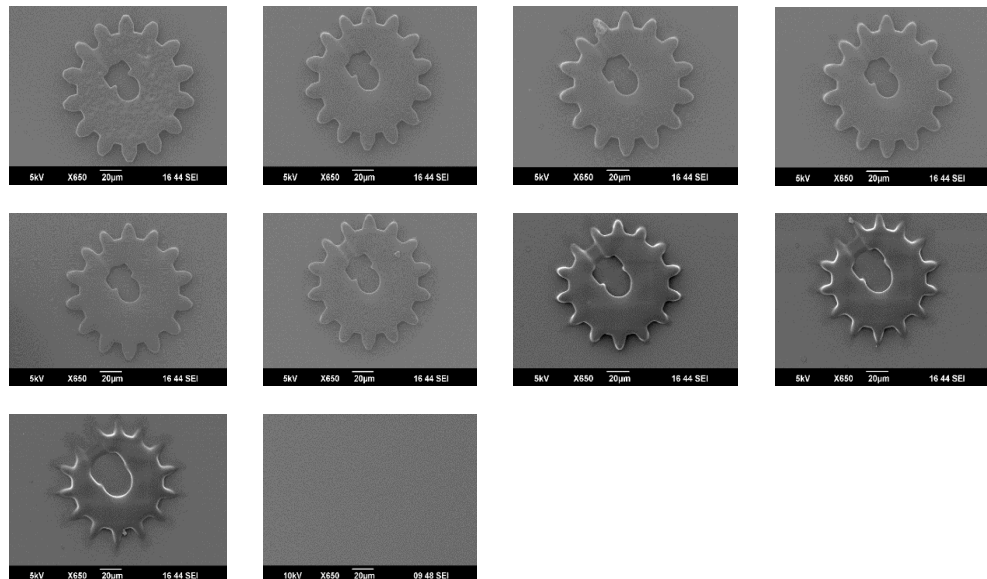


**Figure 3.21: SEM images of HEODA:EEMA co-polymer structures at 5% PI concentration. Left to right: 30, 20, 18.8, 18.18, 17.14, 15, 10, 7.5, 6 and 5 pJ.**

### *3.2.2.2 Operating window determination for GPOTA using the woodpile design on AUTOCAD graphics software*

In order to determine the optimal PI concentration for a particular material, a simple structure should be employed to attain the widest operating window possible. This allows for the operating window to be used as a reference when during fabrication of complex architectures. Therefore, the woodpile structure was utilised to identify the optimal PI concentration for GPT.

The woodpile was designed on AutoCAD software. The general trend is the structure appears damaged and then gradually a complete structure is fabricated at 1.2, 1.8, 2.4, 3.0 and 3.3 pJ. The structure is then fabricated incomplete at 0.6 pJ and no structure is present at 0.3 pJ (Figure 3.22, bottom 3<sup>rd</sup> from the left). This is an expected general trend that was previously observed with the gear design. However, the woodpile design appears to have defects on the right-hand side on all the fabricated structures, appearing as white spots on each rod in 1.2, 1.8 and 2.4 pJ SEM images (Figure 3.22, 2<sup>nd</sup> row and 3<sup>rd</sup> row first from the left). This was attributed to errors in the AutoCAD design. The structure consisted of a row of cylinders with another row of cylinders resting on top. The cylinders on top were directed manually onto the underlying layer therefore human error may have caused slight tilting onto one side of the structures. Hence, the white spots in Figure 3.22, 3<sup>rd</sup> row 2<sup>nd</sup> figure. These indicate more polymerisation occurring in those regions since the cylinders are overlapping more on the right side compared to the rest of the structure. The white spots are also clearly visible in the structures 1.2, 1.8, 2.4 and 3.0 pJ.

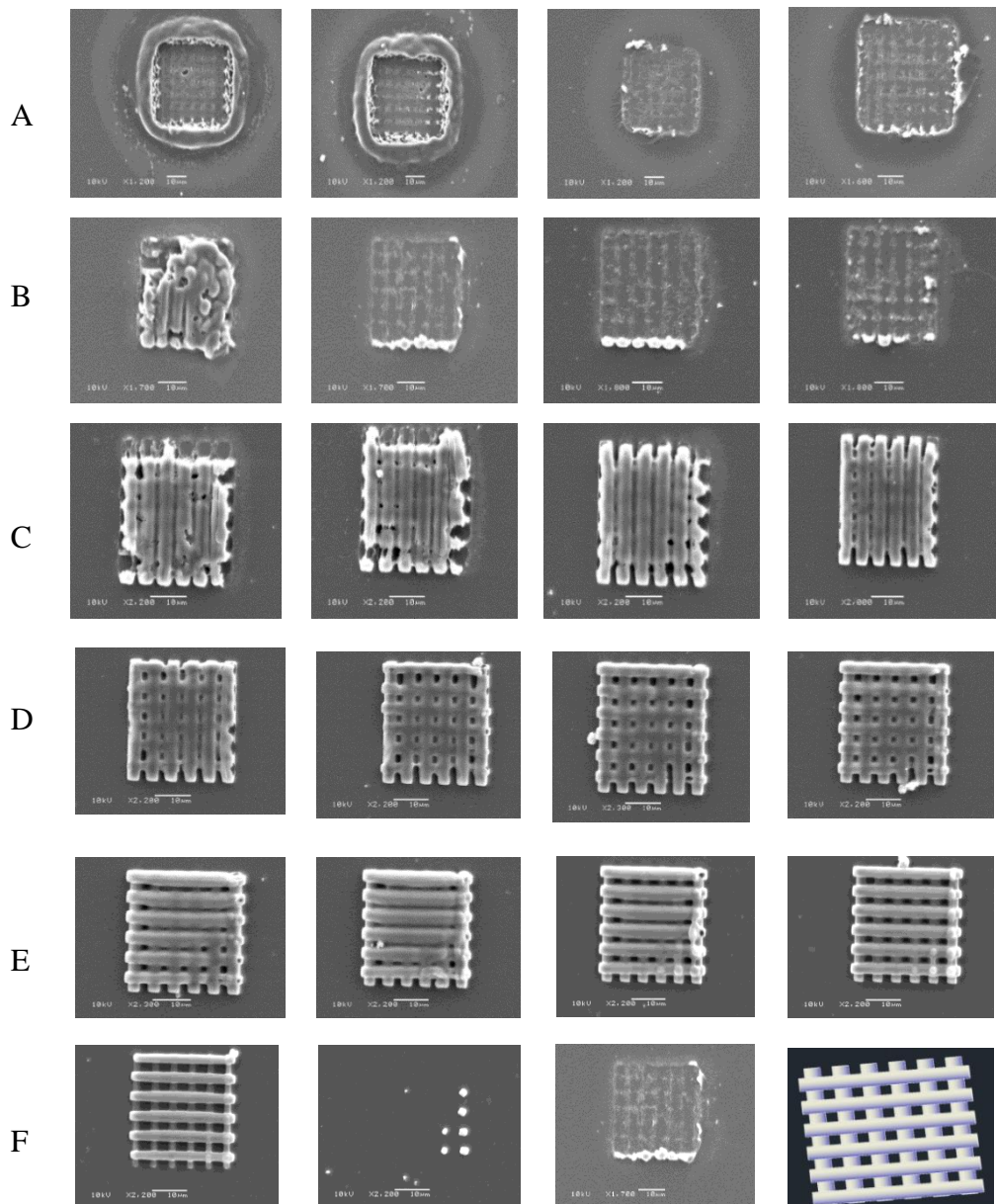


**Figure 3.22: Power sweep of woodpile structures, from highest to lowest energy absorption. SEM images of woodpile structures at energy values (from left to right) A: 60, 50, 42.9, 37.5, B: 33.3, 30, 24, 20, C: 17.1, 15, 10 and 7.5 pJ. D: 6, 4.8, 3.6, 2.4, E: 1.8, 1.2, 1.0, 0.9, and F: 0.8, 0.6 and 0.3 pJ.**

**Lower right: Woodpile structure design on AutoCAD which was the ultimate structure desired to be processed.**



### 3.2.2.3 Woodpile design using Describe

The woodpile design on AutoCAD did not accurately reflect structure damage, as stated in section 3.2.2.2 Operating window determination for GPOTA using the woodpile design on AUTOCAD graphics software. The Describe coding software resulted in more accurate fabrication without leaning towards any particular side of the structure (Figure 3.23)

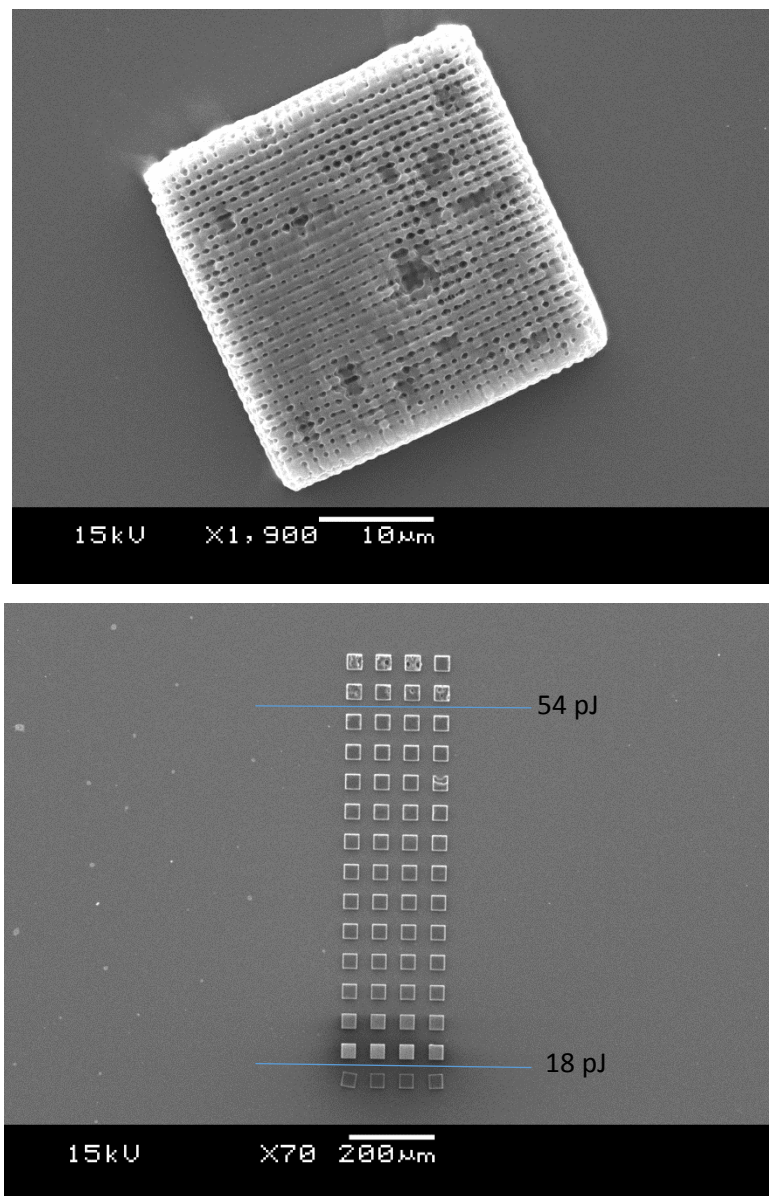


**Figure 3.23: SEM image of woodpile design generated by Describe software. Damage is evident throughout the whole structure which indicates consistency within the whole design. Woodpile array of GPOTA at 3% PI concentration. The lines indicate Emax and Emin at 54 pJ and 18 pJ respectively.**



The thin film array fabrication at 3% I369 concentration with glycerol propoxylate triacrylate showed that the operating window is between 18 pJ and 54 pJ (Figure 3.23, top). This is much wider compared to the operating window of the gear design fabricated using GPOTA (Figure 3.14). The results indicate the structure design itself plays a role in terms of which parameters can be applied for complete structure fabrication.

When the thin film array was fabricated using hexanediol ethoxylate diacrylate (HEODA), the operating window was found to be much narrower at the same photoinitiator concentration, the same design and the same laser power values (Figure 3.24).

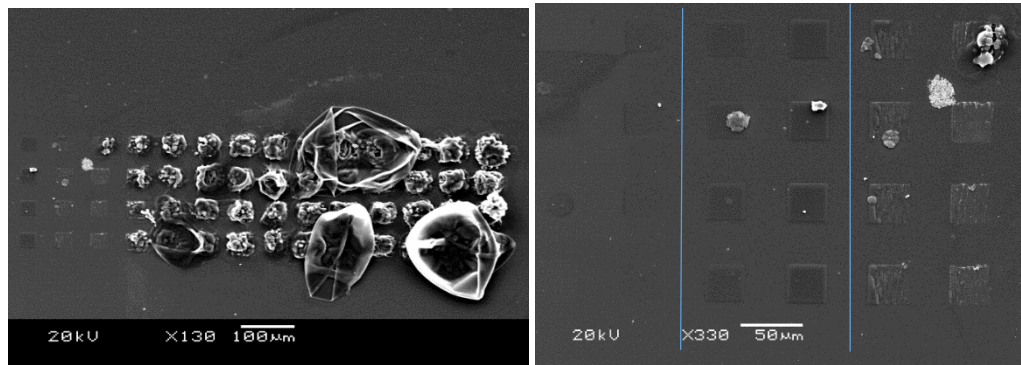


**Figure 3.24: SEM images of woodpile arrays for HEODA. Whole woodpile array (left) from lowest laser power to highest laser power (left to right). SEM image zoom of left side of the array illustrating the point at which structures begin to fade and the operating window is shown by the blue lines (25-30 pJ).**

Not all diacrylates showed the same results. TCDMDA had a considerably wider operating window than HEODA (Figure 3.25).

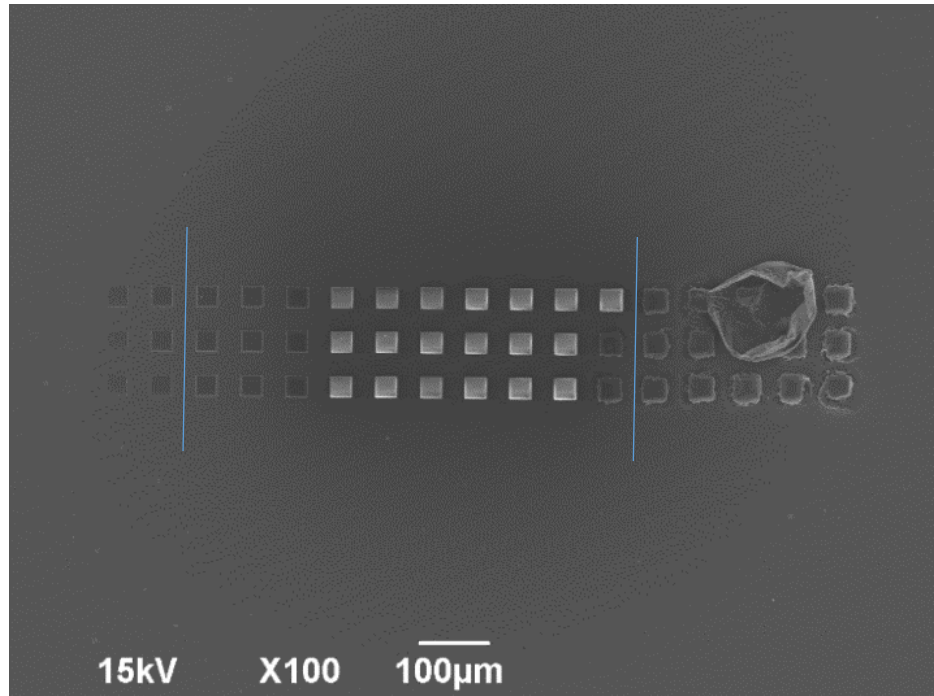


**Figure 3.25: SEM image of TCDMDA at 3% PI concentration of the woodpile array from lowest to highest laser power values (left to right).**

TCDMDA showed a much larger operating window compared to HEODA. Even though both are diacrylates, there was considerable difference in the range of energy values that could produce complete structures without defects. The working range for TCDMDA was 17-42 pJ. This is a much wider operating window compared to HEODA and structure quality appeared clearer.

The woodpile arrays were tested at lower PI concentrations on the co-polymers that were found amenable to 2PL (Table 3.4) to observe whether the co-polymers were worth taking over to CM attachment experiments. SEM images show co-polymer PPGDA:GPOTA had a good working range at 1% PI concentrations. The other 3 co-polymers had much narrower operating windows (Figure 3.26).

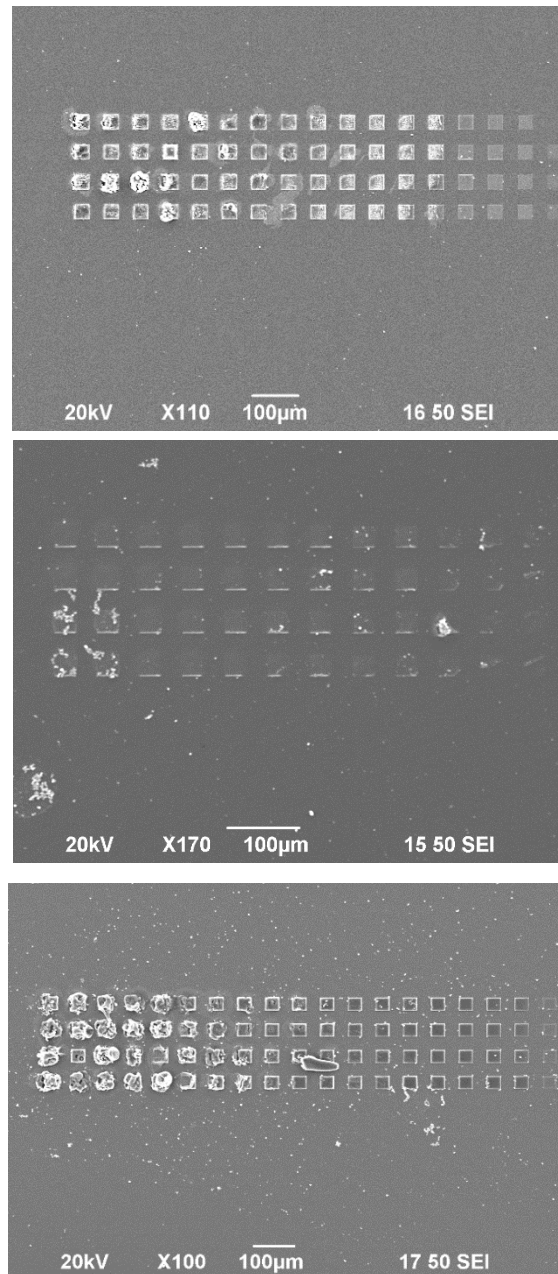


**Figure 3.26: SEM images of woodpile arrays of BDDA:GPOTA, HEODA:PPGDA and PPGDA:GPOTA copolymers at 1% PI concentration.**

### 3.2.3 Complex architecture design for 2-photon lithography

Once polymers that were able to support CMs and were amenable to 2PL were found, namely TCDMDA, GPOTA and PETrA, design of varying topologies for CM culture were commenced. Complex architectures of the anatomical heart and the DNA double helix were fabricated as example structures to observe whether operating window parameters would change.

The next stage of fabrication a rectangular box structure which is defined in this section as a 'platform'. The purpose of the platform was to provide stability for the open-channel structures that were placed on top. The open-channel structures were the first structures fabricated to serve as grooves.

Flat structures were designed to be utilised as controls in the CM attachment experiments. A flat structure does not have the topology variable and so served as a good control. Afterwards, complex structures with varying groove depths were designed, as this had not been investigated by 2PL before.

#### 3.2.3.1. Anatomical Heart

A stable anatomical heart structure was fabricated at 100% laser power and 14,000  $\mu\text{m/s}$ . According to the midpoint of the operating window for GPOTA at 3% PI concentration is  $3.33\text{E-}11$  pJ which is equivalent to 100% laser power and 18,000  $\mu\text{m/s}$ . The table of calculations was used to determine which scanspeed could be used with 50 mW to attain the same energy value of 33 pJ. The value found was 18,000  $\mu\text{m/s}$  (2.1.4.1 Calculation of Total Spot Energy Absorption and Reverse Calculation to Achieve Workable Scanspeed values for 2PL). Therefore, the combination of 50 mW and 18,000  $\mu\text{m/s}$  was used as a starting point during the fabrication of the DNA and the anatomical heart designs. Both designs were fabricated with high accuracy utilizing these parameters (Figure 3.27 and 3.28). No trial-and-error was required in regard to the parameter identification on the 2-photon system, demonstrating that the operating window was an excellent reference point from which to commence fabrication of complex architectures.

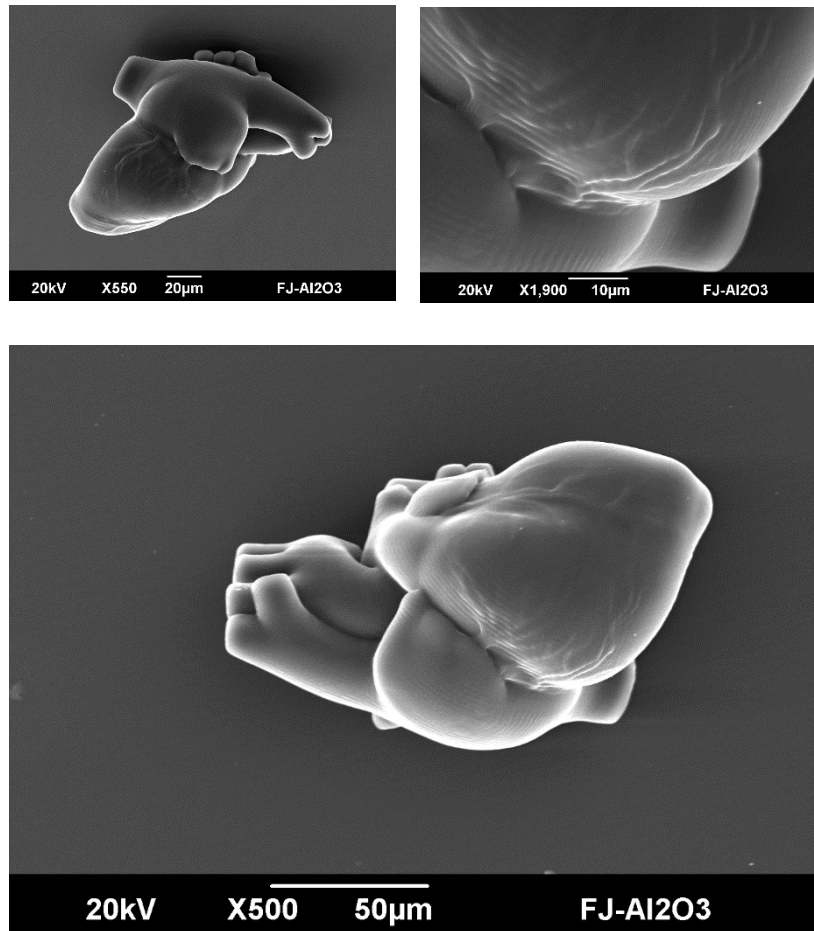


**Figure 3.27: SEM images of anatomical heart structures fabricated by 2PL. Top left: Aerial view of the heart veins and aorta. Top right: Zoomed in image of the vessels on the heart surface, detailing slicing lines. Bottom: Aerial view of the whole heart structure.**

### 3.2.3.2 DNA double helix

A similar systematic approach was used to find the optimal parameters to fabricate the DNA double helix structures with GPOTA at 3% PI concentration. The parameters used for the DNA double helix structure were 100% laser power in combination with 18,000  $\mu\text{m/s}$ , identical parameters to the ones applied to the anatomical heart structure. The resulting DNA double helix structures had no visible damage and were fabricated complete, without missing or broken parts (Figure 3.28).

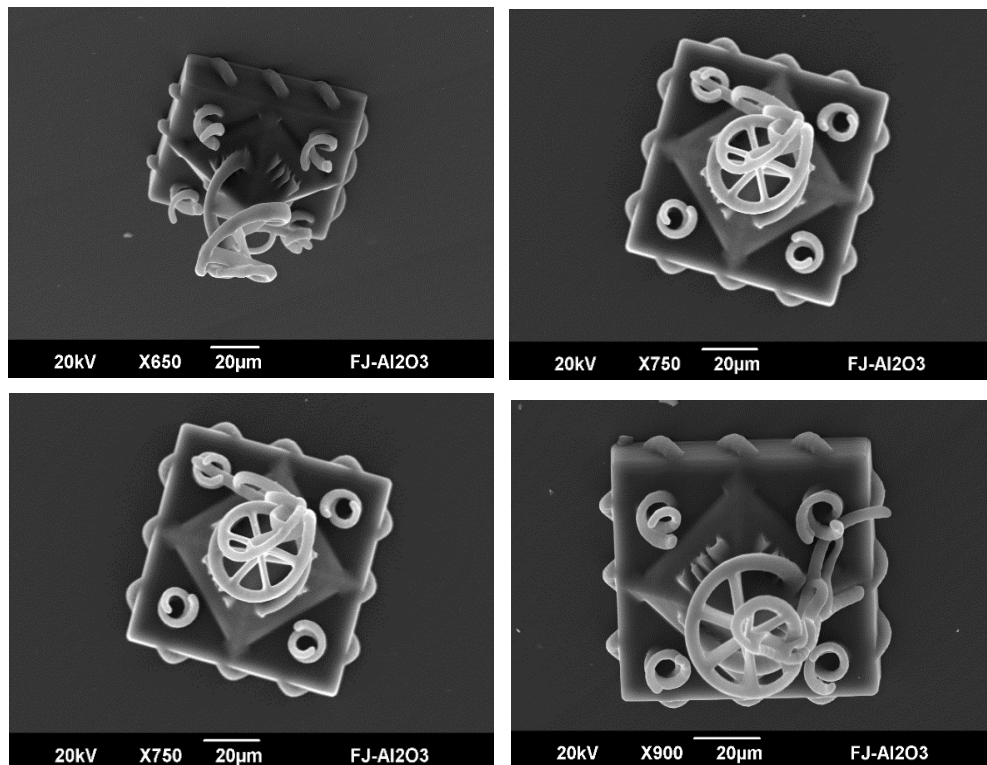


**Figure 3.28: Aerial views of the DNA double helix structures fabricated by 2PL.**

The anatomical heart and DNA double helix have similar optimal fabrication parameters as they were both fabricated with GPOTA at the same PI concentration. The midpoint of the woodpile array operating window was used as a reference to commence fabrication of these complex architectures. This novel approach by which complex architectures are fabricated by using a simple structure's operating window's reference method is extremely useful when moving onto building more sophisticated designs. This is one of the key findings of the 2-photon lithography experiments during this PhD project.

This additional parameter to consider during 2-photon fabrication is the structure design itself, in terms of complexity. The more details, curves, twists and corners a design has the more likely it is to have a narrower operating window (3.2.2 Operating window determination for 2-photon amenable homopolymers). This renders the need for guidance prior to complex architecture fabrication.

A way to visualize this is to think of a series of concentric circles. Each circle represents an operating window for a specific structure (Figure 3.29).

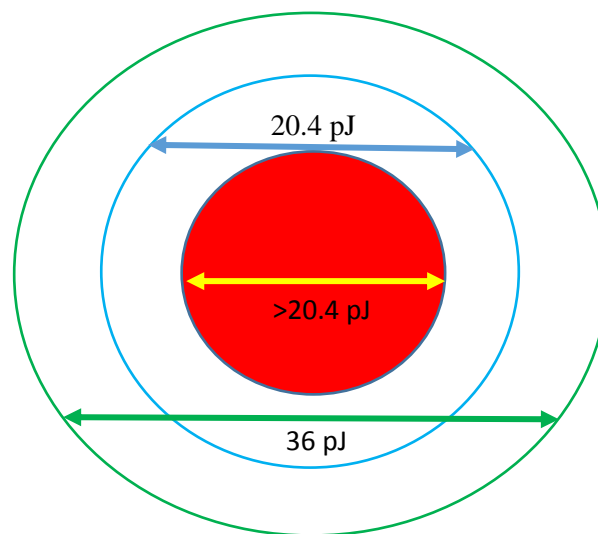


**Figure 3.29: Schematic illustrating the concept of how the operating windows of various structure designs relate to each other.**

The green circle represents the operating window for the woodpile array. The blue circle would represent the operating window for the gear design structures. The red circle in the centre represents the complex architectures of the anatomical heart and DNA double helix structures. Any woodpile structure fabricated within the green circle, therefore all regions, will be complete and stable. Any gear structure fabricated within the boundaries of the blue circle will be complete and stable however outside of the blue circle they would appear either very damaged or unstable or no fabrication would be visible. The complex architectures can be fabricated in a complete, stable state only within the confines of the red circle. Any structures outside this region, even if they



are within the blue or green circles, will appear damaged, faded or not fabricated. The operating window of the red region is labelled  $<20.4$  pJ as the exact operating windows of the complex architectures fabricated are unknown. Further to the trend observed between the woodpile and gear designs the operating window for the complex architectures is predicted to be narrower than the prior two. Additional experiments determining the specific  $E_{max}$  and  $E_{min}$  values of the complex architectures is required to support this.

### 3.2.4 2-photon fabricated topologies for CM attachment

Designs relevant to CM attachment were fabricated by 2PL. Printing parameters were adjusted according to the operating window of the monomer being utilized. The monomers used for fabrication were TCDMDA, GPOTA and PETrA as they possessed sufficiently wide operating windows for 2-photon fabrication.

#### 3.2.4.1 Open-channels of various curvatures

Initial design work on the open-channels proved that the end-product would be reached in a step-by-step process. The open-channels were fabricated as a starting point. This was followed by fabrication of these open-channel curvatures on a platform for stability and organisation. The degrees of curvature were  $50^\circ$  and  $100^\circ$ .

The structure fabricated at 42 pJ possessed a very large hole (Figure 3.30, top left). This is due to the laser power being too high for the fabrication of this open-channel design. The woodpile array structures were fabricated without defects at 42 pJ. This reiterates the fact that complex architectures will have different working parameters to simple ones. When the laser power was reduced to attain an energy of 39 pJ the defects were not as large but evidence of damage still remained on the surface of the structure as small spots (Figure 3.30, top right). The laser power was reduced further to obtain 36 pJ of energy, which greatly improved the quality of the structure surface. However, some damage was still visible on one side of the structure (Figure 3.30, bottom).



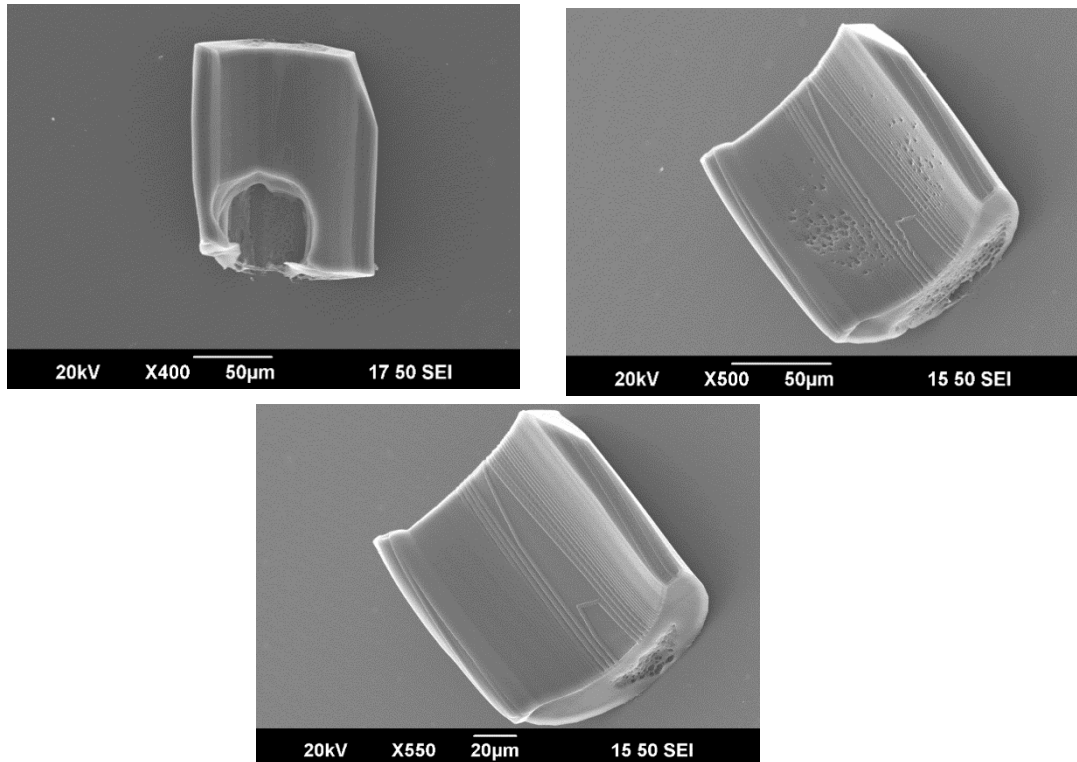


**Figure 3.30: SEM images of 50° open-channel structures fabricated by 2PL. Top left: 42 pJ, top right: 39 pJ and bottom: 36 pJ.**

39 pJ was selected as the energy value to commence with as the 50° open-channel structures started to show reduced defects when fabricated with this energy (Figure 3.30). There were massive defects at 39 pJ with the 100° open-channels (Figure 3.31, top left). The defect was very similar albeit slightly smaller at 30 pJ. The damage completely disappeared at 27 pJ (Figure 3.31, middle left), indicating that there are energy values between 27 and 30 pJ that show gradually decreasing defects down to 27 pJ. One side of the structure showed minute defects (Figure 3.31, middle right) compared to the other side (Figure 3.31, bottom).

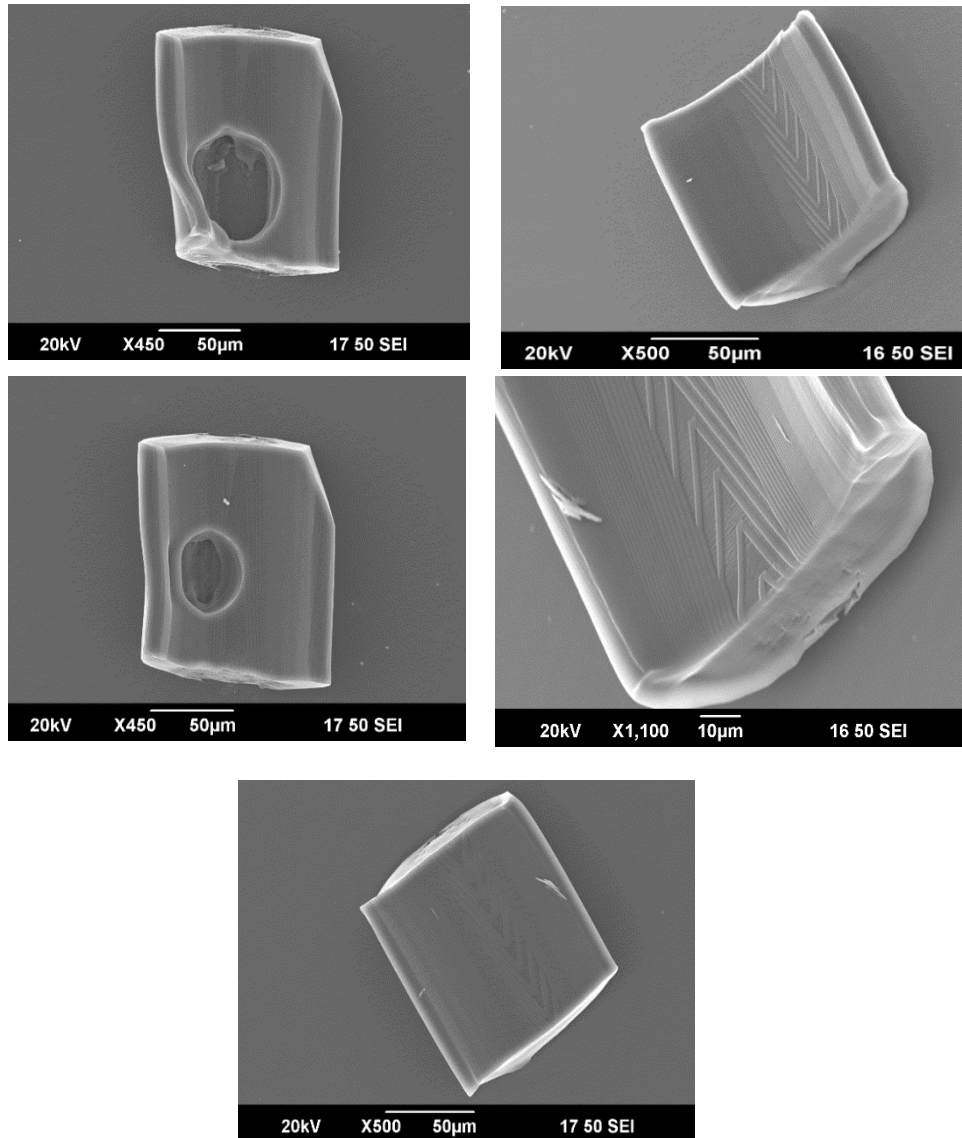


**Figure 3.31: SEM images of  $100^\circ$  open-channel structures fabricated by 2PL. Top left: 39 pJ, Top right: 30 pJ, Middle left: 27 pJ, Middle right: Enlarged image of structure fabricated with 27 pJ showing damaged side. Bottom: Image of structure fabricated with 27 pJ showing complete side.**

Once the optimal parameters were determined for the open-channel structures, a platform was designed to stabilize the open-channels. The platform (rectangular support below curvatures) was designed on AutoCAD and the open-channels were slightly embedded into the platform to ensure stability (Methodology Section 2.7.6). The combined open-channel and platform design were exported as one .stl file. The resulting structure was stable and fabricated with high quality at 27 pJ. More specifically, there were no microexplosions during fabrication and neither was the structure incomplete (Figure 3.32).

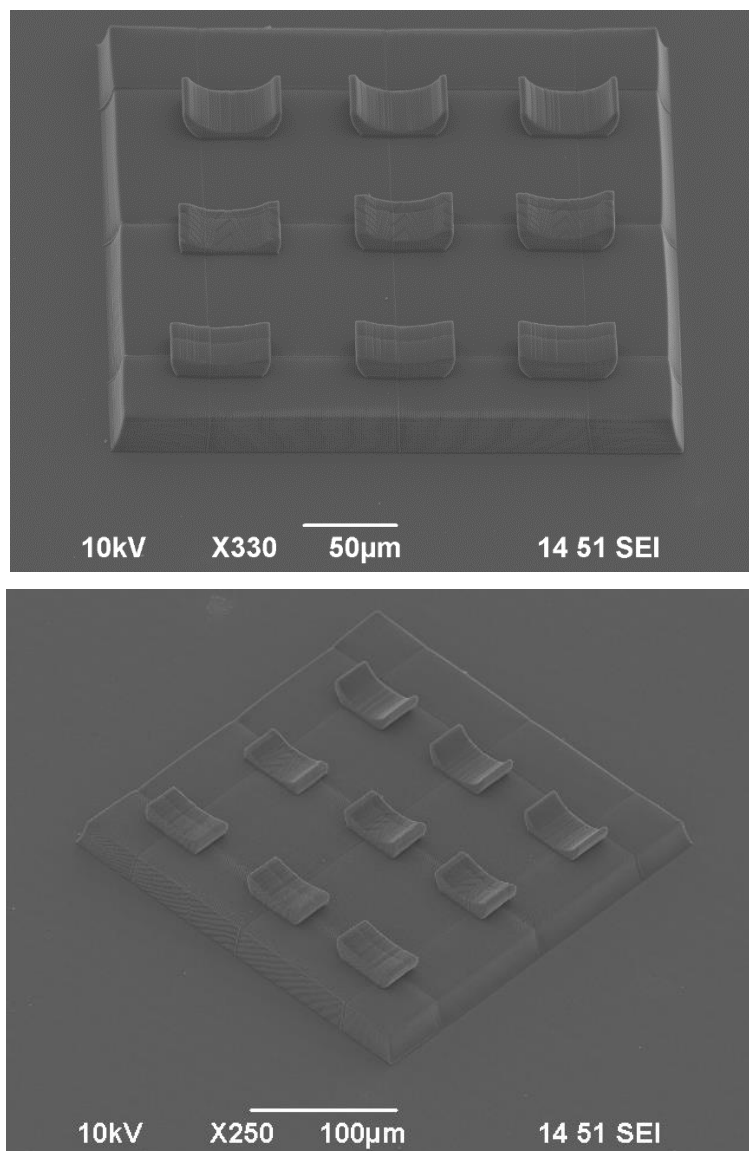


**Figure 3.32: SEM images of open-channel structures on the platform design. The open-channels at the front have 160° curvatures, the ones in the middle 100° curvature and the ones at the back have 50° curvatures.**

Further analysis of the SEM images revealed that the open-channel structures were fabricated with high resolution (Figure 3.33). Both the hatching distance and slicing distance for the whole design had been set to fabricate at 0.3 µm. Naturally, the hatching distance of the fabricated structure was smaller than 0.3 µm due to polymerization shrinkage (Figures 3.34, 3.35 and 3.36). This occurs due to the reduction in size as the monomers join to form the polymer chains, making the molecule more compact.

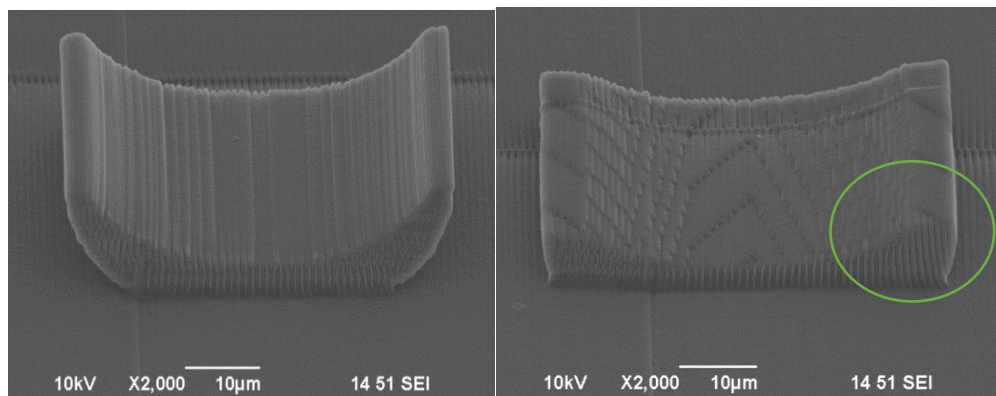
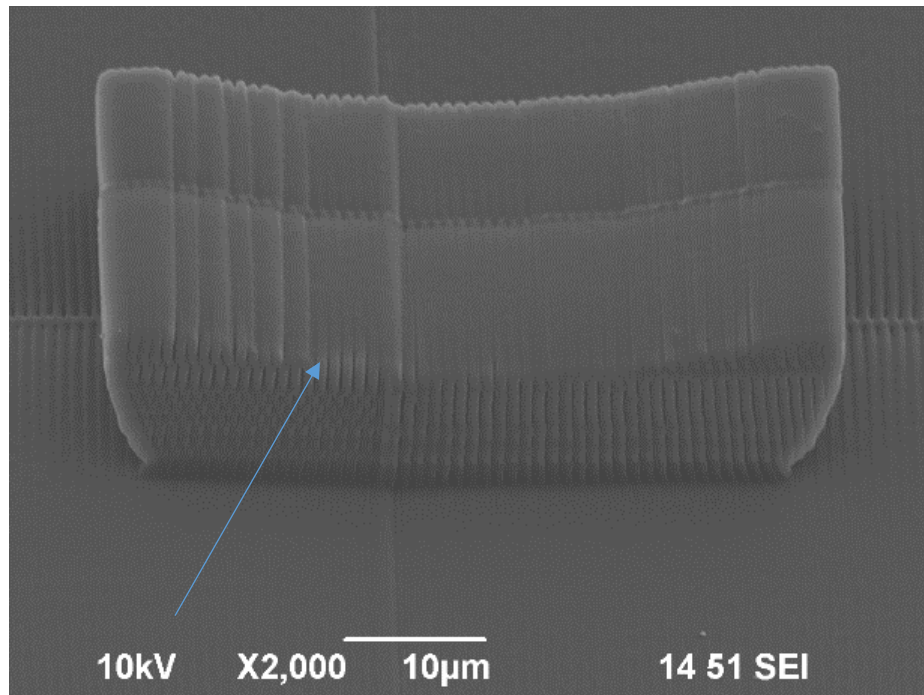


**Figure 3.33: SEM images of each open-channel structure that were fabricated simultaneously on the platform. Top: 160° curvatures, bottom left: 100° curvature and bottom right: 50° curvatures.**

The hatching distances measured on the 160° curvature structure were almost equal to each other (Figure 3.34). This signifies the consistency of fabrication of the hatching lines for this particular structure. Lack of sculpting errors and less curvature compared to the 50° structure may be the reason hatching lines were more evenly distributed which resulted in almost equal hatching distances.



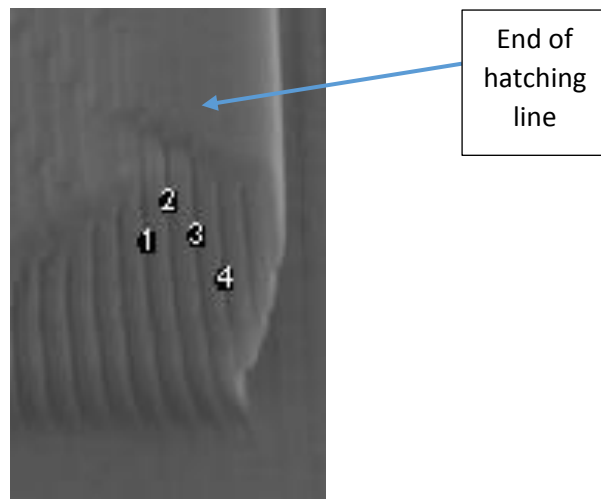
| Measurement number | Length ( $\mu\text{m}$ ) |
|--------------------|--------------------------|
| 1                  | 0.202                    |
| 2                  | 0.203                    |
| 3                  | 0.204                    |
| 4                  | 0.203                    |

**Figure 3.34: Top: Enlarged SEM image of 160° curvature structure. Measurements of hatching distance were made at the locations of labelled numbers on ImageJ software. Bottom: Table of hatching distance measurements.**

The 100° curvature structure showed uneven hatching lines. This was due to the inaccurate sculpting procedure performed on AutoCAD at the stage where the cylinder was longitudinally split in half (Methodology 2.7.6). The cylinder was not split at a 90° angle to the z-axis which resulted in the uneven patterns on the surface of the structure (Figure 3.33, bottom right). This fabrication attempt demonstrates the flaws in design that require improvement.

The 100° curvature open-channel structure showed uneven hatching lines and this is easily visible on the cross-sectional area (Figure 3.35). Not all the hatching lines from the surface continue down to the front of the structure. The blue arrow indicates an example of this. The hatching line ends at the point of the arrow as opposed to the hatching lines to the left and the right of the arrow, which continue down to the platform. Hatching distance measurements were made to the bottom right side of the structure where this sculpting effect did not occur, shown by the regions labelled with numbers 1, 2, 3 and 4 (Figure 3.35). The hatching distances were all less than 0.3  $\mu\text{m}$  and is a result of

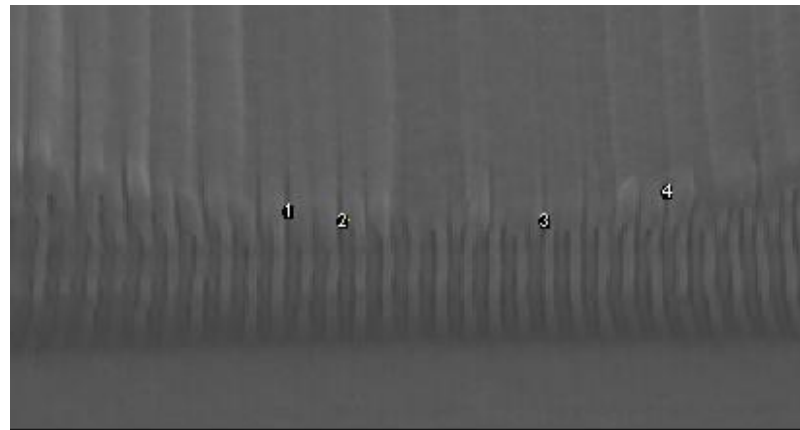
polymerization shrinkage. In addition, the hatching distances also varied from each other. This is possibly due to the uneven hatching, which causes some parts of the structure to bend and lean towards the right (Figure 3.35). As a result, the sections closer to the platform contain hatching lines closer to each other compared to the top section, which explains the measurements 1, 2 and 3. Measurement 1 was lower than measurement 2 and measurement 3 was lower than measurement 2 hence their corresponding hatching distances followed the pattern low to high to low again. Measurement 4 showed a relatively expected hatching distance as that section was at the lateral end of the structure with hatching lines on the right gradually getting shorter with increased height (Figure 3.35).



| Measurement number | Length (µm) |
|--------------------|-------------|
| 1                  | 0.104       |
| 2                  | 0.208       |
| 3                  | 0.147       |
| 4                  | 0.208       |

**Figure 3.35: Top: Enlarged SEM image of 100° curvature structure. Measurements of hatching distance were made at the locations labelled as numbers on ImageJ software. Bottom: Table of hatching distance measurements.**

The hatching distances were measured as labelled (Figure 3.36). All are less than the 0.3  $\mu\text{m}$  set by the Describe software during design. The structure experiences polymerization shrinkage which causes the polymer chain to reduce in size therefore the hatching distance decreases and some hatching lines converge (Figure 3.36). The distances were; 0.211, 0.222 and 0.211 and 0.222  $\mu\text{m}$  as measured on ImageJ software (Figure 3.36). They did not differ from each other as opposed to the 100° curvature structure as all hatching lines were fabricated completely (Figure 3.36).



| Measurement number | Length ( $\mu\text{m}$ ) |
|--------------------|--------------------------|
| 1                  | 0.211                    |
| 2                  | 0.222                    |
| 3                  | 0.211                    |
| 4                  | 0.222                    |

**Figure 3.36: Top: Enlarged SEM image of 50° curvature structure with measurements of hatching distance done on ImageJ software labelled by number. Bottom: Table of hatching distance measurements.**

#### *3.2.4.2 Open-channel multiplex structures*

2-photon fabricated open-channel structures were stable on the rectangular platform (Figure 3.32), however the open-channels were required to be joined together since these structures will be seeded with CMs. The current design may result in seeding on some parts of the structure while missing others. Therefore, it was only logical to design a structure of curvatures with little or no spacing (Figure 3.37). The grooves were also designed to be longer to guarantee as many cells as possible will settle down and could be visualized easily (Figure 3.37). The left-hand side of the region was the lowest curvature region, possessing the shallowest grooves, measuring 3  $\mu\text{m}$ . The medium grooves region measured 5  $\mu\text{m}$  and the deepest region measured 10  $\mu\text{m}$ . Each region consisted of 16 grooves (Figure 3.37). The structure appeared complete with some peeling of the corners on the right-hand side (Figure 3.37, top). This is due to the deletion of the silanisation step as samples prepared for SEM cannot be used for cell culture. Silanisation serves the purpose of ensuring samples do not detach from the glass surface since there are many rinsing steps prior to CM attachment experiments. Samples for SEM do not undergo these extensive rinsing procedures so silanisation was not performed. This is why some peeling was observed (Figure 3.37). The fabrication shows that TCDMDA polymer was suitable for building open-channel structures, illustrated by the complete structure details without damage or incomplete parts (Figure 3.37, bottom).



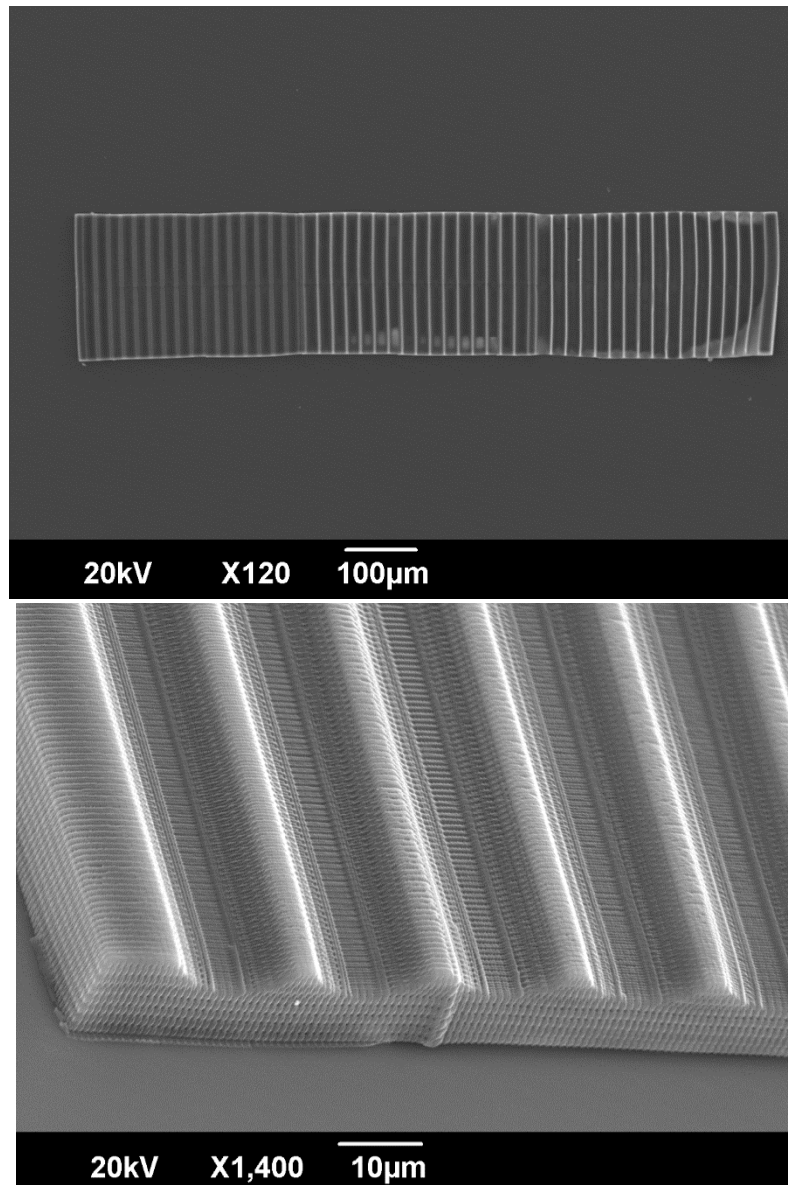


**Figure 3.37: SEM images of open-channel multiplex structure fabricated with TCDMDA at 27 pJ. Top: Aerial view and Bottom: Enlarged image of left-hand corner of the structure showing criss-cross 90° hatching direction.**

Flat controls are required for the CM attachment experiments to be accurate since various topologies are being compared. It is only logical that the reference point would be a flat structure composed of the same material utilised to fabricate the grooves. Hence, the structure was further developed by the addition of a flat region next to the region composed of grooves. The flat region was fabricated at 2 µm which is sufficient for fabrication and thin so as to reduce fabrication time.

The new multiplex structure (Figure 3.38) was fabricated in a complete manner, albeit slightly damaged shown by the small holes dispersed around the structure surface. The interface between the flat and shallow grooves region fabricated a stable, solid structure. This indicates that inserting a flat region slightly overlapping the grooves design from underneath is able to be fabricated in a complete and stable way (Figure 3.38). This multiplex structure was fabricated at the same energy value as the structure composed of grooves only (Figure 3.38). Surprisingly, this structure displays damage which could be due to resetting of the Nanoscribe default laser power during an engineer visit. When this occurs, a lower laser power than was previously used to fabricate a structure has to be applied to attain the same quality construct. This is usually in the range of 5-10% lower than the laser power applied previously. The regions with grooves were fabricated complete, with few errors (Figure 3.38).

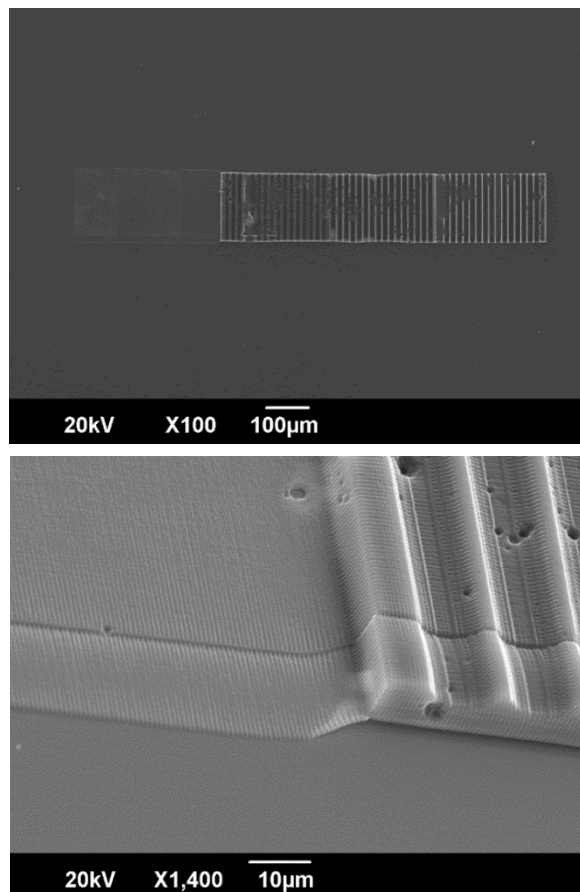


**Figure 3.38: SEM images of multiplex structure fabricated with TCDMDA at 27 pJ. Top: Aerial view of multiplex structure. Bottom: Enlarged image of the flat region and shallow grooves region interface.**

The same results were observed in the medium-depth grooves region (Figure 3.39, top) and the deepest grooves region (Figure 3.39, bottom). The structures were fabricated with high quality and resolution. The hatching lines and the spaces between can be easily observed (Figure 3.39).

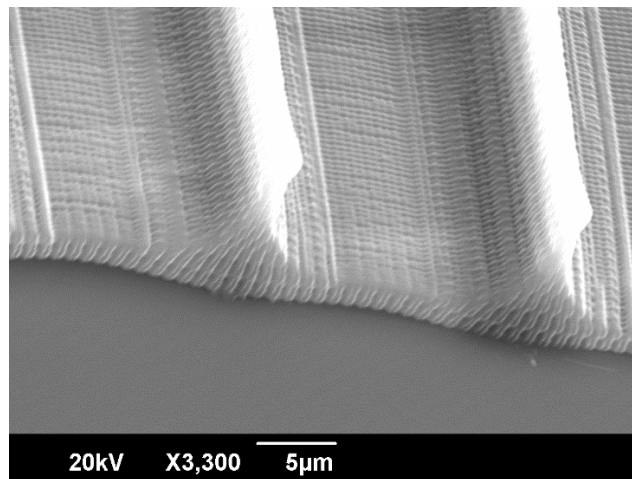
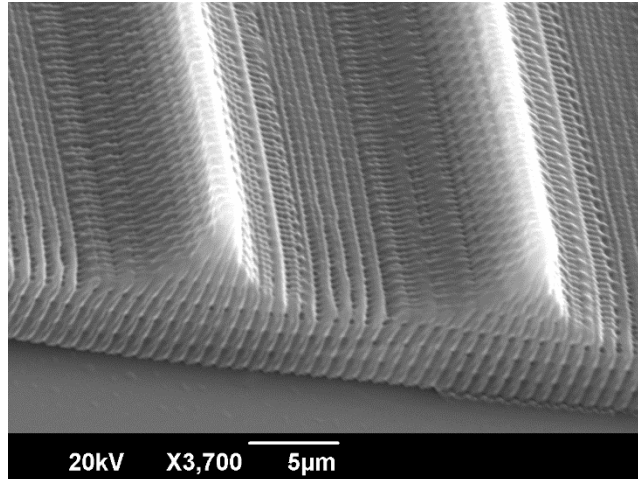
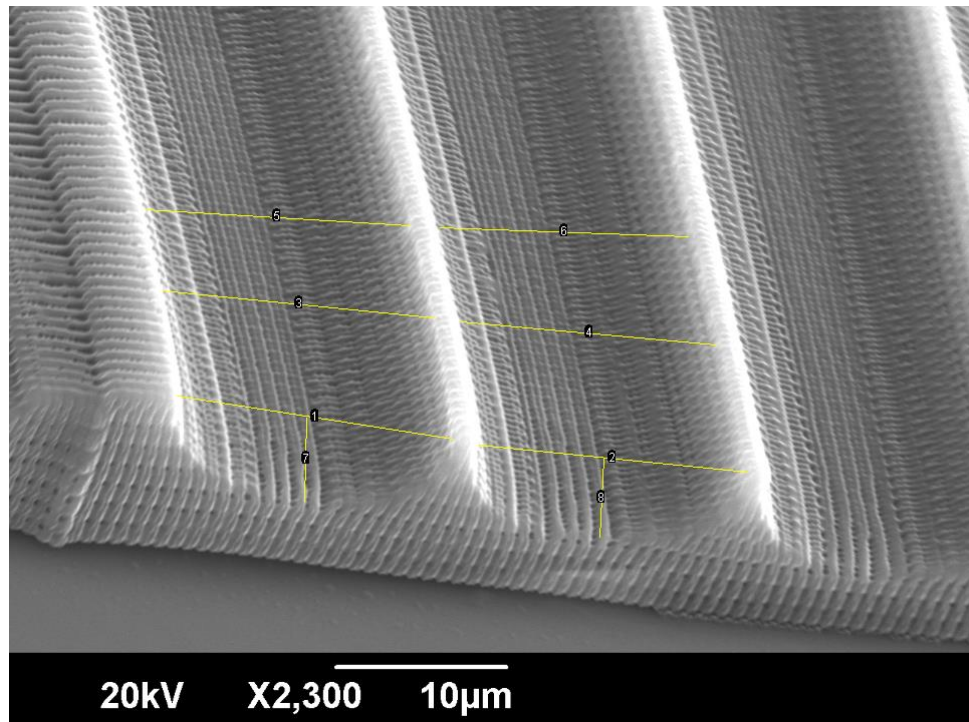


**Figure 3.39: SEM images of medium-depth 5 μm grooves (top) and deepest 10 μm grooves region of TCDMDA multiplex structure.**

The groove dimensions on the fabricated product varied from the design dimensions in the medium-depth grooves (Figure 3.40). This fabrication error can be attributed to polymerization shrinkage, which cannot be controlled by the user. This knowledge is valuable for future fabrication.



| Measurement Number | Length (μm) | Design Dimension (μm) | Difference (μm) |
|--------------------|-------------|-----------------------|-----------------|
| 1                  | 16.277      | 17                    | 0.723           |
| 2                  | 15.752      | 17                    | 1.248           |
| 3                  | 15.868      | 17                    | 1.132           |
| 4                  | 14.914      | 17                    | 2.086           |
| 5                  | 15.408      | 17                    | 1.592           |
| 6                  | 14.454      | 17                    | 2.546           |
| 7                  | 4.855       | 5                     | 0.145           |
| 8                  | 4.74        | 5                     | 0.26            |

**Figure 3.40: SEM image of 5 μm medium-depth grooves labelled with measurements made on groove width and depth on ImageJ software. Table of all measurements (bottom).**

The groove dimensions on the fabricated deepest grooves were also smaller compared to the design dimensions as is expected due to polymerization shrinkage. The differences found by the measurements between fabricated dimensions and design dimensions however were lower compared to the 5 micron grooves (Figure 3.41).

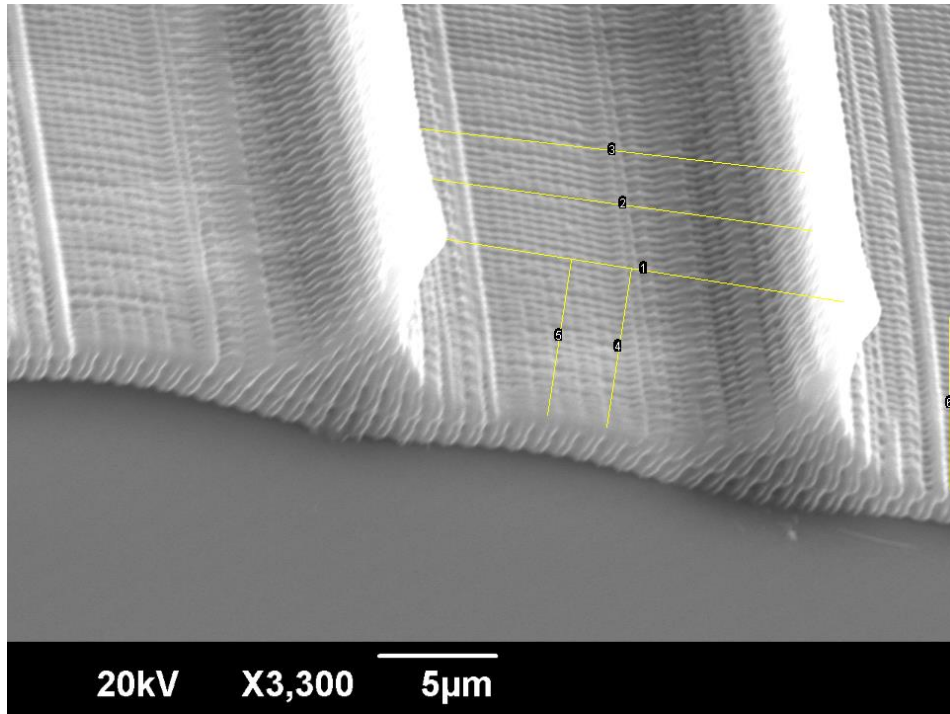


**Figure 3.41: SEM image of 10 µm deep grooves labelled with measurements made on groove width and depth on ImageJ software. Table of all measurements (bottom).**

| Measurement number | Length (µm) | Design Dimension (µm) | Difference (µm) |
|--------------------|-------------|-----------------------|-----------------|
| 1                  | 16.635      | 17                    | 0.365           |
| 2                  | 15.881      | 17                    | 1.119           |
| 3                  | 16.003      | 17                    | 0.997           |
| 4                  | 6.677       | 8                     | 1.323           |
| 5                  | 6.509       | 8                     | 1.491           |
| 6                  | 7.131       | 8                     | 0.869           |

Column 4 in Figure 3.41 shows the differences between measurements on design and fabricated grooves. The width measurement differences (rows 1-3 in column 4) are lower than the width measurement differences in the 5 micron grooves (Figure 3.40, column 4, rows 1-6). This may be due to the fewer hatching lines along the ridges on the deep grooves therefore less chances of polymerization shrinkage compared to the medium-depth grooves.

#### *3.2.4.3 Multiplex structure relevant to CM attachment*

The multiplex structures designed so far, were too small to accommodate enough cell attachment for visualisation and data acquisition. The more cells

that can be visualized, the more data can be collected on CM attachment. One mature CM is approximately 120  $\mu\text{m}$  in length therefore the width of the construct was adjusted to 1000  $\mu\text{m}$ . The other dimensions of the construct such as the length and height were compromised so as to ensure each groove had a design dimension width of 27  $\mu\text{m}$  (Table 3.8). Describe software automatically readjusts the structure according to a predefined aspect ratio when one of the dimensions is changed. However, when the width was set to 1000  $\mu\text{m}$ , the height automatically readjusted to 50  $\mu\text{m}$ . This is too thick and the structure would require extremely long fabrication times, even with large hatching and slicing distances. This setting was disabled so that the structure width was set to 1000  $\mu\text{m}$  and then the structure was increased in small increments from 0 gradually to 15  $\mu\text{m}$ , at which the structure design regained its original shape. The flat region was adjusted to the lowest height possible (2  $\mu\text{m}$ ) to shorten fabrication time but at the same time thick enough to be visible and ensure attachment to the glass substrate.

**Table 3. 8: Dimensions of the readjusted dimensions for the multiplex design.**

| <i>Parameters</i>           | <i>Flat Region</i> | <i>Grooves Region</i>         |
|-----------------------------|--------------------|-------------------------------|
| <b><i>Length</i></b>        | 2000 $\mu\text{m}$ | 2000 $\mu\text{m}$            |
| <b><i>Width</i></b>         | 1000 $\mu\text{m}$ | 1000 $\mu\text{m}$            |
| <b><i>Height</i></b>        | 2 $\mu\text{m}$    | 15 $\mu\text{m}$              |
| <b><i>Diameter</i></b>      | N/A                | 27 $\mu\text{m}$ (per groove) |
| <b><i>Groove Depths</i></b> | N/A                | 6, 9 and 12 $\mu\text{m}$     |

#### 3.2.4.4 Introduction of hatching directions to multiplex structures

Previously, the grooves were fabricated with a hatching direction of  $90^\circ$ . This adds an extra variable to the experiment. Groove depth is being tested. However, if hatching direction is also varied then it would be impossible to deduce whether differential cell behaviour is due to the groove depth or the hatching direction. Therefore, the flat region was divided into 4 sections each with different hatching directions;  $0^\circ$ ,  $90^\circ$ ,  $60^\circ$  and  $120^\circ$ . The grooves region was reduced so that each groove depth section was composed of 4 grooves instead of 16. This vastly reduced fabrication time and separated the testing of two variables; hatching direction and groove depth.

Multiplex structures with various hatching directions were successfully fabricated using both TCDMDA and PETrA. The complete TCDMDA structure was successfully fabricated as shown in the SEM image in Figure 3.42. All fine features demonstrating hatching lines were clearly visible on SEM samples with high magnification (Figure 3.43). The hatching direction of the structure design influenced the energy value required for fabrication of a complete structure.

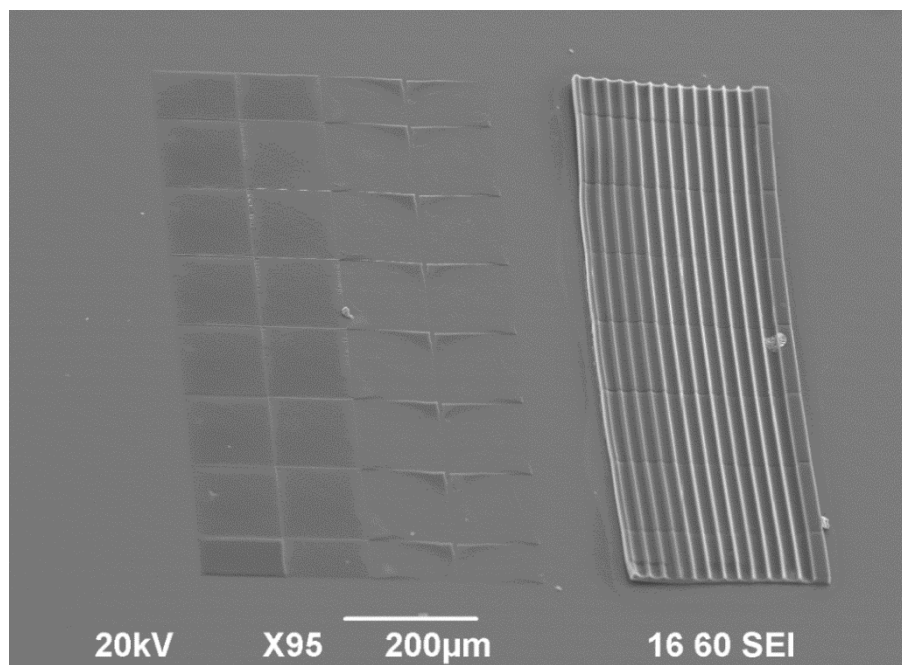


**Figure 3.42: SEM image of multiplex structure with flat region and grooves region. The two were separated by a small gap. The polymer used for fabrication was TCDMDA.**



The flat region with various hatching directions were fabricated complete with few errors. Some regions show slightly uneven lines (Figure 3.43).

Nevertheless, this structure will serve the purposes of the CM attachment experiment as a 2-dimensional flat control. Whether the CMs would respond to the hatching direction was a question that would be answered in Chapter 5.

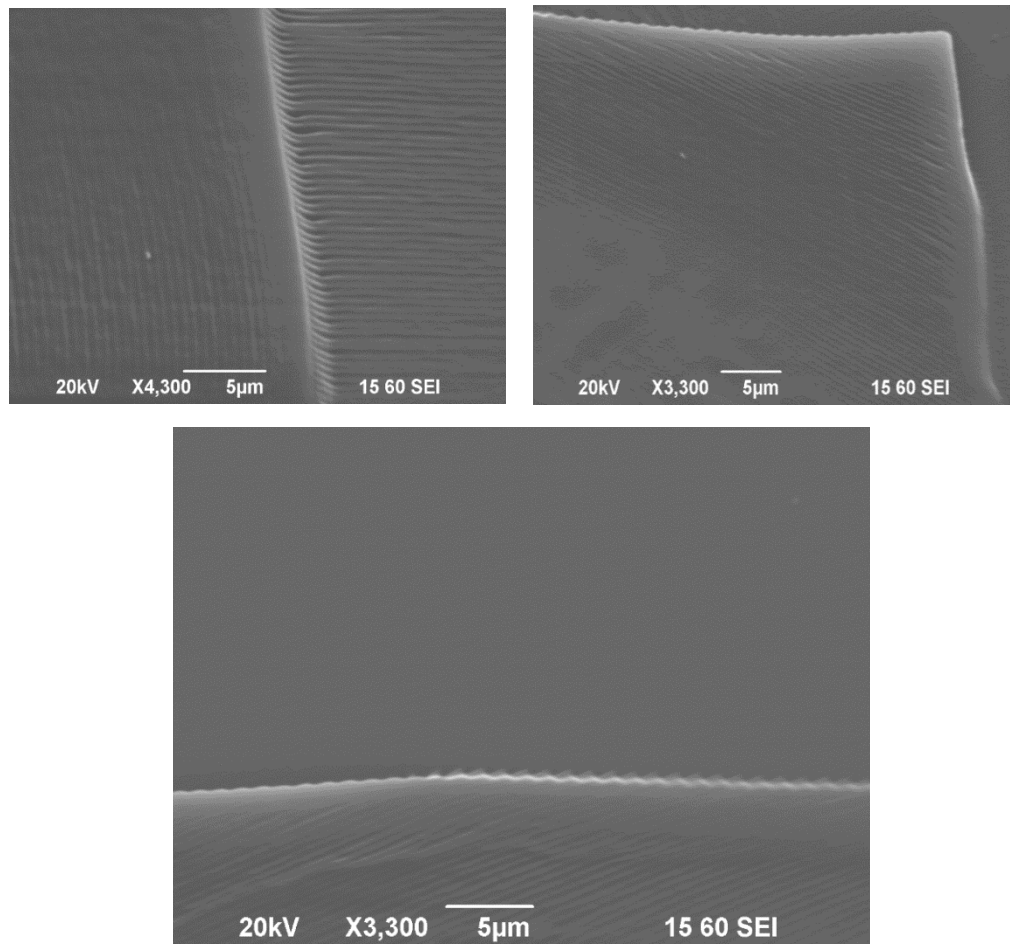


**Figure 3.43: SEM images showing the flat region of the fabricated TCDMDA multiplex construct with 0 and 90 (top, left and right side), 60 (middle) and 120 bottom degrees hatching directions.**



The grooves region of the PErA multiplex structure was fabricated complete and without damage. The 0° hatching direction was easily visible on SEM images (Figure 3.44).

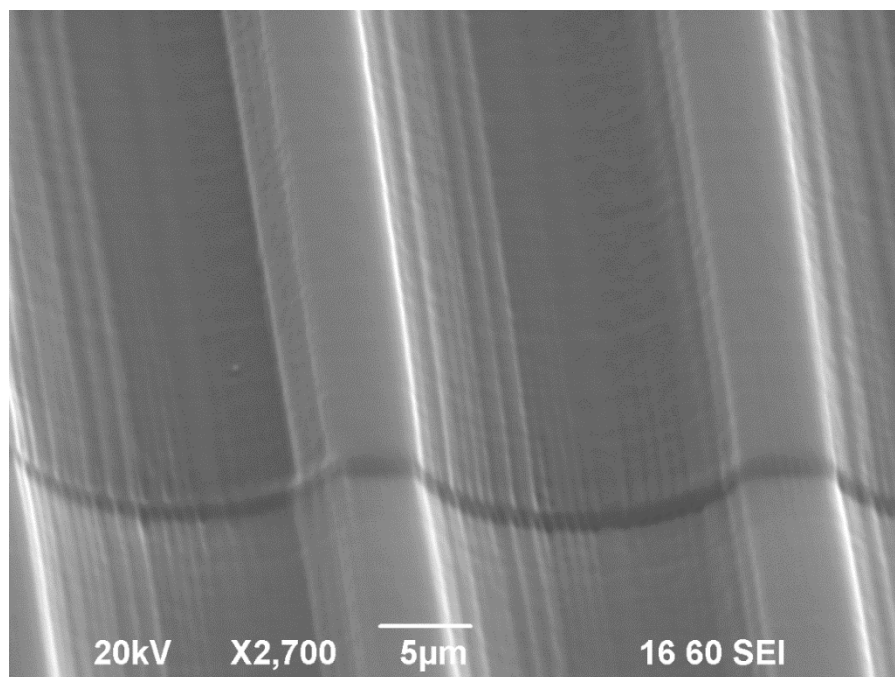
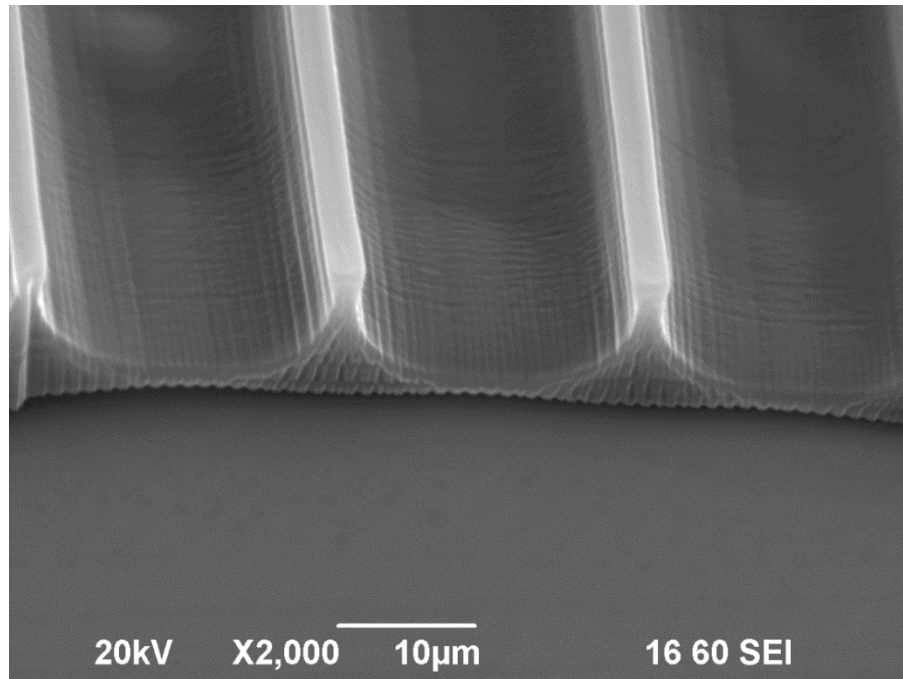


**Figure 3.44: PErA multiplex construct showing 0° hatching distance**

The hatching directions for PETrA were fabricated complete except for some damage on the right side of the 0° hatching direction (Figure 3.45, top, left side shown by the blue arrow).

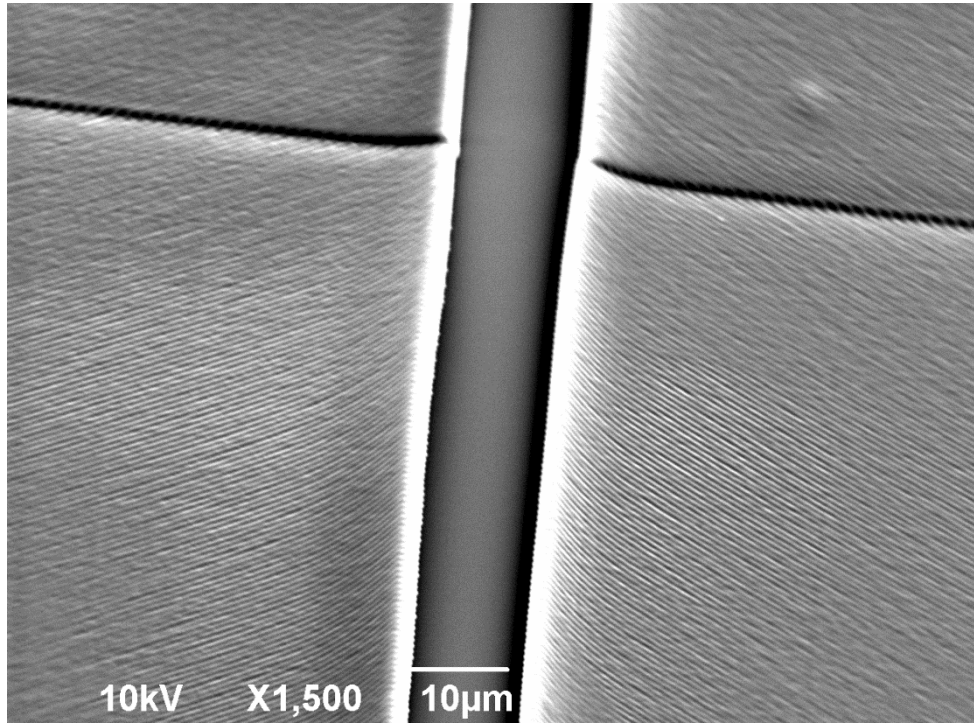
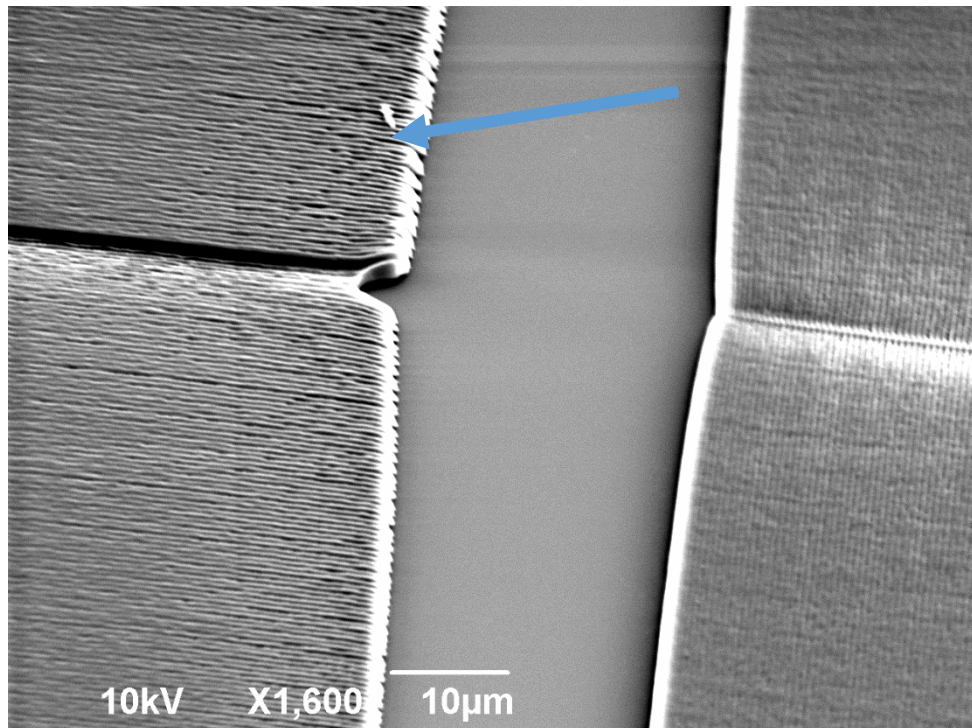


**Figure 3.45: PETrA multiplex construct showing the flat region and hatching directions from top left: 90°, top right: 0°, bottom left: 60° and bottom right: 120°.**

Figure 3.45 SEM images leads to the finding that each region with its specific hatching direction requires a different laser power and scanspeed combination in order to be fabricated without damage. This is why it was important to split the 4 regions in the AutoCAD design software before exporting as .stl files. The four separate .stl files could then be opened in Describe software one by one to set the hatching direction and each region's required laser power and scanspeed values for optimized fabrication. This was done by trial-and-error using an optimally fabricated structure's energy values as a reference point to modify the laser power above or below that value to find the ideal parameters.

### 3.3 Discussion and Conclusions

All of the monomers found to be amenable to the 2-photon system were either diacrylates or triacrylates (Table 3.6), specifically, with 2 or 3 functional groups. This gave a good indication as to the types of polymers to utilise in future fabrication studies and CM attachment experiments. The results explained why monoacrylates or methacrylates are not likely to be amenable to 2-photon lithography. This is due to their lower number of functional groups giving them a lower chance of attaining radicalised monomers to participate in the propagation step of the polymerisation reaction (Carragher, 2007). The steric hindrance effects of methyl groups in the functional groups of methacrylates make it much more difficult for the free radical initiator to attack the carbonyl-carbon of the functional group to initiate the reaction (Jansen et al., 2003). These two factors meant the polymerisation reaction is much slower when methacrylates are involved, compared to diacrylates and triacrylates. There is an additional reason for why methacrylates still react when exposed to UV light but not with 2PL; 2PP requires 2 photons to be absorbed by the photoinitiator in a near-simultaneous fashion to subsequently propagate the polymer chains. The presence of methyl groups and less acrylate groups in a polymer makes the likelihood of 2-photon absorption even lower as opposed to the 1-photon absorption requirement in a UV polymerisation reaction. This is why the polymers found to be amenable to 2PL were diacrylates and triacrylates, as opposed to methacrylates. Formulations composed of methacrylates have been used previously and successfully fabricated by 2PL

(Claeyssens, 2009 #223), however a different photoinitiator with a higher absorption spectrum was used in that case. Photoinitiators with a higher 2PA cross-section could perhaps be used to fabricate methacrylates successfully in future studies. An alternative could be cross-linkers incorporated into the methacrylate monomer (such as thiol or multi-functional acrylates) which also improve structure resolution (Emons, 2012 #90). PIs synthesised from scratch to improve 2PA cross-sections by addition of benzene rings in the centre of the molecule and donor-to-acceptor terminal end groups could drastically increase the library of acrylate materials amenable to 2PL. Nevertheless, the work in this chapter provided a good working protocol towards identification of 2PL-amenable materials using specific conditions and reagents. The knowledge was valuable towards the operating window determination and complex structure fabrication.

When it was observed that a diacrylate could be processed, further diacrylates were attempted with 2-photon lithography which proved successful. The following trials with triacrylates then proved successful as expected.

Triacrylates had been extensively used in previous microfabrication studies (Tayalia, 2008 #59), as well as for biological applications (Claeyssens, 2009 #223). One common feature among all the successful polymers was their relatively high viscosity and insolubility in water. It has already been shown that viscosity has an influence on the operating window of 2PL-amenable materials (Zandrini, 2019 #192). This meant the process would be limited to polymers insoluble in water. This correlated with the fact that di- and tri-acrylates have a higher rate of polymerization than methacrylates (Jansen et al., 2003). This is due to steric hindrance caused by the methyl group in methacrylates which inhibits nucleophilic attack by free radicals during the initiation stage of polymerisation (Jansen et al., 2003). Two-photon polymerisation requires the simultaneous absorption of two photons by the photo initiator molecule whereas UV polymerisation requires the absorption of one photon only. This means the photo initiator molecule needs to have a large quantum yield (long lifetime in the excited triplet state) to complete the process of absorption by two photons.

Not all multi-functional acrylates fabricated with high precision across a range of energy values by 2PL. A specific example of this is the difference between

the operating windows of GPOTA versus that of HEODA. GPOTA possessed a much wider operating window which leaves large room for fabrication error. This could also even be applied to lower PI concentrations for GPOTA, down to 1%. HEODA could not fabricate any structure until 4% PI concentration. The same effect was observed with HDDA. HEODA and HDDA were both observed to be less viscous than GPOTA. This led to the suggestion that viscosity may be a factor in the polymerization reaction rate. One study had shown that an increase in viscosity affects the rate of polymerization by lowering the termination rate constant (De Schrijver and Smets, 1966). When the monomer is more viscous, the radical monomers are impeded by the viscosity so that more time is required for them to reach other radical monomers to terminate the reaction. Similar findings are in B.W.Brooks's study of methyl methacrylate in which viscosity does not affect the photoinitiator efficiency however influence of viscosity is observed in the translational diffusion of the polymer radicals (Brooks, 1977). It was also found that radicals over a specific size were affected by the solution viscosity (Brooks, 1977). Therefore, it is possible that HEODA and HDDA polymers have narrower operating windows than the more viscous GPOTA, PETrA and TCDMDA in 2PL due to the reduced translational diffusion of their polymer radicals.

The initial use of the gear design was to be able to get a clear observation of processing to determine which homopolymers would be useful for the 2-photon system. However, in the long-run, the utilisation of a gear design as a reference was not practical since various complex structures will be created with a material that is successfully processed with the 2-photon system and can support CM attachment as well as enhance CM maturity. Therefore, the woodpile design was created using AutoCAD which is simple, easy to observe and an array can be designed to observe processing over a large range of laser power values to determine the operating window at each photo initiator concentration. The operating window for the woodpile structure was much smaller, possibly due to the design defects of the second layer of cylinders. This highlights the importance of the fact that the operating window of a given material varies immensely depending on the material design, shape and hatching distance. Creation of the simpler woodpile design using coding

software of Nanoscribe provided a useful operating window reference for the creation of more complex structures. All other variables were kept constant, including photo initiator concentration and energy absorption. These experiments pave way to using a reference design for optimal photo initiator concentration determination which will be simple and have a hatching distance larger than the slicing distance so that this variable is negligible.

HEODA:PPGDA, HEODA:PPGA, BDDA:GPOTA and PPGDA:GPOTA, were the 4 co-polymers amenable to 2PL at 70:30 ratios of major monomer to minor monomer. The first 3 co-polymers had narrow operating windows which can be attributed to the fact that all the major monomers in these co-polymers (HEODA and BDDA) were the multi-functional acrylates. The major monomer in a co-polymer has the most influence in terms of fabrication. The influences of major and minor monomer are different when it comes to cell attachment (Patel et al., 2015) as for example HEODA as a homopolymer did not support a high number of cells however as a co-polymer with EEMA it supported the highest number of cells (Patel et al., 2015). The aim of this study is to find a polymer that has a good working range for the purposes of 2PL as this will be the technology used throughout the project for the purposes of investigating sub-micron feature effects on CMs. Only the homopolymers found amenable to 2PL were utilised in CM attachment experiments. The 7 homopolymers amenable to 2PL (Table 3.6) were carried onto the next series of experiments to determine CM attachment.

Fabrication of complex architectures using optimal energy values based on the calculations between laser power, scanspeed and energy values (Table 2.2 and 2.3) produced complete and undamaged structures. This demonstrates the usefulness of these calculations as a reference point when new complicated structures need to be built without the need for trial and error of a large range of energy values.

Measurements of hatching distances on open channel structures show that there is a difference in the hatching distance values between fabricated structures and design dimensions, with the former being smaller. This is attributed to polymerization shrinkage and is useful guideline to consider when planning



structure fabrication. Polymerization shrinkage is a known limitation in 2PL. The process has been found to occur in previous 2PL studies (Baldacchini, 2011 #213) as well as various other polymerization techniques (Schricker, 2017 #227). One particular study concluded the polymerization shrinkage to be 2% per micron of material polymerised (Zhou, 2015 #73). The average polymerization shrinkage for 5 micron deep grooved structures was approximately 4% (3.2.4.2 Open-channel multiplex structures). The process depends on photo initiator concentration and the polymer being used, among other factors. Pre-compensation for polymerization shrinkage on 2PP structures have been done previously (Sun, 2004 #226) in which allowance for the design dimensions were made prior to fabrication. Some materials were found to not even require any pre-adjustments due to polymerization shrinkage. Ultra-high resolution structures were fabricated by merely adjusting the mol% of inorganic component in the formulation with wafer-thin structures up to 13 micron heights (Ovsianikov, 2008 #225). This finding of precompensation is applied in Chapter 5 in the construction of grooves for cardiomyocyte attachment experiments.

### 3.4 Future Work

The number of functional groups on an acrylate polymer and whether the functional group contains a methyl (-CH<sub>3</sub>) group has an effect on the rate of polymerisation. 2-photon polymerisation is determined by a number of factors; the polymer being tested, the photoinitiator, laser power, scanspeed, photoinitiator concentration and material composition in the case of copolymers. A more extensive literature search of available photo initiators with higher 2PA cross sections would definitely add to the acrylate amenable to 2PL, namely methacrylates. The more efficient PIs would enable their amenability to 2PL since they pose steric hindrance effects.

All of these factors were taken into account and 2-photon amenability determined in the most efficient way possible with polymers available. The operating window of a polymer also depends on structure design as illustrated by the gear versus woodpile designs in this study. The gear is more complex

with all the jagged corners of the teeth compared to the woodpile design which is merely series lines laid on top of one another. This means the more complex a structure is the narrower the operating window. The system requires more energy to fabricate all the complex parts of a structure which would naturally decrease  $E_{max}$  and increase  $E_{min}$ . Complex structures for the future could include hearth patches or a multi-layered scaffold in which endothelial cells could also be seeded to support CMs (Fleischer, 2017 #221).

Future work on the scaffolds for CM seeding could involve testing a wider range of groove depths and combining CM seeding with endothelial cell seeding for vascularisation. Perhaps using novel materials that can be fabricated with water-soluble PIs such as P2CK could widen the range of 2PL-amenable materials.



## CHAPTER 4: Cardiomyocyte attachment experiments on UV-polymerized constructs

### 4.1 Introduction

The work done in Chapter 3 identified a set of acrylate monomers amenable to 2PL. The next step was to determine which of these had the capability to support CM attachment. 2PL was a relatively slow process compared to other light-assisted fabrication methods. The aim here was to identify CM attachment only. UV polymerisation was applied to simultaneously polymerize all candidate materials, followed by CM attachment. Several factors were varied to observe changes in CM attachment capability and the degree of cure of the resulting polymers was compared. Silanisation of the surfaces the polymers were in contact with was done and the need for this pre-treatment discussed.

Overall, this chapter determined the necessity of silanisation during UV polymerisation of acrylate polymers. In addition, 2PL-amenable polymers from Chapter 3 were tested for their ability to support CMs. This enabled the polymers with the most desirable characteristics to be utilised for CM maturity experiments (discussed in Chapter 5).

## 4.2 Results

### 4.2.1 Determination of the correct solvent at a suitable concentration for silanisation for polymer attachment to polystyrene plates

The solvents chosen for investigation following review of the literature were acetone and isopropanol. The solvents were tested independently of silane first, by filling wells with the solvents only. The results show that acetone solvent turned cloudy whereas isopropanol remained clear (Table 4.1). This was done to validate that acetone solvent is not suitable for experiments with polystyrene. The wells containing TMSPMA only also turned slightly cloudy, indicating a reaction happening between polystyrene and TMSPMA as well (Table 4.1). The next experiment was then designed to determine how much silane can be added to isopropanol until the solution turns cloudy (Table 4.2).

**Table 4. 1: The effect of 2 solvents and TMSPMA on polystyrene 96-well bottom surfaces.**

| <b>Solvent</b>     | <b>Appearance</b>   |
|--------------------|---------------------|
| <b>Acetone</b>     | All cloudy          |
| <b>Isopropanol</b> | All clear           |
| <b>TMSPMA</b>      | All Slightly cloudy |

The wells containing isopropanol solvent all showed cloudy patches in the solution except for the last well with volume 0.025  $\mu\text{l}$  (Table 4.2). This means the maximum volume of TMSPMA that can be used without resulting in a cloudy solution is 0.025  $\mu\text{l}$  TMSPMA in 15  $\mu\text{l}$  of isopropanol which is equivalent to a concentration of 1.67  $\mu\text{l}/\text{ml}$ .

**Table 4. 2: The effect of silane at a range of volumes in each of the solvents acetone and isopropanol.**

| <b>Silane volume (<math>\mu\text{l}</math>)</b> | <b>Isopropanol</b> |
|---|--------------------|
| <b>1</b>  | Cloudy             |
| <b>0.5</b>                                      | Cloudy             |
| <b>0.25</b>                                     | Cloudy             |
| <b>0.1</b>                                      | Cloudy             |
| <b>0.05</b>                                     | Cloudy             |
| <b>0.025</b>                                    | Clear              |

Now that isopropanol was deemed as the suitable solvent with 1.67  $\mu\text{l}/\text{ml}$  silane concentration, the effects of polymerising acrylates under UV light had to be determined. This is described in the next section.

#### 4.2.2 Determination of the necessity of silanising wells for UV polymerisation

The three polymers TCDMDA, GPOTA and PETrA were selected for this experiment as they would be used for future CM attachment experiments (Chapter 5).

It took 1 minute for TCDMDA and PETrA silanised wells to form white rings as shown by the blue arrows. In contrast, GPOTA silanised wells remained clear and all non-silanised wells appeared clear (Table 4.3). The plate was then placed back under the UV lamp (Blak-Ray® XX-15L, 15 Watt, 365 nm). 20 minutes of UV exposure showed that TCDMDA and PETrA silanised samples appeared to have increased cloudiness whereas GPOTA still remained clear (Table 4.3). Meanwhile, the non-silanised samples of TCDMDA and PETrA showed very slight signs of cloudiness and GPOTA remained clear (Table 4.3). All silanised and non-silanised polymers showed yellow colour formation, with GPOTA being the strongest shade of yellow (Table 4.3). Yellowing occurs due to thermal oxidation of the polymer backbone, which is due to UV light exposure. The longer the duration of UV polymerisation the more yellowing occurs.

Further UV exposure showed that the silanised wells typically appeared to exhibit even more cloudiness after 45 minutes of UV exposure compared to the same wells after 20 minutes of UV exposure (Table 4.3). TCDMDA and PETrA had the same white rings as they did after 1 minute of UV exposure however GPOTA did not. All non-silanised samples remained clear (Table 4.3).

This experiment showed that silanisation is an influential factor in forming these white rings, and the time spent under UV light. However, it also shows that silanisation is not the only factor causing the cloudiness observed. This is polymer dependent as TCDMDA and PETrA showed cloudiness in non-silanised wells too (Table 4.3).

These experiments above were designed so as to make surfaces on which UV polymerisation could be performed that were consistent with the surfaces of glass cover slips used for 2PP, i.e. so that both would be silanised. However, it was observed silanisation proved to be an issue in UV polymerisation as the polymers showed cloudiness. This meant observation of any CM attachment may be hindered as well as influence CM attachment and behaviour, which is not desirable.

**Table 4. 3: Comparison of the effects of silane on 3 different acrylate polymers. Non-silanised solutions were also tested. All conditions were in isopropanol solvent at the concentration previously determined (1.67 ul/ml).**

| Polymer | Time taken for cloudiness to appear (minutes) |                |
|---------|---|----------------|
|         | Silanised                                     | Non-silanised  |
| TCDMDA  | 1   | 20             |
| GPOTA   | Remained clear                                | Remained clear |
| PETrA   | 1   | 20             |

It was postulated that the volume of the formulations may be related to white ring formation. Polymerization shrinkage is a common occurrence in which the material shrinks upon polymerisation due to increased bond formation and

packing of the polymer molecules. Polymerization shrinkage may therefore cause the polymer to accumulate around the edges of the well which may be giving the ‘ring’ appearance. Therefore, a follow-up experiment to determine if there was a minimum monomer volume needed to cover the well surface was performed and so prevent this ‘white ring’ formation. Five different volumes were tested: 15, 20, 25, 30 and 35  $\mu$ l. Each volume set had 5 repeats of TCDMDA, GPOTA and PETrA monomers with 1% PI formulations. The samples were not silanised.

The 15, 20 and 25  $\mu$ l formulations all showed gaps in the middle of the well surface. The largest gap was at the 15  $\mu$ l formulation loading as expected. This is most apparent in the TCDMDA samples (Table 4.4). The 30 and 35  $\mu$ l samples showed no gaps or openings on the well surface (Table 4.4).

**Table 4. 4: Results of monomer volume effects on gap formation during polymerisation of acrylates.**

| Polymer       | Volume ( $\mu$ l) |     |     |         |         |
|---------------|-------------------|-----|-----|---------|---------|
|               | 15                | 20  | 25  | 30      | 35      |
| <b>TCDMDA</b> | Gap               | Gap | Gap | No Gaps | No Gaps |
| <b>GPOTA</b>  | Gap               | Gap | Gap | No Gaps | No Gaps |
| <b>PETrA</b>  | Gap               | Gap | Gap | No Gaps | No Gaps |

The size of the rings at any one volume varied among different monomers. At 15  $\mu$ l volume TCDMDA possesses the largest ring on the well bottom with GPOTA and PETrA having smaller gaps (Table 4.4). Meanwhile, the 30 and 35  $\mu$ l volume wells showed no gaps on the well bottom surface indicating that polymerization shrinkage is insufficient in creating these gaps at these particular volumes (Table 4.4). However, a problem arose with high volumes, i.e. liquid monomer was still present. When a pipette tip was placed on the surface liquid monomer remained. 90 minutes of UV exposure was required to solidify the construct. Further analysis into whether higher monomer volume decreased cloudiness in silanised solutions would be required. However, experiments were paused here as it was observed that low monomer volume resulted in poor visibility and increasing monomer volume then resulted in incomplete polymerisation which could cause cytotoxicity.

### 4.2.3 Induced pluripotent stem cell (IPSC) culture

After the experiments for determining the requirement of silanisation of 96-well plates, cell culture procedures were commenced. IPSC maintenance and IPSC to cardiomyocyte (CM) differentiation protocols were performed by following a previously established protocol (Burridge et al., 2014) used in the STEM Group, University of Nottingham. Once the CMs were obtained, they were seeded onto the 96-well plates to determine which polymers were able to support their attachment. The section below outlines the IPSC maintenance and the stages of differentiation procedure.

#### 4.2.3.1 IPSC feeding

IPSCs were fed every day and during differentiation to cardiomyocytes on specific days according to the protocol described in 2.6.1.4 Differentiation to CMs.

The IPSC flask media appeared slightly cloudy right before feeding. The media also turned from the characteristic red colour of E8 medium to a dark orange colour. This is due to the pH change in the medium caused by the carbon dioxide released by the metabolically-active cells. If the medium appeared very cloudy or very pale yellow, then it was checked for contamination. Bacterial contamination typically appears as many small spots distributed around the cells. Fungal contaminations appear as small particulates near the cells with outgrowths.

#### 4.2.3.2 IPSC Splitting

IPSCs were split every 72 hours during maintenance. The cells are ready for splitting when they have formed dense colonies with high confluency of approximately 70%. The confluency of cells is a definition of what percentage of the flask bottom is covered by cells. White streaks appear within the colonies (Figure 4.1) which indicate the IPSCs are accumulating debris on top of them as cell proliferation levels reach a threshold (Figure 4.1).

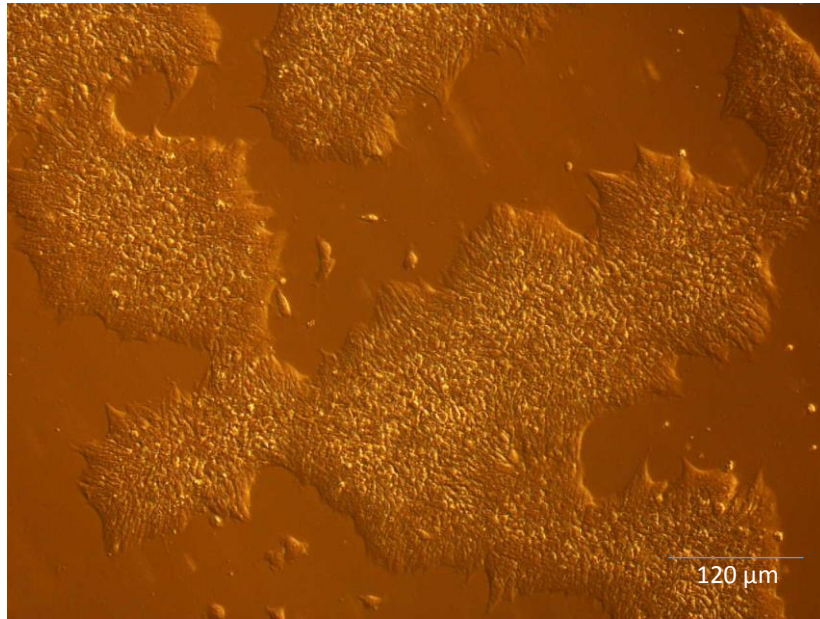


**Figure 4.1: IPSC colonies ready for splitting after 72 hours.**

IPSCs appeared as sparse, small colonies 24 hours following a split (Figure 4.2). This is characteristic of IPSCs as they require time to attach to the flask bottom and start to proliferate.

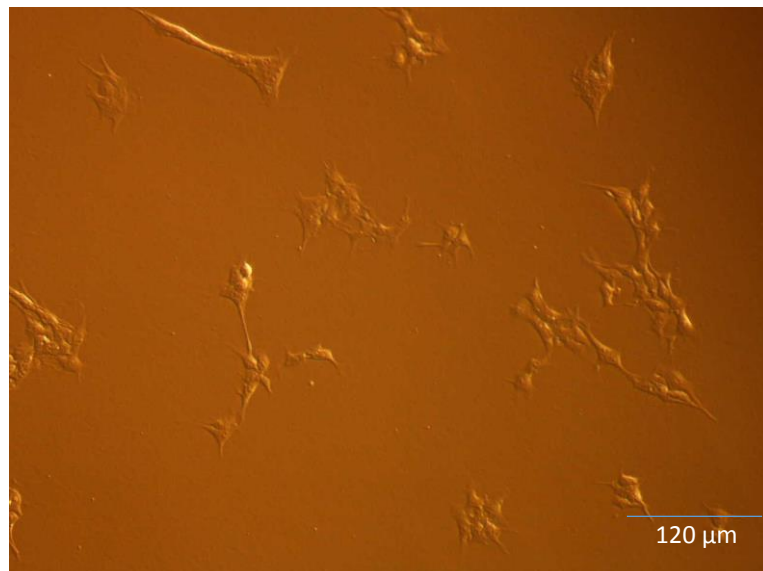


**Figure 4.2: IPSCs 24 hours after splitting.**

IPSCs proliferate rapidly for the next 24 hours, giving rise to large colonies (Figure 4.3). White streaks begin to appear on top of the colonies however the cells themselves still have fairly sharp edges compared to cells 72 hours after splitting (Figure 4.2).

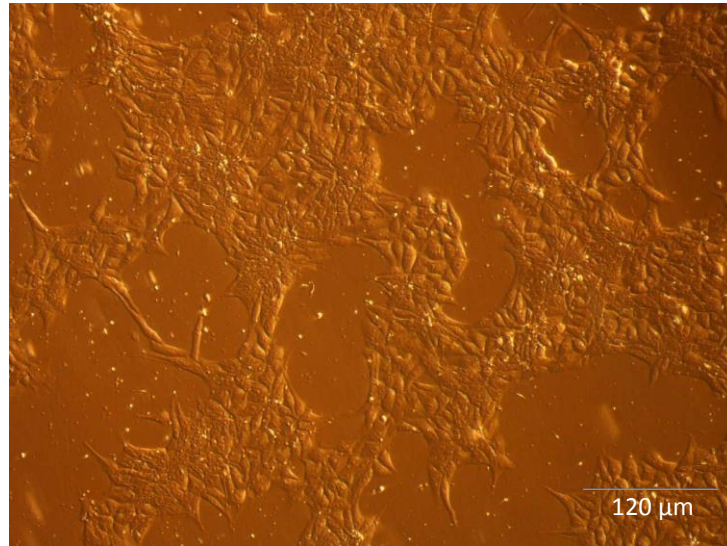


**Figure 4.3: IPSC colonies 48 hours after splitting.**



#### 4.2.4 iPSC differentiation to cardiomyocytes

Day 0: iPSCs adopted the characteristic ‘cheese’ morphology that is observed after Matrigel and Bmp4 were added on day -1 (Figure 4.4). The cells cluster very tightly together so their edges are not visible. Large holes form intermittently in the flask giving the overall ‘cheese’ morphology (Figure 4.4).

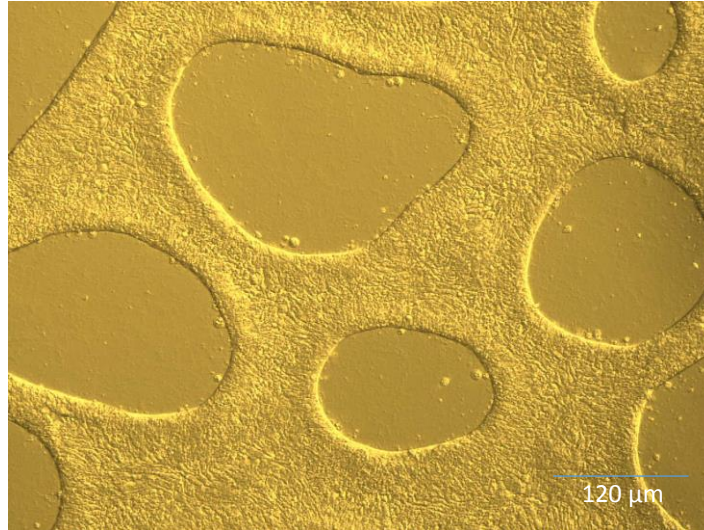


**Figure 4.4: Characteristic ‘cheese’ morphology on day 0 of cardiac differentiation.**

Day 2: Cells lose the ‘cheese’ morphology. A lot of cell death occurs at this stage (Figure 4.5a) therefore it is difficult to see the cells at the bottom of the flask. They are much easier to visualize after feeding (Figure 4.5b).

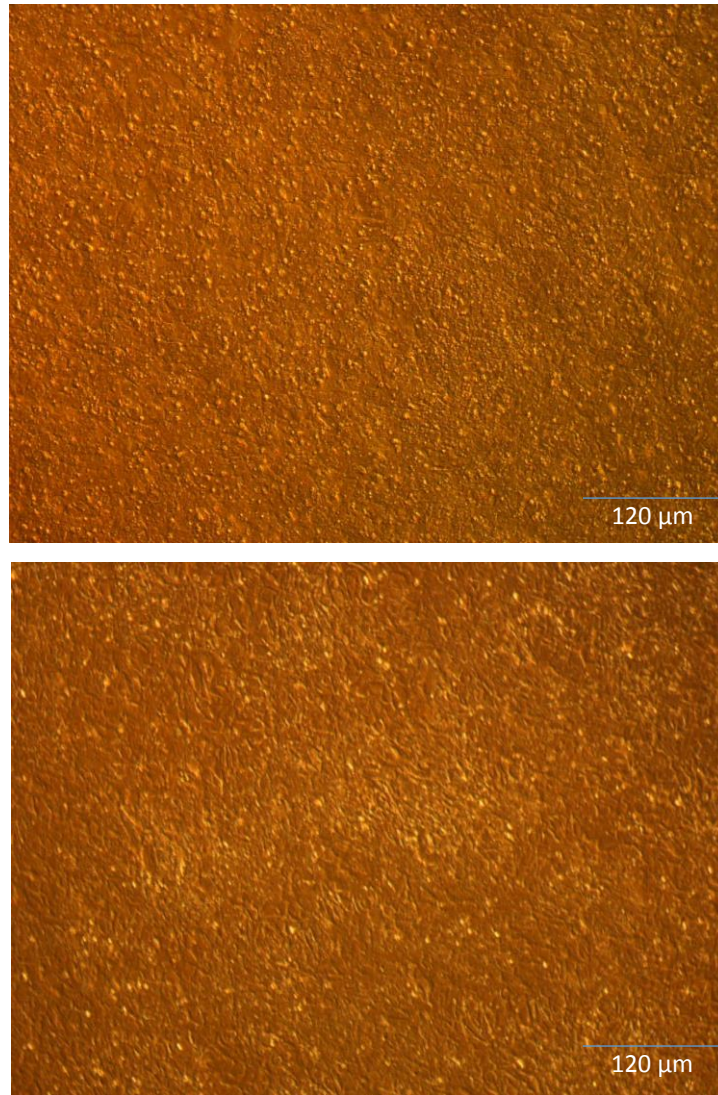


**Figure 4.5a: Cells on day 2 of differentiation b: before feeding and**

**Bottom: after feeding.**

Cells form a monolayer on the bottom of the flask (Figure 4.5b). The norm is a significant amount of cell death therefore it may not be visible before cell feeding. However, shaking the flask while viewing under the microscope may help with observing the colony underneath the dead cells. This cell death is due to the cells having to adapt to a new type of metabolism which involves feeding on glucose instead of lactate. iPSCs in their proliferative stage feed on lactate.



Day 4: The cell monolayer can be clearly observed at this stage (Figure 4.6). There is still numerous cell death so the same guidelines apply as on day 2.

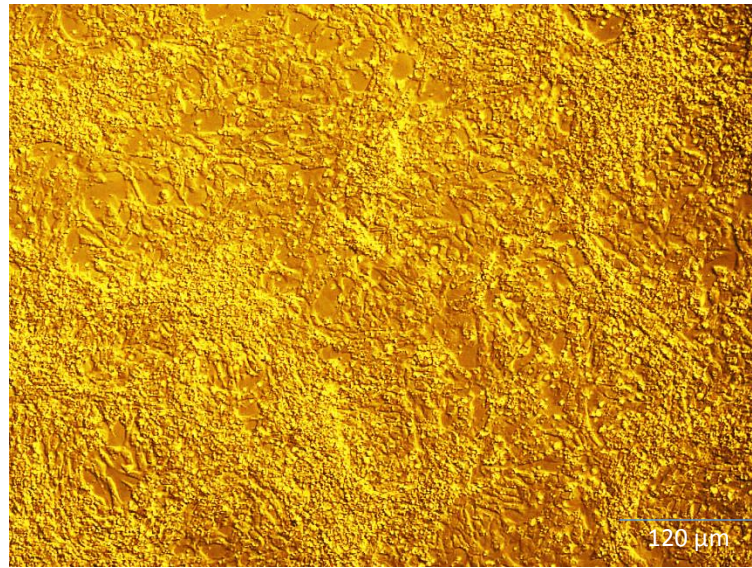


**Figure 4.6: Cells on day 4 of cardiac differentiation. The monolayer can be clearly observed at this stage.**

Day 6: Another stage where numerous cell death occurs is on day 4 (Figure 4.7). This is due to the addition of insulin to the medium. The cells have to adjust to having insulin in their media and change their signalling mechanism as KY and XAV lose their effectiveness. This is because insulin blocks KY and XAV small molecules.



**Figure 4.7: Day 6 of cardiac differentiation. Cell death occurs again at this step.**

Day 8: Cells on day 8 have clearly formed the monolayer and taken on individual cardiomyocyte morphology (Figure 4.8). These are elongated cells which unlike iPSCs, do not possess spiky edges. Cardiomyocyte beating can be observed from this day onwards.

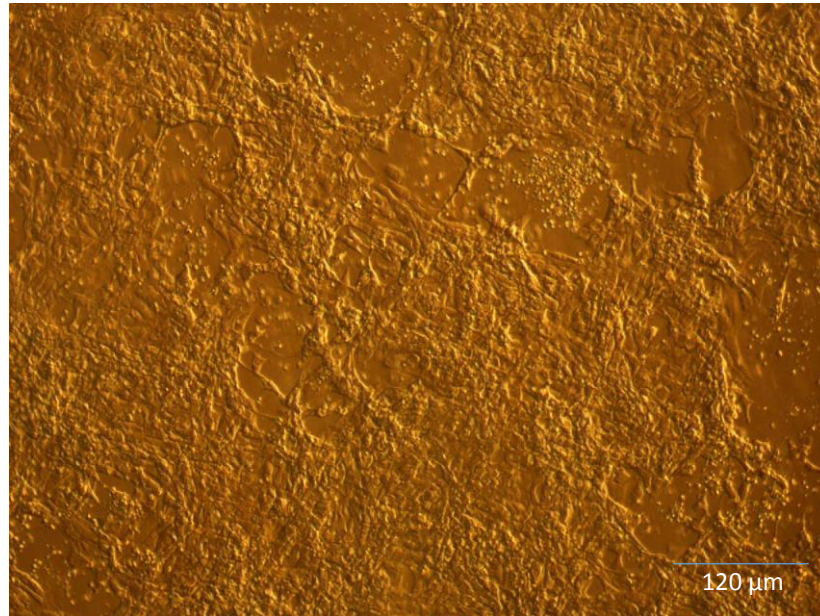


**Figure 4.8: Day 8 of cardiac differentiation. Beating can be observed from this day onwards however they are not ready for dissociation yet.**



Days 10-14: Cardiomyocytes have formed large colonies and partly dissociated from the flask bottom. The edges of the colonies are attached to the flask and beating is more rigorous (Figure 4.9). This stage can begin from day 10 to day 14 depending on the iPSC batch used for the differentiation. It is crucial that cardiomyocytes are dissociated before they detach themselves from the flask completely. This will mean the cells will float in the medium and eventually apoptose.

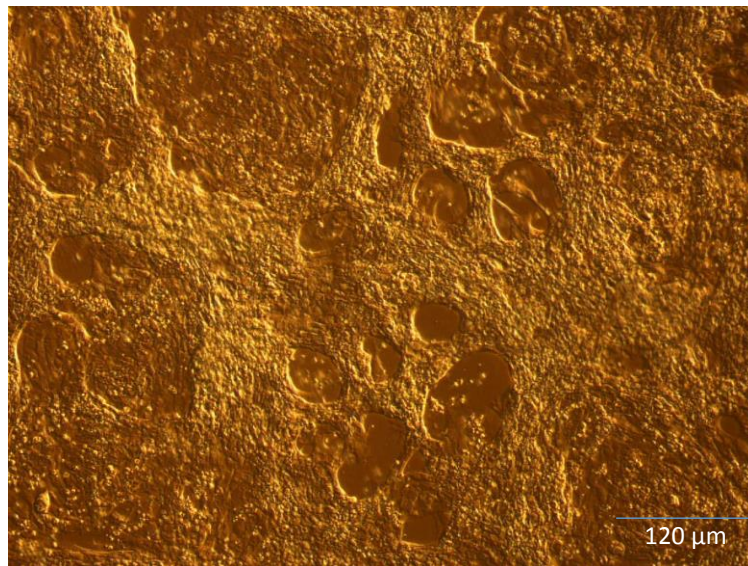


**Figure 4.9: Days 10-14 of differentiation. Cardiomyocytes are ready for dissociation at this stage.**

#### 4.2.5. Cardiomyocyte attachment to UV-polymerised constructs

CM attachment varied according to PI formulation used and the polymer being tested (Figure 4.10). GPOTA exhibited the highest % cell viability in the DMPA:IPA formulation whereas it showed considerably lower viability in the DMPA formulation. The highest % cell viability for DMPA formulation was with the TCDMDA polymer. GPOTA also demonstrated the highest % cell viability with the I369 formulation.

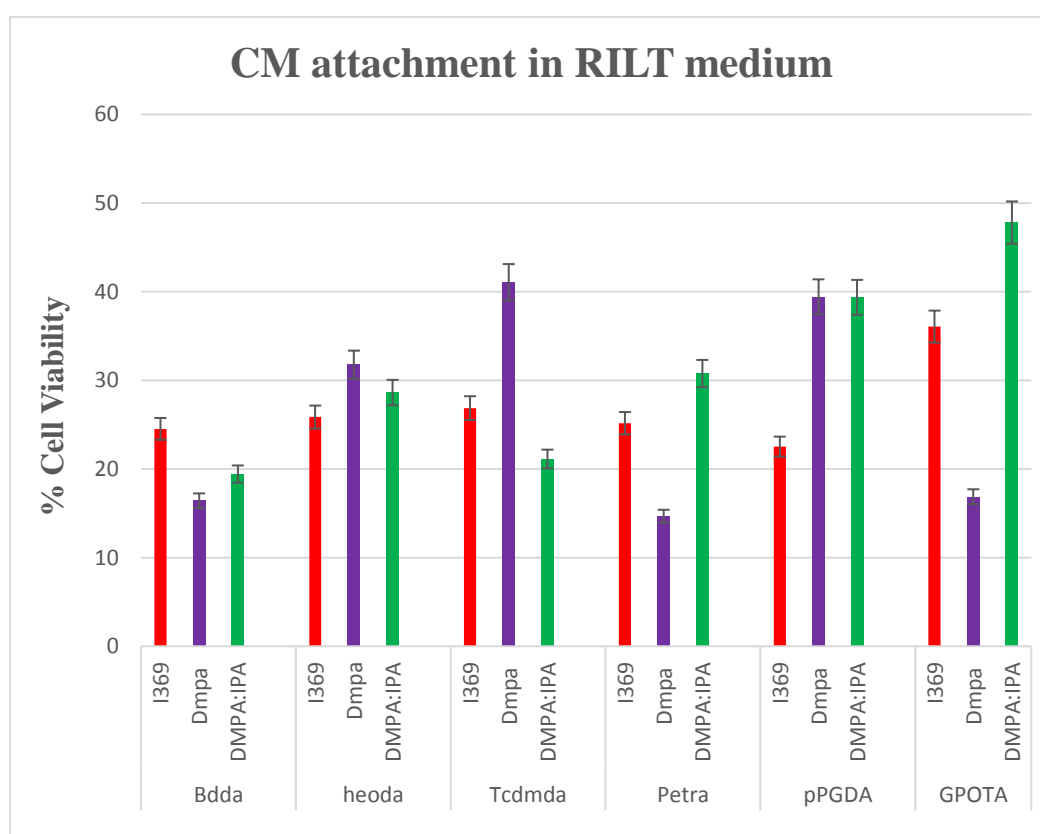


**Figure 4.10: Quantitative Analysis of CM attachment on all polymers with 3 different photoinitiator formulations in RILT medium.**

Statistical tests showed that some of the differences percentage cell viability were significant. GPOTA, PetRa and BDDA were the three polymers that showed significant differences due to various PI formulations they were prepared in (Table 4.5).

**Table 4. 5: Results of ANOVA single-factor analysis of cell viability, highlighting the polymers that demonstrated significant differences among the 3 different PI formulations.**

| Polymer | F value         | F-critical value |
|---------|-----------------|------------------|
| GPOTA   | <b>129.7692</b> | <b>9.552094</b>  |
| PetRa   | <b>34.0063</b>  | <b>9.552094</b>  |
| BDDA    | <b>9.944392</b> | <b>9.552094</b>  |

PetRa and BDDA showed significant differences between I369 and DMPA:IPA formulations compared to the viability differences between the other PI formulation combinations. I369 may have dissolved these acrylate monomers more successfully compared to DMPA:IPA which improves cell viability.

GPOTA showed the biggest difference in cell viability between DMPA and DMPA:IPA formulations. This may have been due to the use of IPA solvent in the DMPA:IPA formulation which helped to dissolve the solid DMPA photoinitiator more efficiently which reduced cytotoxicity (Table 4.6).

**Table 4. 6: Results of student's t-tests showing the %cell viability with significant differences based on the polymer tested from ANOVA results in Table 4.5.**

| <b>Polymers that showed Significant Difference in %Cell Viability</b> |                 |
|---|-----------------|
| <b>PI Comparison</b>  | <b>Polymers</b> |
| <b>I369 vs. DMPA</b>  | PetRa           |
| <b>I369 vs. DMPA:IPA</b>  | PetRa and BDDA  |
| <b>DMPA vs. DMPA:IPA</b>  | GPOTA           |

I369 and DMPA:IPA formulations showed the largest variance among the 6 polymers tested (Table 4.7). The exact polymers that showed significant differences between each other are described in the next section (Table 4.7).

**Table 4. 7: Results of ANOVA single-factor analysis of cell viability, highlighting the PI formulations that resulted in significant differences among the 6 polymers tested for CM attachment.**

| Photoinitiator | F value         | F-critical value |
|----------------|-----------------|------------------|
| I369           | <b>5.954384</b> | <b>4.387374</b>  |
| DMPA:IPA       | <b>73.2646</b>  | <b>4.387374</b>  |

Table 4.7 lists the polymer combinations that showed the largest significant differences in cell viability in I369 or DMPA:IPA formulations. GPOTA was a significant component of the majority of these results. Referring to the bar chart, GPOTA did have the highest cell viability in both I369 and DMPA:IPA formulations. The other polymer combinations followed accordingly. GPOTA was able to dissolve I369 PI very quickly compared to PetRA or TCDMDA by observation during experimental conduction which may explain the results here. The differences between HEODA and PPGDA and PETRA and PPGDA for example, showed smaller differences in cell viability compared to the combinations that involved GPOTA.

**Table 4. 8: Results of student’s t-tests showing the polymers that differed significantly from each other in each PI formulation found to have significant differences by ANOVA (Table 4.4).**

| PI formulation |                 |
|----------------|-----------------|
| <b>I369</b>    | <b>DMPA:IPA</b> |
| PETRA:GPOTA    | BDDA:PETRA      |
| PPGDA:GPOTA    | BDDA:PPGDA      |
|                | BDDA:GPOTA      |
|                | TCDMDA:GPOTA    |
|                | HEODA:GPOTA     |
|                | TCDMDA:PETRA    |
|                | TCDMDA:PPGDA    |
|                | PPGDA:GPOTA     |
|                | PETRA:GPOTA     |
|                | PETRA:PPGDA     |
|                | HEODA:PPGDA     |

GPOTA also had the highest % cell viability with I369 formulation in RPMI B27 medium (Figure 4.12). TCDMDA and PPGDA both showed high viability in DMPA:IPA formulation. TCDMDA and GPOTA showed the highest cell percentage cell viability with the DMPA formulation. This is contrast to



GPOTA showing the one of the lowest % cell viability values with the DMPA formulation in the RILT medium (Figure 4.11). GPOTA also demonstrated a considerably higher % cell viability in RPMI B27 medium compared to RILT medium. These results indicate that PI formulation, polymer identity and cell culture medium influences percentage cell viability. These results were based on one measurement per condition therefore statistical tests could not be conducted.

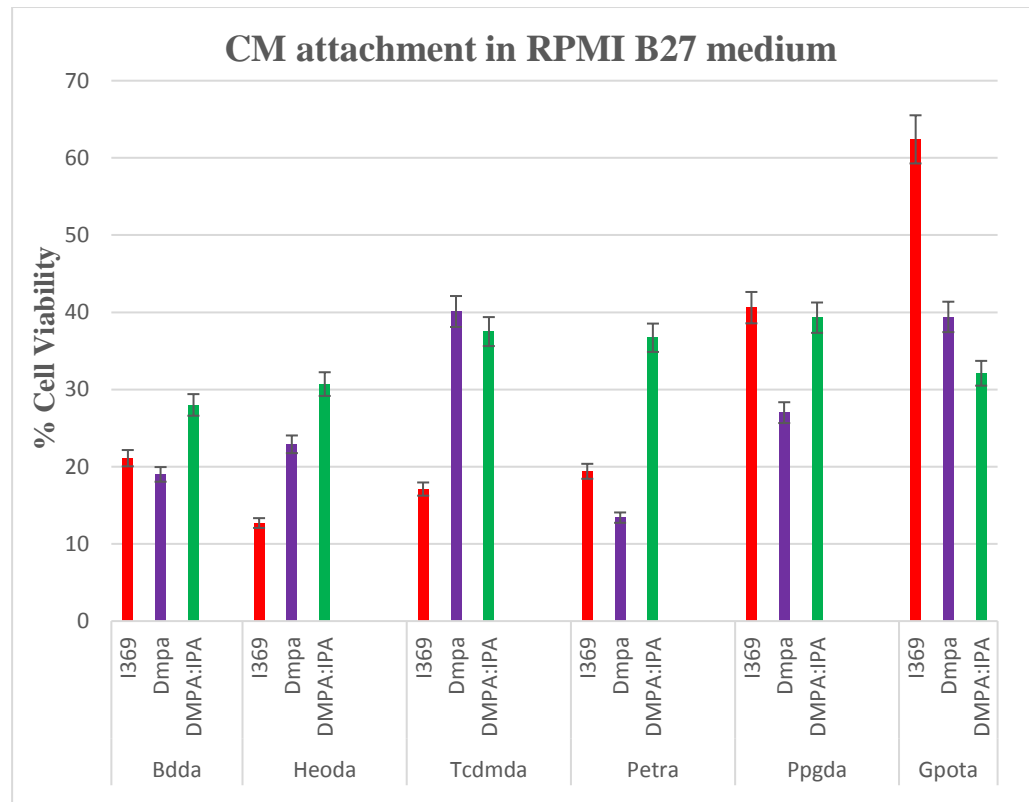


**Figure 4.11: Quantitative Analysis of CM attachment on all polymers with 3 different photoinitiator formulations in RPMI B27 medium.**

#### *4.2.5.3 Raman spectroscopy to compare the degree of cure achieved with the photo initiators applied for CM attachment*

Raman spectroscopy was used to investigate whether the different photoinitiator formulations had an effect on the degree of cure and potentially, CM attachment. The spectra were taken from PETrA under the formulations using I369, DMPA and DMPA:IPA solvent. All 3 raman spectra showed the characteristic C=C and C=O peaks at 1640 and 1720  $\text{cm}^{-1}$  respectively (Figure 4.18). All 3 spectra showed a decrease in the C=C peak and a widening of the C=O peaks from uncured to cured states of PETrA. The DMPA and DMPA:IPA spectra showed small peaks next to the C=C peak at approximately 1590  $\text{cm}^{-1}$  which indicated remaining photoinitiator in the samples.

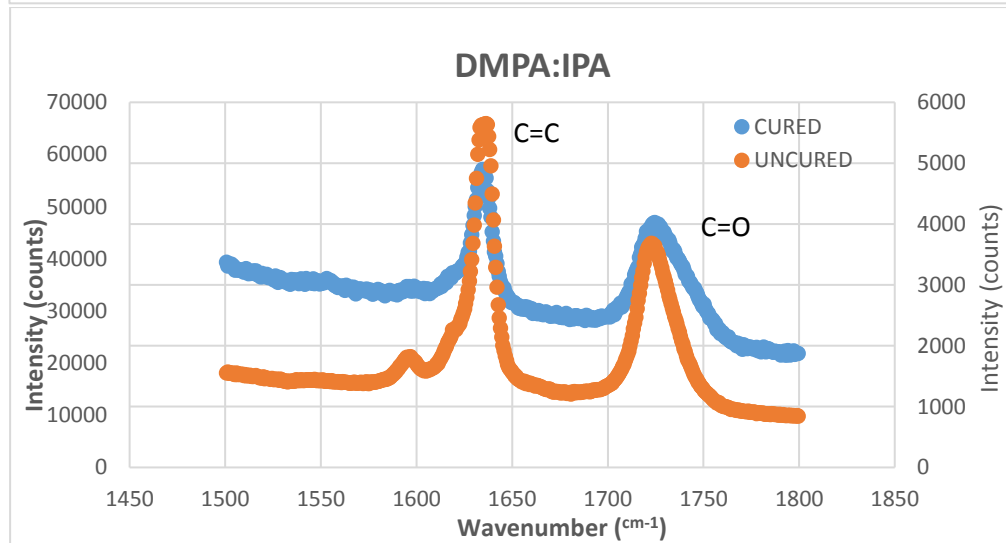
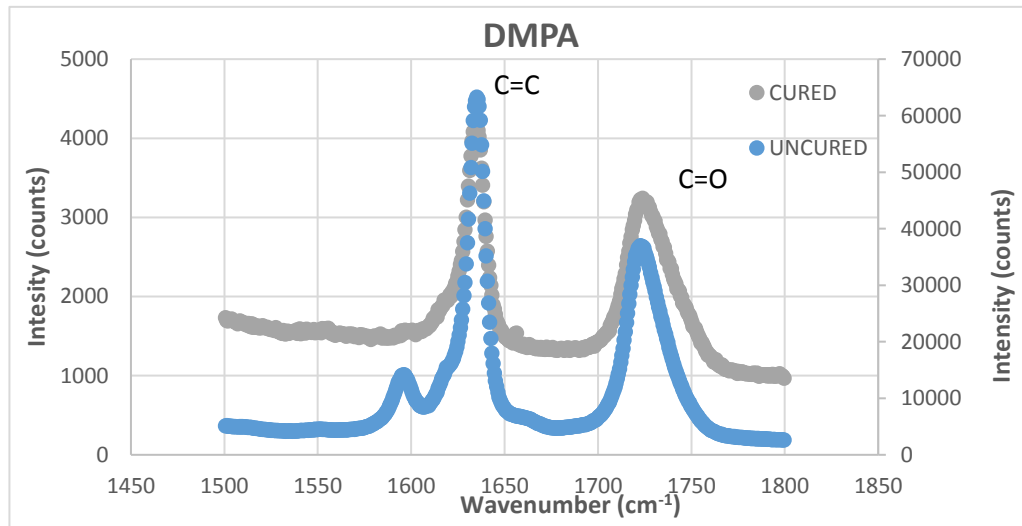
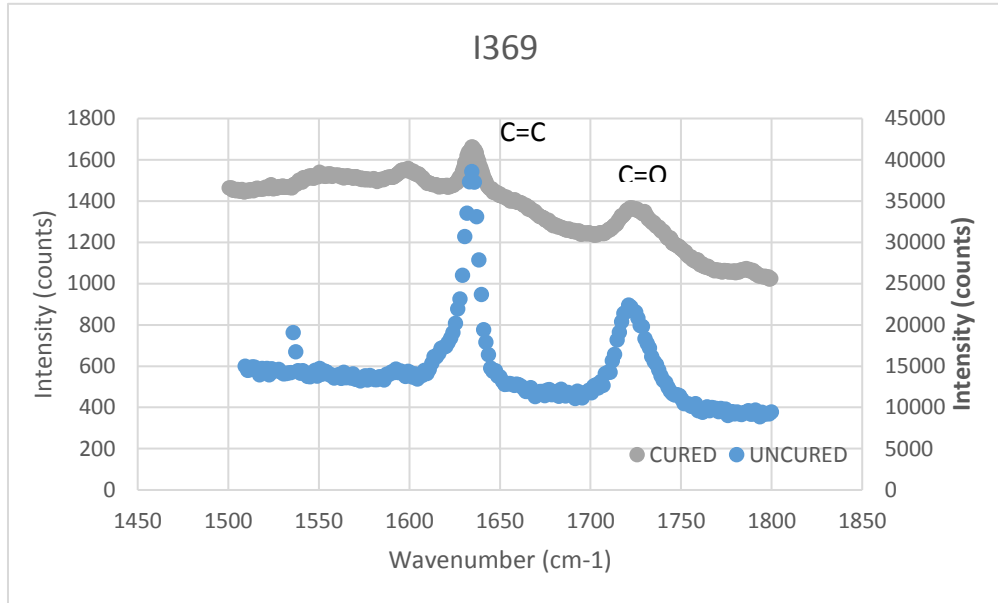


**Figure 4.18: Raman spectra of PETrA polymer in the 3 different formulation types.**

It was immediately obvious that the DOC of DMPA was much lower than the one of I369. This could explain the lower CM attachment on constructs polymerized with DMPA in RILT medium compared to good attachment on constructs polymerised with I369 (Figure 4.18). Constructs polymerised with DMPA:IPA solvent on PetRa showed a few CMs attached, however more attachment was expected since the DOC value of this cured formulation was found to be 58% (Table 4.6).

**Table 4. 9: Degree of cure of PETrA polymer which was made using the 3 different formulations. Raw data in (conditions. Table**

| <b>Formulation</b> | <b>DOC (%)</b> |
|--------------------|----------------|
| I369               | <b>59</b>      |
| DMPA               | <b>36</b>      |
| DMPA:IPA           | <b>58</b>      |

#### *4.2.5.4 Discussion of UV polymerisation results*

Many variables were investigated in this series of experiments. It was concluded that the photoinitiator type has an effect on cell viability. This is evident by the differences in cell viability between some polymers with I369 and constructs polymerized with DMPA:IPA formulations when both sets were maintained in RILT medium. Most of the cell viability differences were present within polymer combinations that involved GPOTA, highlighting the importance this polymer had on cell viability and reduction of cytotoxicity. I369 photoinitiator had been previously used to fabricate scaffolds for biological applications (Doraiswamy, 2006 #89) with little or no cytotoxicity on established cell lines however the experiments were not performed on iPSC-derived CMs. The sensitivity of the cells being tested should also be kept in mind as they are derived from iPSCs and are a different cell type altogether. DMPA:IPA formulations have been used to test specifically for CM attachment (Patel, 2015 #44). GPOTA was found to be a low-scoring polymer for cell viability in the Patel studies even though the same PI formulation and media

were used (Patel, 2015 #44). The limitations of the experiment performed in this section are firstly that 3 repeats were done within one 96-well plate. Biological repeats need to be performed in order to attain a better outlook on cell viability and draw more viable conclusions. Secondly, a different cell source (iPSCs) were tested which can change cell response to surfaces as these cells will exhibit different characteristics compared to adult CMs or ESC-derived CMs (Bird, 2003 #94) (Jiang, 2018 #188). Various cell lines can respond differently, even with the same PI of the same concentration (Williams, 2005 #222).

It was observed that the medium the CMs are maintained made a considerable difference to attachment. 5 out of the 6 polymers (BDDA, HEODA, TCDMDA, PETrA and pPGDA) showed CM attachment in RILT medium but not in RPMI B27 medium when the same photoinitiator (I369) was used (Refer to Appendix 1.3 Qualitative Results for CM attachment on UV-polymerised acrylates). This means RILT medium probably contains components that help sustenance of CM during attachment to these 5 polymers. Indeed, RILT medium contains thioglycerol and ascorbic acid that are antioxidants (Patel, 2015 #44). GPOTA did not show attachment in RILT medium whereas CMs in RPMI B27 attached to GPOTA. There are two possible reasons in this case; the RPMI B27 medium contains components that supports CM attachment to GPOTA or GPOTA polymer possesses the necessary surface chemistry for CM attachment in RPMI B27. In other words, it may be a combination of GPOTA surface chemistry and components in RPMI B27 that confer the necessary changes and signals for the cells to attach to the GPOTA polymer surface. As stated previously, conclusions on cell viability could not be drawn based on the RPMI B27 medium as only 1 dataset was obtained.

The highest DOC was found to be DMPA:IPA formulation in the Raman spectroscopy measurements. In order to prove the cytotoxicity of DMPA compared to I369, Raman measurements need to be made on the rest of the polymers of each formulation type.

Referring to the results from chapter 3, complete structures could only be fabricated using at least 3% photoinitiator concentration for BDDA and

HEODA. In contrast, GPOTA, TCDMDA and PETrA all showed fabrication of good quality structures as low as 1% photoinitiator concentration. This is an important consideration in an effort to reduce the risk of cytotoxicity for the cells. These 3 polymers also had wide operating windows relative to BDDA, HEODA and pPGDA (Chapter 3, Results section) which allows more room for fabrication error when producing complex architectures for CM attachment to various topologies which will be described and discussed in Chapter 5. Hence, it would only be feasible to move forward with TCDMDA, PETrA and GPOTA for further Raman spectroscopy, CM attachment and maturity experiments using 2PL.

Toluene solvent was used for the silanisation of glass cover slips referring to a previously determined protocol. Toluene is efficient in maintaining an anhydrous environment which is crucial to the formation of a SAM of silane (Vandenberg et al., 1991). This ensured that the acrylic polymer resin was not lost during all the rinsing processes and cell culture experiments. Structures on non-silanised glass cover slips were lost frequently therefore the silanisation procedure for 2-photon fabricated constructs on glass cover slips was found obligatory. The 2-photon fabricated constructs to be utilised for SEM for observation or for Raman spectroscopy were not processed on silanised slides as these techniques did not have any rinsing procedures which also saved experimental time.

### 4.3 Discussion and Conclusions

The multi-functional polymers suitable for CM attachment by UV polymerisation and at the same time amenable to 2PL were discovered in this chapter. The methodology applied was to first identify the polymers that could support CMs prior to analysing their amenability to 2PL. This made the process much quicker as UV polymerisation only takes a short time and the polymers could be tested simultaneously in one UV session. Cell viability measurements showed significant differences depending on the PI and polymer combinations and was able to provide a quantitative insight into the observations. The higher cell viability in GPOTA showed this material as a possible candidate for future experiments. GPOTA has been shown before to support cells of other types, including dental pulp stem cells, which shows promise for dental therapy (Vining, 2018 #228). A majority of the polymer combinations that showed significant differences in cell viability involved GPOTA and a few involved either pPGDA or BDDA, indicating the ability of these polymers to support CMs. Branched versions of the BDDA polymer had been previously used in gene transfection studies with applications in a wide variety of cell types (Zhou, 2016 #230). This may be why BDDA showed some significant cell viability levels in this doctoral study.

PPGDA and BDDA unfortunately did not have a wide enough operating window for 2PL fabrication purposes. GPOTA had a good working range for 2PL therefore it was carried onto the work in Chapter 5. However, biological repeat experiments were found to be necessary in order to choose polymers for future work based on this data. The viability results on cells in RPMI B27 medium showed GPOTA as the only polymer to have CM attachment with I369 photoinitiator. Triplicate results within the 96-well plates need to be done in order to draw conclusions in regards to this.

Raman spectroscopy has shown that DMPA is more cytotoxic than I369 as shown by the differences in CM attachment in the case of PETrA. Despite this finding, DMPA combined with IPA was shown to attach CMs on numerous polymer surfaces (Patel, 2015 #44) but UV microcontact printing was used in that particular study. That meant only minute spots of monomer were placed on slides as opposed to much larger volumes used in this study. This may have

also affected the DOC measurements and subsequently the cytotoxicity. DMPA was already known to have a high degree of conversion, even at low concentrations (Mucci, 2012 #229), albeit the results obtained in this doctoral project projected DMPA as the PI with the lowest DOC. This was because DOC depends highly on PI concentration and the monomer being tested (Mucci, 2012 #229). Future work in this area could include making Raman measurements of the remaining polymers prepared using the 3 different formulation types.

Additional studies leading up to the silanisation of glass cover slips and polystyrene plates were performed. The ideal solvent for silanising 96-well plates was isopropanol with a minimum silane type of TMSPMA and concentration of 0.025  $\mu\text{l/ml}$ . Different solvents are compatible with different surfaces and silane types (Cisneros-Pineda et al., 2014). This is useful information however it was discovered in this chapter that silanisation of 96-well plates was not essential to prevent polymer construct loss. This is due to the depth of the wells and the fact that the polymer construct is attached to the sides of the well walls. As a result, silanisation was not done on 96-well plates for CM attachment experiments to reduce experimental time.

#### 4.4 Future Work

Following biological repeats of the CM attachment experiments, polymers can be selected more accurately based on their cell viability values for CM maturity tests on 2PL structures. A larger number of samples would be required to draw conclusions on CM attachment in RILT medium. In addition, Raman spectroscopy should be done on the remaining polymers in order to compare DOC values among the PI formulations. That way, the most optimal PI type and concentration can be determined for the polymer desired for 2PL. That particular PI concentration could then be used to investigate the operating window for the polymer in 2PL.



## Chapter 5: Investigation of the effect of 3D architecture on CM attachment and maturity. Additional effect of post-fabrication method in an attempt to improve degree of cure

### 5.1 Introduction

CM attachment and maturity was known to differ on various surface topologies, as discussed in the Literature Review. Structures with variable groove depths were tested for their ability to support CMs and the maturity of these CMs were compared to 2D flat control structures. Differential CM attachment and maturity characteristics were analysed by measurements of sarcomere length and nuclear roundness, both of which change with increased maturity. Cell orientation was also compared on flat versus grooved regions to prove cell alignment. Structures involving grooves had been studied and tested previously as well as other constructs such as tubules and meshes (1.2: Literature Review). The novel approach here was the utilisation of groove depth variation and its effect on CM maturity on the TCDMDA polymer.

Various post-fabrication treatment methods were performed and their effects on degree of cure and CM maturity described. Post-fabrication treatment methods include vacuum, UV-light or a combination of both. Vacuum and UV-light treatment post-fabrication were known to improve degree of cure which was the reason for testing these methods as less cytotoxic monomer would remain in the reaction mixtures. 3 acrylate monomers TCDMDA, GPOTA and PetRa were treated using each method. The outcome of the treatments on the 3 different polymerised materials is discussed.

## 5.2 Results

CM attachment was tested in 3 separate experiments. They tested CM attachment on 2-photon fabricated constructs of TCDMDA with post-fabrication vacuum treatment, post-fabrication UV light treatment and without post-fabrication treatment. These treatments were applied to reduce cytotoxicity caused by unreacted monomer and photoinitiator molecules. Afterwards, analysis of cell characteristics was performed.

### 5.2.1 Raman Spectroscopy Measurements

#### *5.2.1.1 Degree of cure of 2-photon fabricated constructs treated with vacuum and post-fabrication UV cure*

All 3 polymers benefited from post-fabrication vacuum treatment and UV light treatment (5.2.2.2 CM attachment to TCDMDA and analysis of cell characteristics). The DOC difference was greater in samples treated with vacuum only compared to constructs treated with UV light only post-fabrication. No anomalies were observed, the constructs with no post-fabrication treatment all had lower DOC than constructs with either treatment demonstrating the importance of taking multiple Raman readings of each sample.

The spectra of all 3 polymers TCDMDA, GPOTA and PETrA showed the characteristic peaks of C=C and C=O and the new addition of the ether peak between 820 and 890  $\text{cm}^{-1}$  as a result of wider spectral readings (Appendix, 1.1 Raman Spectroscopy).

All 3 uncured monomers showed typical area intensity counts where the C=C peak area is markedly higher than the C=O peak area. TCDMDA possesses the highest C=C/C=O ratio compared to GPOTA and PETrA ratio values. This may be due to the fact that GPOTA and PETrA are triacrylates which means they have a higher number of unreacted C=C bonds which increase the overall ratio. Being triacrylates they also have a higher number of C=O bonds but the signal of the C=O bonds is greatly reduced due to the oxygen atom next to the C=O attracting electrons from the C=O bond, rendering the C=O to C-O<sup>+</sup>. Their

corresponding spectra showed characteristic peaks for C=C, C=O and the ether peak at approximately 820 cm<sup>-1</sup> (Appendix 1.1 Raman Spectroscopy).

Polymers without post-fabrication treatment differed in their DOC (Appendix 1.1.1 Polymers with no UV or vac treatment). TCDMDA had the highest DOC compared to GPOTA and PETrA which had the lowest. The cross-linking feature in the polymerization of the triacrylate GPOTA and PETrA may be causing a lower DOC due to the PI not being able to reach all of the C=C bonds in inside the polymer network. PETrA would have an even denser network due to the free -OH group in its structure. This also participates in electrostatic attraction and hydrogen bonding to form an even denser network than GPOTA, hence it will possess even more unreacted C=C bonds which reduces the DOC. All 3 polymers produced spectra with characteristic peaks at C=C, C=O and the ether group (Appendix 1.1.1 Polymers with no UV or vac treatment). The ether peak intensity counts were much lower compared to the ether peak intensity when the polymers had no post-fabrication treatment. This means part of the ether-containing chemical, which is PGMEA, is removed by vacuum treatment.

All 3 polymers showed an increase in DOC when subjected to vacuum treatment compared to no treatment post-fabrication (Appendix 1.1.2 Polymers with vacuum treatment).

**Table 5.1: C=C/C=O ratio values for the 3 polymers under each post-fabrication treatment condition.**

| <b>Polymer Name</b> | <b>No treatment</b> | <b>Vacuum</b> | <b>UV</b>   |
|---------------------|---------------------|---------------|-------------|
| TCDMDA              | <b>0.69</b>         | <b>0.54</b>   | <b>0.69</b> |
| GPOTA               | <b>0.74</b>         | <b>0.74</b>   | <b>0.53</b> |
| PETrA               | <b>0.91</b>         | <b>0.85</b>   | <b>0.88</b> |

All 3 polymers treated by post-fabrication vacuum and UV light produced spectra with the characteristic peaks C=C and C=O and the ether group (Appendix 1.1.3 Polymers treated with post-fabrication UV light). The effect of post-fabrication UV cure on the C=C/C=O is much less compared to the effect of vacuum treatment in the case of TCDMDA (0.69 versus 0.54 vacuum-treated) (Figure 5.1). The ratio is the same between UV versus no treatment for GPOTA.

UV-treated PETrA has a slightly higher ratio of 0.88 compared to its 0.85 vacuum-treated counterpart. This translates to different DOC values between vacuum-treated versus post-fabrication UV light-treated polymers is due to the mechanism with which these treatments work (Table 5.2). Vacuum treatment removes unreacted monomer by evaporation which is a physical process and is a powerful method to remove any remaining liquid monomer from the samples. UV-light treatment is a chemical process which polymerizes the unreacted vinyl bonds in the polymer network. If the polymer is an already solidified mesh, unreacted monomer molecules will not be able to reach other unreacted vinyl bonds as quickly compared to the vacuum process.

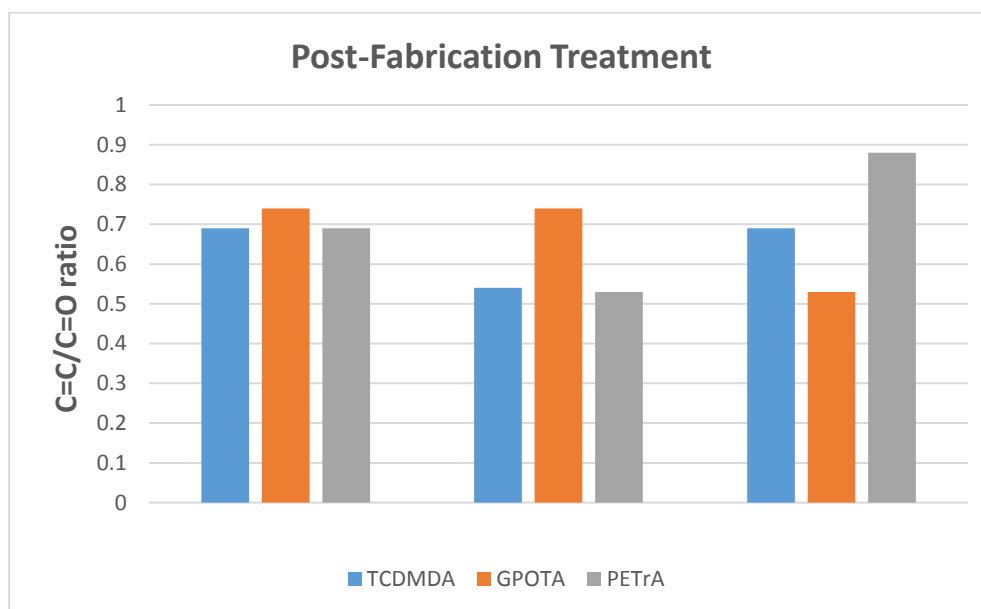


**Figure 5.1: Comparison of all C=C to C=O ratio values of the 3 polymers under each post-fabrication treatment condition.**

### 5.2.1.2 Summary of Raman Spectroscopy Results

Overall, the Raman spectra of all 3 polymers under the 4 different conditions of untreated, vacuum only, UV only and both UV and vacuum treatment showed the characteristics peaks of acrylate monomer/polymer molecules which are C=C and C=O with vacuum treatment having the largest influence (Table 5.2).

**Table 5.2: Summary of DOC values from Raman spectroscopy measurements.**

| Polymer       | No UV or vacuum treatment (%) | Vacuum only (%) | Post-fabrication UV treatment only (%) | Post-fabrication UV and vacuum treatment (%) |
|---------------|-------------------------------|-----------------|--|--|
| <b>TCDMDA</b> | 57.9                          | 66.8            | 58.0                                   | 67.1   |
| <b>GPOTA</b>  | 46.7                          | 47.0            | 47.1                                   | 52.0   |
| <b>PETRA</b>  | 28.2                          | 33.1            | 30.2                                   | 33.5   |

Further investigation into the ether group presence demonstrated that the ether moiety remains even after the IPA wash, indicated in Table 5.3 samples without post-fabrication treatment. This is especially apparent in GPOTA and TCDMDA prior to vacuum treatment. The vacuum is the most effective treatment in terms of removing both unreacted vinyl (C=C) bonds as well as ether moieties of PGMEA (Table 5.3).

**Table 5.3: Summary of Ether Peak Intensity Values pre- and post-vacuum treatment.**

| Polymer Name  | Prior to Vacuum treatment Intensity (Counts) | Post-vacuum treatment Intensity (Counts) | Intensity Difference (Counts) |
|---------------|--|--|-------------------------------|
| <b>TCDMDA</b> | 28197.625                                    | 2672.42                                  | 25525.205                     |
| <b>GPOTA</b>  | 44486.75                                     | 7197.62                                  | 37289.13                      |
| <b>PETrA</b>  | 8276.2825                                    | 682.98                                   | 7593.3025                     |

## 5.2.2 Comparison of CM attachment and maturity on 2-photon fabricated constructs without post-fabrication treatment versus constructs treated with vacuum and post-fabrication UV cure

### 5.2.2.1 Introduction

In order to select the appropriate polymers for CM attachment experiment, their suitability was assessed. Two specific criteria needed to be fulfilled, the first one being the polymer's amenability to 2PL and whether the polymer showed CM attachment on UV-polymerised constructs (Chapter 4, Section 4.2.5). Six polymers were tested for CM attachment on the UV-polymerised constructs (Chapter 4, Section 4.2.5). BDDA and HEODA are amenable to 2PL but have a narrow operating window and could only produce complete structures between 3 and 4% photoinitiator concentration (Chapter 3, Section 3.2.1). PPGDA was found to not be amenable to 2PL by testing for polymer fabrication at highest possible laser power and scanspeed combination (Chapter 3, Section 3.2.1). TCDMDA, GPOTA and PETrA all demonstrated good amenability to 2PL with wide operating windows (Chapter 3, Section 3.2.1 and 3.2.3). They also showed CM attachment on the UV-polymerised constructs (Chapter 4, Section 4.2.5). Therefore, TCDMDA and GPOTA were selected for the CM attachment experiments on 2-photon polymerised constructs of various topologies. The 2-photon fabricated constructs were based on the designs described in Chapter 4, Section 4.2.6.2). The flat region consisted of the 4 sub-regions with various hatching directions and the grooved region had 3 different sub-regions consisting of groove depths 6, 9 and 12  $\mu\text{m}$ . GPOTA was tested for CM attachment and TCDMDA constructs subject the three different post-fabrication treatments; UV light, vacuum and no post-fabrication treatment. TCDMDA was focussed on due to its consistent ability to support CMs on the UV-polymerisation experiments (Chapter 4, Section 4.2.5).

CMs attached to the 2 polymer constructs TCDMDA and GPOTA in the presence of fetal bovine serum (FBS). Cells treated with serum are more robust and therefore will attach to most materials since they are given the extra nutrients for efficient attachment. The project aim is to observe changes in cell attachment and behaviour among various topologies therefore the addition of serum was

seen appropriate to accelerate the process due to time constraints. The attachment varied depending on the topology of the surface which answers one of the questions raised for this research project.

#### *5.2.2.2 CM attachment to TCDMDA and analysis of cell characteristics*

##### *5.2.2.2.1 TCDMDA without post-fabrication treatment*

TCDMDA constructs without post-fabrication treatment demonstrated cell attachment (Figure 5.20). The flat region showed cell attachment in the 4 regions composed of the hatching directions 0°, 60°, 90° and 120°. However, visualisation of cell attachment poses a challenge due to the small size of the grooves and the reflection of light along the groove edges (Figure 5.1). Immunostaining images enable much clearer visualisation of the cells and their cardiomyocyte identity as described later in this section. Cells also attached to the area outside the construct due to the robustness they gained with the addition of serum during dissociation.

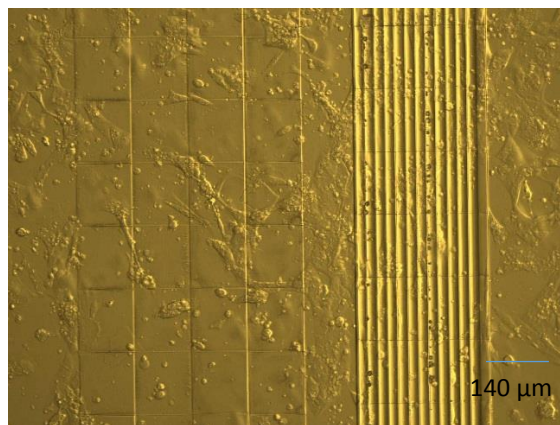


**Figure 5.2: Light microscopy image at 10X magnification of TCDMDA construct without post-fabrication treatment. The grooved region shows some cell attachment however visualisation is a challenge for this region therefore immunostaining is performed.**

Constructs without post-fabrication treatment were all sterilised and washed with DI water prior to cell seeding as explained in Chapter 4 and this Chapter, Methodologies Section. The constructs all supported CM attachment, including the glass surrounding them. As stated previously, serum renders the cells very

robust which assists them in attachment to many surfaces. Each surface type and its respective cell response is described here.

The glass cover slip surrounding the immediate vicinity of the TCDMDA construct also supported CM attachment (Figure 5.2). This was used as a comparison against TCDMDA as a flat control without the influence of polymer chemistry. Immunostaining analysis demonstrated the cells' identity as cardiomyocytes by the positive staining of cardiac Troponin-T. CMs appeared to be extending in random directions, some being more extended than others. The cells in the middle of the image in Figure 5.3 appear to be extending in a long straight line whereas the rest appear to be more rounded in morphology and pointing in random directions. This behaviour of cells' extending in random directions is possibly due to the absence of any topological differences along the glass surface (Figure 5.3).

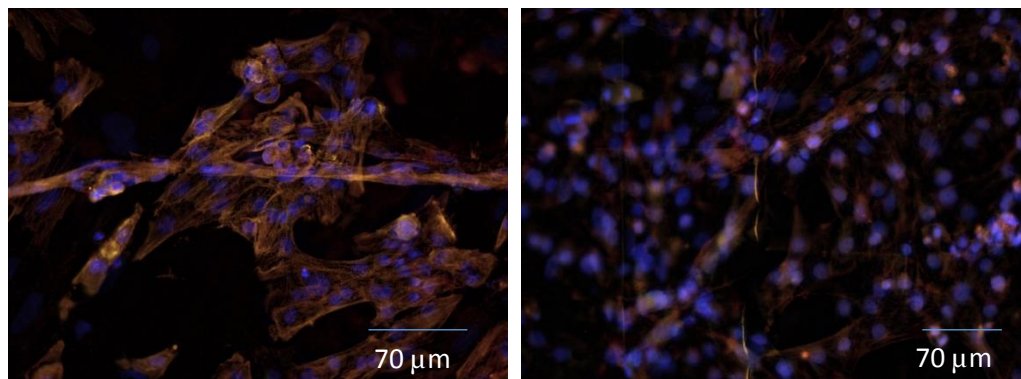


**Figure 5.3: Immunostained image of cardiomyocytes attached to glass cover slip surface surrounding the TCDMDA construct (left) and TCDMDA flat region (right) without post-fabrication treatment.**

The flat region of the TCDMDA construct appeared to have cells extending in random directions, similar to the glass control (Figure 5.3). The cells are cardiomyocytes, evident by the positive staining for cardiac-troponin T (Figure 5.3). The CMs appear to be stretching more extensively compared to the CMs on the glass control. This is measured quantitatively in the statistical sarcomere length measurement.



The overall fluorescent microscopy images taken of the whole TCDMDA construct shows the distinction between the flat region and the grooved-region (Figure 5.4). The beginning of the grooves can be faintly seen but if a line were to be drawn it could be easily visualised where this begins. The cells for the most part align in the same direction on the right side of the image compared to the left side. Most of the cells have stained positive for cardiac troponin-T (Mei et al.). The cells that did not stain red could possibly be fibroblasts in the cardiomyocyte culture.

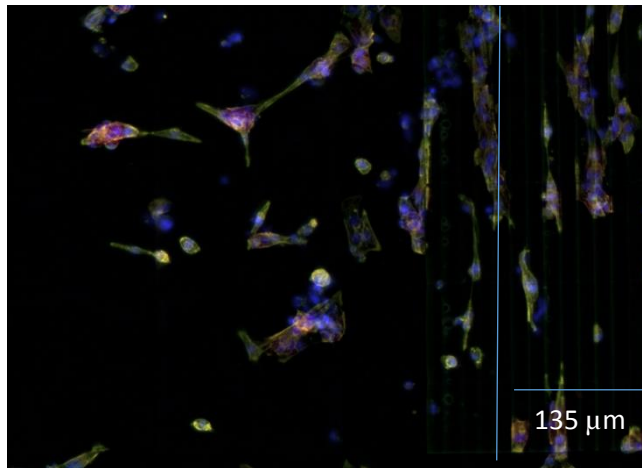


**Figure 5.4: Tcdmda without post-fabrication treatment overall at 20X magnification on the Exciter Wide-field microscope.**

The constructs and attached cells were visualised at a higher magnification of 63X (Figure 5.5) to observe sarcomere units more clearly. The distinct green staining for  $\alpha$ -actinin and red staining for cardiac troponin-T could be observed on some cells such as the one shown by the blue arrow in Figure 5.5.

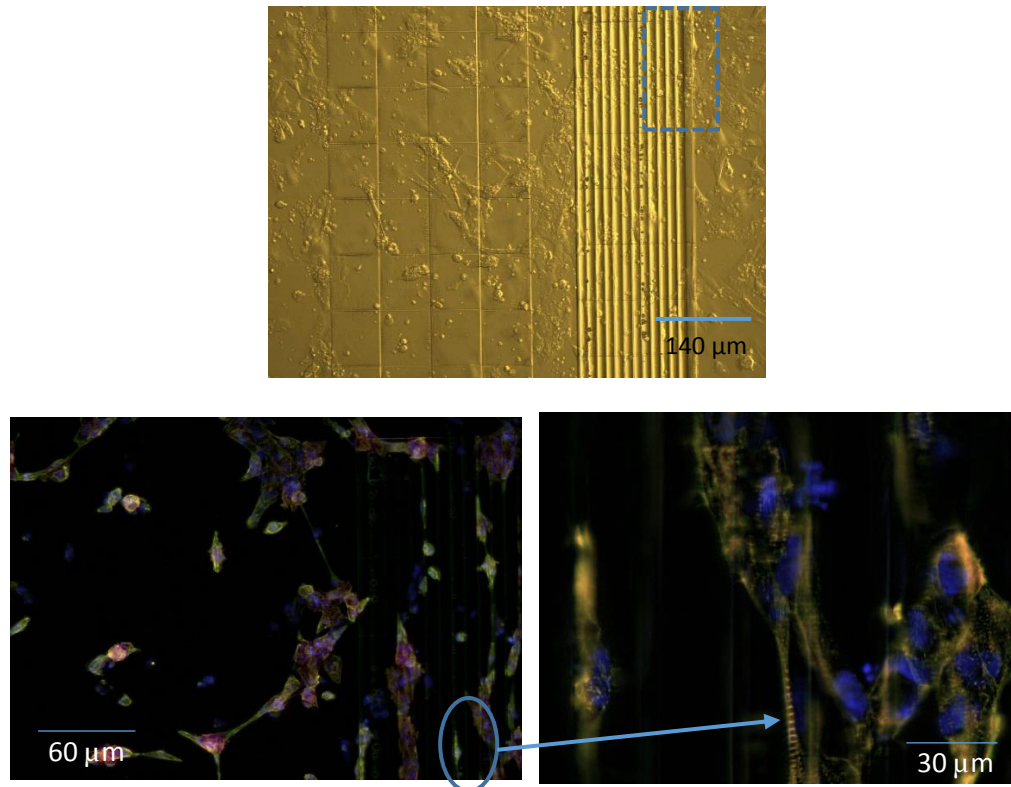


**Figure 5.5: 40X (left) and 63X (right) wide-field images of cells on the TCDMDA construct without post-fabrication UV cure. The 63X image highlights the clarity at which sarcomere bands can be visualised, complete with troponin (red) and  $\alpha$ -actinin (green) band staining. Top: Light microscopy image from Figure 5.1 indicating where the fluorescent images correspond to.** The ANOVA statistical test on sarcomere length measurements showed the calculated F value was lower than the critical F value meaning there is no significant difference between any of the 5 groups representing sarcomere length on the construct without post-fabrication treatment (Table 5.3). Sarcomere length values are displayed in the 1.2 Statistical tests on CMs.

**Table 5.4: Results of ANOVA statistical analysis of sarcomere length on TCDMDA construct without post-fabrication treatment.**

| Source of Variation | SS       | df | MS       | F               | P-value   | F crit          |
|---------------------|----------|----|----------|-----------------|-----------|-----------------|
| Between Groups      | 0.892653 | 2  | 0.446327 | <b>0.756837</b> | 0.4902832 | <b>3.885294</b> |
| Within Groups       | 7.07672  | 12 | 0.589727 |                 |           |                 |
| Total               | 7.969373 | 14 |          |                 |           |                 |

The longest sarcomere length values were found in the CMs that attached to the medium and deep-grooved regions (Figure 5.6). This means the CMs did not

extend along these grooves and were not contracting. The shallow-grooved region enabled the CMs to extend more along the topology compared to the rest of the grooved regions however the flat region of the construct caused the cells to contract the most, resulting in the lowest average sarcomere length (Figure 5.6). The differences were not significant enough to state that the various topologies altered CM movement or behaviour as proved by the ANOVA statistical analysis (Table 5.7).

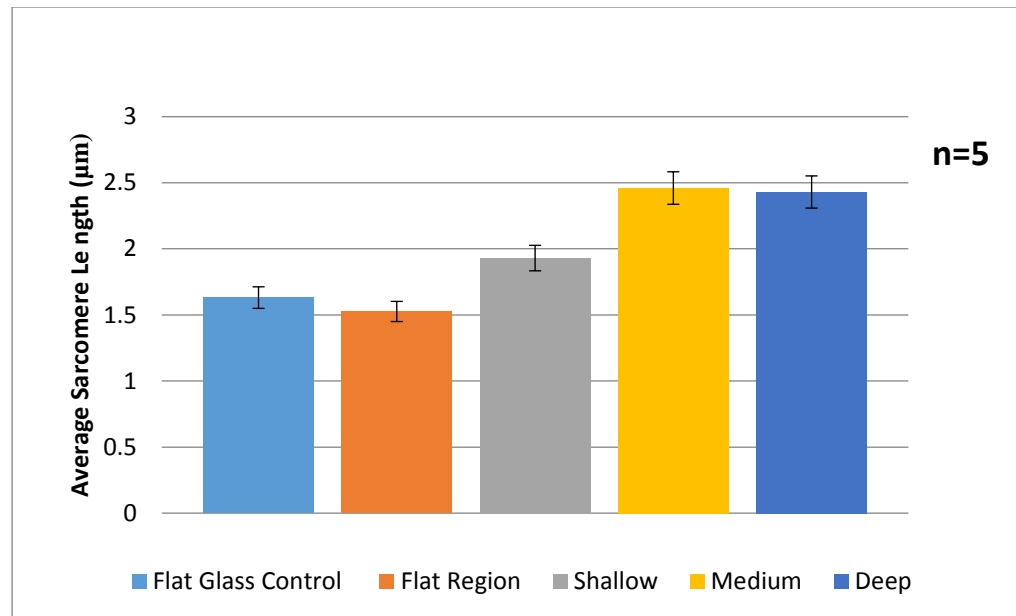


**Figure 5.6: Comparison of average sarcomere length against groove depth in TCDMDA construct without post-fabrication treatment.**

The average nuclei roundness value for the glass control was 0.75 (Table 5.4). This is considered as fairly round as the scale indicates 1 as completely round (circle) shape and 0 indicates no roundness in for example, a square. The roundness value is expected to be closer to a circle shape in the case of the flat glass control since the cells are extending in random directions and are not in contractile state compared to the cells in the grooved regions. The cells in the grooved regions are expected to have a lower roundness factor due to their extension along the topology which is further described in the next sections. Image J software applies an algorithm to calculate the roundness of shapes depending on the number of pixels. The lowest pixel threshold number is determined first in order for the software to recognise a particle as a shape. Another function termed ‘watershed’ is applied to separate big particles as

separate, smaller particles which is shown by the yellow lines across the black particles which represent individual nuclei (Raw data in Appendix 1.2 Statistical tests on CMs).

**Table 5.5: Results of ANOVA statistical analysis of nuclear roundness on TCDMDA construct without post-fabrication treatment.**

| Source of Variation | SS          | df  | MS         | F          | P-value   | F crit   |
|---------------------|-------------|-----|------------|------------|-----------|----------|
| Between Groups      | 0.093604964 | 2   | 0.04680248 | 2.24923031 | 0.1084537 | 3.046433 |
| Within Groups       | 3.724671629 | 179 | 0.02080822 |            |           |          |
| Total               | 3.818276593 | 181 |            |            |           |          |

It is clear that the grooved region had a lower roundness value compared to the flat region and the glass control (Figure 5.7). The ANOVA analysis concludes that the differences between these 3 groups were not significant.

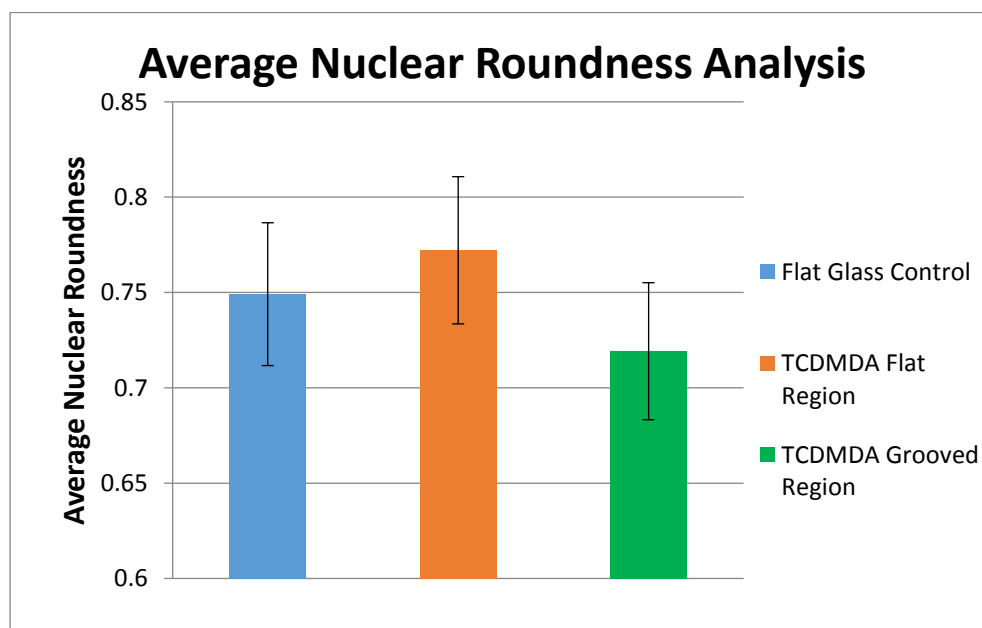


**Figure 5.7: Bar chart showing the levels of roundness in each topological region of TCDMDA without post-fabrication treatment.**

Orientation analysis in cell culture is important when determining whether the cells have responded to topological cues on a material surface. Each region of the construct was tested for orientation distribution of the cells that attached. The images in Figure 5.8 shows that the cells display an array of colours which means

they are demonstrating a diverse number of orientations. This is quantitatively proven by the histogram below which indicates a fairly even distribution of cell orientation along the range of angles for the two flat regions but a bias towards  $90^\circ$  for the grooved region (Figure 5.8).

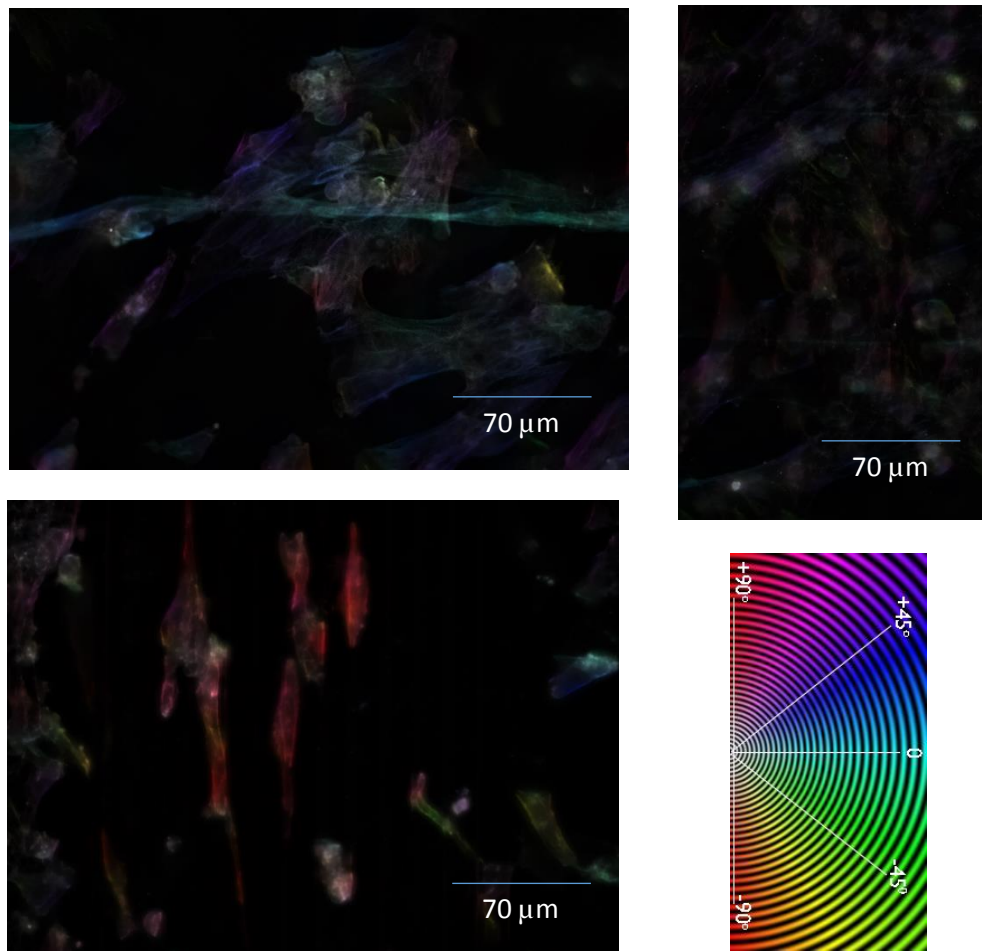


**Figure 5.8: Image of colour-coded cells after ImageJ Orientation plugin was applied on the flat glass control (top), TCDMDA flat region (top right) and grooves region (bottom) without post-fabrication treatment. Colour chart of orientation degrees (bottom right).**

Figure 5.8 shows all of the regions of TCDMDA orientation analysis data. The image, although faint, shows a variety of colours similar to the flat glass control (Figure 5.8). The distribution is fairly even along the degree values despite the lower quality of the image. The algorithm for the orientation plugin uses the pixel values throughout image to create the distribution pattern. The lower quality of this image may have resulted in the slightly uneven

distribution here compared to Figure 5.8. However, a direct visualisation of the image indicates the cells spread in various directions and is in line with cell response to flat topologies.

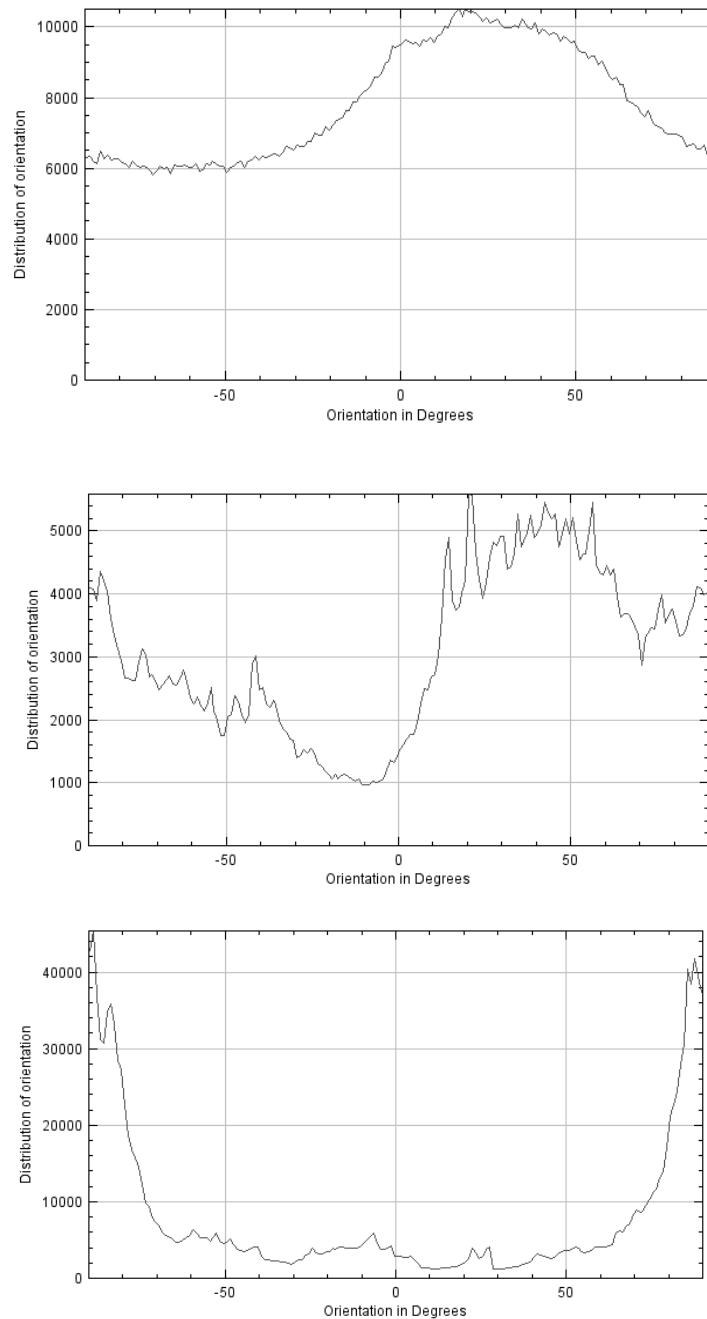


**Figure 5.9: Orientation distribution of flat glass control (top), flat region of construct (middle) and grooves region (bottom) on TCDMDA without post-fabrication treatment.**

The grooves region of TCDMDA without post-fabrication treatment displayed cells with a specific bias in orientation which was in a perpendicular manner.

Almost all cells displayed  $90^\circ$  or  $-90^\circ$  orientation as can be seen in the histogram (Figure 5.9, bottom). The algorithm does not distinguish individual cells however the encircled structures appear to be cells and the important finding is that the majority of the cells show up red in colour after the algorithm is applied. The colour chart also shows cells with a dark pink or red colour were close to or at  $90^\circ/-90^\circ$  orientation (Figure 5.8).

#### 5.2.2.2.2 TCDMDA with post-fabrication UV cure

Light microscopy imaging showed that the TCDMDA constructs treated with UV light supported cell attachment. Many cells were observed to have attached to the construct and the region with grooves shown by the rectangle (Figure 5.10). Cells also attached to the glass surrounding the construct and this is due to the serum used during cell dissociation. Serum renders cells very robust giving them the ability to attach to many surfaces. At first glance, there appear to be more cells attached to this construct compared to TCDMDA without post-fabrication treatment.

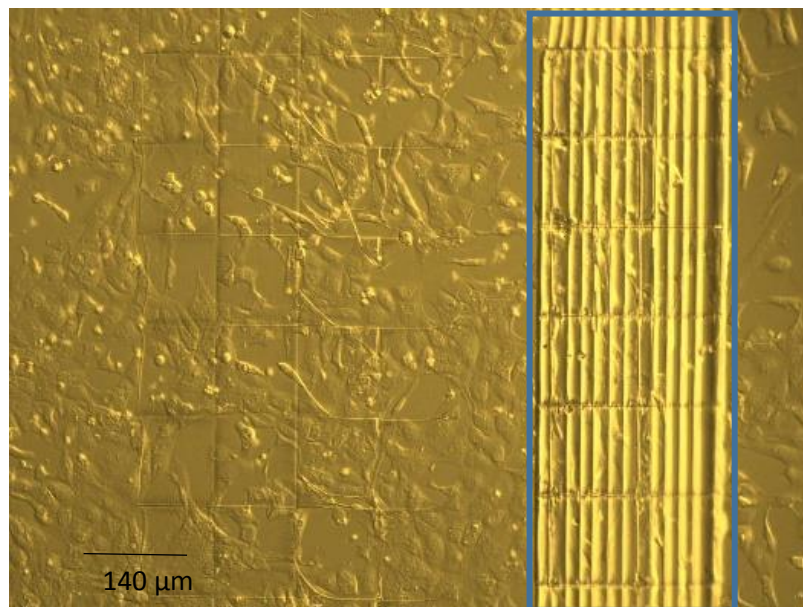


**Figure 5.10: Light microscopy image of TCDMDA construct with post-fabrication UV light treatment at 10X magnification.**

Z-stack photographs take on the wide-field microscope were analysed on image J and snapshots taken for visualization on this thesis report. The flat glass control



is a snapshot of the cells that settled onto the glass around the construct. This served as a flat control without the influence of underlying polymer chemistry (Figure 5.11). Another photograph of the cells settled onto the flat section of the TCDMDA polymer construct served as the flat control for the purposes of topology (Figure 5.11).

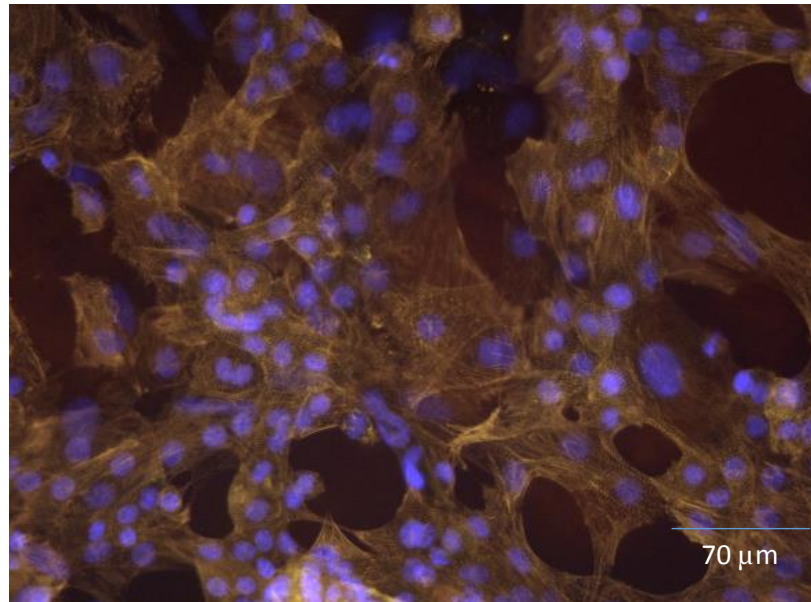


**Figure 5.11: Flat glass control showing cells immunostained for cardiac Troponin-T (red),  $\alpha$ -actinin (green) and DAPI (blue). The red and green channels appear orange when all channels are merged.**



Constructs with post-fabrication UV cure showed similar results to the constructs without any post-fabrication treatment with respect to topological response. The cells appear to extend in random directions on the flat region and align along the grooves in the grooved region of the construct (Figures 5.12 top and bottom). However, a denser cell network is observed here compared to constructs without post-fabrication treatment.

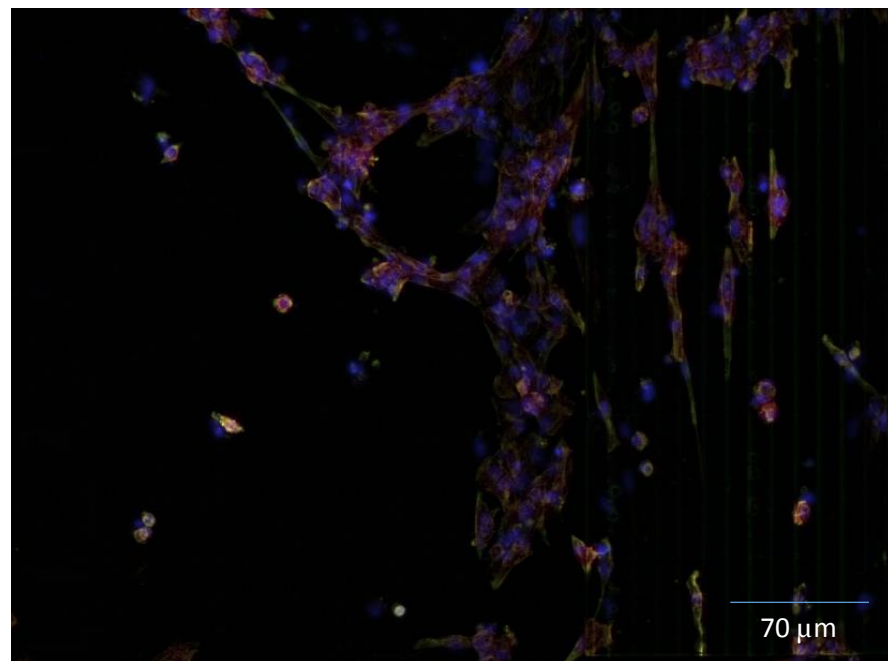
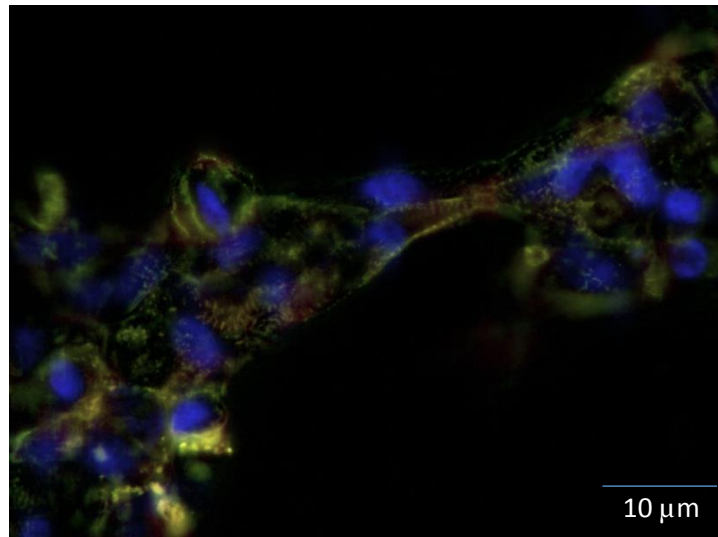


**Figure 5.12: Cells attached to the flat region of the TCDMDA construct with post-fabrication UV cure. Red staining is for cardiac-troponin T, green for  $\alpha$ -actinin and blue staining for DAPI in the cell nuclei (top) and cells on a TCDMDA construct with post-fabrication UV cure. Red staining is for cardiac-troponin T, green for  $\alpha$ -actinin and blue staining for DAPI in the cell nuclei (bottom).**

Sarcomere length measurements were made on 5 cells representative of each grooved region; shallow, medium and deep. It appears the average sarcomere length is the largest in the medium grooves area closely followed by the deep grooves region. The shallow region had shorter sarcomere units on average (Figure 5.13).

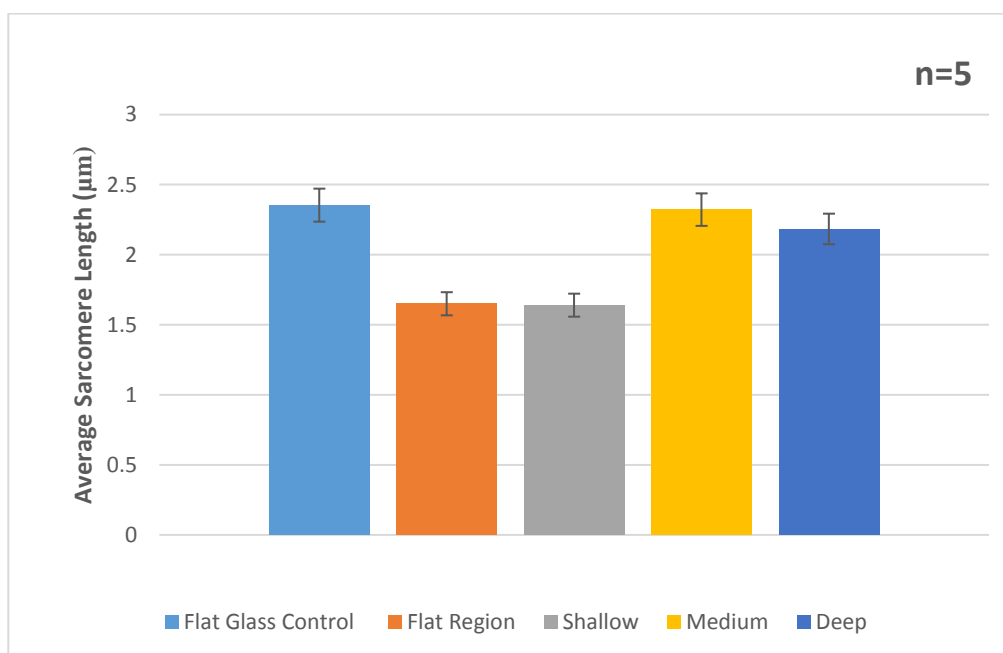


**Figure 5.13: Comparison of average sarcomere length of CMs on topologically different regions of TCDMDA with post-fabrication UV light treatment.**

It appears that the average sarcomere length in the shallow grooved region is fairly lower compared to the medium and deep region average sarcomere length values. The ANOVA test can give information on whether there is a significant difference existing in the 3 groups but it cannot provide which groups specifically differ. The results show there is a significant difference present in the sarcomere length units (Table 5.5).

**Table 5.6: Single-factor ANOVA statistical analysis displaying the calculated F-value, the expected (critical) F-value and the P-value.**

| Source of Variation | SS       | df | MS        | F          | P-value   | F crit    |
|---------------------|----------|----|-----------|------------|-----------|-----------|
| Between Groups      | 3.062736 | 4  | 0.765684  | 8.38638873 | 0.0001961 | 2.7587105 |
| Within Groups       | 2.28252  | 25 | 0.0913008 |            |           |           |
| Total               | 5.345256 | 29 |           |            |           |           |

Student's t-test results on pairwise combinations of all regions proved that every region showed a significant difference in sarcomere length with each other (Table 5.5). Detailed numerical results of each test are shown in the Appendix. The medium and deep-grooved regions showed a significant difference between sarcomere length values. (Table 5.10). The flat region of TCDMDA had topological differences at the microscale with the hatching direction being the only difference (Chapter 4, Section 4.2.6). The calculated F value 8.34 is greater than the critical F-value of 2.76. In addition, the P-value is less than 0.05 meaning the null hypothesis is rejected and the user hypothesis is accepted which is that there is significant difference existing between the average sarcomere length values. T-test results showed that the significant difference was between the shallow and medium-grooved regions and also between the shallow and deep-grooved regions (Table 5.10). The same result applies the flat region and the shallow grooves region of the TCDMDA construct treated with post-fabrication UV light. This is evident by the p-value of 1 which is lower than the critical t-value of 2.22 (Appendix 1.2 Statistical tests on CMs). The flat glass control possessed sarcomere length measurements similar to the medium and deep-grooved regions. This is in contrast to the flat part of the TCDMDA construct which supported CMs with shorter sarcomere lengths.

**Table 5.7: Student's t-test results of pairwise comparison on sarcomere length measurements of all regions on TCDMDA construct with post-fabrication UV cure.**

|                           | <b>Flat Glass Control</b> | <b>Flat region</b> | <b>Medium</b> | <b>Deep</b> |
|---------------------------|---------------------------|--------------------|---------------|-------------|
| <b>Flat glass control</b> | -----                     | YES                | YES           | YES         |
| <b>Flat region</b>        | -----                     | -----              | YES           | YES         |
| <b>Shallow</b>            | YES                       | YES                | YES           | YES         |
| <b>Medium</b>             | -----                     | -----              | -----         | YES         |

The flat glass control had longer sarcomere length compared to the shallow-grooved region. The shallow grooves possibly induced CMs to extend along these topologies, rendering them to contract and adopt shorter sarcomeres. This is shown by the p-value versus the larger critical t-value (Appendix 1.2.1 Statistical Tests on Sarcomere Length) and the positive t-test result. This could be due to the various hatching directions present in the flat region of the TCDMDA construct which caused the cells to extend along these topologies, resulting in shorter sarcomere length. The more a CM stretches the shorter the gaps between individual sarcomere units. The flat glass control has a uniform surface topology which means the cells are not induced to extend, giving them longer gaps between sarcomere units.

Statistical analysis of nuclear roundness values using the ANOVA one-way test of the 3 different groups showed that the calculated F value was much smaller than the critical F value. In addition, the P-value was much greater than the chosen  $\alpha$ -value of 0.05 meaning the null hypothesis was accepted that there is no significant difference between the nuclear roundness of cells between shallow, medium and deep-grooved regions (Table 5.7).

There was a much larger significant difference between the medium-grooved region and the flat section of the TCDMDA construct treated with post-fabrication UV light. The p-value was much lower than the critical t value (Appendix 1.2 Statistical tests on CMs).

**Table 5.8: Single-factor ANOVA statistical analysis displaying the calculated F-value, the expected (critical) F-value and the P-value for TCDMDA treated with post-fabrication UV light.**

| <i>Source of Variation</i> | <i>SS</i> | <i>df</i> | <i>MS</i>  | <i>F</i>   | <i>P-value</i> | <i>F crit</i> |
|----------------------------|-----------|-----------|------------|------------|----------------|---------------|
| Between Groups             | 0.024672  | 2         | 0.01233575 | 0.44051263 | 0.6450868      | 3.097698      |
| Within Groups              | 2.520285  | 90        | 0.02800317 |            |                |               |
| Total                      | 2.544957  | 92        |            |            |                |               |

It can be clearly seen that when this data is represented in a bar chart, the flat glass control has a higher value of nuclear roundness compared to the other regions (Figure 5.14). Nevertheless, the statistical analysis results prove that this difference is not significant (Table 5.7).

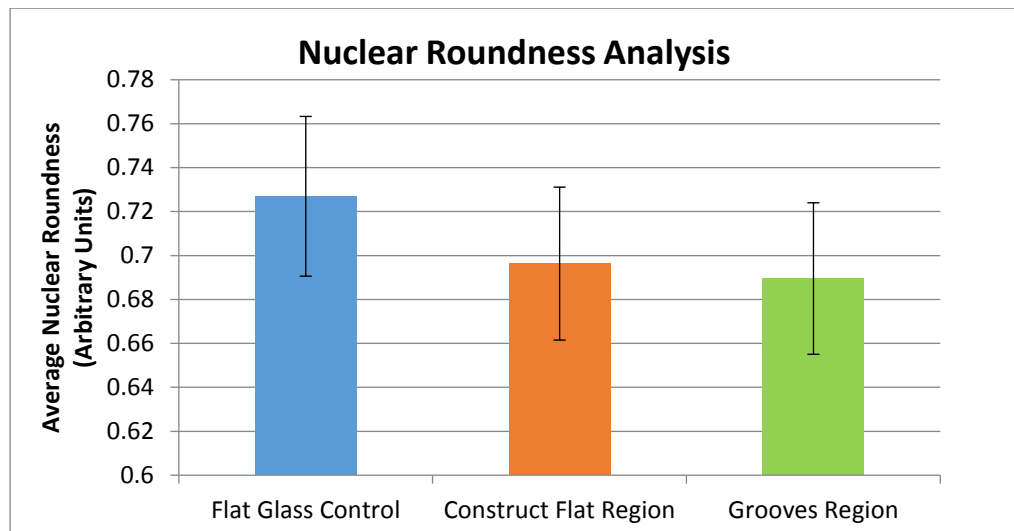


**Figure 5.14: Bar chart showing nuclear roundness levels on the various topological features of TCDMDA with post-fabrication UV light treatment.**

To investigate the distribution of cell orientation only one colour channel could be used therefore the red channel was selected as this had the least background fluorescence and is also the most accurate indicator of CM orientation. The red fluorescent channel stains for cardiac-troponin T which is an indicator of fairly mature CMs.

Cell orientation is an important indicator as to whether cells respond to the topologies they attach to. ImageJ plugin orientationJ analysis showed a random distribution of cells on the flat glass control (Figure 5.15). The colours indicate different degree of orientation as indicated on the colour chart. The colours in the image show that there is a range of several different colours among the cells. This proves the cells on the flat glass control orient themselves in many different directions which is expected of a flat structure (Figure 5.15).

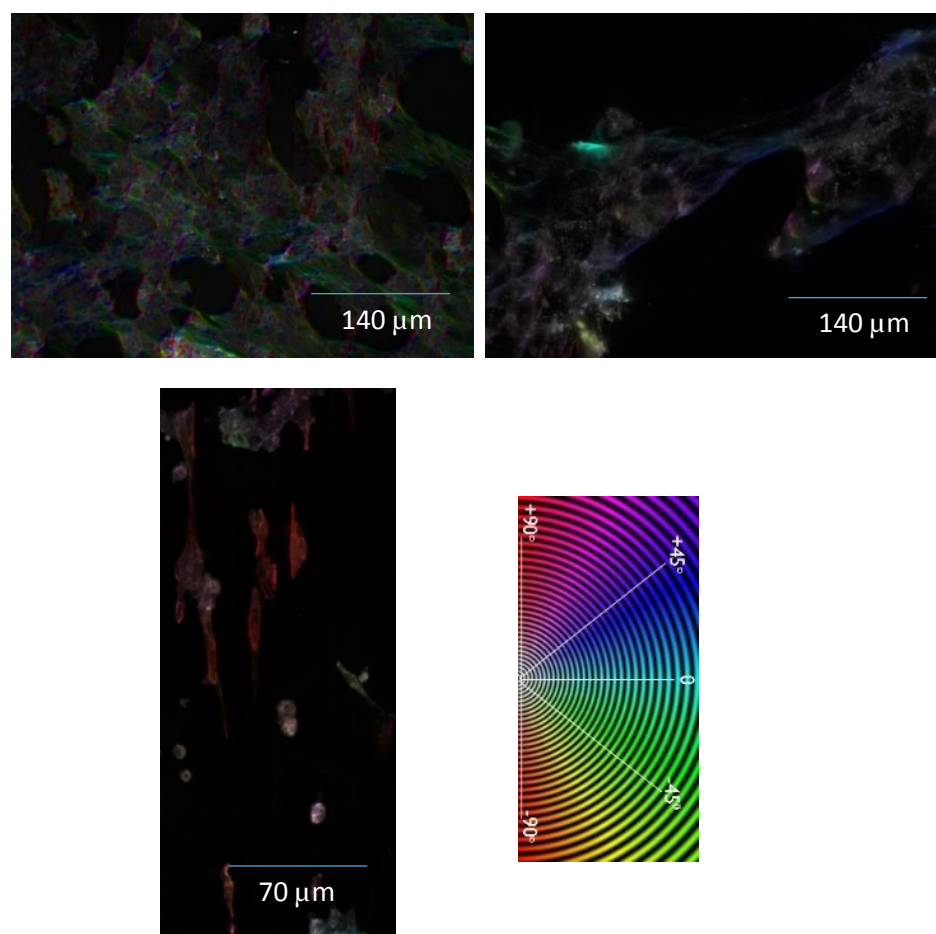


**Figure 5.15: Cell Orientation Colour Survey image and informational colour chart (bottom right) on flat glass control (top left), flat region (top right) and grooves region (bottom) of TCDMDA flat glass control with post-fabrication UV light treatment.**

The distribution of the cells is fairly even throughout all degree values (Figure 5.16). There is a peak at  $-30^\circ$  and a trough at  $50^\circ$  but this indicates a random distribution for the most part which is expected from cells attached to a flat surface. The cells aligned along the grooves on the construct which is demonstrated in the orientation analysis of the region (Figure 5.16). Most of the cells are red and some are pink and the histogram reveals a bias to  $90^\circ$  and  $-90^\circ$  which are both in the direction of the grooves.

Cells that attached to the flat region of TCDMDA extended in a variety of directions, similar to the glass control (Figure 5.16). The difference here was that a number of cells were biased towards  $30^\circ$  orientation as can be seen in the histogram of distribution. This corresponds to dark blue on the chart and the

image shows the cells stretching along that direction. This may be due to the hatching direction of the microgrooves in the flat region of the construct on which some cells responded and aligned along these microgrooves and some did not.

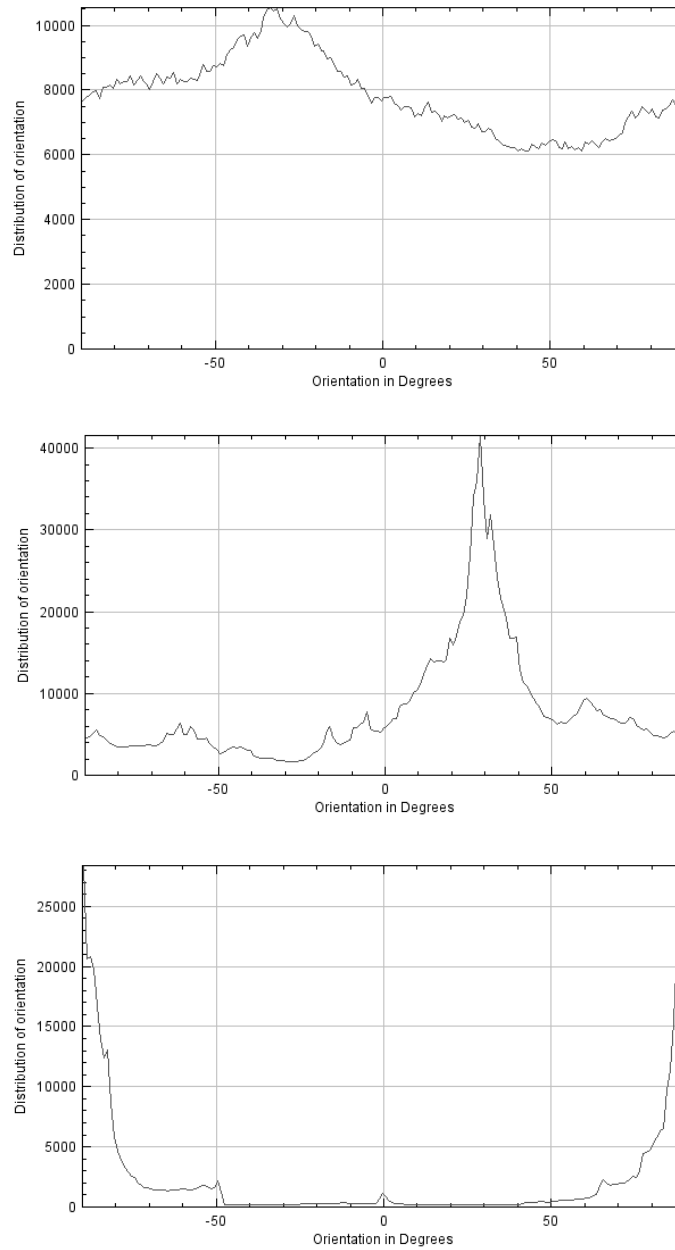


**Figure 5.16: Orientation distribution histograms of flat glass control (top), flat region (middle) and grooves region (bottom) of TCDMDA with post-fabrication UV light treatment.**

#### 5.2.2.2.3 TCDMDA with post-fabrication vacuum treatment

The flat glass control for the construct treated by vacuum after fabrication showed similar cell attachment to the other treatment types (Figure 5.17, top left).

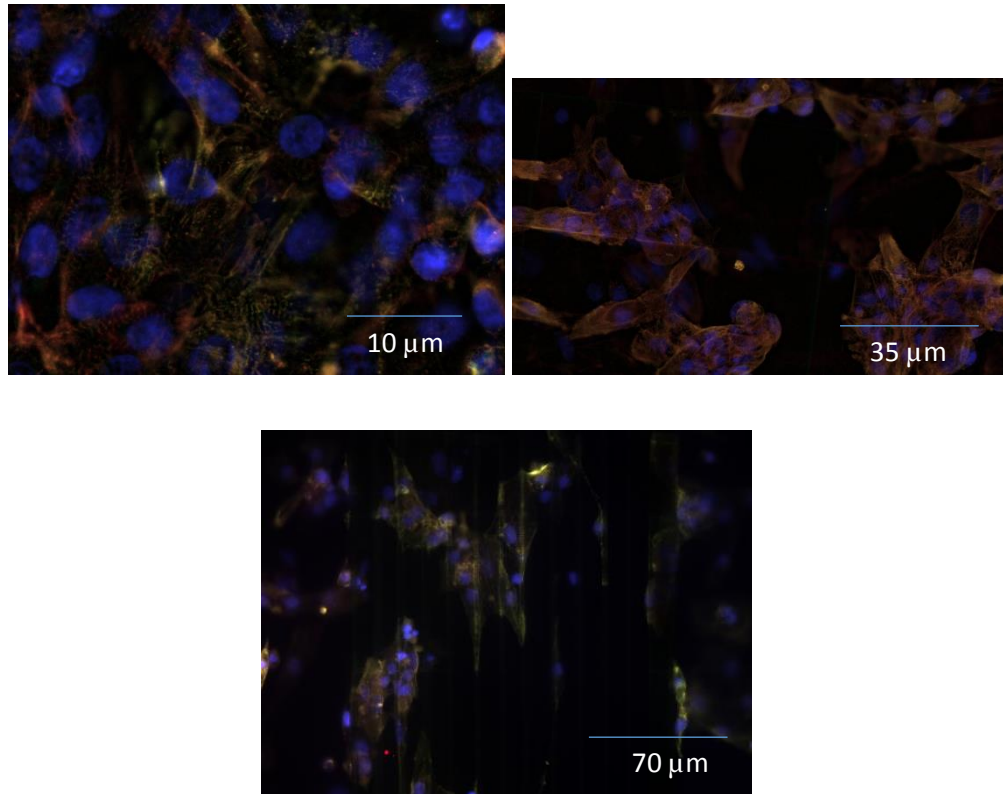


**Figure 5.17: Immunostaining image of cells attached to flat glass control (left), TCDMDA flat region (right) and grooved region (bottom) used in the experiments with TCDMDA post-fabrication vacuum treatment.**

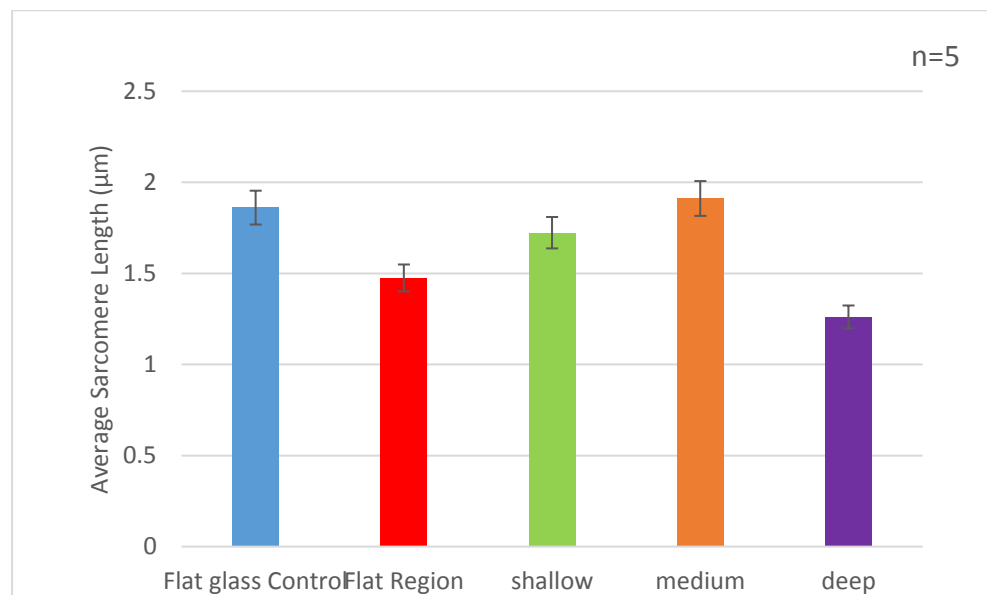
The flat region of TCDMDA also showed cell attachment in various directions. Cells were successfully stained for  $\alpha$ -actinin and cardiac troponin T with the latter proving their CM identity. The cells attached to the grooved of TCDMDA treated with vacuum after fabrication. Cells align along all grooved regions, regardless of groove depth. Immunostaining shows cardiac troponin T (red) which indicated mature CM presence (Figure 5.17). ANOVA statistical analysis showed the F value to be lower than the F critical value which means there is no significant difference in sarcomere length along the various topological features of the TCDMDA construct with post-fabrication vacuum treatment (Table 5.8).



**Table 5.9: NOVA statistical analysis of the 5 groups representing sarcomere lengths on 5 different topological fine features.**

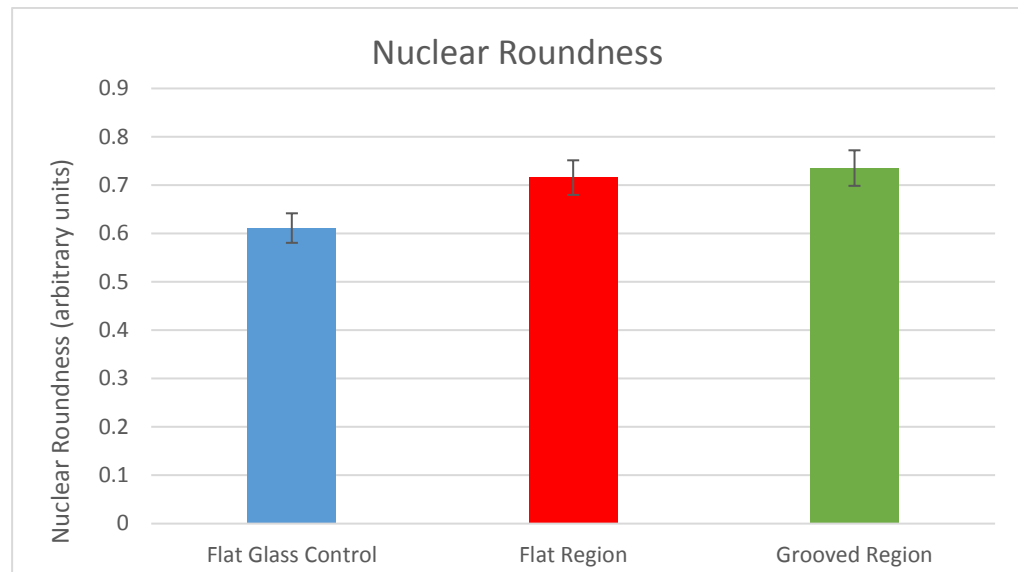
| Source of Variation | SS         | df | MS         | F          | P-value   | F crit  |
|---------------------|------------|----|------------|------------|-----------|---------|
| Between Groups      | 1.80058781 | 4  | 0.45014695 | 1.56471414 | 0.2145389 | 2.75871 |
| Within Groups       | 7.1921596  | 25 | 0.28768638 |            |           |         |
| Total               | 8.99274741 | 29 |            |            |           |         |

Figure 5.18 shows that the highest average sarcomere length belongs to the flat glass control and the medium grooved regions. This is similar to the constructs without post-fabrication treatment and with post-fabrication UV-light treatment. Longer sarcomere lengths indicate more mature CMs. Out of all post-fabrication treatments, vacuum treated constructs showed cells with the shortest sarcomere lengths on all topological fine features. The construct without post-fabrication treatment had the longest sarcomere length in all regions of the construct.



**Figure 5.18: Column chart comparing the average sarcomere length on each topological feature of TCDMDA treated with vacuum post-fabrication.**

Nuclear roundness was the highest on the grooves topologies compared to the flat regions (Figure 5.19).



**Figure 5.19: Column chart showing comparing the average nuclear roundness on each topological feature of TCDMDA treated with vacuum post-fabrication.**

Anova statistical analysis shows that the F value is higher than the F critical value. This means there is a statistically significant difference between 2 of these 3 groups (Table 5.9).

**Table 5.10: ANOVA statistical analysis to determine presence of a significant difference between the 3 groups of nuclear roundness.**

| Source of Variation | SS         | df  | MS         | F          | P-value    | F crit     |
|---------------------|------------|-----|------------|------------|------------|------------|
| Between Groups      | 0.25027209 | 2   | 0.12513605 | 5.17803655 | 0.00634317 | 3.03670994 |
| Within Groups       | 5.34084025 | 221 | 0.0241667  |            |            |            |
| Total               | 5.59111234 | 223 |            |            |            |            |

In order to analyse which of these 2 groups differ significantly, t-tests were performed pair-wise for all double group combinations. The results show the p values were lower than the t-critical values between the flat glass control and both the flat region and the grooved region (Table 5.10).

**Table 5. 11: Student's t-test results of nuclear roundness between the flat glass control versus the flat region, the flat glass control versus the grooved region (middle) and the flat region versus the grooved region of TCDMDA with post-fabrication vacuum treatment.**

|                    | Flat Region | Grooved Region |
|--------------------|-------------|----------------|
| Flat Glass Control | YES         | YES            |
| Grooved Region     | YES         | -----          |

The flat glass control showed no particular bias in orientation as expected and in line with previous results (Figure 5.20).

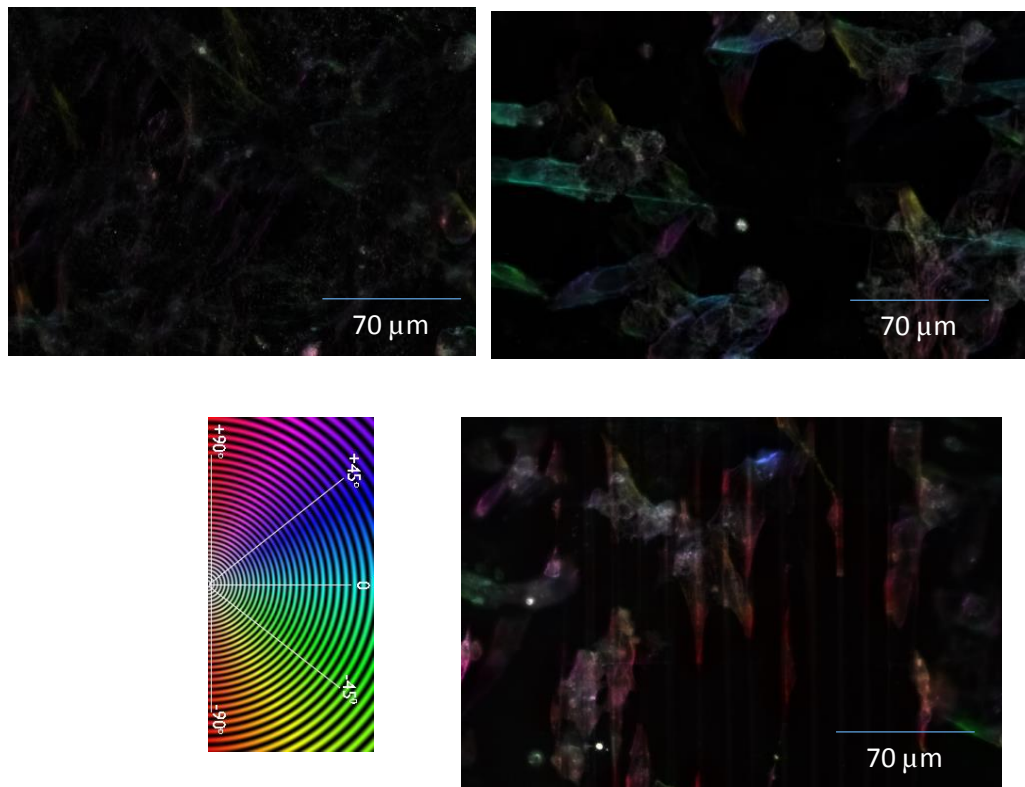


**Figure 5.20: Colour survey of flat glass control (top left), flat region (top right) and grooves region (bottom) for TCDMDA with post-fabrication vacuum treatment. The colour chart indicates how each colour corresponds to a specific angle (bottom left).**

The flat region of TCDMDA with post-fabrication vacuum treatment showed similar results to the flat glass control with some bias towards 10° degrees as shown by the turquoise colour on the colour survey image. This indicates some of the cells stretched along a hatching line in the structure (Figure 5.21).

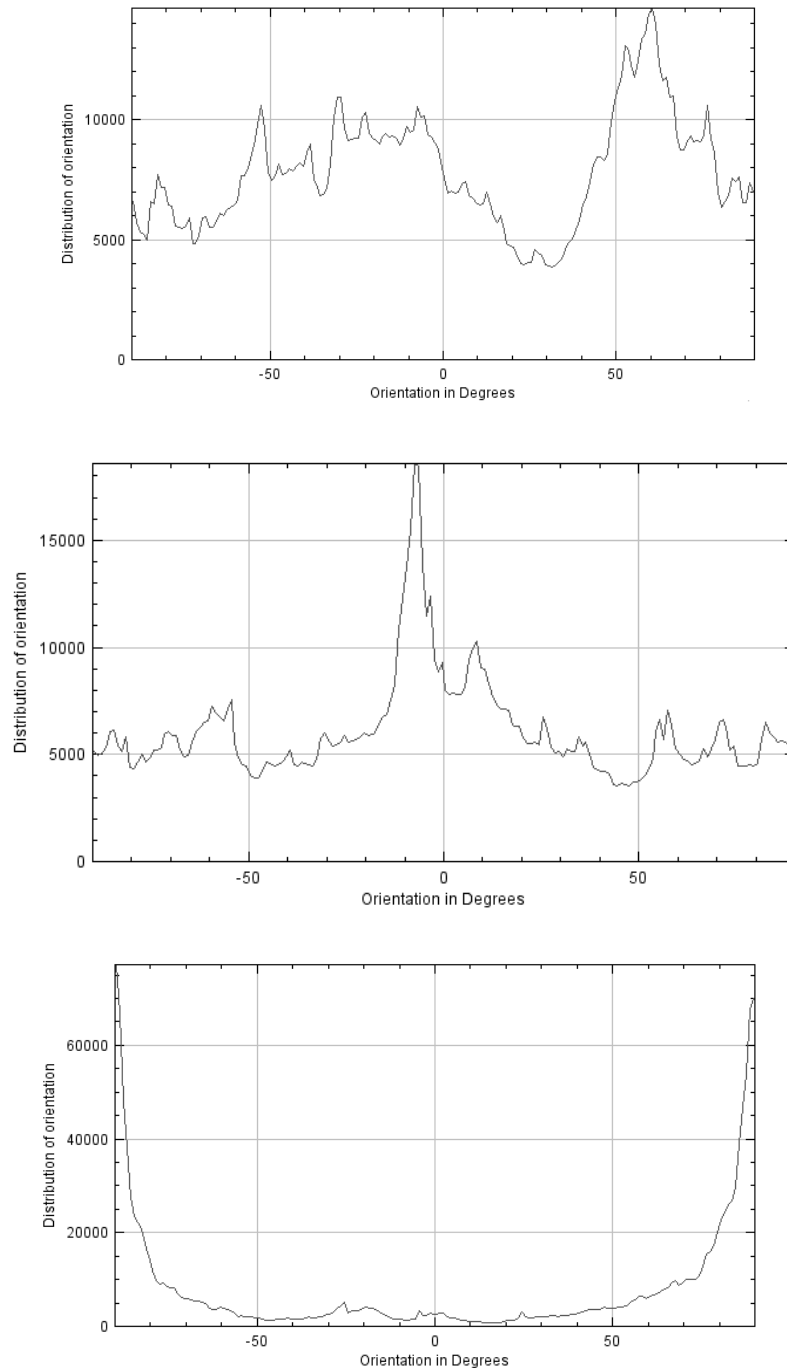


**Figure 5.21: Orientation distribution histogram of flat glass control (top), flat region (middle) and grooves region (bottom) of TCDMDA construct with post-fabrication vacuum treatment.**

The grooved region showed an overall response to the grooves. Cells aligned along the grooves which showed as a red colour in the colour survey image and a bias towards 90° and -90° in the orientation distribution histogram (Figure 5.20).

Colour surveys combined with images and histograms only give an overall perception of orientation. The raw distribution data which was used to generate the histogram was analysed and the standard deviation calculated for each post-fabrication treatment on the grooved regions. The aim was to observe whether there was any difference in orientation distribution among post-fabrication treatments. The vacuum-treated construct had the largest standard deviation (Table 5.12) which coincides with the appearance of the more abundance of red colour in the corresponding image (5.2.2.2 CM attachment to TCDMDA and analysis of cell characteristics). The construct with post-fabrication UV light treatment also possessed a larger standard deviation compared to the construct without post-fabrication treatment. The vacuum treatment may have created a smoother surface for ease of cell extension. The UV light may have cured residual monomer on the surface to facilitate cell attachment and extension.

**Table 5.12: Standard deviation values of the 3 post-fabrication treatments on grooved region of TCDMDA.**

| <i>Without post-fabrication treatment</i> | <i>Post-fabrication UV light treatment</i> | <i>Post-fabrication vacuum treatment</i> |
|---|--|--|
| 1323.9                                    | 5026.6                                     | 12881.6                                  |

### 5.3 Discussion and Conclusions

The experiments performed in this chapter reveal that the cells on the topologies are cardiomyocytes as evident from the cells on constructs expressing cardiac Troponin-T as expected. Even though not all cells expressed this protein, this was also expected as not all CM populations are pure and will contain a certain number of fibroblasts (Denning et al., 2016).

The cells with the largest sarcomere length value were on the 9  $\mu\text{m}$  depth grooves regardless of post-fabrication treatment (5.2.2.2 CM attachment to TCDMDA and analysis of cell characteristics). This is shown in all the bar chart figures for each treatment condition. However quantitative statistical analysis showed that only the constructs with post-fabrication UV light treatment showed significant differences among their sarcomere lengths on the different groove depths. Student's t-tests revealed that all groups were significantly different to one another albeit the difference between the flat region and the various grooves regions compared to the differences between the grooves of different depths (6, 9 and 12 microns). The fact that CMs on the grooves adopted larger sarcomere lengths is due to their change in morphology during extension along the grooves. The deeper grooves also allowed them to extend even more possibly due to less opportunity for them to spread. Whereas the shallow 6  $\mu\text{m}$  grooves renders more spreading and less extension. Raman spectroscopy results revealed that post-fabrication UV light treatment increased the degree of cure (DOC) in TCDMDA which supports the possible fact that this additional DOC may have created a more favourable polymer surface for CM attachment due to less probability of cytotoxicity (Section 5.2.1). Even though one study found optimal groove width to be between 800 and 1000 nm (Carson, 2016 #38) and another between 30 and 80 microns (Salick, 2014 #46), the grooved widths fabricated in this study were 27 microns. This was to ensure many CMs were guaranteed to fall within each groove during the seeding process. According to the immunostaining results, CMs were visible and quantitative comparisons could be made. Sarcomere length values reported in this doctoral project are similar to what has been reported in previous CM maturity studies. A mature adult CM has a sarcomere length of 2.2  $\mu\text{m}$  and fetal CMs 1.6  $\mu\text{m}$  (Jiang, 2018 #188). The sarcomere length

values found for CMs attached to structures without post-fabrication treatment and treated with post-fabrication UV-cure were all more than 2 microns for the 9 and 12  $\mu\text{m}$  deep grooves. This demonstrates the sarcomere lengths that can currently be achieved from iPSC-derived CMs by altering groove depth. This did not apply to the structures with post-fabrication vacuum treatment. Due to this, biological repeats of these experiments are necessary to draw definite conclusions.

The 2PL structures fabricated for the purpose of comparing CM maturation provide novel insights into the influence of these parameters. It has been shown before that grooves induced CMs to align and stretch along the structures fabricated by 2PL (Silbernagel, 2020 #199). Micro-channels have been used to guide CMs in the fabrication of patches (Schaefer, 2018 #210) and in the form a 'biowire' (Nunes, 2013 #211). The work done in this doctoral project adds more to this fact by identifying the range of groove depths that support more mature CMs. Multi-layered scaffolds combining both CMs and endothelial cells to seed inside and around the channels respectively have proved beneficial (Fleischer, 2017 #221). Vascularization could be the next step in improving the maturation of CMs.

Nuclear roundness measurements showed that only the constructs with post-fabrication vacuum treatment revealed a significant difference. Nuclear roundness was used as an indicator of overall cell roundness, which was a measure of CM maturity (Denning, 2016 #32). The less the circularity, the more mature the CM. The nuclei of cell muscle fibres have been found to undergo morphological changes during contraction. The nuclei are squeezed as the cell contracts hence losing their circularity (Roman, 2017 #231). Unexpectedly, the grooved region possessed the roundest nuclei and the largest difference was between the flat glass control and the grooves region. It was expected that the grooves would have caused the CMs to align and extend. Perhaps seeding them in clusters resulted in direct attachment rather than extension along the groove, which resulted in the rounder nuclei. Vacuum treatment may have removed any residual monomer from the surface and rendered it smoother for the cells to spread. Raman spectroscopy showed significantly higher DOC values in TCDMDA with post-fabrication vacuum treatment compared to the polymer

without post-fabrication treatment, supporting this possibility. This may have resulted in less extension of the cells and more spreading to give rounder nuclei. The dispute here is that, if a CM happens to have long sarcomeres and stretch along a groove structure, it can still retain its nuclear circularity. This does not necessarily mean it's lost its maturity. A possible reason could be that a group of cells were clustered together in the same groove instead of aligning synchronously.

Cell orientation studies showed that, overall, cells respond to grooves and orient themselves along the grooves. This is demonstrated in all of the orientation analyses in all post-fabrication treatments. Cell orientation in response to topological structures has shown similar results (Lee, 2008 #49) (Silbernagel, 2020 #24). Those studies showed that CMs could be guided along the topological structure fabricated, whether a rod or a channel. The experiments in this chapter 5 proved that CMs follow the direction of the grooves regardless of post-fabrication treatment. The flat regions and flat glass controls show randomly oriented cells and the grooved regions show oriented cells. The most significant orientation distribution is on the post-fabrication vacuum-treated constructs. The highest percentage of cells with the most bias towards 90 or -90° lies in this construct. One possible reason could be the treatment of vacuum inducing a smooth surface for the cells to facilitate their extension along the grooves. UV-light treatment also may have improved cell extension which is demonstrated in the Raman spectroscopy experiments (Section 5.2.1).

The Raman spectral data show that vacuum has a larger influence on DOC compared to UV light as a post-fabrication treatment in all three polymers TCDMDA, GPOTA and PETrA. Post-fabrication UV light treatment was already known to improve overall DOC (Oakdale, 2016 #176). However, vacuum treatment has also been used as a post-fabrication treatment (Taormina, 2018 #177). The results from this doctoral project confirmed that vacuum treatment was more effective in 3 different polymers. This is demonstrated by the measurement of the same samples 4 consecutive times which was done in the 2<sup>nd</sup> set of Raman measurements. TCDMDA possesses the highest DOC before any post-fabrication treatment and this is due to TCDMDA having the cyclic ring structure which provides high curing speeds. The cyclic ring is



sterically hindered which means the monomer can remain in the radicalised state for a longer time which increases its chances of encountering another radicalised monomer chain. UV light also increases DOC of all 3 polymers compared to polymers without any post-fabrication treatment. This is due to the UV light activating any remaining photo initiator in the mixture which can then go on to form radicalised monomers to commence chain propagation. The removal of unreacted monomer by vacuum treatment may be crucial to eliminating cytotoxicity as the solvent mostly remains on the polymer surface. However, this did not directly translate to the cells as CM attachment was also observed on UV-light treated constructs and polymers without any post-fabrication treatment. This may be due to the use of serum during cell dissociation which may have given the cells the initial extra strength to survive and attach to the polymers. The use of serum was carried out due to time constraints as cell attachment was not being observed on polymers without use of serum during cell dissociation.

All experiments involved  $n=5$  as a cell count as this was the available number to clearly observe and measure sarcomere length. In addition, the number of cells that actually landed on the grooves during seeding were much less than the initial seeding density calculated. This was due to some cells not settling onto the construct and moving onto the sides or falling off the construct. This is why future work on these experiments will be biological repeats to prove that each cell seeding procedure has this limitation. Other strategies could include overcoming this limitation by isolating the scaffold within a chamber so the cells do not fall off the construct during seeding.

In summary, different regions of each construct produced different results and this also depended on post-fabrication treatment. However, the general trend in sarcomere length is that 9  $\mu\text{m}$  groove depth supported the highest sarcomere length under all treatment conditions. All sarcomere length results showed a similar pattern in which the 6  $\mu\text{m}$  grooves had the lowest sarcomere length which increased to the highest in the 9  $\mu\text{m}$  grooves and then decreased slightly in the deeper 12  $\mu\text{m}$  grooves. Statistical analysis however showed that the difference is only significant on the construct with post-fabrication UV cure (Table 5.13).

**Table 5.13: Summary of CM response to topology and post-fabrication treatments.**

| <i>Significant differences</i> | <i>No treatment</i> | <i>UV</i> | <i>vacuum</i>                      |
|--------------------------------|---------------------|-----------|------------------------------------|
| <i>Sarcomere length</i>        | No                  | Medium    | No                                 |
| <i>Nuclear roundness</i>       | No                  | No        | Roundness lowest on grooves region |
| <i>Cell orientation</i>        | No                  | No        | Yes                                |

Nuclear roundness and cell orientation distribution demonstrated significant differences in post-fabrication vacuum-treated constructs. The whole process of cell attachment and maturity is dependent on many factors therefore testing each component individually is a challenge. In this study, many factors were simultaneously tested by utilising the technology of 2PL to fabricate complex architectures comprised of various fine features. The conclusion drawn in this chapter is that groove depth had an influence on sarcomere length of iPSC-CMs.

#### 5.4 Future Work

These results are crucial to understand what exactly makes CMs more mature. The structures fabricated provided the results that topological variations affect CM maturity. This is a big step toward the advancement of a universal platform to grow mature CMs. The groove depths between 9 and 12  $\mu\text{m}$  could be investigated. Novel structures with a minimum depth of 9  $\mu\text{m}$  could be designed such as a cube or a bowl to observe how this affects CM maturity. Experimentation with all possible factors influencing CM maturity throughout time will lead to a universal platform on which iPSC-derived CMs can be tested and used for drug screening.

## Chapter 6: Overall Conclusions for the PhD Hypothesis and Future Perspectives

### 6.1 Overall Conclusions

The hypothesis that ‘3D architectures produced and controlled by 2-photon lithography (2PL) affects cardiomyocyte attachment and maturity’ can be accepted based on the findings of all 3 chapters.

The experiments performed in chapter 3 investigated which acrylate polymers were amenable to 2PL as well as the types of acrylate polymers that were likely to be amenable, namely the multifunctional acrylate polymers. Acrylates with at least 2 acrylate functional groups are amenable to 2PL with the photoinitiator I369. The purpose of Chapter 3 was to find which polymers, which previously showed cardiomyocyte (CM) attachment, could be processed by 2PL. 8 multifunctional polymers were proven to be amenable to 2PL and 3 of these polymers, GPOTA, HEODA and HDDA processing parameters were determined. The operating window of the acrylate polymers depended on the identity of the polymer itself.

Chapter 4 experiments on silanisation of polystyrene plates showed that the procedure was not beneficial when performed with acrylate polymers as cloudiness was observed. The CM attachment experiments showed varying results depending on the photoinitiator and media type used. They showed that all polymers tested except GPOTA could support CMs when PI I369 was used in the presence of RILT medium. When other PIs were used on the polymers in the presence of RILT medium no CM attachment was observed on any of them. Whereas when RPMI B27 media was used only GPOTA supported CMs with I369 PI. The other 2 PI formulations; DMPA and DMPA+IPA did not support CM attachment, regardless of the polymer tested. The 2-photon lithography structural analysis studies revealed differences in measurements of hatching distance between fabricated structures and the design of the structure on Describe software. This conclusion led to making allowance for this difference during complex architecture design.

Raman spectroscopy analysis and differential CM attachment and maturity studies completed the findings to reach the overall conclusion of this PhD study. Raman studies showed that vacuum treatment was the most effective in increasing degree of cure (DOC) of all 3 polymers TCDMDA, GPOTA and PETrA. Sarcomere length measurements showed that CMs mostly prefer the 9  $\mu\text{m}$  and 12  $\mu\text{m}$  groove depths compared to the 6  $\mu\text{m}$  and flat part of the constructs. CM attachment on TCDMDA showed an overall random cell orientation on the flat regions versus the groove regions which showed preference for  $90^\circ$  alignment along the grooves on all post-fabrication treatment types. Nuclear roundness measurements were only significantly different on the constructs with post-fabrication vacuum treatment. Nuclei had the highest roundness on the grooves region compared to the flat region. All of this information gathered together indicates that CMs prefer groove depths of approximately between 9 and 12  $\mu\text{m}$ , compared to 6  $\mu\text{m}$  and flat controls, when the groove width is kept constant at 27  $\mu\text{m}$ . Post-fabrication UV light treatment contributed to CM maturation, as the CMs on the deeper grooves had the longest sarcomeres.

## 6.2 Future Perspectives

The finding that only multi-functional acrylate polymers were amenable to 2PL when using I369 photoinitiator increases the efficiency of future investigations into which materials are suitable for the technology. This way, there will be no need to test a whole library of polymers but rather refine the list to only multi-functional acrylate. Of course, this will depend on the PI being used. However, this shows a good starting point for 2PL-amenable material discovery.

The generation of the operating window is crucial to determining whether it is worth taking the polymer material onto the next stage, which is in construction of complex architectures. Even though some polymer maybe amenable to 2PL, they do not have a wide enough operating window for the complete fabrication of structures, as found with BDDA and HEODA (Chapter 3, 3,2,2). Future projects can then rely on analysis of previously determined operating windows to decide whether to utilise the polymer or not. All of this aids in speeding up

the process of not only finding 2PL-amenable materials but also using operating window data in the selection of complex architecture fabrication.

CM attachment was proved on several combinations of polymer, media and photoinitiator formulations. The conclusion drawn from the work in Chapter 4 is that the ability of CM attachment depends on a combination of polymer chemistry, photoinitiator formulation and media type used. The most CM attachment is observed using I369 photoinitiator in the presence of RILT media. Using UV polymerisation to test for cell attachment is the most efficient method to determine which polymers can support the cells prior to making the decision on whether to use polymers to construct complex architectures by 2PL. The setup of 2PL would have meant each polymer would have to be fabricated separately as only one formulation could be used per fabrication period which would have taken much longer. This way of testing polymers for cell attachment first serves as an example for other studies involving cell culture. As additional knowledge, future experiments involving different photoinitiator concentrations could be tested to determine cytotoxicity levels.

The fact that a significant difference was observed in sarcomere length between deeper grooves 9 and 12  $\mu\text{m}$  compared to other regions on the TCDMDA construct showed that CMs respond to the topologies they adhere to and 2PL can be used to control how CMs mature *via* fabrication of varying groove depth. A more detailed future study exploiting the high-resolution features 2PL can fabricate would be to investigate the differences between 7, 8, 9, 10, 11 and 12  $\mu\text{m}$  groove depths. This would allow identification of any minute differences, if present, in CM attachment and maturity between these features. Other topological features that could be tested are cones and pillars with variable spacing, ideally at the nanoscale. Functional tests on the CMs would have provided information on electrophysiological performance and response to cardiac drugs. These would then be compared to adult heart cells to determine exactly how mature these cells are. The CMs on the 9 and 12  $\mu\text{m}$  deep grooves possessed sarcomere lengths larger than most mature iPSC-CMs to date (Jiang et al., 2018).

Overall, this PhD project has contributed information towards how iPSC-CMs can be triggered to a mature form. 2PL has been used to facilitate the fabrication of high-resolution structures to come this far. The polymers found to be amenable to 2PL are not as vast as the ones that can be used in UV lithography techniques, but the list will grow as more polymers are tested for amenability. It is crucial that a combination of construct topology, polymer chemistry and post-fabrication treatment are found so that this iPSC-CM to mature CM path is crossed.

## Appendix

### 1.1 Raman Spectroscopy

All 3 polymers TCDMDA, GPOTA and PETrA without post-fabrication UV cure or vacuum treatment showed the expected degree of cure that most acrylate polymer possess after 2PL. The degree of cure ranged between 35% and 53% and these differences can only be attributed to the polymers' chemical properties as reaction conditions were identical during fabrication. The characteristic peaks for C=C and C=O vibrations are easily observed on all spectra with Raman shift values of  $1640\text{ cm}^{-1}$  and  $1720\text{ cm}^{-1}$  respectively. Some spectra showed a small peak at approximately  $1610\text{ cm}^{-1}$  which most likely corresponds to the photoinitiator I369 (Figure A.1). The degree of cure in polymers with vacuum treatment were considerably higher compared to the degree of cure in polymers without any treatment or with post-fabrication UV cure only treatment.

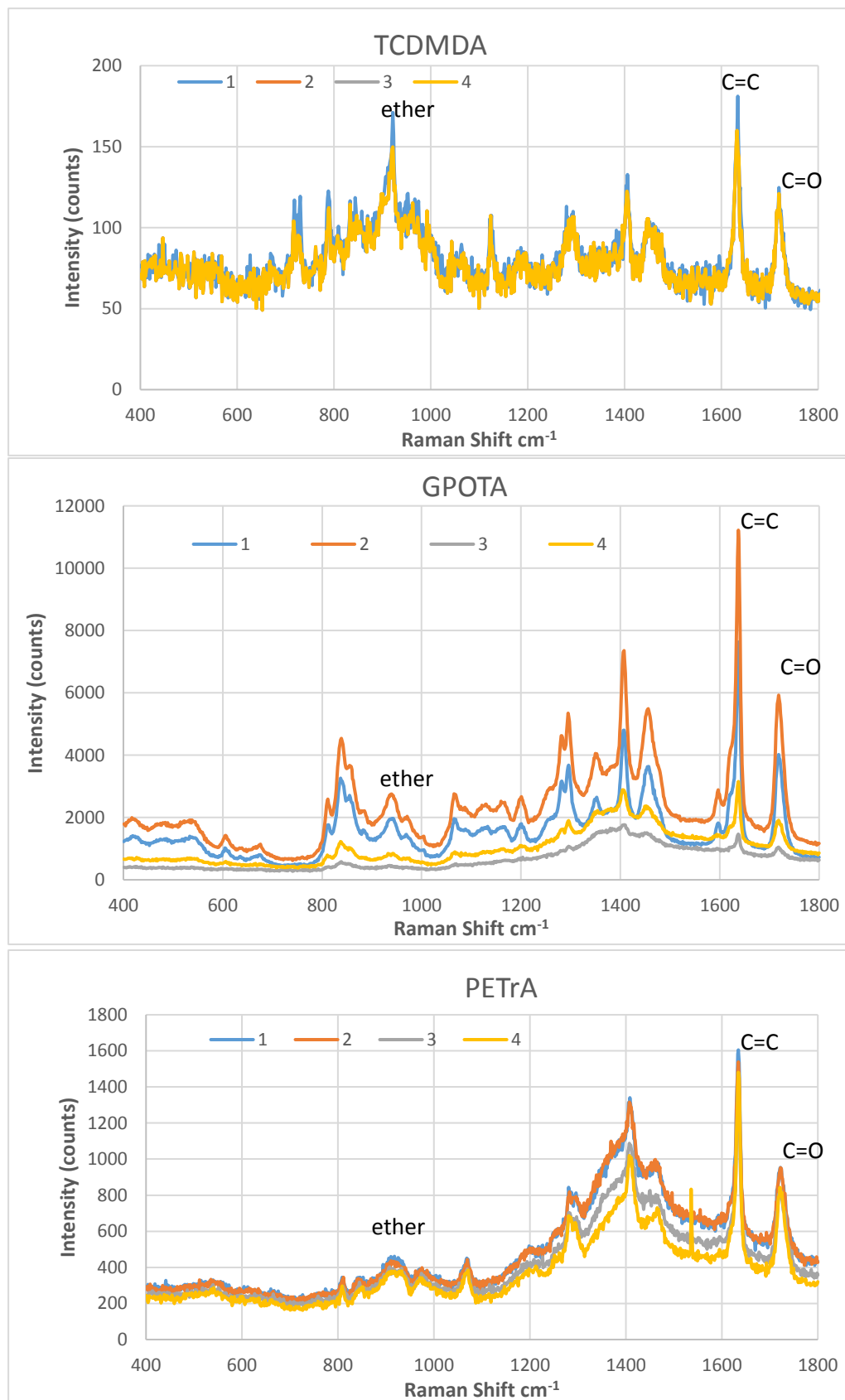


**Figure A1: Spectra of uncured TCDMDA, GPOTA and PETrA displaying all 4 repeat measurements.**



All polymers showed considerably higher peaks for C=C compared to the C=O peaks at first glance. GPOTA and PETrA showed a small bump on the bottom left side of the C=C peak which may be an indicator of a signal from the photoinitiator molecule merging with the C=C peak. The C=O peaks appear at the expected value of  $1720\text{ cm}^{-1}$ . The ratio of C=C to C=O is calculated by measuring the area under both peaks and dividing the C=C peak by the C=O peak since C=C is the bond that will participate in the polymerisation reaction. Therefore, it is expected that the area under the peak for C=C will be larger than the area of the peak under the C=O peak. This is apparent in the values shown in Table A.1.

**Table A 1: Area under the peaks of interest of uncured monomers that were tested for CM attachment in their polymerized form. All intensity values are taken as an average of 4 measurements (n=4).**

| <b>Polymer name</b> | <b>Ether peak Intensity (counts)</b> | <b>C=C Intensity (counts)</b> | <b>C=O Intensity (counts)</b> | <b>Ratio C=C/C=O (Arbitrary Units)</b> |
|---------------------|--------------------------------------|-------------------------------|-------------------------------|--|
| <b>TCDMDA</b>       | <b>981.68</b>                        | <b>1280.3</b>                 | <b>781.2</b>                  | <b>1.64</b>                            |
| <b>GPOTA</b>        | <b>32647.96</b>                      | <b>32263</b>                  | <b>23179.23</b>               | <b>1.39</b>                            |
| <b>PETrA</b>        | <b>814.22</b>                        | <b>12291.58</b>               | <b>9645.72</b>                | <b>1.27</b>                            |

#### 1.1.1 Polymers with no UV or vac treatment

All 3 polymers showed the characteristic peaks for C=C and C=O at  $1640\text{ cm}^{-1}$  and  $1720\text{ cm}^{-1}$  respectively (Figure A.2). TCDMDA and GPOTA also showed a small separate peak next to the C=C peak which is an indicator of photoinitiator presence. This implies there is unreacted PI remaining in the sample. No reaction is 100% efficient therefore this is expected. The PETrA spectrum did not exhibit this small separate peak which may mean that the PI is utilised more efficiently in the polymerisation reaction.

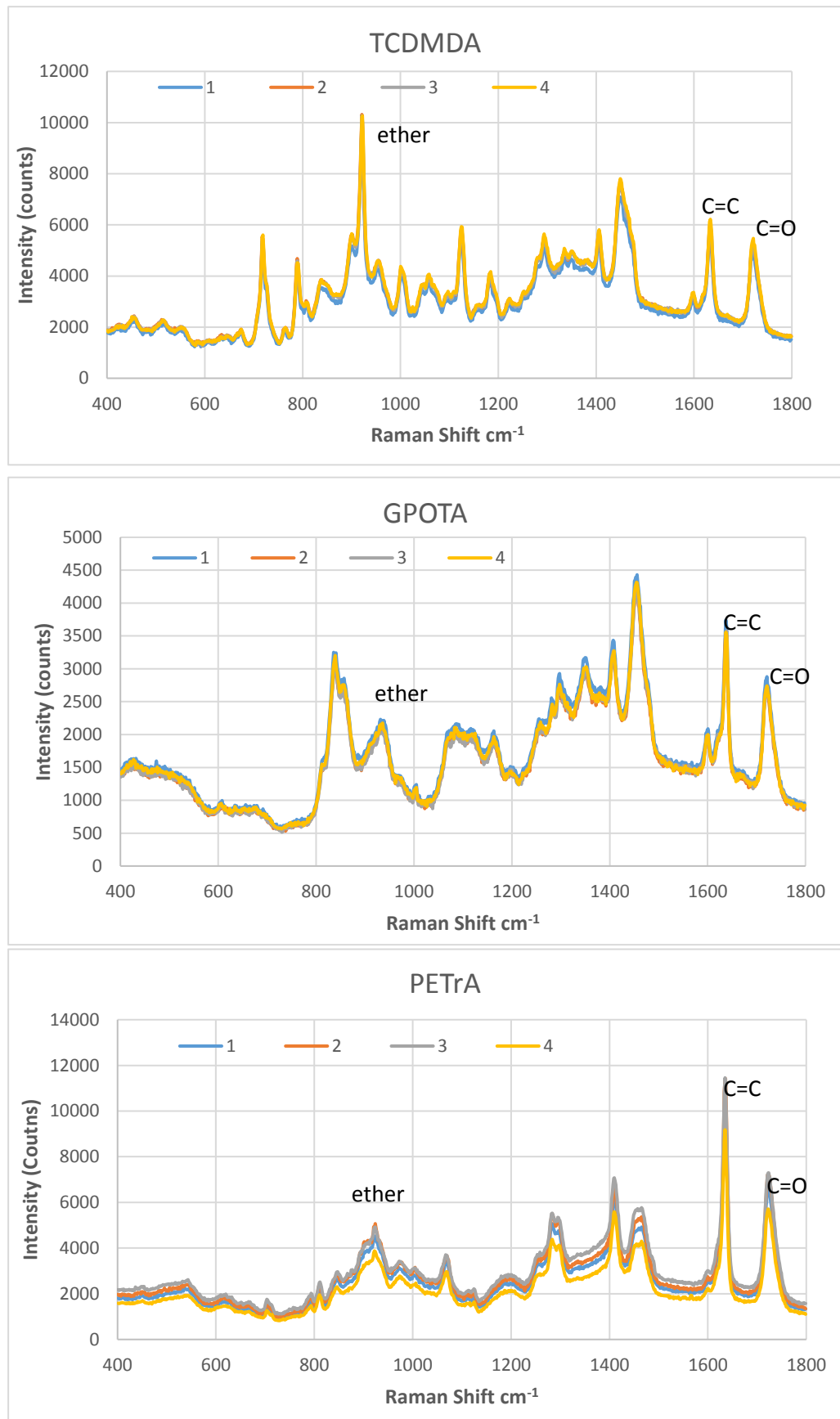


**Figure A.2: Spectra of polymers TCDMDA, GPOTA and PETrA with no post-fabrication treatment.**

The area under the C=O peak was larger than the area under the C=C peak which is expected after a polymerisation reaction as C=C bonds are converted to C-C bonds (Table A.2).

**Table A 2: Area under the peaks of interest of polymers cured by 2PL only (no vacuum or post-fabrication UV light treatment). All intensity values are taken as an average of 4 measurements (n=4).**

| <b>Polymer name</b> | <b>Ether peak Intensity (counts)</b> | <b>C=C Intensity (counts)</b> | <b>C=O Intensity (counts)</b> | <b>Ratio C=C/C=O (Arbitrary Units)</b> | <b>DOC (%)</b> |
|---------------------|--------------------------------------|-------------------------------|-------------------------------|--|----------------|
| <b>TCDMDA</b>       | <b>28197.625</b>                     | <b>48770.025</b>              | <b>70793.275</b>              | <b>0.69</b>                            | <b>57.9</b>    |
| <b>GPOTA</b>        | <b>44486.75</b>                      | <b>28369.575</b>              | <b>38274.675</b>              | <b>0.74</b>                            | <b>46.7</b>    |
| <b>PETrA</b>        | <b>8276.2825</b>                     | <b>112611.425</b>             | <b>123511.5</b>               | <b>0.91</b>                            | <b>28.2</b>    |

The degree of cure (DOC) varies depending on polymer identity (Table A.2). TCDMDA exhibited the highest DOC at 52.9% among the 3 polymers, followed by GPOTA at 43.7% and PETrA at 35.1%. The DOC is usually not above 50% for most polymers treated with UV light for 60 seconds (Khalil et al., 2007) therefore these results are expected. Some polymers show lower DOC due to their chemical structure. Usually, the polymers that cross-link exhibit extensive branching which would slow down the PI from reaching all the C=C bonds inside the polymer network, slowing down the polymerization reaction hence showing a lower DOC.

#### 1.1.2 Polymers with vacuum treatment

All 3 polymers showed the characteristic C=O and C=C peaks (Figure 5.3). The PI peak is also present in all 3 spectra. Vacuum treatment increases the DOC of all 3 polymers (Table A.3).

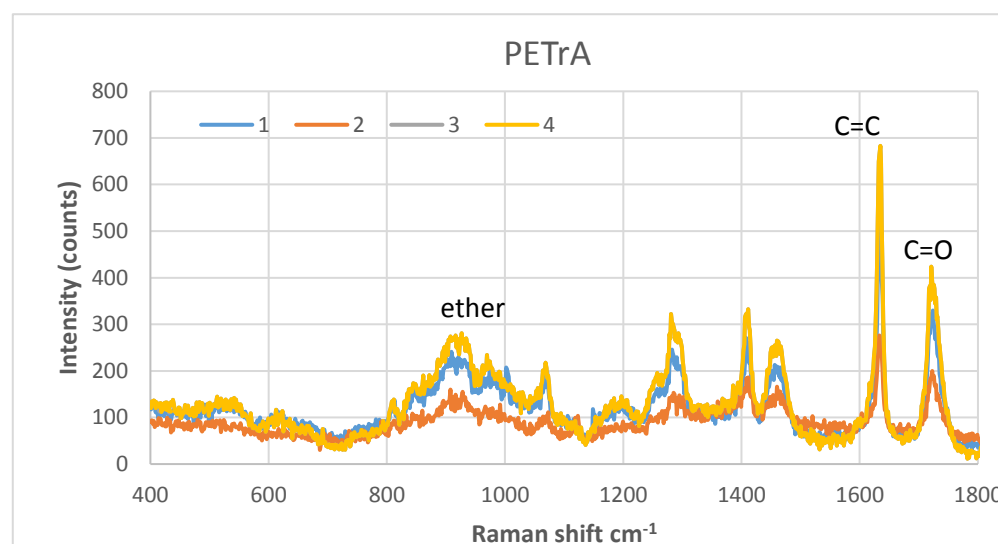
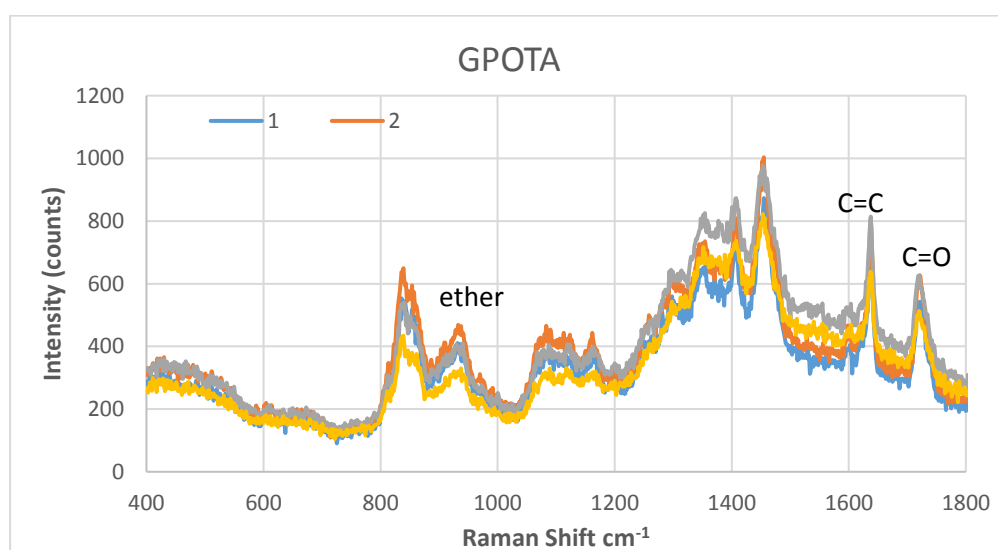
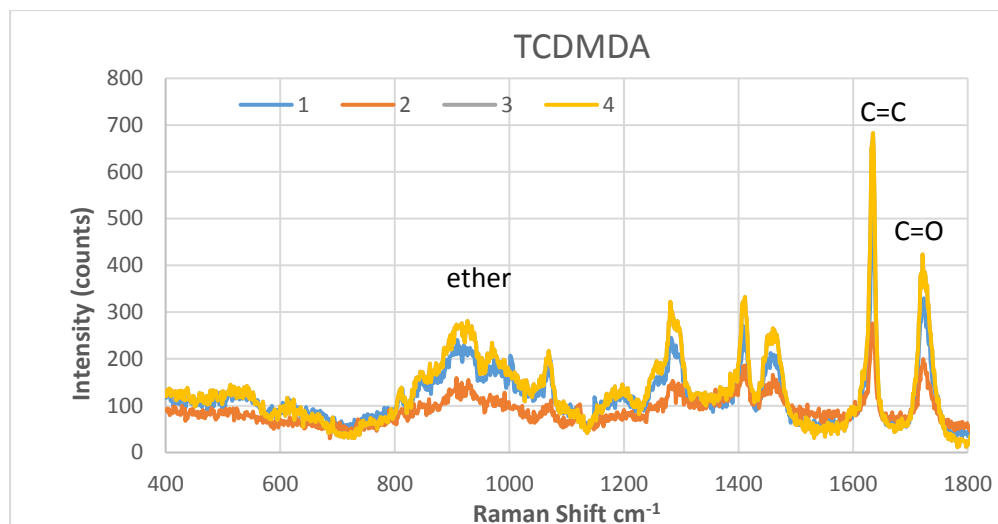


**Figure A.3: Spectra of polymers TCDMA, GPOTA and PETrA with post-fabrication vacuum treatment.**

The DOC of GPOTA was markedly higher when treated with vacuum compared to polymerisation without any treatment with DOC 43.7% (Table A.2). Perhaps the DOC of GPOTA is lowest due to the amount uncured free monomer remaining in the sample post-polymerisation. Vacuum treatment causes evaporation of the free monomer which results in a large DOC difference.

**Table A 3: Area under the peaks of interest of polymers subject to vacuum treatment only. All intensity values are taken as an average of 4 measurements (n=4).**

| <b>Polymer name</b> | <b>Ether peak Intensity (counts)</b> | <b>C=C Intensity (counts)</b> | <b>C=O Intensity (counts)</b> | <b>Ratio C=C/C=O (Arbitrary Units)</b> | <b>DOC (%)</b> |
|---------------------|--------------------------------------|-------------------------------|-------------------------------|--|----------------|
| <b>TCDMDA</b>       | <b>2672.42</b>                       | <b>4538.785</b>               | <b>8344.665</b>               | <b>0.54</b>                            | <b>66.8</b>    |
| <b>GPOTA</b>        | <b>7197.62</b>                       | <b>4694.85</b>                | <b>6359.09</b>                | <b>0.74</b>                            | <b>47.0</b>    |
| <b>PETrA</b>        | <b>682.98</b>                        | <b>5947.57</b>                | <b>6964.13</b>                | <b>0.85</b>                            | <b>33.1</b>    |

### 1.1.3 Polymers treated with post-fabrication UV light

The polymer constructs treated with post-fabrication UV cure produced spectra with characteristic peaks of C=C and C=O. TCDMDA spectrum showed a small PI peak. GPOTA and PETrA showed small humps on the bottom left of the C=C peak (Figure A.4).

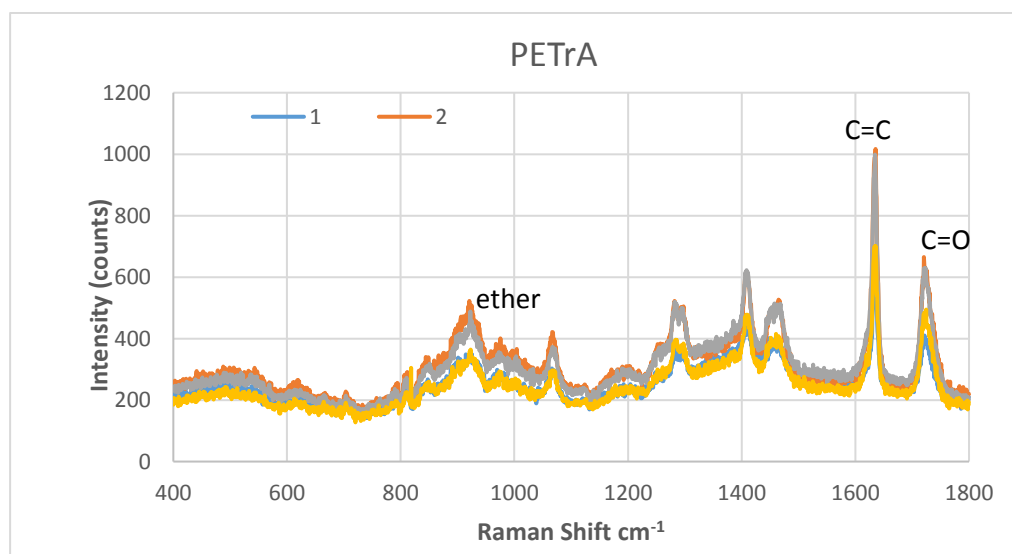
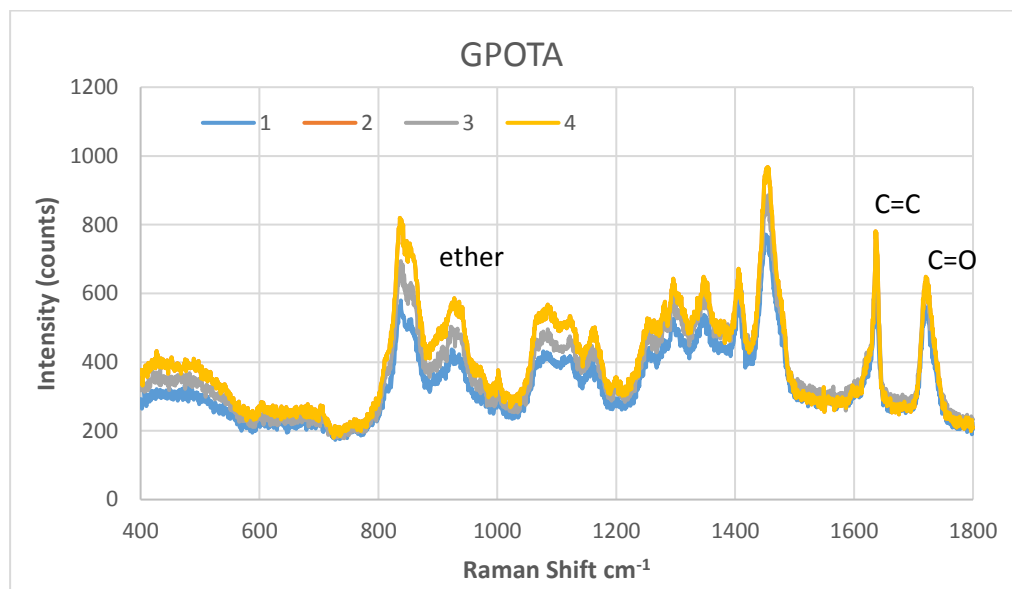
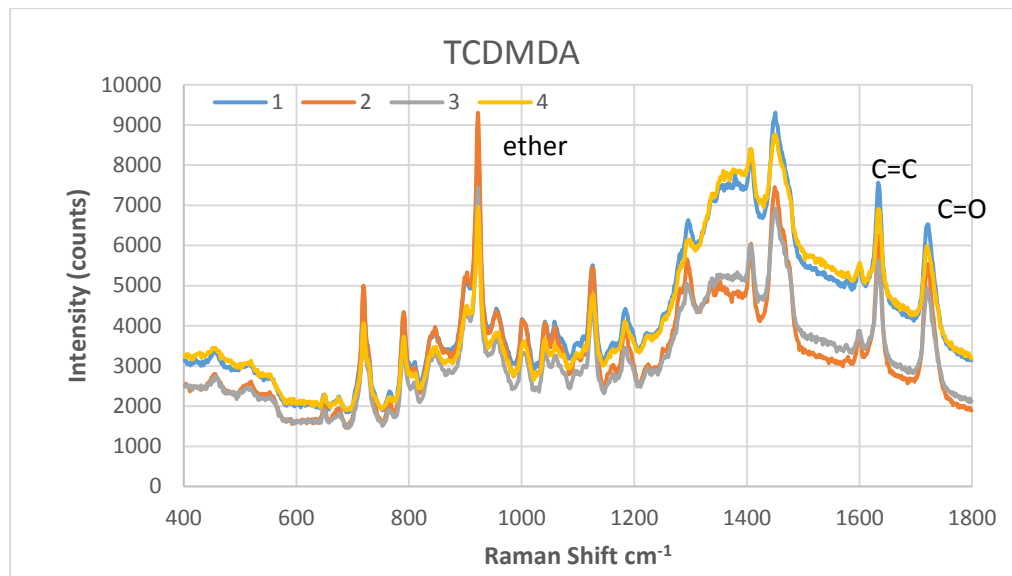


**Figure A.4: Spectra of polymers TCDMA, GPOTA and PETrA with post-fabrication UV light treatment.**

Post-fabrication UV cure increases the DOC of GPOTA and TCDMDA compared to polymers without any post-fabrication treatment (Table A.4).

**Table A 4: Area under the peaks of interest of polymers subject to post-fabrication UV cure treatment only. All intensity values are taken as an average of 4 measurements (n=4).**

| <b>Polymer name</b> | <b>Ether peak Intensity (counts)</b> | <b>C=C Intensity (counts)</b> | <b>C=O Intensity (counts)</b> | <b>Ratio C=C/C=O (Arbitrary Units)</b> | <b>DOC (%)</b> |
|---------------------|--------------------------------------|-------------------------------|-------------------------------|--|----------------|
| <b>TCDMDA</b>       | <b>19584.975</b>                     | <b>38076.825</b>              | <b>55258.475</b>              | <b>0.69</b>                            | <b>58.0</b>    |
| <b>GPOTA</b>        | <b>9085.485</b>                      | <b>5484.1025</b>              | <b>7462.005</b>               | <b>0.53</b>                            | <b>47.1</b>    |
| <b>PETrA</b>        | <b>659.753</b>                       | <b>5516.723</b>               | <b>6224.9925</b>              | <b>0.88</b>                            | <b>30.2</b>    |

TCDMDA and GPOTA exhibit a higher DOC compared to no post-fabrication treatment at all whereas PETrA has a lower DOC. This is most likely an anomaly and is further investigated by running more Raman spectroscopy readings. The differences between the DOC in post-fabrication treatments of UV and vacuum, the latter seems to have a larger influence on DOC in the case of TCDMDA and GPOTA.

These sets of experiments need multiple Raman measurements performed on the same polymer construct which was not done in this first series of experiments. The next set of results (Section 5.2.1.2) prove that DOC increases with both vacuum and UV treatment without any anomalies by averaging the DOC values from 4 repeat measurements.

## 1.2 Statistical tests on CMs

### 1.2.1 Statistical Tests on Sarcomere Length

**Table A 5: Sarcomere length measurements from 5 representative cells in each grooves region and their resulting average values on constructs without post-fabrication treatment.**

| Sarcomere Length ( $\mu\text{m}$ )         | Flat Glass Control | Flat Region | Shallow | Medium | Deep |
|--|--------------------|-------------|---------|--------|------|
|  | 1.239              | 1.96        | 2.09    | 3.77   | 2.31 |
|  | 1.899              | 1.17        | 1.97    | 2.24   | 2.1  |
|  | 2.207              | 1.87        | 2.09    | 1.21   | 3.79 |
|  | 1.561              | 1.26        | 1.33    | 1.88   | 1.87 |
|  | 1.249              | 1.37        | 2.17    | 3.2    | 2.1  |
| Average Sarcomere Length ( $\mu\text{m}$ ) | 1.631              | 1.526       | 1.93    | 2.46   | 2.43 |

**Table A 6: Sarcomere length measurements from 5 representative cells in each grooves region and their resulting average values on constructs with post-fabrication UV light treatment.**

| Sarcomere Length ( $\mu\text{m}$ )         | Flat glass Control | Flat Region | shallow | medium | deep   |
|--|--------------------|-------------|---------|--------|--------|
|  | 1.904              | 1.436       | 2.812   | 2.727  | 0.988  |
|  | 1.219              | 1.436       | 1.84    | 1.797  | 0.988  |
|  | 1.904              | 1.135       | 0.658   | 2.276  | 1.517  |
|  | 2.931              | 1.933       | 1.561   | 1.975  | 1.81   |
|  | 1.347              | 1.436       | 1.746   | 0.781  | 1.001  |
| Average Sarcomere Length ( $\mu\text{m}$ ) | 1.861              | 1.4752      | 1.7234  | 1.9112 | 1.2608 |



**Table A.7: Sarcomere length measurements from 5 representative cells in each grooves region and their resulting average values on constructs with post-fabrication vacuum treatment.**

| Sarcomere Length ( $\mu\text{m}$ )         | Flat glass |             |         |        |        |
|--|------------|-------------|---------|--------|--------|
|  | Control    | Flat Region | shallow | medium | deep   |
|  | 1.904      | 1.436       | 2.812   | 2.727  | 0.988  |
|  | 1.219      | 1.436       | 1.84    | 1.797  | 0.988  |
|  | 1.904      | 1.135       | 0.658   | 2.276  | 1.517  |
|  | 2.931      | 1.933       | 1.561   | 1.975  | 1.81   |
|  | 1.347      | 1.436       | 1.746   | 0.781  | 1.001  |
| Average Sarcomere Length ( $\mu\text{m}$ ) | 1.861      | 1.4752      | 1.7234  | 1.9112 | 1.2608 |

All student's t-tests show a significant difference between all regions of TCDMDA with post-fabrication UV light treatment (Table A.6).

**Table A. 8: Student's t-test of all groove regions on constructs with post-fabrication UV light treatment.**

|                            | <i>Shallow</i> | <i>Medium</i> |
|----------------------------|----------------|---------------|
| <b>P(T&lt;=t) two-tail</b> | 0.00041573     |               |
| <b>t Critical two-tail</b> | 2.36462425     |               |

|                            | <i>Shallow</i> | <i>Deep</i> |
|----------------------------|----------------|-------------|
| <b>P(T&lt;=t) two-tail</b> | 0.00037463     |             |
| <b>t Critical two-tail</b> | 2.30600414     |             |

|                            | <i>Medium</i> | <i>Deep</i> |
|----------------------------|---------------|-------------|
| <b>P(T&lt;=t) two-tail</b> | 1             |             |
| <b>t Critical two-tail</b> | 2.36462425    |             |

|                     | <i>Flat Glass Control</i> | <i>Flat Region</i> |
|---------------------|---------------------------|--------------------|
| P(T<=t) two-tail    | 0.987186347               |                    |
| t Critical two-tail | 2.262157163               |                    |

|                     | <i>Flat Region</i> | <i>Shallow</i> |
|---------------------|--------------------|----------------|
| P(T<=t) two-tail    | 1                  |                |
| t Critical two-tail | 2.228138852        |                |

|                     | <i>Flat Glass Control</i> | <i>Medium</i> |
|---------------------|---------------------------|---------------|
| P(T<=t) two-tail    | 1                         |               |
| t Critical two-tail | 2.228138852               |               |

| <i>Column1</i>      | <i>Flat Glass Control</i> | <i>Deep</i> |
|---------------------|---------------------------|-------------|
| P(T<=t) two-tail    | 1                         |             |
| t Critical two-tail | 2.262157163               |             |

|                     | <i>Flat Region</i> | <i>Medium</i> |
|---------------------|--------------------|---------------|
| P(T<=t) two-tail    | 2.85922E-05        |               |
| t Critical two-tail | 2.262157163        |               |

|                     | <i>Flat Region</i> | <i>Deep</i> |
|---------------------|--------------------|-------------|
| P(T<=t) two-tail    | 2.58741E-05        |             |
| t Critical two-tail | 2.228138852        |             |

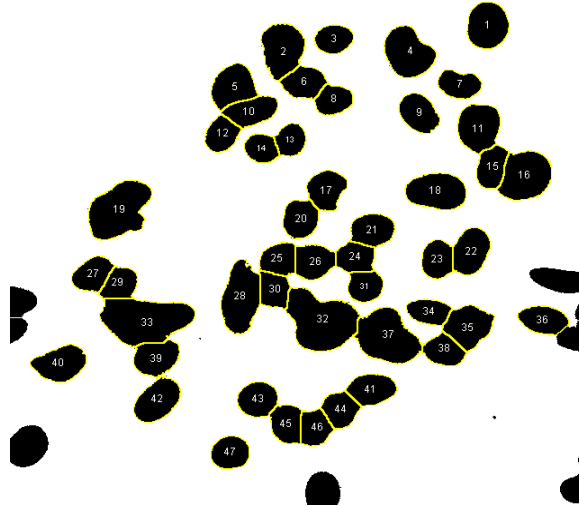
|                     | <i>Flat Glass Control</i> | <i>Shallow</i> |
|---------------------|---------------------------|----------------|
| P(T<=t) two-tail    | 1                         |                |
| t Critical two-tail | 2.262157163               |                |

**Table A.9: Nuclear roundness student's t-tests on tcdmda construct with post-fabrication vacuum treatment.**

|                                     | <i>Flat Glass Control</i> | <i>Flat Region</i> |
|-------------------------------------|---------------------------|--------------------|
| <b>Mean</b>                         | 0.611263158               | 0.715652542        |
| <b>Variance</b>                     | 0.036864316               | 0.025139922        |
| <b>Observations</b>                 | 19                        | 119                |
| <b>Hypothesized Mean Difference</b> | 0                         |                    |
| <b>df</b>                           | 22                        |                    |
| <b>t Stat</b>                       | -2.250541234              |                    |
| <b>P(T&lt;=t) one-tail</b>          | 0.017371976               |                    |
| <b>t Critical one-tail</b>          | 1.717144374               |                    |

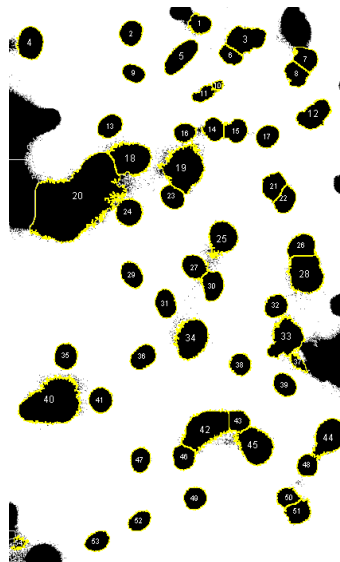
|                                     | <i>Flat Glass Control</i> | <i>Grooved Region</i> |
|-------------------------------------|---------------------------|-----------------------|
| <b>Mean</b>                         | 0.611263158               | 0.735380952           |
| <b>Variance</b>                     | 0.036864316               | 0.020366331           |
| <b>Observations</b>                 | 19                        | 85                    |
| <b>Hypothesized Mean Difference</b> | 0                         |                       |
| <b>df</b>                           | 23                        |                       |
| <b>t Stat</b>                       | -2.65841411               |                       |
| <b>P(T&lt;=t) one-tail</b>          | 0.007019984               |                       |
| <b>t Critical one-tail</b>          | 1.713871528               |                       |

|                                     | <i>Flat Region</i> | <i>Grooved Region</i> |
|-------------------------------------|--------------------|-----------------------|
| <b>Mean</b>                         | 0.715652542        | 0.735380952           |
| <b>Variance</b>                     | 0.025139922        | 0.020366331           |
| <b>Observations</b>                 | 119                | 85                    |
| <b>Hypothesized Mean Difference</b> | 0                  |                       |
| <b>df</b>                           | 191                |                       |
| <b>t Stat</b>                       | -0.929114911       |                       |
| <b>P(T&lt;=t) one-tail</b>          | 0.177001129        |                       |
| <b>t Critical one-tail</b>          | 1.652870547        |                       |



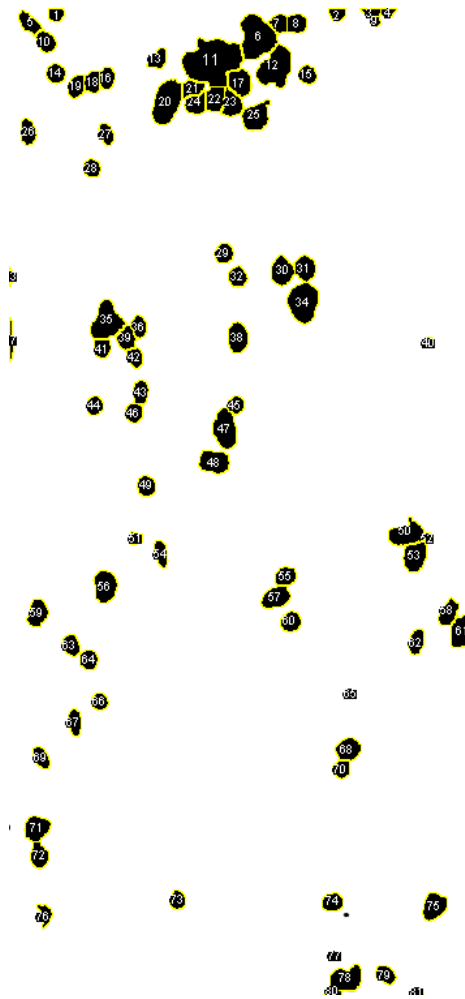
**Figure A.5: Image of the nuclei analysed on flat glass control of the TCDMDA constructs experiments without post-fabrication treatment using ImageJ software.**

Image J software was utilised to determine what exactly were individual cells in the image based on the number of pixels within each shape (Figure A.5). The average nuclear roundness calculated for the TCDMDA flat region was 0.77 (Table A.7). This is slightly higher than the average nuclear roundness value obtained from the flat glass control.



**Figure A.6: Image of the nuclei analysed on TCDMDA flat region of the constructs without post-fabrication treatment using ImageJ software.**

Below is the screenshot from the Image J software of the whole grooves region of the TCDMDA construct without post-fabrication treatment (Figure A.7).



**Figure A.7: Image of the nuclei analysed on the grooved region of the TCDMDA construct without post-fabrication treatment using ImageJ software.**

ANOVA statistical analysis showed that the calculated F value was lower than critical F value meaning there was no significant difference in nuclear roundness of the cells on the flat regions compared to the grooved regions (Table A.7).

**Table A.10: Absolute intensity values for C=C and C=O peaks of uncured PETrA under the 3 different formulation conditions.**

| Peak type                         | I369            | DMPA             | DMPA:IPA         |
|-----------------------------------|-----------------|------------------|------------------|
| C=C                               | 13189.8         | 757954           | 402865           |
|                                   | 11295.7         | 742305           | 312641           |
|                                   | 11332.7         | 628155           | 362048           |
|                                   | 13348.1         | 619279           | 597861           |
| <b>Average Intensity (counts)</b> | <b>12291.58</b> | <b>686923.25</b> | <b>418853.75</b> |
| C=O                               | 10524.6         | 742796           | 270517           |
|                                   | 8499.97         | 721706           | 203301           |
|                                   | 9204.82         | 578309           | 252654           |
|                                   | 10353.5         | 603408           | 479558           |
| <b>Average Intensity (counts)</b> | <b>9645.72</b>  | <b>661554.75</b> | <b>301507.5</b>  |

**Table A.11: Absolute intensity values for C=C and C=O peaks of cured PETrA under the 3 different formulation conditions.**

| Peak type                         | I369            | DMPA            | DMPA:IPA       |
|-----------------------------------|-----------------|-----------------|----------------|
| C=C                               | 108431          | 30085.3         | 26922.3        |
|                                   | 73113.3         | 36696           | 26337.5        |
|                                   | 111634          | 36862.3         | 27032.5        |
|                                   | 97525.2         | 39293           | 28240.1        |
| <b>Average Intensity (counts)</b> | <b>97675.86</b> | <b>35734.15</b> | <b>27133.1</b> |
| C=O                               | 193313          | 48780.5         | 43497.4        |
|                                   | 152446          | 55993.6         | 46901.6        |
|                                   | 222446          | 54639.7         | 49038.6        |
|                                   | 189629          | 54397.8         | 46699.2        |
| <b>Average Intensity (counts)</b> | <b>189458.5</b> | <b>53452.9</b>  | <b>46534.2</b> |

## 1.3 Qualitative Results for CM attachment on UV-polymerised acrylates

### 1.3.1 CMs in RILT thioglycerol medium

#### 1.3.1.1 Constructs polymerized with I369

BDDA showed CM attachment on all 3 polymer repeats in RILT medium. This is evident by the extended and stretched cells (Figure A.8). This is true for all 3 repeats of the polymer, with similar results obtained from HEODA, TCDMDA and PETrA (Figures A.9, A.10 and A.11).

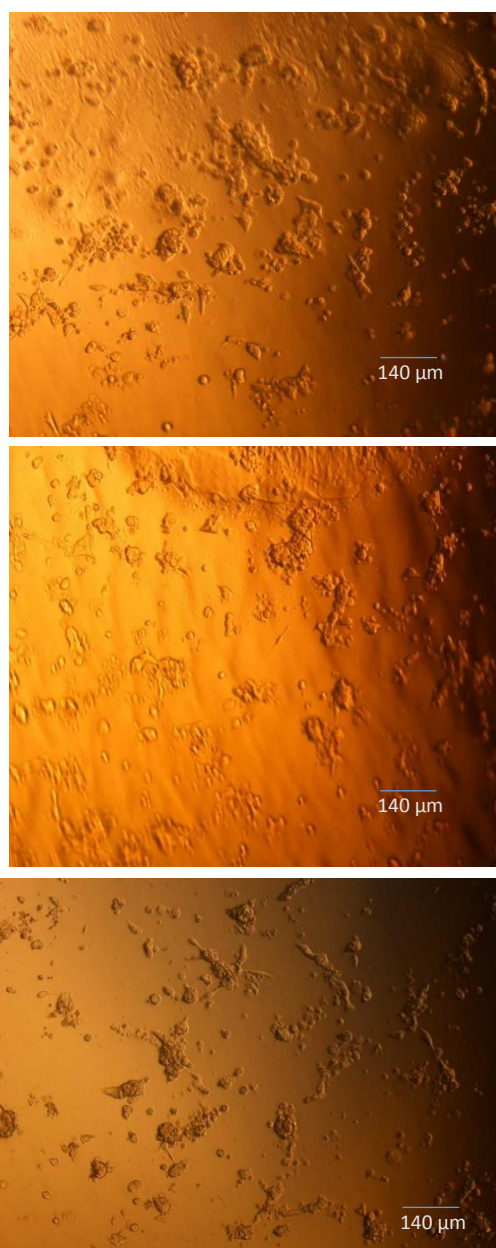


**Figure A.8: Light microscopy images of BDDA polymer with CMs attached.**

Figures A.9, A.10, A.11 and A.12 show that HEODA, TCDMDA, PETrA and pPGDA all showed CM attachment in all 3 repeats of each polymer in the absence of serum grown in RILT medium.

The results for GPOTA were not the same as the other polymers cultured in these conditions. GPOTA did not support CM attachment in RILT medium.

These results potentially showed that RILT medium is a good nutritional environment since the CMs attached to most of the constructs. However, more solid evidence was required to confirm whether it was the RILT medium providing the CMs with the correct environment for attachment.

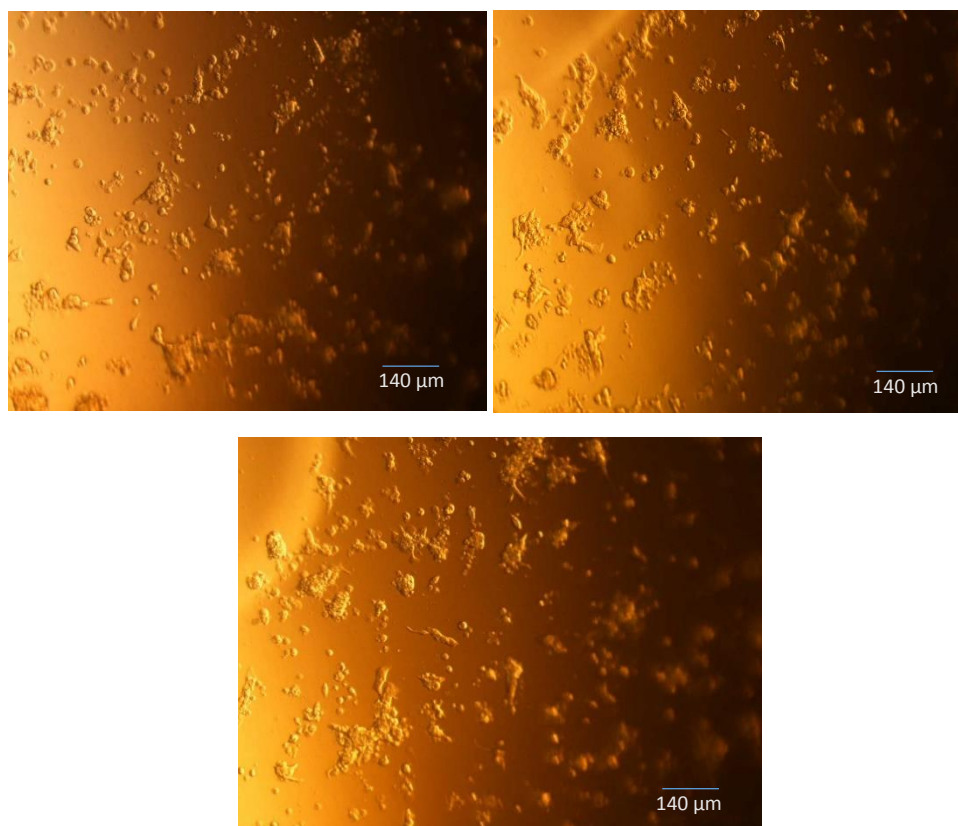


**Figure A.9: Light microscopy images of HEODA polymer with CMs attached.**



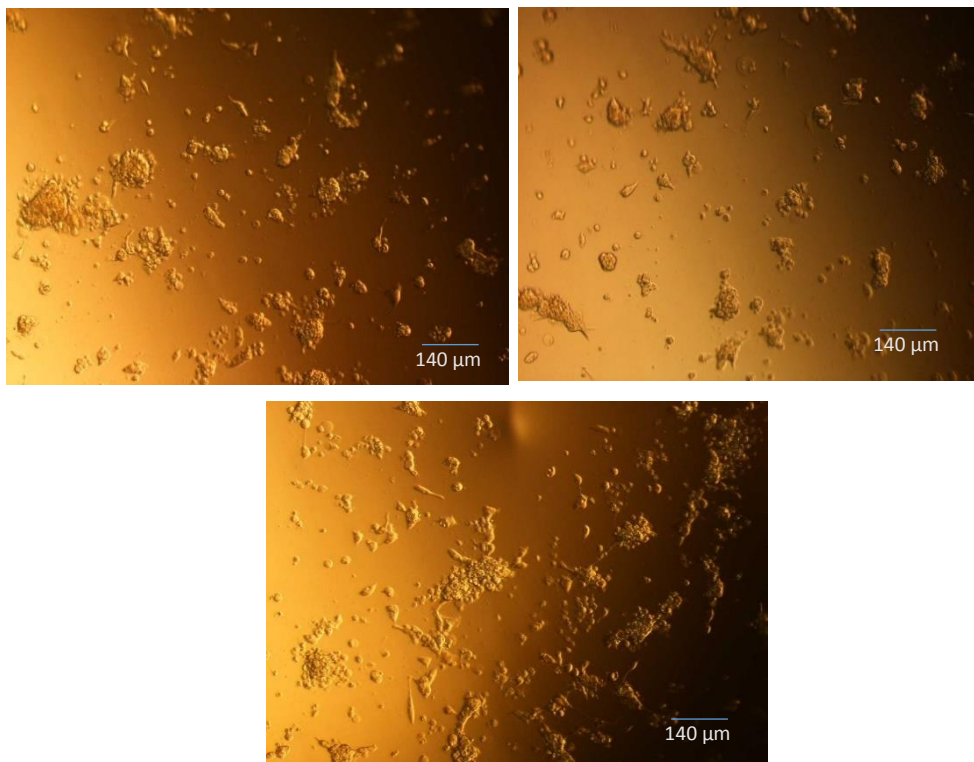
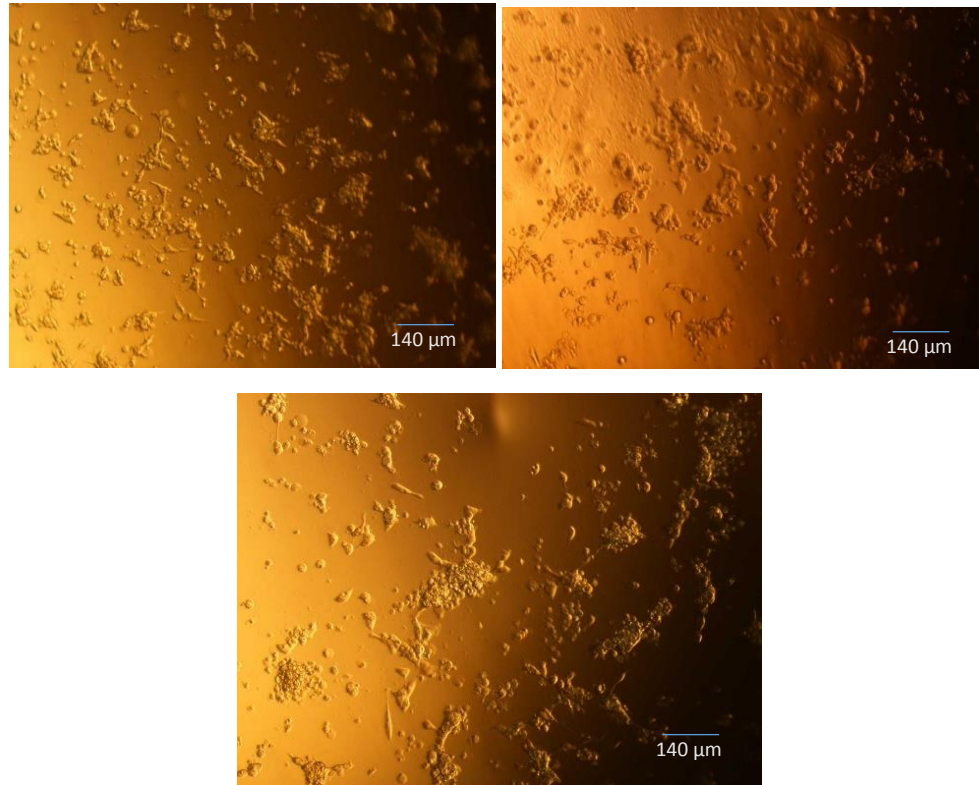


**Figure A.10: Light microscopy images of TCDMDA polymer with CMs attached.**



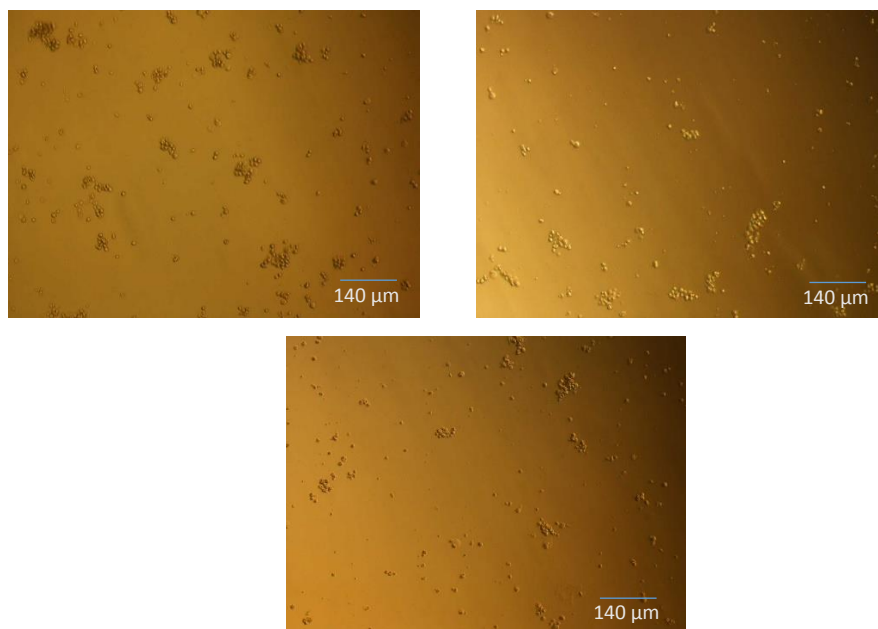
**Figure A.11: Light microscopy images of PETrA polymer with CMs attached.**

Figure A.12 shows pPGDA repeats. All three appear to have CMs attached, apparent by the extended parts of the cells.



**Figure A.12: Light microscopy images of pPGDA polymer with CMs attached.**

In contrast, GPOTA did not demonstrate any CM attachment due to the absence of any extended parts of the cells. Instead, cells appeared small and round (Figure A.13).



**Figure A.13: Light microscopy images of GPOTA showing no attachment and round, dead cells.**

All of the multi-functional polymers except GPOTA supported CM attachment in the presence of RILT medium when they were polymerised with I369 photoinitiator. This signifies that perhaps either RILT medium or I369, or the combination of both, is aiding the attachment of the CMs. RILT medium contains the antioxidants ascorbic acid and thioglycerol which may be enhancing cell survival. It is also possible that simply the polymer chemistry is inducing CM attachment. For clarification on which of these factors was important a second series of polymerisation of the same polymers prepared using DMPA as the photoinitiator and RPMI B27 are tested for CM attachment. DMPA is more easily dissolved in monomer solutions and was shown to support CM attachment on GPOTA in the presence of RILT medium previously (Patel et al., 2015).

Therefore, the results in other polymerization conditions tested, which are the DMPA and the DMPA+IPA and the CMs grown in B27 medium need to be analysed prior to making any conclusions.

#### 1.3.1.2 Constructs polymerized with DMPA

BDDA showed no cell attachment in any of the 3 repeats as can be clearly seen in Figure A.14. The round shape and small size of the cells clearly indicate cell death. This is in stark contrast to the cell attachment on BDDA polymerized with I369 (Figure A.8). This could be due to the photo initiator DMPA used. Perhaps this particular PI did not dissolve completely in BDDA or DMPA was significantly more cytotoxic to the cells compared to I369. Unreacted free monomer could also have been the reason for cell death however degree of cure (DOC) measurements were not made for the UV polymerisation experiments as only the polymers' ability to support CM attachment were to be determined.

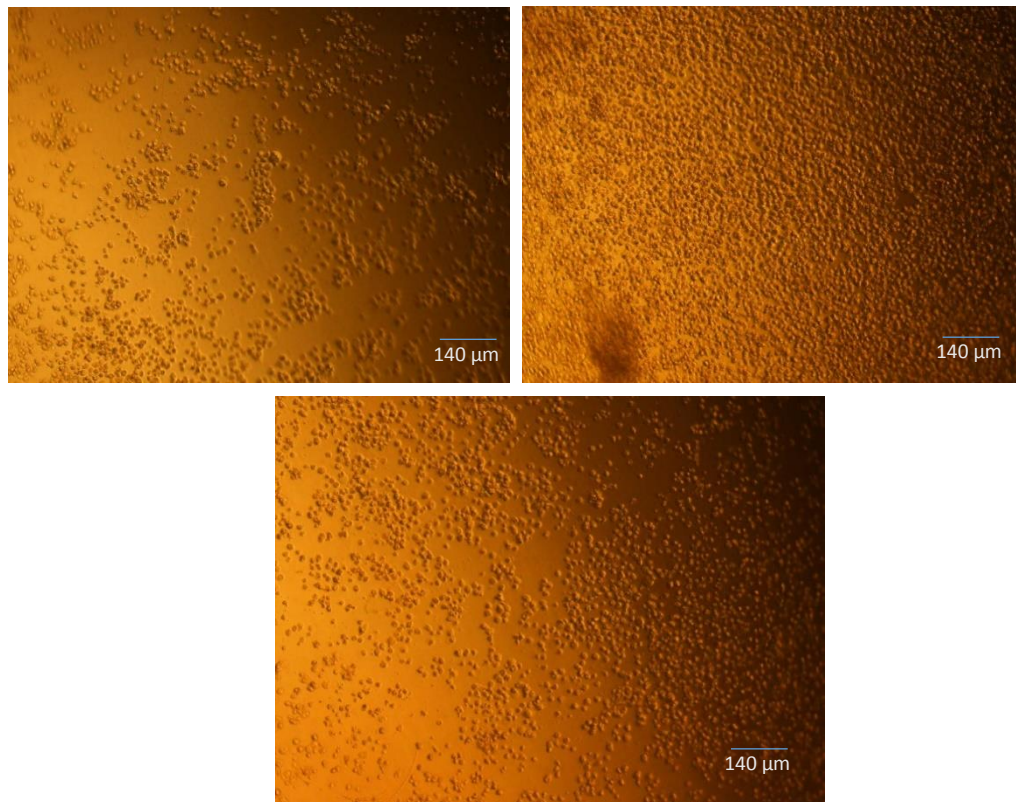


**Figure A.14: Light microscopy images of BDDA polymer showing no attachment and round, dead cells.**



As opposed to the results of BDDA with DMPA as a PI (Figure A.14), HEODA showed CM attachment (Figure A.15) as shown by some of the cells extending along the surface of the polymer. The number of CMs attached to the polymer appear less than the number of CMs attached to HEODA polymerised with I369 PI (Figure A.9). This could again be due to the inability of DMPA to dissolve in HEODA or the significant cytotoxic effect of DMPA or free monomer on the CMs.

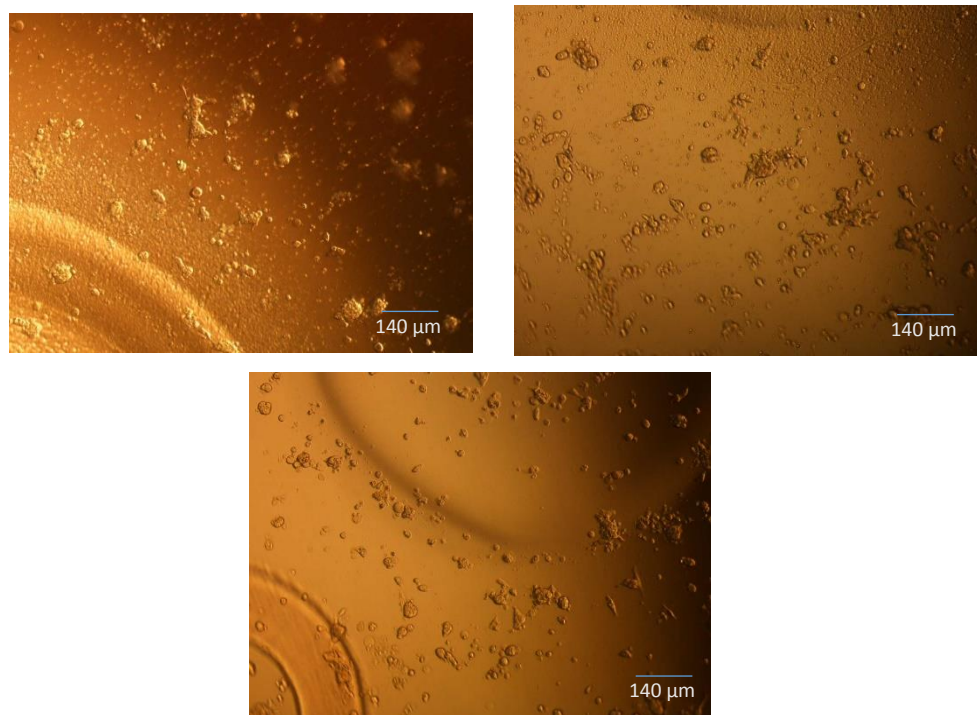


**Figure A.15: Light microscopy images of HEODA polymer with CMs attached.**

Similar results were observed with TCDMDA in which constructs polymerised with DMPA showed less CM attachment in 2 of the samples (Figure A.16). One sample did not show any CM attachment (Figure A.16, top). The samples that showed CM attachment had fewer cells attached compared to TCDMDA samples polymerised with I369 (Figure A.10).

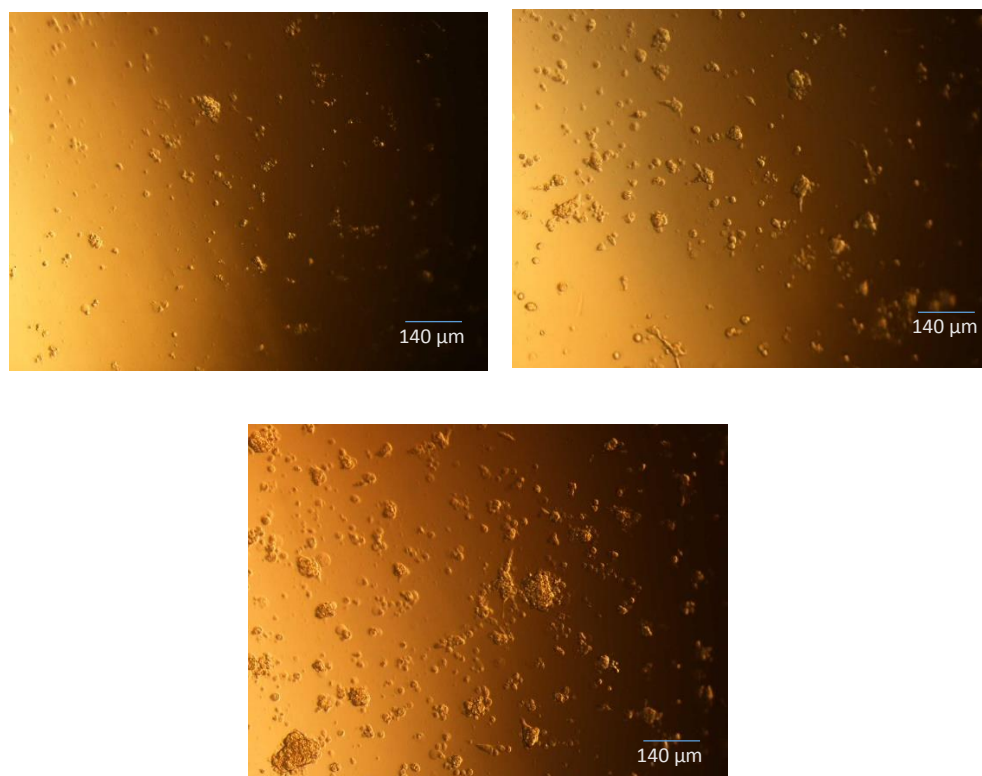


**Figure A.16: Light microscopy images of TCDMDA polymer showing no attachment and round, dead cells and with CMs attached (right and bottom).**

Even though PETrA polymer constructs showed CM attachment with I369 (Figure A.11), their DMPA-polymerised counterparts did not show any CM attachment (Figure A.17) as illustrated below by the round morphology of the cells, typical of apoptosis.

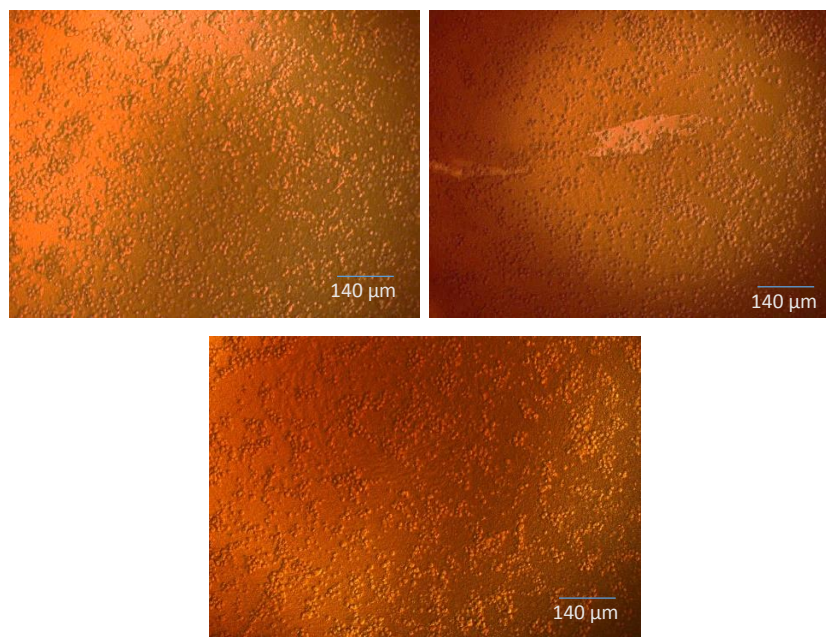


**Figure A.17: Light microscopy images of PETra polymer with the round morphology of dead cells.**

The same results apply to pPGDA (Figure A.18). This polymer showed good CM attachment on the I369-polymerised constructs but not on the DMPA-polymerised constructs.

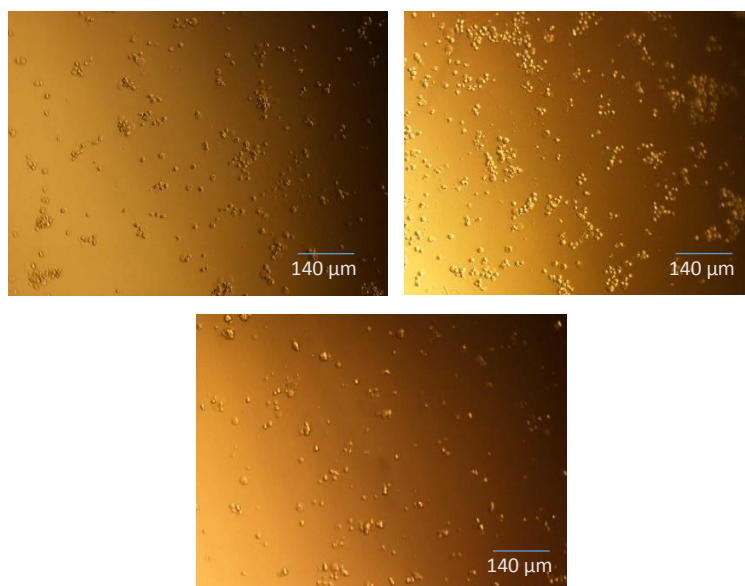


**Figure A.18: Light microscopy images of pPGDA polymer showing no attachment and round, dead cells.**

GPOTA showed no CM attachment on DMPA-polymerised constructs, which was the same results obtained from the I369-polymerised constructs (Figure A.19).



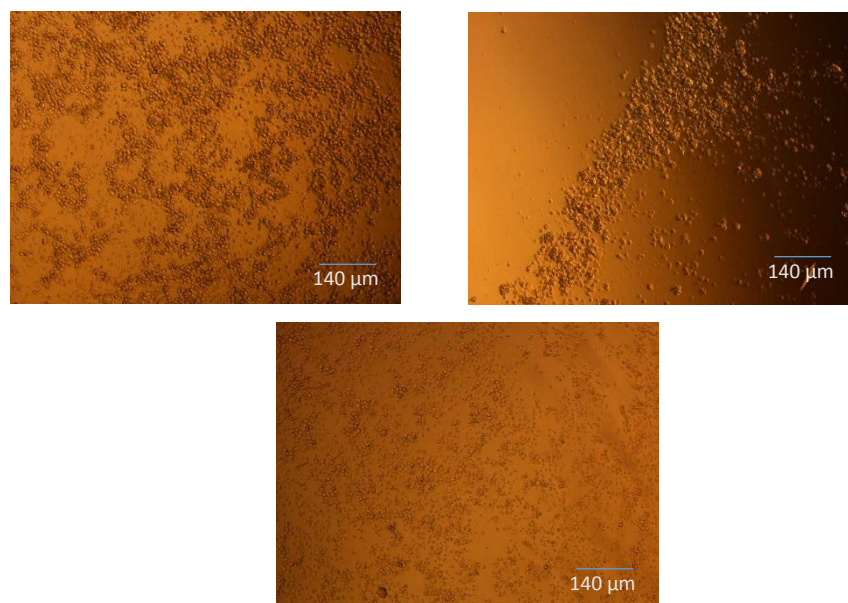


**Figure A.19: Light microscopy images of GPOTA polymer showing no attachment and round, dead cells.**

The results overall indicate that I369 photoinitiator supports CM attachment markedly better than DMPA photoinitiator, except for GPOTA which did not show CM attachment with either photoinitiator. All constructs were maintained in the same medium and both photo initiators were used at the same concentration for all polymers. The same batch of iPSCs were used in the differentiation process to obtain CMs. The only variable between these 2 sets of data were the photoinitiator type. The figures qualitatively signify that PI type has an effect on CM attachment at varying levels depending on the polymer being tested. More specifically, the attachment difference is largest in PETrA, pPGDA and BDDA in which the I369-polymerised showed a lot of CM attachment whereas their DMPA-polymerised counterparts showed no attachment at all. This is in contrast to HEODA and TCDMDA, which showed less attachment on their DMPA-polymerised constructs.

### 1.3.1.3 Constructs polymerized with DMPA in IPA solvent

This was an experiment prepared to act as a control for comparison to the constructs polymerised with DMPA and the constructs polymerised with I369 photo initiators. Therefore, the results in this section served as a confirmation of the results obtained by Patel et al., 2015.

BDDA showed very little to negligible cell attachment, which coincides with its DMPA-polymerised construct counterpart (Figure A.20).

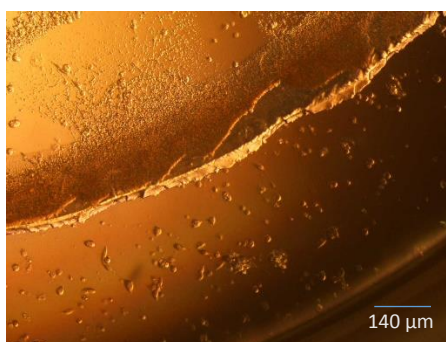


**Figure A.20: Light microscopy image of BDDA polymer with CMs attached.**

HEODA polymer only exhibited a few CMs attached, the same as the DMPA-polymerised constructs (Figure A.21). It appears that mixing DMPA with IPA solvent does not make a difference to CM attachment.

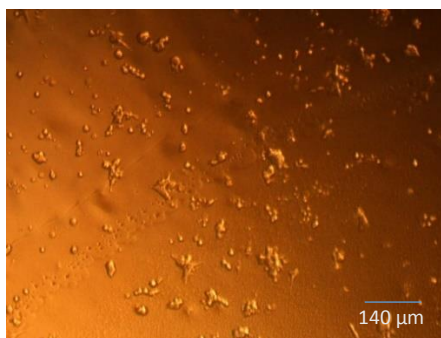


**Figure A.21: Light microscopy image of HEODA polymer with CMs attached.**

TCDMDA showed some CM attachment (Figure A.22), similar to DMPA-polymerised constructs albeit slightly less.

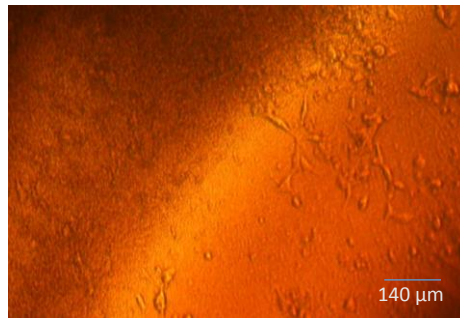


**Figure A.22: Light microscopy image of TCDMDA polymer with CMs attached.**

The PETrA constructs also showed CM attachment however there were fewer cells attached compared to PETrA constructs polymerized by DMPA-only or I369 photo initiators (Figure A.23).

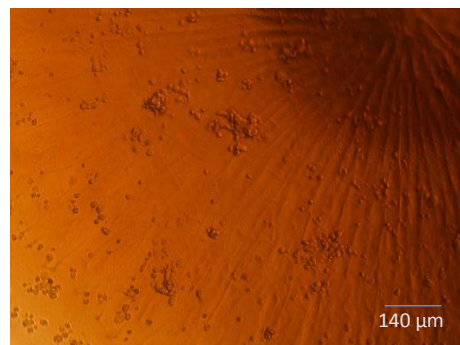


**Figure A.23: Light microscopy images of PETrA polymer with few CMs attached.**

Meanwhile, the pPGDA constructs showed different results compared to their counterparts polymerized by I369 and DMPA-only (Figure A.24). pPGDA constructs polymerized by DMPA with IPA solvents showed no cell attachment as cells appeared small and round (Figure A.24).

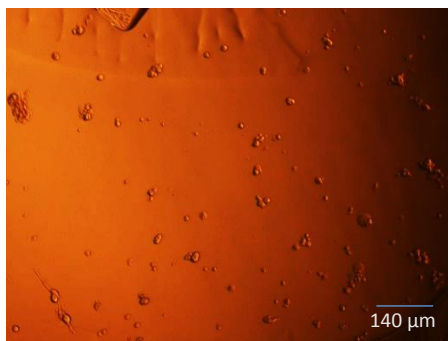


**Figure A.24: Light microscopy images of pPGDA polymer showing no attachment and round, dead cells.**

GPOTA constructs did not show cell attachment as evident by the small and rounded morphology of the cells (Figure A.25). This is the same result as for the GPOTA constructs polymerized by DMPA-only and I369 photo initiators.

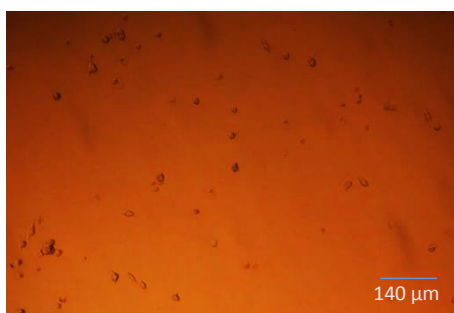


**Figure A.25: Light microscopy images of GPOTA polymer showing no attachment and round, dead cells.**

PETrA, pPGDA and GPOTA showed negligible or no CM attachment with DMPA and IPA mixture. This is identical to the results obtained from constructs polymerised with DMPA only for these 3 polymers.

In summary, adding IPA solvent at a 50:50 ratio to the DMPA and free-monomer mixture did not alter CM attachment. The relative amount of CM attachment did not alter significantly for any one of the materials polymerized with DMPA only and the DMPA/IPA mixture. This further strengthens the idea that DMPA may be a more cytotoxic photoinitiator to the cells or DMPA could have poor solubility in all of these polymers or a combination of both.

### *1.3.2 CMs in RPMI B27 medium*

RPMI B27 medium is the only medium currently used in the established protocol for iPSC-CM differentiation (Burrige et al., 2014). This is why the medium was selected to decide whether it could be used in future experiments. As mentioned before, RILT medium contains more antioxidant molecules, including ascorbic acid, thioglycerol and insulin-transferrin-selenium, which may be aiding CM attachment by preventing cell death after dissociation. 5 of the 6 polymers showed CM attachment in RILT medium in the presence of I369. It was expected that RPMI B27 may not be as successful in supporting CMs under the same conditions due to this medium containing less antioxidants.



### 1.3.2.1 Constructs polymerized with I369

In these experiments with this differing medium, none of the polymer constructs tested showed any CM attachment aside from GPOTA (Figure A.26). This is in stark contrast to the constructs in RPMI RILT medium which showed high cell attachment on all constructs except GPOTA 1.3.1 CMs in RILT thioglycerol medium. It is possible that RILT thioglycerol contains components that sustain the CMs for these specific polymers and have a role in their attachment.

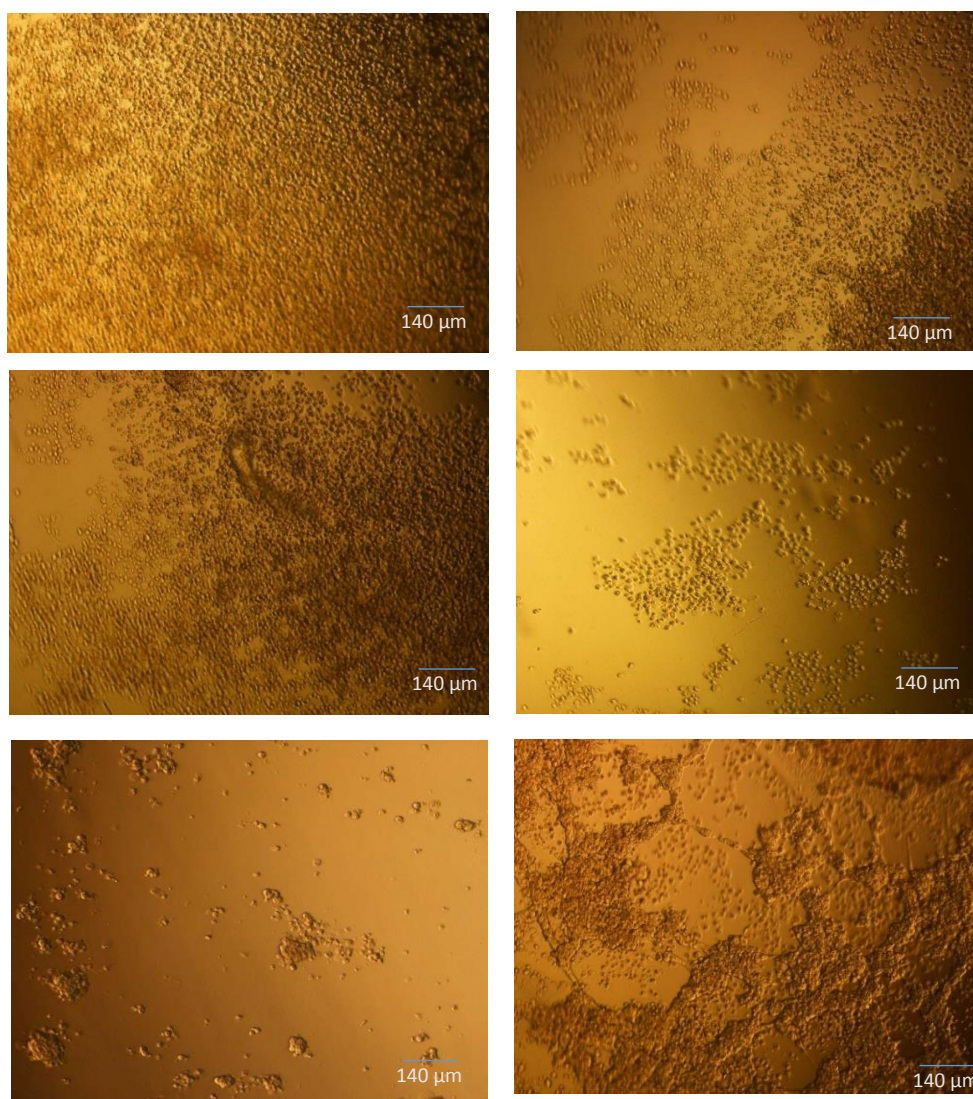


**Figure A.26: Light microscopy images of BDDA, HEODA, TCDMDA, PTrA, pPGDA and GPOTA polymerised with I369. None show cell attachment and the round morphology of the cells indicate apoptosis except for GPOTA on the bottom right.**

### 1.3.2.2 Constructs polymerized with DMPA

RPMI B27 medium had a similar effect on the DMPA-polymerised constructs (Figure A.27). None of the polymers supported CM attachment whereas some of the polymers maintained in RILT thioglycerol medium with the same DMPA photoinitiator had shown small amounts of cell attachment. This further supported the observations made with I369-polymerised constructs in RILT medium and that this medium possibly has components within its mix that were essential to sustain the cells.

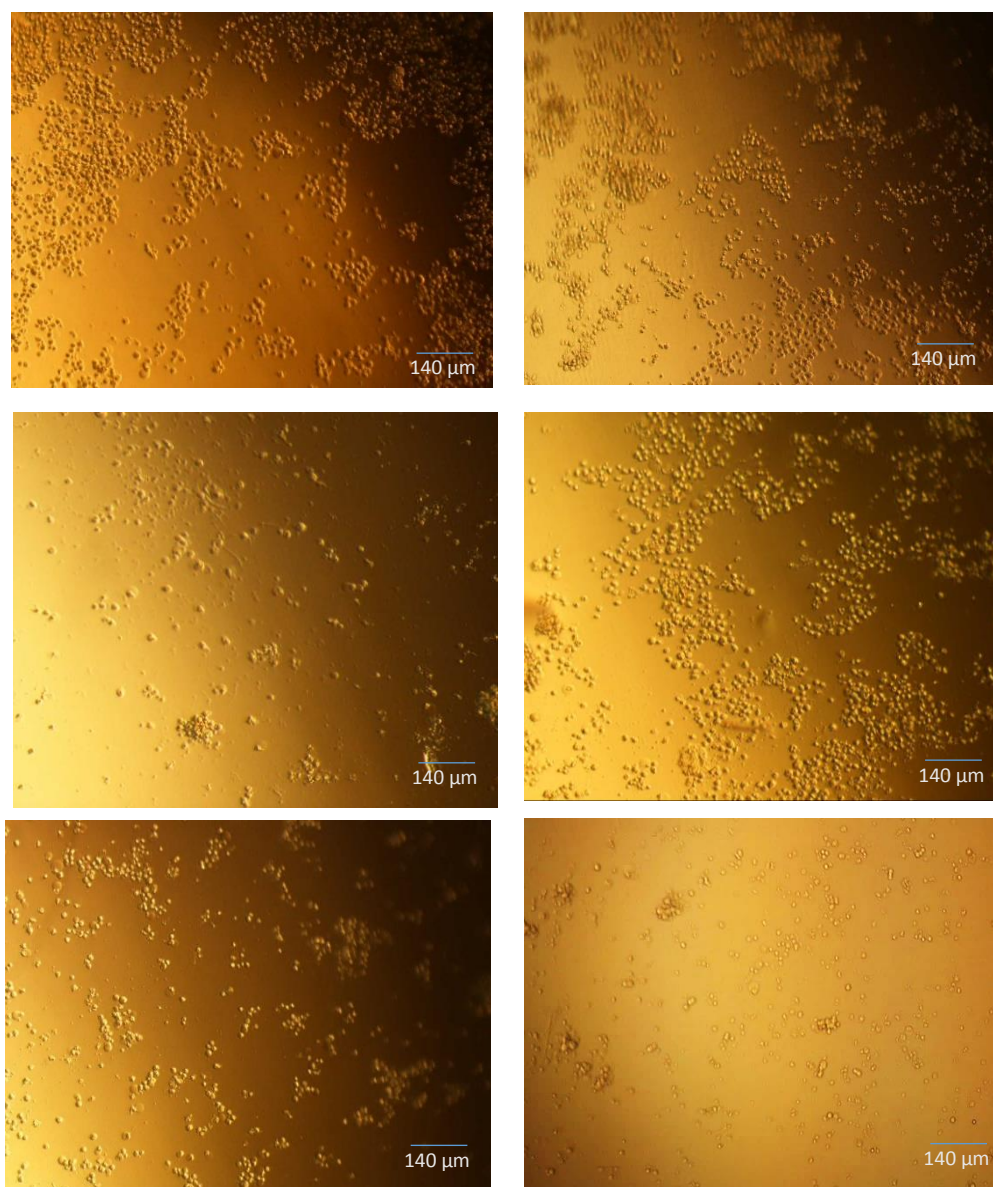


**Figure A.27: Light microscopy images of BDDA, HEODA, TCDMDA, PETrA, pPGDA and GPOTA polymerised with DMPA. None show cell attachment and the round morphology of the cells indicate apoptosis.**



### 1.3.2.3 Constructs polymerized with DMPA in IPA solvent

Again the polymers tested did not support CM attachment in DMPA IPA solvent (Figure A.28). Some of the polymers supported CM attachment when they were maintained in RILT thioglycerol medium as found in 1.3.1 CMs in RILT thioglycerol medium which implies the maintenance medium is an important factor that affects CM attachment.

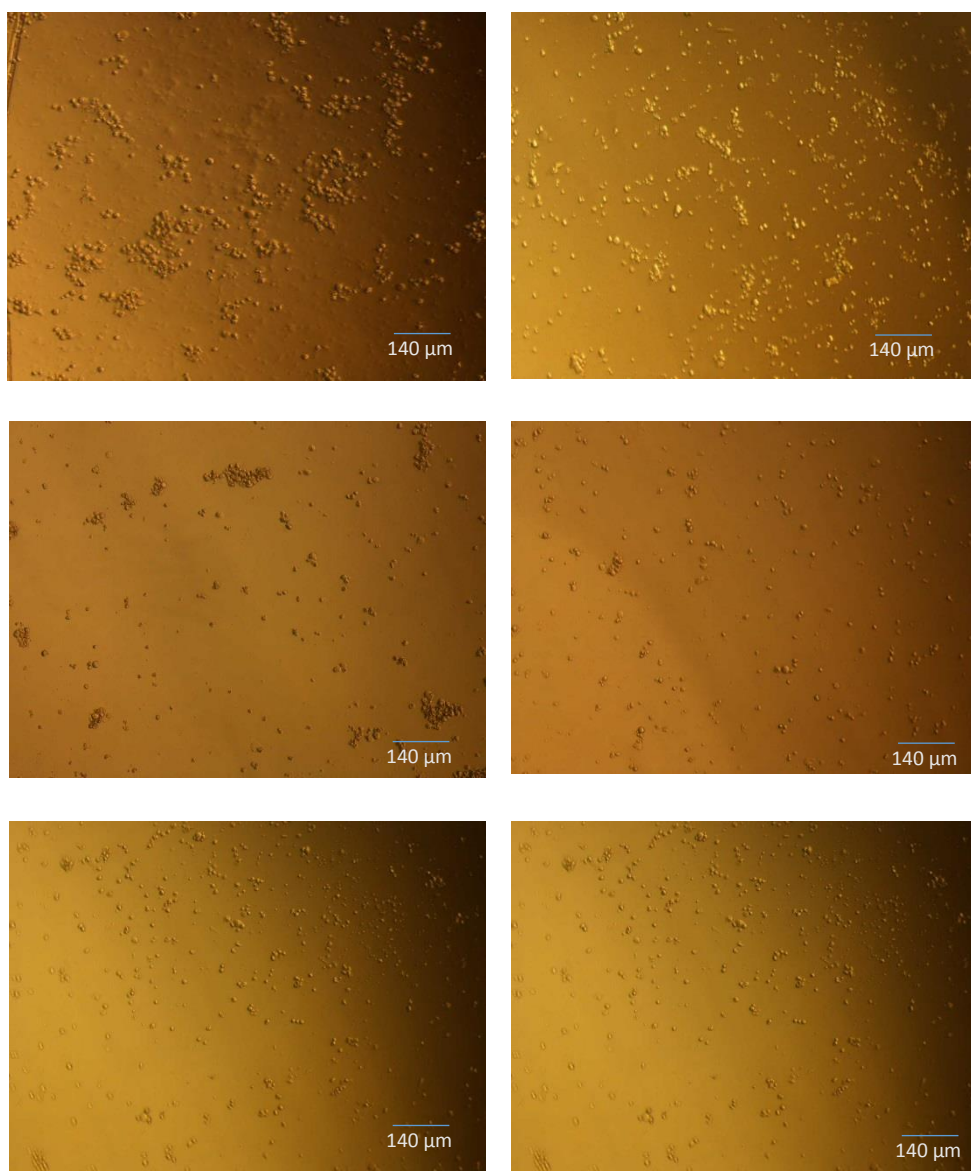


**Figure A.28: Light microscopy images of BDDA, HEODA, TCDMDA, PETrA, pPGDA and GPOTA polymerised with DMPA in IPA solvent. None show cell attachment and the round morphology of the cells indicate apoptosis.**



## Bibliography

- ABADI, P. P. S. S., GARBERN, J. C., BEHZADI, S., HILL, M. J., TRESBACK, J. S., HEYDARI, T., EJTEHADI, M. R., AHMED, N., COPLEY, E., AGHAVERDI, H., LEE, R. T., FAROKHZAD, O. C. & MAHMOUDI, M. 2018. Engineering of Mature Human Induced Pluripotent Stem Cell-Derived Cardiomyocytes Using Substrates with Multiscale Topography. *Advanced Functional Materials*, 28, 1707378.
- AISSAOUI, N., BERGAOUI, L., LANDOULSI, J., LAMBERT, J.-F. & BOUJDAY, S. 2012. Silane Layers on Silicon Surfaces: Mechanism of Interaction, Stability, and Influence on Protein Adsorption. *Langmuir*, 28, 656-665.
- AKBAY, E. & ONUR, M. A. 2019. Investigation of survival and migration potential of differentiated cardiomyocytes transplanted with decellularized heart scaffold. *J Biomed Mater Res A*, 107, 561-570.
- ALMEIDA, J. F., FERREIRA, P., LOPES, A. & GIL, M. H. 2011. Photocrosslinkable biodegradable responsive hydrogels as drug delivery systems. *Int J Biol Macromol*, 49, 948-54.
- ANKAM, S., SURYANA, M., CHAN, L. Y., MOE, A. A., TEO, B. K., LAW, J. B., SHEETZ, M. P., LOW, H. Y. & YIM, E. K. 2013. Substrate topography and size determine the fate of human embryonic stem cells to neuronal or glial lineage. *Acta Biomater*, 9, 4535-45.
- ASAY, D. B. & KIM, S. H. 2005. Evolution of the adsorbed water layer structure on silicon oxide at room temperature. *J. Phys. Chem. B*, 109, 16760.
- AZUMA, T., TERAMURA, Y. & TAKAI, M. 2016. Cellular Response to Non-contacting Nanoscale Sublayer: Cells Sense Several Nanometer Mechanical Property. *ACS Appl Mater Interfaces*, 8, 10710-6.
- BAGHERI-HOSSEINABADI, Z., SALEHINEJAD, P. & MESBAH-NAMIN, S. A. 2017. Differentiation of human adipose-derived stem cells into cardiomyocyte-like cells in fibrin scaffold by a histone deacetylase inhibitor. *BioMedical Engineering OnLine*, 16, 134.
- BAJAJ, P., SCHWELLER, R. M., KHADEMHOSEINI, A., WEST, J. L. & BASHIR, R. 2014. 3D biofabrication strategies for tissue engineering and regenerative medicine. *Annu Rev Biomed Eng*, 16, 247-76.

- BALDACCHINI, T. 2011. Three-Dimensional Microfabrication by Two-Photon Polymerization. *Generating Micro- and Nanopatterns on Polymeric Materials*.
- BALDACCHINI, T., LAFRATTA, C. N., FARRER, R. A., TEICH, M. C., SALEH, B. E. A., NAUGHTON, M. J. & FOURKAS, J. T. 2004. Acrylic-based resin with favorable properties for three-dimensional two-photon polymerization. *Journal of Applied Physics*, 95, 6072-6076.
- BAUER, F., DECKER, U., NAUMOV, S. & RIEDEL, C. 2014. Photoinitiator-free UV curing and matting of acrylate-based nanocomposite coatings: Part 3. *Progress in Organic Coatings*, 77, 1085-1094.
- BENEDIKT, S., WANG, J., MARKOVIC, M., MOSZNER, N., DIETLIKER, K., OVSIANIKOV, A., GRÜTZMACHER, H. & LISKA, R. 2016. Highly efficient water-soluble visible light photoinitiators. *Journal of Polymer Science Part A: Polymer Chemistry*, 54, 473-479.
- BERIAT, N. C., ERTAN, A. A., CANAY, S., GURPINAR, A. & ONUR, M. A. 2010. Effect of different polymerization methods on the cytotoxicity of dental composites. *European journal of dentistry*, 4, 287-292.
- BETTINGER, C. J., LANGER, R. & BORENSTEIN, J. T. 2009. Engineering substrate topography at the micro- and nanoscale to control cell function. *Angew Chem Int Ed Engl*, 48, 5406-15.
- BIGGS, M. J., RICHARDS, R. G., GADEGAARD, N., WILKINSON, C. D. & DALBY, M. J. 2007. The effects of nanoscale pits on primary human osteoblast adhesion formation and cellular spreading. *J Mater Sci Mater Med*, 18, 399-404.
- BIRD, S. D., DOEVENDANS, P. A., VAN ROOIJEN, M. A., BRUTEL DE LA RIVIERE, A., HASSINK, R. J., PASSIER, R. & MUMMERY, C. L. 2003. The human adult cardiomyocyte phenotype. *Cardiovasc Res*, 58, 423-34.
- BRAAM, S. R., TERTOOLEN, L., VAN DE STOLPE, A., MEYER, T., PASSIER, R. & MUMMERY, C. L. 2010. Prediction of drug-induced cardiotoxicity using human embryonic stem cell-derived cardiomyocytes. *Stem Cell Res*, 4, 107-16.
- BROOKS, B. W. 1977. Viscosity Effects in the Free-Radical Polymerization of Methyl Methacrylate. *Proceedings of the Royal Society of London. Series A, Mathematical and Physical Sciences*, 357, 183-192.

- BROUGHTON, K. M. & RUSSELL, B. 2015. Cardiomyocyte subdomain contractility arising from microenvironmental stiffness and topography. *Biomech Model Mechanobiol*, 14, 589-602.
- BURRIDGE, P. W., KELLER, G., GOLD, J. D. & WU, J. C. 2012. Production of de novo cardiomyocytes: human pluripotent stem cell differentiation and direct reprogramming. *Cell Stem Cell*, 10, 16-28.
- BURRIDGE, P. W., MATSA, E., SHUKLA, P., LIN, Z. C., CHURKO, J. M., EBERT, A. D., LAN, F., DIECKE, S., HUBER, B., MORDWINKIN, N. M., PLEWS, J. R., ABILEZ, O. J., CUI, B., GOLD, J. D. & WU, J. C. 2014. Chemically defined generation of human cardiomyocytes. *Nat Methods*, 11, 855-60.
- CARRAHER, C. E. 2007. *Introduction to polymer chemistry*, Boca Raton, Fla.; London, CRC/Taylor & Francis.
- CARSON, D., HNILOVA, M., YANG, X., NEMETH, C. L., TSUI, J. H., SMITH, A. S., JIAO, A., REGNIER, M., MURRY, C. E., TAMERLER, C. & KIM, D. H. 2016. Nanotopography-Induced Structural Anisotropy and Sarcomere Development in Human Cardiomyocytes Derived from Induced Pluripotent Stem Cells. *ACS Appl Mater Interfaces*, 8, 21923-32.
- CASPI, O., LESMAN, A., BASEVITCH, Y., GEPSTEIN, A., ARBEL, G., HABIB, I. H. M., GEPSTEIN, L. & LEVENBERG, S. 2007. Tissue Engineering of Vascularized Cardiac Muscle From Human Embryonic Stem Cells. *Circulation Research*, 100, 263-272.
- CELIZ, A. D., SMITH, J. G., LANGER, R., ANDERSON, D. G., WINKLER, D. A., BARRETT, D. A., DAVIES, M. C., YOUNG, L. E., DENNING, C. & ALEXANDER, M. R. 2014a. Materials for stem cell factories of the future. *Nat Mater*, 13, 570-9.
- CELIZ, A. D., SMITH, J. G. W., PATEL, A. K., LANGER, R., ANDERSON, D. G., BARRETT, D. A., YOUNG, L. E., DAVIES, M. C., DENNING, C. & ALEXANDER, M. R. 2014b. Chemically diverse polymer microarrays and high throughput surface characterisation: a method for discovery of materials for stem cell culture. *Biomaterials Science*, 2, 1604-1611.
- CHARRAS, G. & SAHAI, E. 2014. Physical influences of the extracellular environment on cell migration. *Nat Rev Mol Cell Biol*, 15, 813-24.
- CHRISTMAS, B., KEMMERER, R. & KOSNIK, F. UV/EB Curing Technology: A Short History. 1986 Dordrecht. Springer Netherlands, 331-337.

CISNEROS-PINEDA, O. G., HERRERA KAO, W., LORIA-BASTARRACHEA, M. I., VERANES-PANTOJA, Y., CAUICH-RODRIGUEZ, J. V. & CERVANTES-UC, J. M. 2014. Towards optimization of the silanization process of hydroxyapatite for its use in bone cement formulations. *Mater Sci Eng C Mater Biol Appl*, 40, 157-63.

CIUCIU, A. I. & CYWIŃSKI, P. J. 2014. Two-photon polymerization of hydrogels – versatile solutions to fabricate well-defined 3D structures. *RSC Advances*, 4, 45504-45516.

CURTIS, A. S., FORRESTER, J. V., MCINNES, C. & LAWRIE, F. 1983. Adhesion of cells to polystyrene surfaces. *J Cell Biol*, 97, 1500-6.

DAHLMANN, J., KENSAH, G., KEMPF, H., SKVORC, D., GAWOL, A., ELLIOTT, D. A., DRÄGER, G., ZWEIGERDT, R., MARTIN, U. & GRUH, I. 2013. The use of agarose microwells for scalable embryoid body formation and cardiac differentiation of human and murine pluripotent stem cells. *Biomaterials*, 34, 2463-2471.

DALBY, M. J., GADEGAARD, N., TARE, R., ANDAR, A., RIEHLE, M. O., HERZYK, P., WILKINSON, C. D. & OREFFO, R. O. 2007. The control of human mesenchymal cell differentiation using nanoscale symmetry and disorder. *Nat Mater*, 6, 997-1003.

DATTOLA, E., PARROTTA, E. I., SCALISE, S., PEROZZIELLO, G., LIMONGI, T., CANDELORO, P., COLUCCIO, M. L., MALETTA, C., BRUNO, L., DE ANGELIS, M. T., SANTAMARIA, G., MOLLACE, V., LAMANNA, E., DI FABRIZIO, E. & CUDA, G. 2019. Development of 3D PVA scaffolds for cardiac tissue engineering and cell screening applications. *RSC Advances*, 9, 4246-4257.

DAVIDSON, R. S. 1999. *Exploring the Science, Technology and Applications of U.V. and E.B. Curing*, Sita Tecnology Limited.

DE SCHRIJVER, F. & SMETS, G. 1966. Polymerization kinetics in highly viscous media. *Journal of Polymer Science Part A-1: Polymer Chemistry*, 4, 2201-2210.

DECKER, C. 1998. The use of UV irradiation in polymerization. *Polymer International*, 45, 133-141.

DECKER, C. 2001. UV-radiation curing chemistry. *Pigment & Resin Technology*, 30, 278-286.

DECKER, C., NGUYEN THI VIET, T. & PHAM THI, H. 2001. Photoinitiated cationic polymerization of epoxides. *Polymer International*, 50, 986-997.

DENNING, C., BORGDORFF, V., CRUTCHLEY, J., FIRTH, K. S., GEORGE, V., KALRA, S., KONDRASHOV, A., HOANG, M. D., MOSQUEIRA, D., PATEL, A., PRODANOV, L., RAJAMOHAN, D., SKARNES, W. C., SMITH, J. G. & YOUNG, L. E. 2016. Cardiomyocytes from human pluripotent stem cells: From laboratory curiosity to industrial biomedical platform. *Biochim Biophys Acta*, 1863, 1728-48.

DENT, S. A. 2005. Introduction, Basic Theory and Principles. *Modern Raman Spectroscopy – A Practical Approach*.

DORAISWAMY, A., JIN, C., NARAYAN, R. J., MAGESWARAN, P., MENTE, P., MODI, R., AUYEUNG, R., CHRISEY, D. B., OVSIANIKOV, A. & CHICHKOV, B. 2006. Two photon induced polymerization of organic-inorganic hybrid biomaterials for microstructured medical devices. *Acta Biomater*, 2, 267-75.

EFE, J. A., HILCOVE, S., KIM, J., ZHOU, H., OUYANG, K., WANG, G., CHEN, J. & DING, S. 2011. Conversion of mouse fibroblasts into cardiomyocytes using a direct reprogramming strategy. *Nat Cell Biol*, 13, 215-22.

EMONS, M., OBATA, K., BINHAMMER, T., OVSIANIKOV, A., CHICHKOV, B. N. & MORGNER, U. 2012. Two-photon polymerization technique with sub-50 nm resolution by sub-10 fs laser pulses. *Optical Materials Express*, 2, 942-947.

EVANS-ANDERSON, H. J., ALFIERI, C. M. & YUTZEY, K. E. 2008. Regulation of cardiomyocyte proliferation and myocardial growth during development by FOXO transcription factors. *Circ Res*, 102, 686-94.

GANJI, Y., LI, Q., QUABIUS, E. S., BÖTTNER, M., SELHUBER-UNKEL, C. & KASRA, M. 2016. Cardiomyocyte behavior on biodegradable polyurethane/gold nanocomposite scaffolds under electrical stimulation. *Materials Science and Engineering: C*, 59, 10-18.

GRADY, M. C., SIMONSICK, W. J. & HUTCHINSON, R. A. 2002. Studies of higher temperature polymerization of n-butyl methacrylate and n-butyl acrylate. *Macromolecular Symposia*, 182, 149-168.

GUCK, J., LAUTENSCHLAGER, F., PASCHKE, S. & BEIL, M. 2010. Critical review: cellular mechanobiology and amoeboid migration. *Integr Biol (Camb)*, 2, 575-83.

HARRISON, R. G. 1912. The cultivation of tissues in extraneous media as a method of morpho-genetic study. *The Anatomical Record*, 6, 181-193.

HOOKE, A. L., SCURR, D. J., BURLEY, J. C., LANGER, R., ANDERSON, D. G., DAVIES, M. C. & ALEXANDER, M. R. 2013. Analysis and prediction of defects in UV photo-initiated polymer microarrays. *Journal of Materials Chemistry B*, 1, 1035-1043.

HUANG, S., YANG, Y., YANG, Q., ZHAO, Q. & YE, X. 2018. Engineered circulatory scaffolds for building cardiac tissue. *J Thorac Dis*, 10, S2312-S2328.

HUYER, L. D., MONTGOMERY, M., ZHAO, Y., XIAO, Y., CONANT, G., KOROLJ, A. & RADISIC, M. 2015. Biomaterial based cardiac tissue engineering and its applications. *Biomed Mater*, 10, 034004.

IFKOVITS, J. L. & BURDICK, J. A. 2007. Review: photopolymerizable and degradable biomaterials for tissue engineering applications. *Tissue Eng*, 13, 2369-85.

JANSEN, J. F. G. A., DIAS, A. A., DORSCHU, M. & COUSSENS, B. 2003. Fast Monomers: Factors Affecting the Inherent Reactivity of Acrylate Monomers in Photoinitiated Acrylate Polymerization. *Macromolecules*, 36, 3861-3873.

JIANG, L. J., CAMPBELL, J. H., LU, Y. F., BERNAT, T. & PETTA, N. 2016. Direct Writing Target Structures by Two-Photon Polymerization. *Fusion Science and Technology*, 70, 295-309.

JIANG, Y., PARK, P., HONG, S.-M. & BAN, K. 2018. Maturation of Cardiomyocytes Derived from Human Pluripotent Stem Cells: Current Strategies and Limitations. *Molecules and cells*, 41, 613-621.

JUODKAZIS, S., MIZEIKIS, V., SEET, K. K., MIWA, M. & MISAWA, H. 2005. Two-photon lithography of nanorods in SU-8 photoresist. *Nanotechnology*, 16, 846-849.

KAMALAK, H., KAMALAK, A., TAGHIZADEHGHALEHJOUGHFI, A., HACIMÜFTÜOĞLU, A. & NALCİ, K. A. 2018. Cytotoxic and biological

effects of bulk fill composites on rat cortical neuron cells. *Odontology*, 106, 377-388.

KATTMAN, S. J., WITTY, A. D., GAGLIARDI, M., DUBOIS, N. C., NIAPOUR, M., HOTTA, A., ELLIS, J. & KELLER, G. 2011. Stage-Specific Optimization of Activin/Nodal and BMP Signaling Promotes Cardiac Differentiation of Mouse and Human Pluripotent Stem Cell Lines. *Cell Stem Cell*, 8, 228-240.

KHALIL, S. K. H., ALLAM, M. A. & TAWFIK, W. A. 2007. Use of FT-Raman Spectroscopy to Determine the Degree of Polymerization of Dental Composite Resin Cured with a New Light Source. *European journal of dentistry*, 1, 72-79.

KIM, K., DOI, A., WEN, B., NG, K., ZHAO, R., CAHAN, P., KIM, J., ARYEE, M. J., JI, H., EHRLICH, L. I., YABUUCHI, A., TAKEUCHI, A., CUNNIFF, K. C., HONGGUANG, H., MCKINNEY-FREEMAN, S., NAVEIRAS, O., YOON, T. J., IRIZARRY, R. A., JUNG, N., SEITA, J., HANNA, J., MURAKAMI, P., JAENISCH, R., WEISSLEDER, R., ORKIN, S. H., WEISSMAN, I. L., FEINBERG, A. P. & DALEY, G. Q. 2010. Epigenetic memory in induced pluripotent stem cells. *Nature*, 467, 285-90.

KLEINMAN, H. K., LUCKENBILL-EDDS, L., CANNON, F. W. & SEPHEL, G. C. 1987. Use of extracellular matrix components for cell culture. *Anal Biochem*, 166, 1-13.

KLEINMAN, H. K., MCGARVEY, M. L., LIOTTA, L. A., ROBEY, P. G., TRYGGVASON, K. & MARTIN, G. R. 1982. Isolation and characterization of type IV procollagen, laminin, and heparan sulfate proteoglycan from the EHS sarcoma. *Biochemistry*, 21, 6188-93.

KLIMANSKAYA, I. 2019. Chapter 7 - Embryonic Stem Cells: Derivation, Properties, and Challenges. In: ATALA, A., LANZA, R., MIKOS, A. G. & NEREM, R. (eds.) *Principles of Regenerative Medicine (Third Edition)*. Boston: Academic Press.

KULANGARA, K. & LEONG, K. W. 2009. Substrate topography shapes cell function. *Soft Matter*, 5, 4072-4076.

LEE, M.-J., KIM, M.-J., KWON, J.-S., LEE, S.-B. & KIM, K.-M. 2017. Cytotoxicity of Light-Cured Dental Materials according to Different Sample Preparation Methods. *Materials*, 10, 288.

- LEE, S. H., MOON, J. J. & WEST, J. L. 2008. Three-dimensional micropatterning of bioactive hydrogels via two-photon laser scanning photolithography for guided 3D cell migration. *Biomaterials*, 29, 2962-8.
- LEWANDOWSKI, J., ROZWADOWSKA, N., KOLANOWSKI, T. J., MALCHER, A., ZIMNA, A., RUGOWSKA, A., FIEDOROWICZ, K., ŁABĘDŹ, W., KUBASZEWSKI, Ł., CHOJNACKA, K., BEDNAREK-RAJEWSKA, K., MAJEWSKI, P. & KURPISZ, M. 2018. The impact of in vitro cell culture duration on the maturation of human cardiomyocytes derived from induced pluripotent stem cells of myogenic origin. *Cell Transplantation*, 27, 1047-1067.
- LIANG, G. & ZHANG, Y. 2013. Genetic and epigenetic variations in iPSCs: potential causes and implications for application. *Cell Stem Cell*, 13, 149-59.
- LUNDY, S. D., ZHU, W. Z., REGNIER, M. & LAFLAMME, M. A. 2013. Structural and functional maturation of cardiomyocytes derived from human pluripotent stem cells. *Stem Cells Dev*, 22, 1991-2002.
- MAGUIRE, C. T., SUNDERLAND, R., DEMAREST, B., GORSI, B., JACKSON, J., LOPEZ-IZQUIERDO, A., TRISTANI-FIROUZI, M., YOST, H. J. & CONDIC, M. L. 2018. Deriving Cardiomyocytes from Human Amniocytes. *bioRxiv*, 475624.
- MARUO, S., NAKAMURA, O. & KAWATA, S. 1997. Three-dimensional microfabrication with two-photon-absorbed photopolymerization. *Optics Letters*, 22, 132-134.
- MCGOVERN, M. E., KALLURY, K. M. R. & THOMPSON, M. 1994. Role of Solvent on the Silanization of Glass with Octadecyltrichlorosilane. *Langmuir*, 10, 3607-3614.
- MEI, Y., SAHA, K., BOGATYREV, S. R., YANG, J., HOOK, A. L., KALCIOGLU, Z. I., CHO, S.-W., MITALIPOVA, M., PYZOCHA, N., ROJAS, F., VAN VLIET, K. J., DAVIES, M. C., ALEXANDER, M. R., LANGER, R., JAENISCH, R. & ANDERSON, D. G. 2010. Combinatorial development of biomaterials for clonal growth of human pluripotent stem cells. *Nature materials*, 9, 768-778.
- MONTICELLI, F., TOLEDANO, M., OSORIO, R. & FERRARI, M. 2006. Effect of temperature on the silane coupling agents when bonding core resin to quartz fiber posts. *Dent Mater*, 22, 1024-8.



MOORMAN, A., WEBB, S., BROWN, N. A., LAMERS, W. & ANDERSON, R. H. 2003. Development of the heart: (1) formation of the cardiac chambers and arterial trunks. *Heart (British Cardiac Society)*, 89, 806-814.

NAKAGAWA, T., TANAKA, T., NIWA, D., OSAKA, T., TAKEYAMA, H. & MATSUNAGA, T. 2005. Fabrication of amino silane-coated microchip for DNA extraction from whole blood. *J Biotechnol*, 116, 105-11.

NARITA, H., SHIMA, F., YOKOYAMA, J., MIYAGAWA, S., TSUKAMOTO, Y., TAKAMURA, Y., HIURA, A., FUKUMOTO, K., CHIBA, T., WATANABE, S., SAWA, Y., AKASHI, M. & SHIMODA, H. 2017. Engraftment and morphological development of vascularized human iPS cell-derived 3D-cardiomyocyte tissue after xenotransplantation. *Scientific Reports*, 7, 13708.

NAZIR, R., DANILEVICIUS, P., CIUCIU, A. I., CHATZINIKOLAIDOU, M., GRAY, D., FLAMIGNI, L., FARSARI, M. & GRYKO, D. T. 2014.  $\pi$ -Expanded Ketocoumarins as Efficient, Biocompatible Initiators for Two-Photon-Induced Polymerization. *Chemistry of Materials*, 26, 3175-3184.

NIKKHAH, M., EDALAT, F., MANOUCHERI, S. & KHADEMHOSEINI, A. 2012. Engineering microscale topographies to control the cell-substrate interface. *Biomaterials*, 33, 5230-46.

NUNES, S. S., MIKLAS, J. W., LIU, J., ASCHAR-SOBBI, R., XIAO, Y., ZHANG, B., JIANG, J., MASSÉ, S., GAGLIARDI, M., HSIEH, A., THAVANDIRAN, N., LAFLAMME, M. A., NANTHAKUMAR, K., GROSS, G. J., BACKX, P. H., KELLER, G. & RADISIC, M. 2013. Biowire: a platform for maturation of human pluripotent stem cell-derived cardiomyocytes. *Nature methods*, 10, 781-787.

OUELLETTE, R. J. & RAWN, J. D. 2015. 15 - Synthetic Polymers. In: OUELLETTE, R. J. & RAWN, J. D. (eds.) *Principles of Organic Chemistry*. Boston: Elsevier.

PASTERNAK, R. M., RIVILLON AMY, S. & CHABAL, Y. J. 2008. Attachment of 3-(aminopropyl)triethoxysilane on silicon oxide surfaces: Dependence on solution temperature. *Langmuir*, 24, 12963.

PATEL, A. K., CELIZ, A. D., RAJAMOHAN, D., ANDERSON, D. G., LANGER, R., DAVIES, M. C., ALEXANDER, M. R. & DENNING, C. 2015. A defined synthetic substrate for serum-free culture of human stem cell derived cardiomyocytes with improved functional maturity identified using combinatorial materials microarrays. *Biomaterials*, 61, 257-65.

PETERSEN, R. C., REDDY, M. S. & LIU, P. R. 2018. Advancements in Free-Radical Pathologies and an Important Treatment Solution with a Free-Radical Inhibitor. *SF journal of biotechnology and biomedical engineering*, 1, 1003.

PHILLIPS, D. H. & FARMER, P. B. 1994. Evidence for DNA and protein binding by styrene and styrene oxide. *Crit Rev Toxicol*, 24 Suppl, S35-46.

PULAY, P. 2008. *Vibrational Spectroscopy of Polymers: Principles and Practice* Edited by Neil J. Everall (ICI Measurement Science Group, Wilton, U.K.), John M. Chalmers (VS Consulting, Stokesley, U.K.), and Peter R. Griffiths (University of Idaho, Moscow, ID). John Wiley & Sons, Ltd: Chichester. 2007. xii + 574 pp. \$260. ISBN 978-0-470-01662-6. *Journal of the American Chemical Society*, 130, 5000-5000.

PURTOV, J., VERCH, A., ROGIN, P. & HENSEL, R. 2018. Improved development procedure to enhance the stability of microstructures created by two-photon polymerization. *Microelectronic Engineering*, 194, 45-50.

QUEENEY, K. T., WELDON, M. K., CHANG, J. P., CHABAL, Y. J., GUREVICH, A. B., SAPJETA, J. & OPILA, R. L. 2000. Infrared spectroscopic analysis of the Si/SiO<sub>2</sub> interface structure of thermally oxidized silicon. *J. Appl. Phys.*, 87, 1322.

RICCI, D., NAVA, M. M., ZANDRINI, T., CERULLO, G., RAIMONDI, M. T. & OSELLAME, R. 2017. Scaling-Up Techniques for the Nanofabrication of Cell Culture Substrates via Two-Photon Polymerization for Industrial-Scale Expansion of Stem Cells. *Materials (Basel)*, 10.

SALICK, M. R., NAPIWOCKI, B. N., SHA, J., KNIGHT, G. T., CHINDHY, S. A., KAMP, T. J., ASHTON, R. S. & CRONE, W. C. 2014. Micropattern width dependent sarcomere development in human ESC-derived cardiomyocytes. *Biomaterials*, 35, 4454-64.

SÁNCHEZ, E. J., NOVOTNY, L., HOLTOM, G. R. & XIE, X. S. 1997. Room-Temperature Fluorescence Imaging and Spectroscopy of Single Molecules by Two-Photon Excitation. *The Journal of Physical Chemistry A*, 101, 7019-7023.

SARIG, U., AU-YEUNG, G. C. T., WANG, Y., BRONSHTEN, T., DAHAN, N., BOEY, F. Y. C., VENKATRAMAN, S. S. & MACHLUF, M. 2012. Thick acellular heart extracellular matrix with inherent vasculature: a potential platform for myocardial tissue regeneration. *Tissue engineering. Part A*, 18, 2125-2137.

SAYED, N., LIU, C. & WU, J. C. 2016. Translation of Human-Induced Pluripotent Stem Cells: From Clinical Trial in a Dish to Precision Medicine. *J Am Coll Cardiol*, 67, 2161-2176.

SCHAEFER, J. A., GUZMAN, P. A., RIEMENSCHNEIDER, S. B., KAMP, T. J. & TRANQUILLO, R. T. 2018. A cardiac patch from aligned microvessel and cardiomyocyte patches. *J Tissue Eng Regen Med*, 12, 546-556.

SCHAFER, K. J., HALES, J. M., BALU, M., BELFIELD, K. D., VAN STRYLAND, E. W. & HAGAN, D. J. 2004. Two-photon absorption cross-sections of common photoinitiators. *Journal of Photochemistry and Photobiology A: Chemistry*, 162, 497-502.

SCHOLTEN, K. & MENG, E. 2016. Electron-beam lithography for polymer bioMEMS with submicron features. *Microsystems & Nanoengineering*, 2, 16053.

SILBERNAGEL, N., KÖRNER, A., BALITZKI, J., JAGGY, M., BERTELS, S., RICHTER, B., HIPPLER, M., HELLWIG, A., HECKER, M., BASTMEYER, M. & ULLRICH, N. D. 2020. Shaping the heart: Structural and functional maturation of iPSC-cardiomyocytes in 3D-micro-scaffolds. *Biomaterials*, 227, 119551.

SILBERZAN, P., LEGER, L., AUSSERRE, D. & BENATTAR, J. J. 1991. Silanation of silica surfaces. A new method of constructing pure or mixed monolayers. *Langmuir*, 7, 1647-1651.

SILVA, J. P. & COUTINHO, O. P. 2010. Free radicals in the regulation of damage and cell death - basic mechanisms and prevention. *Drug Discov Ther*, 4, 144-67.

SPATER, D., HANSSON, E. M., ZANGI, L. & CHIEN, K. R. 2014. How to make a cardiomyocyte. *Development*, 141, 4418-31.

SRINIVASAN, S., LEE, M. W., GRADY, M. C., SOROUSH, M. & RAPPE, A. M. 2010. Self-Initiation Mechanism in Spontaneous Thermal Polymerization of Ethyl and n-Butyl Acrylate: A Theoretical Study. *The Journal of Physical Chemistry A*, 114, 7975-7983.

SWORD, E. D. Humidity-induced damage in polyvinyl toluene and polystyrene plastic scintillator. 2017 IEEE International Symposium on Technologies for Homeland Security (HST), 25-26 April 2017 2017. 1-4.

- TAKAHASHI, K. & YAMANAKA, S. 2006. Induction of pluripotent stem cells from mouse embryonic and adult fibroblast cultures by defined factors. *Cell*, 126, 663-76.
- TAORMINA, G., SCIANCALEPORE, C., MESSORI, M. & BONDIOLI, F. 2018. 3D printing processes for photocurable polymeric materials: technologies, materials, and future trends. *Journal of Applied Biomaterials & Functional Materials*, 16, 151-160.
- TAYALIA, P., MENDONCA, C. R., BALDACCHINI, T., MOONEY, D. J. & MAZUR, E. 2008. 3D Cell-Migration Studies using Two-Photon Engineered Polymer Scaffolds. *Advanced Materials*, 20, 4494-4498.
- TEIXEIRA, A. I., ABRAMS, G. A., BERTICS, P. J., MURPHY, C. J. & NEALEY, P. F. 2003. Epithelial contact guidance on well-defined micro- and nanostructured substrates. *J Cell Sci*, 116, 1881-92.
- THAM, W. L., CHOW, W. S. & ISHAK, Z. A. M. 2010. The effect of 3-(trimethoxysilyl) propyl methacrylate on the mechanical, thermal, and morphological properties of poly(methyl methacrylate)/hydroxyapatite composites. *Journal of Applied Polymer Science*, 118, 218-228.
- THOMSON, K. S., KORTE, F. S., GIACHELLI, C. M., RATNER, B. D., REGNIER, M. & SCATENA, M. 2013. Prevascularized microtemplated fibrin scaffolds for cardiac tissue engineering applications. *Tissue Eng Part A*, 19, 967-77.
- TROMAYER, M., GRUBER, P., MARKOVIC, M., ROSSPEINTNER, A., VAUTHEY, E., REDL, H., OVSIANIKOV, A. & LISKA, R. 2017. A biocompatible macromolecular two-photon initiator based on hyaluronan. *Polymer Chemistry*, 8, 451-460.
- VANDENBERG, E. T., BERTILSSON, L., LIEDBERG, B., UVDAL, K., ERLANDSSON, R., ELWING, H. & LUNDSTRÖM, I. 1991. Structure of 3-aminopropyl triethoxy silane on silicon oxide. *J. Colloid Interface Sci.*, 147, 103.
- WANG, C., LIU, W., SHEN, Y., CHEN, J., ZHU, H., YANG, X., JIANG, X., WANG, Y. & ZHOU, J. 2019. Cardiomyocyte dedifferentiation and remodeling in 3D scaffolds to generate the cellular diversity of engineering cardiac tissues. *Biomaterials Science*, 7, 4636-4650.
- WANG, C., YOU, H. & LIN, Y. Facile oxygen-plasma approach for depositing Silicon/nitride oxide on transparent, flexible zinc-oxide thin film transistors.

2014 21st International Workshop on Active-Matrix Flatpanel Displays and Devices (AM-FPD), 2-4 July 2014 2014. 109-112.

WEI, H., TAN, G., MANASI, QIU, S., KONG, G., YONG, P., KOH, C., OOI, T. H., LIM, S. Y., WONG, P., GAN, S. U. & SHIM, W. 2012. One-step derivation of cardiomyocytes and mesenchymal stem cells from human pluripotent stem cells. *Stem Cell Res*, 9, 87-100.

WEISS, P. & WANG, H. 1945. Transformation of Adult Schwann Cells Into Macrophages. *Proceedings of the Society for Experimental Biology and Medicine*, 58, 273-275.

YIM, E. K., PANG, S. W. & LEONG, K. W. 2007. Synthetic nanostructures inducing differentiation of human mesenchymal stem cells into neuronal lineage. *Exp Cell Res*, 313, 1820-9.

YUE, X.-S., FUJISHIRO, M., NISHIOKA, C., ARAI, T., TAKAHASHI, E., GONG, J.-S., AKAIKE, T. & ITO, Y. 2012. Feeder cells support the culture of induced pluripotent stem cells even after chemical fixation. *PloS one*, 7, e32707-e32707.

YUK, H., ZHANG, T., LIN, S., PARADA, G. A. & ZHAO, X. 2016. Tough bonding of hydrogels to diverse non-porous surfaces. *Nature materials*, 15, 190-196.

ZHANG, J., KLOS, M., WILSON, G. F., HERMAN, A. M., LIAN, X., RAVAL, K. K., BARRON, M. R., HOU, L., SOERENS, A. G., YU, J., PALECEK, S. P., LYONS, G. E., THOMSON, J. A., HERRON, T. J., JALIFE, J. & KAMP, T. J. 2012. Extracellular matrix promotes highly efficient cardiac differentiation of human pluripotent stem cells: the matrix sandwich method. *Circ Res*, 111, 1125-36.

ZHONG, N., ZHAO, M., LIAO, Q., ZHU, X., LI, Y. & XIONG, Z. 2016. Effect of heat treatments on the performance of polymer optical fiber sensor. *Opt Express*, 24, 13394-409.

ZHOU, X., HOU, Y. & LIN, J. 2015. A review on the processing accuracy of two-photon polymerization. *AIP Advances*, 5, 030701.

ZIEBER, L., OR, S., RUVINOV, E. & COHEN, S. 2014. Microfabrication of channel arrays promotes vessel-like network formation in cardiac cell construct and vascularization in vivo. *Biofabrication*, 6, 024102.